



HAL
open science

Clogging dynamics of a porous medium by colloidal particles

Nolwenn Delouche

► **To cite this version:**

Nolwenn Delouche. Clogging dynamics of a porous medium by colloidal particles. Mechanics of materials [physics.class-ph]. Université de Rennes, 2021. English. NNT: 2021REN1S137. tel-04416447

HAL Id: tel-04416447

<https://theses.hal.science/tel-04416447>

Submitted on 25 Jan 2024

HAL is a multi-disciplinary open access archive for the deposit and dissemination of scientific research documents, whether they are published or not. The documents may come from teaching and research institutions in France or abroad, or from public or private research centers.

L'archive ouverte pluridisciplinaire **HAL**, est destinée au dépôt et à la diffusion de documents scientifiques de niveau recherche, publiés ou non, émanant des établissements d'enseignement et de recherche français ou étrangers, des laboratoires publics ou privés.

THESE DE DOCTORAT DE

L'UNIVERSITE DE RENNES 1

ECOLE DOCTORALE N° 596

Matière, Molécules, Matériaux

Spécialité : *Physique*

Par

« **Nolwenn DELOUCHE** »

« **Dynamique de colmatage d'un milieu poreux par des particules colloïdales** »

Thèse présentée et soutenue à Rennes, le 15 décembre 2021

Unité de recherche : Institut de physique de Rennes - UMR 6251

Thèse N° :

Rapporteurs avant soutenance :

Martine MEIRELES

Directrice de recherche, LGC - Université de Toulouse III

Alban SAURET

Assistant professor, Engineering II – University of California Santa Barbara

Composition du Jury :

Examineurs : Emilie DRESSAIRE

Assistant professor, Engineering II – University of California Santa Barbara

Janine EMILE

Professeure des universités, IPR - Université de Rennes I

Pascal PANIZZA

Professeur des universités, IPR – Université de Rennes I

Dir. de thèse : Hervé TABUTEAU

Chargé de recherche, IPR – Université de Rennes I

Invité(s)

Pietro DE ANNA

Associate professor, ISTE - University of Lausanne

Olivier LIOT

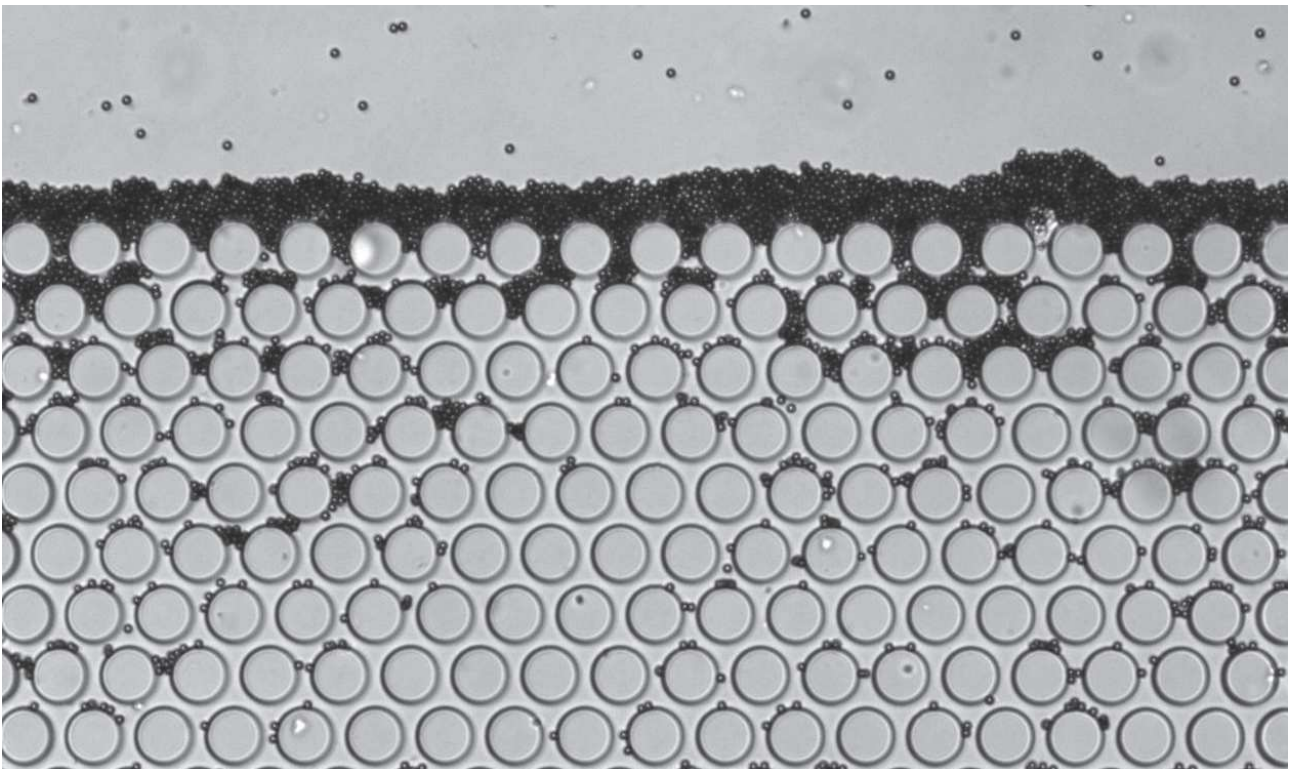
Maître de conférences, IMFT – Université de Toulouse III

Clogging dynamics of a porous medium by colloidal particles

Thesis presented by
Nolwenn DELOUCHE

Supervised by
Hervé TABUTEAU

Thesis defended on December 15th, 2021



(cover picture) A porous medium clogged with 5 μ m particles.

Le travail de thèse que j'ai eu le plaisir de mener à l'Institut de Physique de Rennes n'aurait pas pu se dérouler dans de meilleures conditions grâce à l'accompagnement de plusieurs personnes que je souhaite remercier ici.

Je remercie tout d'abord mon directeur de thèse pour son accompagnement et sa disponibilité tout au long de ma thèse. Hervé, merci de m'avoir donné l'opportunité de m'épanouir dans ma recherche en me laissant libre de choisir la direction à prendre pour ma recherche. Je garderai un excellent souvenir de ces fameuses discussions de 3-4h pour faire avancer ma thèse mais également les différents projets que j'ai pu mener en parallèle et pour lesquels tu m'as accordé ta confiance. Un grand merci pour ton engagement dans ma thèse qui a fait la différence.

Je remercie les gens avec qui j'ai eu le plaisir de collaborer pendant la thèse. Sunniva Pinnabel qui apporte joie et bonheur au laboratoire, Alice Pradel qui m'a énormément apporté scientifiquement et humainement et Julien Gigault pour sa proposition de projet de nanoplastiques fragmentés.

Je voudrais remercier plusieurs personnes qui ont eu beaucoup d'impact pour ce projet de thèse. Janine Emile pour sa confiance dès le début et avec qui j'ai eu le plaisir de partager bureau et discussions pendant la thèse. Pietro de Anna pour m'avoir transmis le goût de la recherche et sans qui cette thèse n'aurait peut-être pas été possible. Luc Oger pour ses conseils et son aide.

Merci également à tous les doctorants et postdoctorants avec qui j'ai pu échanger durant ces trois années. Je remercie mes collègues du département milieux divisés, JB pour ton amitié et ces pauses/balades indispensables, Jean-Luc pour ta générosité et ton écoute. Mais également mes collègues du département matière molle : Donatien, ma première rencontre littéralement à la porte de l'IPR et qui a été un ami mais également un modèle scientifique, Lucas pour tous ces M11 partagés, Charlène pour ta gentillesse, Arnaud pour les repas et tes photos de chats, Théo pour tous nos échanges qui ont refait le monde académique et le café, Alexis pour ton temps que tu donnes sans compter. Aux doctorants d'ailleurs : Lorène pour MT180, le thé, nos balades de rédactions et ton soutien moral indéfectible. Antho et Mayumi pour les appels de toute heure.

Je terminerai par remercier ma famille qui m'a toujours soutenu durant ces études.

Contents

1	Introduction	17
1.1	General introduction	18
1.2	At the particle scale	22
1.2.1	Particle transport	22
1.2.1.1	Hydrodynamics in microchannel	22
1.2.1.2	Forces acting on particles	25
1.2.2	Attachment mechanisms	27
1.2.2.1	Electrostatic interactions	27
1.2.2.2	Van der Waals	28
1.2.2.3	Born repulsion	29
1.2.2.4	The DLVO theory	29
1.2.3	Particle adsorption	30
1.2.3.1	Surface roughness: the first deposited particle	30
1.2.3.2	From the monolayer to the growth of the deposit	31
1.2.3.3	Deposition versus erosion	33
1.3	From the single pore to the porous media clogging	35
1.3.1	Clogging of a single pore	35
1.3.1.1	Particles accumulation behind the clog	40
1.3.1.2	Backwashing of the pore	41
1.3.2	Clogging of porous media	42
1.3.2.1	Pore cross-talk	42
1.3.2.2	Clog front at the entrance of 2D and 3D porous media	42
1.3.2.3	Impact of internal tortuosity and connectivity within a porous medium	43
1.3.2.4	Cake layer	44
1.4	Thesis objectives	45
2	Materials and methods	47
2.1	Description of a typical microfluidic experiment	48
2.1.1	Camera	48
2.1.2	Microscopy and micrometric particle	49
2.1.2.1	Brightfield microscopy	49
2.1.2.2	Fluorescent microscopy	50
2.1.2.3	Diffraction and focal plane	50
2.1.3	Microfluidic technique	52
2.1.3.1	Softlithography and microfabrication	52
2.1.3.2	Hydrodynamic resistance characterization of microfluidic chips	54

2.1.3.3	PDMS microchannel deformation	54
2.1.4	Injection of the suspension in the microfluidic system	55
2.2	Particle suspension	56
2.2.1	Particle stabilization	56
2.2.1.1	Stabilization by surface charges	56
2.2.1.2	Steric stabilization	56
2.2.1.3	Summary of the properties of materials and particles	57
2.2.2	Monodisperse suspensions and aggregates	58
2.2.3	Fast Radial Symmetry (FRS)	58
2.2.3.1	Why the FRS ?	58
2.2.3.2	Definition of the FRS transform	59
2.2.4	Detection of aggregates dimensions	62
2.3	Image analysis	65
2.3.1	Particle tracking	65
2.3.1.1	Information from particle tracking	67
2.3.2	Automated detection of clogged pores in a porous medium	68
3	The impact of aggregates on clogging	75
3.1	There is no perfectly monodisperse suspension	76
3.2	Aggregates are responsible for clogs, whatever the conditions	76
3.3	The more relevant parameters impacting the clogging	78
3.3.1	The capture probability is strongly dependent of the flow rate	78
3.3.2	Ionic strength	79
3.4	Brief summary of the papers	80
4	The flow decline during the pore clogging	109
4.1	Two phases during the flow decline	110
4.2	A section reduction plus a progressive flow paths closure	110
4.3	From a heterogeneous to a homogeneous flow	112
4.4	Brief summary of the paper	112
5	Structure and flow conditions through a colloidal packed bed formed under confinement	135
5.1	How to estimate the features of the particle accumulation?	136
5.1.1	Limitations of the Kozeny-Carman relation	136
5.1.2	Permeability and volume fraction from the particle tracking	136
5.2	Dependence of the particle accumulation with the ionic strength and the pressure	137
5.2.1	Ionic strength	137
5.2.2	Pressure	138
5.3	Backwashing of the channel	138
5.4	Brief summary of the paper	139
6	The clogging of interconnected pores by colloidal particles	159
6.1	Experimental clogging of porous media	160
6.1.1	General description of a clogged porous media	160
6.1.2	Different clogging mechanisms	162
6.1.3	The strong dependence on pore clogging	164

6.1.4	Clogging is independent of the porous medium geometry and flow rate	166
6.2	Simulated clogging of porous media based on statistics	169
6.2.1	Four steps process	169
6.2.2	Modelling of the impact of aggregates on clogging	175
6.3	Conclusion	182
7	Impact of interaction potentials on the clogging of porous media	183
7.1	Description of a clogged porous medium by varying the interaction potentials	184
7.1.1	Towards larger aggregates with the ionic strength	184
7.1.2	Clogs concentration at the inlet whatever the suspension	185
7.2	From the deposit to the clogging	191
7.2.1	Differences in the deposit according to the salinity	191
7.2.2	A new clogging mechanisms based on dendrite	195
7.2.3	A competition between the clogging mechanisms	197
7.3	Variations in hydrodynamic conditions have little effect on clogging	201
7.4	Conclusion	204
8	Flow decline during the clogging of porous media	205
8.1	Context of the study	206
8.2	Experimental results	207
8.2.1	Impact on the particle size on the flow rate	207
8.2.2	Impact on the ionic strength on the flow rate	209
8.3	Modelization of the flow decline	210
8.3.1	Proposal n°1	212
8.3.2	Proposal n°2	214
8.3.3	Proposal n°3	216
8.3.4	Proposal n°4: perspectives	218
8.4	Conclusion	219
9	Clogging with fragmented colloidal plastics	221
9.1	Context of the study	222
9.2	The fragmented nanoplastics	223
9.2.1	Preparation of the fragmented nanoplastics	223
9.2.2	Characterization of the nanoplastic suspension	224
9.3	Importance of the polydispersity of the suspension	226
9.4	Deposition and clogging by NPT in a porous media	229
9.4.1	Quantification of the impact of polydispersity	231
9.4.2	Delay clogging with natural organic matter	234
9.5	Conclusion	235
10	Conclusion and perspectives	239

Résumé français

Introduction

La filtration d'un fluide contaminé à travers une membrane mène quasi-systématiquement à son colmatage. Les exemples les plus connus concernent la filtration d'air ou d'eau. Pendant la filtration, des objets se déposent continuellement à la surface de la membrane et génèrent une importante chute de débit, réduisant l'efficacité du processus de filtration, menant au nettoyage ou au remplacement de la membrane. Actuellement, aucune relation n'est faite entre la dynamique de colmatage de la membrane et cette chute de débit associée. Dans cette thèse, nous étudions le colmatage d'une membrane modèle par des microparticules de latex dispersées dans de l'eau pour faire le lien entre dynamique de formation du bouchon et variation de l'écoulement. Notre approche est multi-échelles et est axée en premier lieu à l'échelle de la particule avant de se concentrer à l'échelle du pore et du milieu poreux. Le processus de colmatage est un processus complexe, dépendant de plusieurs paramètres physico-chimiques comme les interactions inter-particules ou particule-paroi, les interactions hydrodynamiques qui favorisent ou limitent le dépôt d'objets, aussi bien que du degré de confinement, correspondant au ratio taille de particule sur taille du pore. Le premier chapitre de cette thèse présente dans une première partie les outils nécessaires à la compréhension de ces phénomènes, comme le transport des particules dans l'écoulement, les mécanismes d'attachements qui s'exercent à l'échelle de la particule et la description de l'adsorption des objets à la paroi. Les deuxième et troisième partie du chapitre sont consacrées à l'état de l'art du colmatage dit progressif avec des particules de tailles inférieures à la taille du pore en faible concentration, dans un pore uniquement puis dans un ensemble de pores interconnectés les uns aux autres. Pour finir, nous décrivons les objectifs de la thèse dans ce contexte. Nous cherchons notamment à savoir comment se produit le colmatage dit progressif et quelles sont les conséquences du colmatage des pores sur les conditions d'écoulement dans l'ensemble du milieu poreux.

Matériels et méthodes

Nous présentons premièrement dans ce chapitre l'expérience de microfluidique typique en décrivant les différents matériels et techniques utilisés comme la caméra, la microscopie, le processus de micro-fabrication et la mise en écoulement de suspension monodisperse à pression imposée. Nous proposons dans une deuxième partie la mise en place d'une méthode appelée stop-and-go permettant d'imager plus d'un million de particules afin d'obtenir des distributions de tailles fiables et plus détaillées que les méthodes de caractérisations actuelles. Nous avons détecté la présence d'agrégats composés de particules sphériques avec cette méthode. Nous présentons par la suite un traitement d'image développé pendant la thèse pour caractériser les objets, qui identifie le nombre de particule composant un agrégat grâce à l'algorithme de Fast Radial Symmetry et les dimensions des objets. Dans une dernière partie, nous introduisons l'algorithme de particle tracking optimisé pour la recherche d'objet, également développé pendant la thèse, ainsi qu'un algorithme de détection de bouchons basés sur cinq critères, qui nous permet d'automatiser le traitement d'image d'un milieu avec de multiples pores.

La thèse est décomposée en deux parties principales axée sur l'étude du colmate d'un pore unique puis sur le colmatage d'un milieu poreux ordonnées dont les pores sont interconnectés.

Partie I

L'objectif de cette partie est de décrire le processus de colmatage d'un pore unique, de la première particule déposée au colmatage complet du pore, particule par particule, jusqu'à ce qu'une accumulation de particules prenne place derrière le bouchon. Avec le *particle tracking*, nous mesurons la vitesse du fluide en suivant les objets et nous quantifions l'impact de chaque déposition sur l'écoulement. Dans le **chapitre 3**, nous avons constaté grâce à l'analyse d'image la présence d'agrégats composés de plusieurs particules sphériques dans les bouchons malgré l'utilisation de suspension monodisperse et alors que ces objets représentent moins de 1% de la population. Ces objets, même s'ils sont rares, ont été observés systématiquement dans le millier de bouchons analysés durant la thèse pour différentes natures de particules (PS, PMMA), stabilisations (stérique et électrostatique), origines (commerciales ou synthétisées en détail) et tailles. Nous avons également fait varier les conditions expérimentales comme le confinement, le débit ou la force ionique. En observant le comportement des agrégats, nous avons remarqué qu'ils effectuaient des rotations autour de leur centre de masse. A cause de cette rotation mais aussi de leur taille et forme, les bords de l'agrégats peuvent rencontrer la paroi du canal ou le dépôt et favoriser leur capture. Ce mécanisme a lieu quand la rotation de l'agrégat est déstabilisée ou quand l'agrégat tente d'orienter sa plus large dimension dans le sens de l'écoulement pour limiter sa résistance au fluide à l'entrée du pore. La probabilité de capture de ces objets est plus grande que pour des particules sphériques et dépend fortement de leur taille maximale. Une fois capturés, les larges agrégats réduisent la section du pore et permettent la capture de plus petits objets jusqu'à ce que le pore soit complètement colmaté. Puisque leur distribution de taille est large, la structure des bouchons varie beaucoup, dépendant également du nombre d'agrégat impliqués et menant ainsi à une structure unique pour chaque bouchon. Le mécanisme de capture des agrégats est lié à leur interception physique et est seulement affecté par des variations du débit et de la force ionique. Augmenter le débit mène à une érosion des plus petits objets et donc à une augmentation de la taille des agrégats capturés. De la même manière, quand la force ionique augmente proche de la concentration critique de coagulation (CCC), le nombre d'agrégat dans la suspension et dans le bouchon augmente.

Après avoir imagé l'ensemble des événements de dépôt, nous avons tenté dans le **chapitre 4** de comprendre la relation entre le colmatage progressif du pore et la chute de débit associée. Nous avons imagé à une cadence suffisamment importante pour suivre les objets sur une dizaine d'image afin d'obtenir la vitesse moyenne des particules avant leur entrée dans le pore et leur possible déposition. Nous avons ainsi obtenu une chute de vitesse en fonction de l'historique de dépôt des particules. A bas nombre de Reynolds, il est possible de faire l'analogie entre l'écoulement à travers un microcanal et la loi d'Ohm $\Delta P = R_H Q$. A pression constante, il est facile de faire le lien entre une augmentation de la résistance hydrodynamique R_H et la chute de débit. Deux principales contributions à la chute de débit ont été observées. Premièrement, le colmatage du pore, aussi appelée tête de bouchon, en réduisant la section du pore augmente fortement R_H . Par la suite, derrière la tête de bouchon, des particules s'accumulent sur une dizaine de micromètre et contribuent aussi à réduire significativement R_H . Chaque nouvelle déposition de particule contribue à modifier les chemins de répartition du fluide et augmentent leur tortuosité. Cette contribue résultat en une chute de débit presque aussi important que lors de la formation de la tête de bouchon. Nous avons vérifié ces deux contributions numériquement, en reconstruisant le pore particule par particule à l'aide de Comsol, ce qui nous a permis de déterminer les variations d'écoulement dans les pores du bouchon pour chaque nouvelle déposition de particule.

A la suite de la formation du bouchon, l'accumulation augmente significativement et peut atteindre 200 à 300 μm , avec un impact très limité sur la chute de débit. L'accumulation de particule crée un empilement de sphères dont les propriétés structurales comme la perméabilité et la fraction volumique peuvent être déterminé. Nous avons observé que l'augmentation de la longueur du bouchon est inversement proportionnelle à la vitesse du fluide, vérifiant bien que l'écoulement à travers le bouchon est un écoulement de Darcy. Nous avons analysé des images de confocal fournies par Benjamin Dersoir et observé que le milieu poreux formé par les particules est loin d'être homogène. Les particules sont concentrées proches des parois, avec une large zone libre au centre. Cette hétérogénéité exclut l'utilisation de relation comme Kozeny-Carman pour obtenir la perméabilité du bouchon ou sa fraction volumique moyenne. Nous avons donc déterminé dans le **chapitre 5** la fraction volumique en fonction de la longueur du bouchon à partir du nombre exact de particules dans chaque tranche du bouchon. La perméabilité est déduite de la relation entre la vitesse du fluide et la longueur du bouchon. Nous avons étudié l'évolution de la fraction volumique et de la perméabilité avec le débit et l'augmentation de la force ionique, jusqu'à la CCC. Nous avons montré que l'ensemble de la dynamique de l'empilement n'est pas modifié par la variation du débit puisque la fraction volumique moyenne reste constante. Cependant, cette fraction volumique peut être modifié par le confinement, avec un canal de petite section qui favorise la capture des objets à la paroi ou bien encore par l'augmentation du nombre d'agrégats dont la taille et la forme peuvent créer localement des défauts. Ces deux évènements empêchent l'accumulation de particule d'être un empilement idéal et augmente ainsi la perméabilité du bouchon.

Pour finir cette première partie de la thèse sur l'étude du pore unique, nous avons réalisé des expériences de décolmatage, semblable aux procédés de backwashing qui consiste en une inversion du sens de l'écoulement pendant les filtrations industrielles. Pendant le décolmatage, nous avons observé le comportement des accumulations de particules. Un bouchon peut être divisé en deux zones. A l'arrière de la tête de bouchon, une zone labile existe dans laquelle les particules sont uniquement maintenus par l'écoulement. Quand l'écoulement est inversé, les particules quittent l'accumulation individuellement. Nous avons observé des réarrangements dans cette zone, qui pourrait mener à la formation de zones cristallines à la paroi, montrant encore une fois que les particules sont libres de bouger dans cette zone. Cette transition locale d'amorphe à cristallin, même en impliquant un large nombre de particule, n'a aucun impact sur l'écoulement de perméation. A l'opposé, proche de la tête du bouchon, les particules forment une zone cohésive, qui reste compacte avec l'inversion de l'écoulement. La longueur de cette zone cohésive augmente avec le débit et la force ionique, jusqu'à ce qu'il n'y ait plus de zone labile. Nous avons émis l'hypothèse que la mesure de la vitesse des particules n'est pas suffisamment précise, à cause du très petit nombre d'objet impliqué dans l'accumulation pendant un évènement de réarrangement, ou bien que la compaction pourrait créer des chaînes de forces parmi les particules et les parois, qui limiterait la dispersion de l'accumulation pendant l'expérience de décolmatage. L'augmentation du nombre d'agrégat avec la force ionique pourrait aussi consolider les bouchons.

Partie II

Nous avons dans un premier temps décrit toutes les étapes du colmatage, des premières particules déposées au décolmatage d'un pore unique. Dans cette partie, nous étendons notre méthodologie à un milieu poreux 2D, qui peut être considéré comme le plus simple modèle de membrane. Nous voulons décrire la dynamique de colmatage dans l'ensemble du milieu poreux, en prenant en compte que les pores sont connectés les uns aux autres afin de comprendre l'impact du colmatage des pores sur les conditions d'écoulement. Première-

ment, dans le **chapitre 6**, nous avons décrit le colmatage dans un milieu poreux en observant la formation du dépôt et les différents mécanismes de colmatage impliqués. Pendant les expériences, nous avons injectés des particules monodisperses dans un milieu ordonné, avec des piliers ou des collecteurs équidistants, la charge de surface des particules tant suffisamment importante pour prévenir le dépôt de particule par diffusion. Notre principale observation est que le milieu poreux est colmaté à son entrée, quelles que soient les conditions d'écoulement ou la géométrie du milieu. Nous avons identifié deux mécanismes de colmatage, le bouchon dit original, qui est le même que celui décrit dans le pore unique, et le bouchon dit accumulation, formé derrière des bouchons originaux. Les bouchons originaux représentent la vaste majorité des bouchons. Comme avant, la formation des bouchons est liée à l'interception d'agrégat et une fois de plus, nous pouvons supposer que le colmatage du milieu est mené uniquement par la queue de distribution de la suspension et par la forte probabilité de capture des agrégats. Nous avons vérifié cette hypothèse en créant un modèle très simple, sans considération des forces hydrodynamiques ou des forces DLVO, pour comprendre comment la probabilité de capture et la distribution de taille des agrégats modifient la localisation du front de bouchon. Deuxièmement, dans le **chapitre 7**, nous avons modifié les charges de surfaces des objets en ajoutant du sel dans les suspensions, avec $I = 50\text{mM}$ et 300mM au-delà de la CCC. Pour $I = 50\text{mM}$, il n'y a pas de barrière électrostatique entre les particules et la paroi du pore, ce qui favorise le dépôt des objets. Dans ces conditions favorables, nous n'avons pas observé de différence notable pour la position du front de bouchon, excepter que plus de bouchons sont formés à l'intérieur du milieu avant son colmatage. Pour $I = 300\text{mM}$, la déposition d'objets est beaucoup plus importante dans l'ensemble du milieu et est à l'origine d'un troisième mécanisme de colmatage. Nous avons observé la formation de dépôt comme des dendrites aux sommets des piliers composant le milieu qui croissent de manière significative en amont des piliers, réduisant drastiquement les chemins disponibles pour les particules et pouvant mener au colmatage du pore. Nous avons désigné ces bouchons comme les bouchons dendrites. Cependant, quelque soit le mécanisme de colmatage, les milieux poreux sont toujours colmatés à leur entrée, montrant une fois de plus que la capture des agrégats prévaut, à cause de la forte probabilité de capture.

Finalement, nous avons vérifié dans le **chapitre 9** que le colmatage à l'entrée du milieu poreux a aussi lieu pour des suspensions polydisperses, en taille et en forme, en utilisant des suspensions de nanomicroplastiques fragmentés. Leur distribution de taille est centrée autour de 400nm , mais des objets peuvent facilement atteindre $1\text{-}2\mu\text{m}$ dans la queue de distribution. Nous avons étudié le processus de colmatage pour deux types de suspensions, une suspension avec 15% de la population d'objets micrométriques, et une suspension filtrée avec seulement 4% de la population. Le colmatage pour la suspension non filtrée est localisé dès l'entrée du milieu, alors que pour la suspension filtrée, le front de bouchon est situé plus loin dans le milieu. Pour les deux suspensions, les plus larges objets de la suspension sont les principaux contributeurs du colmatage des pores. Cependant ceux de la suspension filtrée, puisque plus petits, ont une plus faible probabilité d'être capturés et se déposent ainsi plus loin dans le milieu avant le colmatage des pores.

Pour conclure sur le colmatage du milieu poreux, dans le **chapitre 8** nous avons associé le degré de colmatage dans un milieu poreux par l'analyse d'image à la chute de débit, grâce au particle tracking comme nous l'avons fait à l'échelle du pore unique. Nous avons imagé la variation des conditions d'écoulement pour différentes tailles de particules et de forces ioniques pour voir leur impact sur la chute du débit puisqu'ils impliquent différents processus de colmatage. Nous avons vérifié expérimentalement une forte dépendance de la formation des bouchons dans la première ligne avec l'augmentation de la résistance hydrodynamique. Initialement, quelques pores sont colmatés sans avoir de réel impact sur la résistance du milieu poreux.

Cependant, quand les pores colmatés sont concentrés dans la même zone alors la résistance hydrodynamique locale augmente fortement et la formation d'un gâteau de filtration est initiée. Ces augmentations locales des résistances hydrodynamiques favorisent le colmatage des pores voisins, puisque les particules sont distribuées dans les pores libres. Nous avons ainsi observé une augmentation du nombre de pores colmatés avec l'apparition dans certaines zones d'accumulation importantes de particule, aussi appelé gâteau de filtration, ainsi que la diminution de la vitesse du fluide. En utilisant de nouveau l'analogie électrique, nous avons établi la relation entre la résistance hydrodynamique équivalente de l'ensemble du milieu et la variation du débit. Nous avons développé un modèle hydrodynamique simple qui prend en compte le colmatage de chacun des pores du milieu ainsi que l'apparition locale du gâteau de filtration. Nous avons utilisé ce modèle pour retrouver nos chutes de débits expérimentales dans le cas d'une suspension stable de microparticules, sans ajout de sel. Nous avons obtenu un très bon accord de la théorie avec l'expérimental, malgré les approximations grossières que nous avons faites. Cependant, beaucoup de travail reste à faire pour vérifier si la forme de la chute du débit ne change pas pour chaque condition de filtration, incluant les conditions de filtration mais également les propriétés de la membrane.

Conclusion

Dans le dernier **chapitre 10** de la thèse, nous proposons plusieurs perspectives à la suite de notre étude. Nous avons montré pendant ce travail de thèse que l'étude dynamique à l'échelle d'un pore uniquement par l'analyse d'image et la mesure du débit avec le particle tracking était robuste pour déterminer quand le colmatage des pores prenait place. Notre approche a cependant été limitée à des systèmes avec des interactions DLVO et hydrodynamiques simples, alors que le colmatage dans d'autres cas peut être une combinaison complexe de processus physique, chimique et biologique. A l'échelle de la particule, les objets peuvent se déformer, ou des réactions bio-chimiques complexes peuvent avoir lieu comme la formation de biofilm, la précipitation, la cristallisation ou l'agrégation. Les propriétés du fluide peuvent également être modifiées, que ce soit sa viscosité ou encore la présence d'un gradient de température. La plupart de ces systèmes ont été étudiés à l'échelle du pore mais avec des pousse-seringues et ne prennent donc pas en compte les chutes de débit au sein des systèmes.

Dans la thèse, nous avons réalisé des expériences avec des milieux poreux ordonnés, qui sont des versions simplistes des vraies membranes. La première modification naturelle de notre milieu poreux modèles serait l'ajout d'une distribution de taille de pores et de rayon de collecteur afin de recréer un milieu poreux désordonné. Nous attendons un couplage complexe entre différents facteurs. D'une part, les pores les plus petits devraient être colmatés assez rapidement puisque ce processus ne nécessite que de l'accumulation de quelques objets mais dont la forte résistance hydrodynamique limite le transport d'objet en leur sein. De plus, la variation spatiale du cisaillement est plus importante dans ces forts confinements et pourrait être modifiée de manière importante la capture des objets de forme irréguliers. D'autre part, la plupart des objets passent dans les pores les plus larges, de plus faible résistance hydrodynamique, dont le colmatage est retardé puisqu'ils nécessitent plus de particules pour être colmatés.

Nous avons également suggéré que l'étude du backwashing, qui consiste à inverser le sens du courant avant d'éliminer le dépôt dans un filtre industriel, pouvait être optimisée grâce à notre système. En effet, actuellement aucune étude par l'analyse d'image ne prend en compte le nettoyage d'un filtre dans son ensemble.

Chapter 1

Introduction

We present in this chapter the state of the art of clogging phenomenon, starting with the transport of single particles and their interaction with others and walls of the channel. The main mechanisms of clogging in a single pore are described starting from the obstruction of the pore and the subsequent accumulation of particles behind the clog. This overview is extended to media with interconnected pores. Thereafter the objectives of the thesis are presented.

Contents

1.1	General introduction	18
1.2	At the particle scale	22
1.2.1	Particle transport	22
1.2.2	Attachment mechanisms	27
1.2.3	Particle adsorption	30
1.3	From the single pore to the porous media clogging	35
1.3.1	Clogging of a single pore	35
1.3.2	Clogging of porous media	42
1.4	Thesis objectives	45

1.1 General introduction

The filtration of a contaminated fluid through a membrane almost systematically leads to its clogging. The best known examples of clogging are those related to air (Liu et al., 2017; Thomas et al., 2001) or water filtration (Hube et al., 2020), with a deposition of contaminating object in or at the membrane surface (figure 1.1). Such membranes are used for the wastewater treatment (Chang et al., 2017; Tay et al., 1995), beverage (Demoulin et al., 2022; Sagu et al., 2014) or food (Garem et al., 2000).

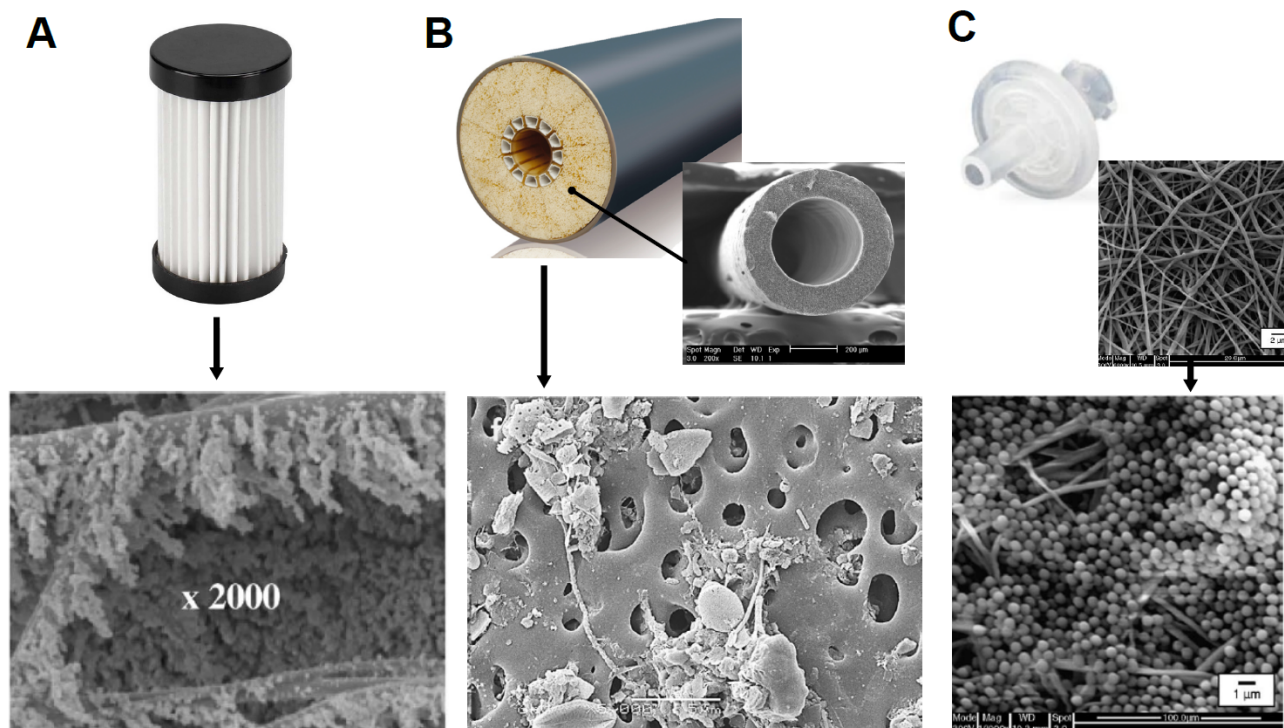


Figure 1.1: (a) Air filtration with a fiber filter. (top) Illustration of such a filter. (bottom) SEM image of a dendritic deposition with $0.18\mu\text{m}$ particles during the filtration, from Thomas et al. (2001). (b) Water filtration with a hollow fiber membrane (HF). (top) Illustration of such a filter (diameter 0.1-1m), with in inset a SEM cross section of a single fiber of the HF membrane (diameter 0.5-1.5mm), from Warsinger et al. (2018). (bottom) SEM image of the filtration of a river sample with HF membrane (diameter pores several micrometers), from Chawla et al. (2017). (c) Water filtration with a PVDF membrane. (top) one use of these membranes in syringe filter, the inset is a SEM image of a nanofibrous membrane realised with electrospun fibers by Gopal et al. (2006). (bottom) SEM image of a colloidal filtration, from Gopal et al. (2006).

There are other examples, both in the industrial and natural domains. Inside the asphalt of the road, fine sediments bring by the tires of cars, rainfall or vegetations, clog the void space of the pavement over many years and retain water (figure 1.2a). More porous or less tortuous asphalt are used to limit this effect, but *in-situ* clogging is still not fully understood (Kayhanian et al., 2012; Razzaghmanesh et al., 2018). In printers, the nozzles of the print heads are often blocked by air bubbles, fibers or colloids that compose the ink (figure 1.2b) (Croom et al., 2021; Fuller et al., 2002). Clogging can also be due to a combination of physical, chemical and biological parameters. Constructed wetlands are artificial wetlands with a gravel bed in which plants grow to treat wastewater to be treated and remove pollutants by circulating water through the porous bed and the plant root system though combination of physical, biological and chemical mechanisms (figure 1.2c). Without any maintenance of these spaces, they are inevitably subject to clogging, especially in the area where wastewater is injected (Vymazal, 2018). In the same way, micro-irrigation sets up, which consists in feeding crops drop by drop to limit water consumption, are subject to clogging (Bounoua et al., 2016). In the organism, arterioles can be clogged by blood clot (figure 1.2d) (Iadecola, 2014) or arteries by cholesterol clogs with fat substances (Ferber, 2000).

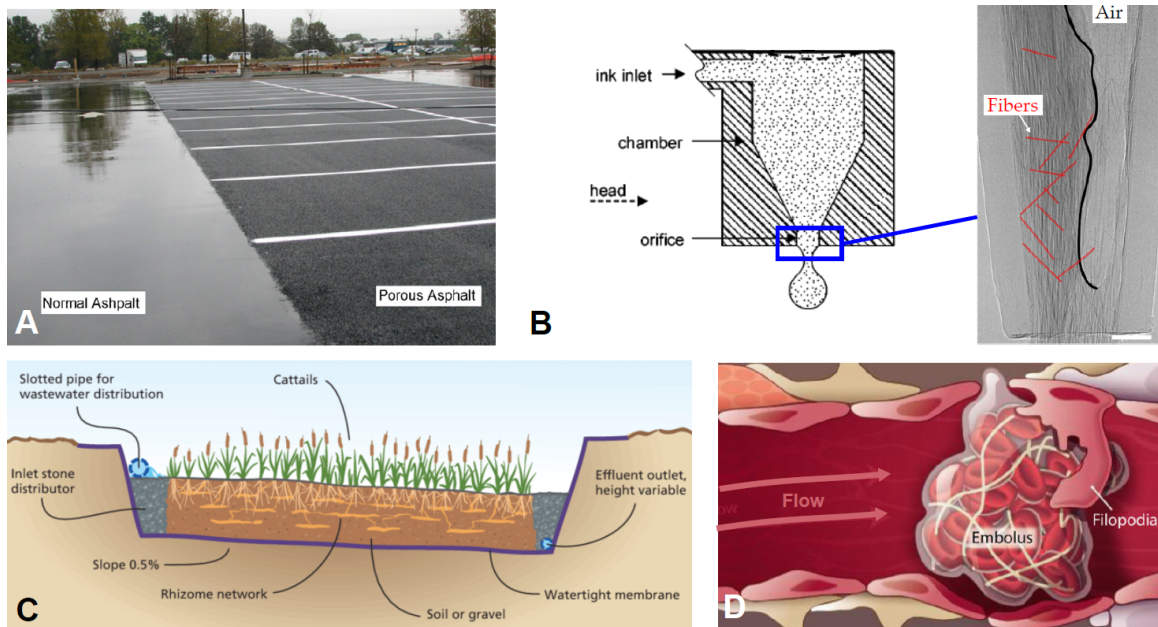


Figure 1.2: (a) Infiltration in a normal and porous asphalt with less fine aggregates and larger space void to limit clogging, from Mullaney et al. (2014). (b) Scheme of a printer head, adapted from Fuller et al. (2002). The blue rectangle shows a nozzle printer, where air bubble or fibers can be trapped and disrupted the flow rate, from Croom et al. (2021). (c) Scheme of a constructed wetland. The wastewater flow horizontally thanks to a hydraulic gradient, through the rhizome and stems of cattails. The watertight membrane prevent any leakage of wastewater, from Grismer et al. (2011). (d) Scheme of an embolus (here a blood clot) retained by a protuberance of the arteriole (here a filopodia) which prevents its removal from the blood flow, adapted from Iadecola (2014).

In this thesis we focus on the clogging of a model membrane by latex particles, dispersed in water and we make the link throughout the manuscript with the clogging of the industrial membrane by a colloidal suspension. It is well known that during the fouling and clogging of membranes, a significant flow decline is measured, whatever the filtration technique like tubular ceramic (Hong et al., 1997), hollow fiber (Sagu et al., 2014), reverse osmosis (Al Ashhab et al., 2017) or other membranes. Trinh et al. (2020) measure such a flow decline through a negatively charged PCTE membrane for different particle charges (figure 1.3). The flow decline appears to be the greatest and sudden for the positively charged particles than the others, while the most negative charges particle have a gradual decline. These different flow declines illustrate the importance of the deposit on the membrane surface. A flow decline results in a loss of filter efficiency and an increase in production cost and is the major issue for membrane. Membranes with a low degree of fouling can be either washed by backwashing or flushed to increased the shear to remove particle (Hilal et al., 2005). In some condition, the membrane is cleaned with chemical agents, by immersing fouled membranes in chemicals, adding chemicals to the feeding suspension or using them in combination with backwashing (Lin et al., 2010). If the clogging is irreversible, the membrane has to be replaced. All these choices generate a cost of use of the membrane.

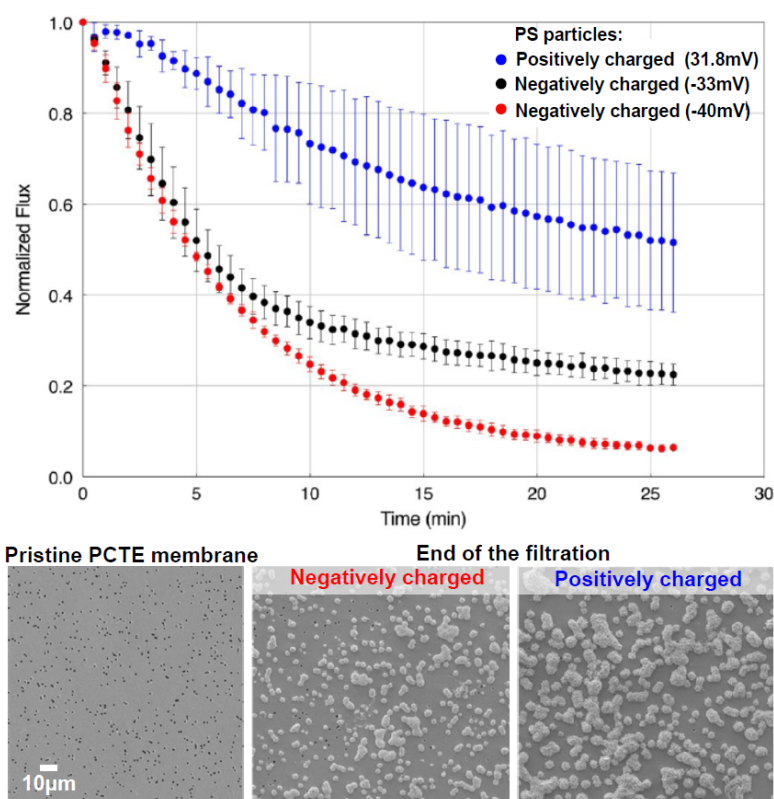


Figure 1.3: (top) Flow decline of three PS particles charged, from Trinh et al. (2020). (bottom) FESEM images the membrane before and after the filtration for the most negatively and positively charged particle. Adapted from Lay et al. (2021).

Currently, no relationship is made between the membrane fouling/clogging dynamics and the associated flow decline, whereas understanding the link between these two phenomena would be crucial to improve cleaning and increase filter life while decreasing costs. The main difficulty lies in the fact that these membranes are not transparent and can not be imaged during the clogging process. In recent years, microfluidics allowed the fabrication of transparent model filters and thus the quantification of some aspects to the clogging thanks to microscopy and various imaging techniques. This technology allows going from the dynamic observation of a single pore of the membrane up to the whole membrane and visualize the three mechanisms of pore clogging (figure 1.4). The passage from one mechanism to the other relies on the

definition of confinement W/D , i.e. the width of the pore over the diameter of the particle, but also on the volume fraction Φ of the solution. Particles that are too large block the pore by sieving, and a suspension that is too concentrated will favour the formation of arches in the pores. The progressive clogging is intermediate and concerned diluted suspensions.

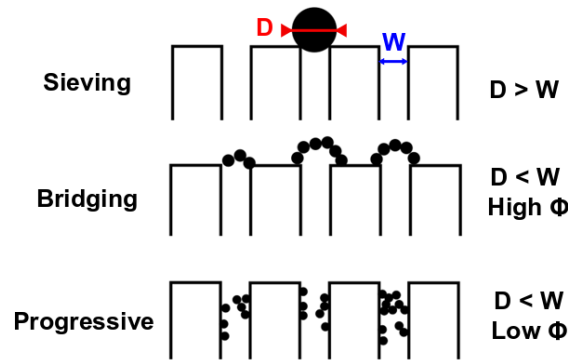


Figure 1.4: The three clogging mechanisms.

Sieving

Sieving occurs for objects larger than the pore size. As soon as an object obstructs a pore, the following ones form a cake layer behind the deposited particle. The permeability and structure of this cake layer depends on the space between pores and the size particle (Hassan et al., 2014; Valencia et al., 2020). The more the pores are covered by the particles, the more the hydrodynamic resistance of the pores increases and the flow decreases. Warkiani et al. (2015) showed that cylindrical pores induced a more important permeability decreases, since particles covered more of the pore surface than for elongated pores (figure 1.5a-b). This clogging mechanism is used to separate small particles from larger ones that remain blocked by sieving (Brans et al., 2007; Yoon et al., 2016).

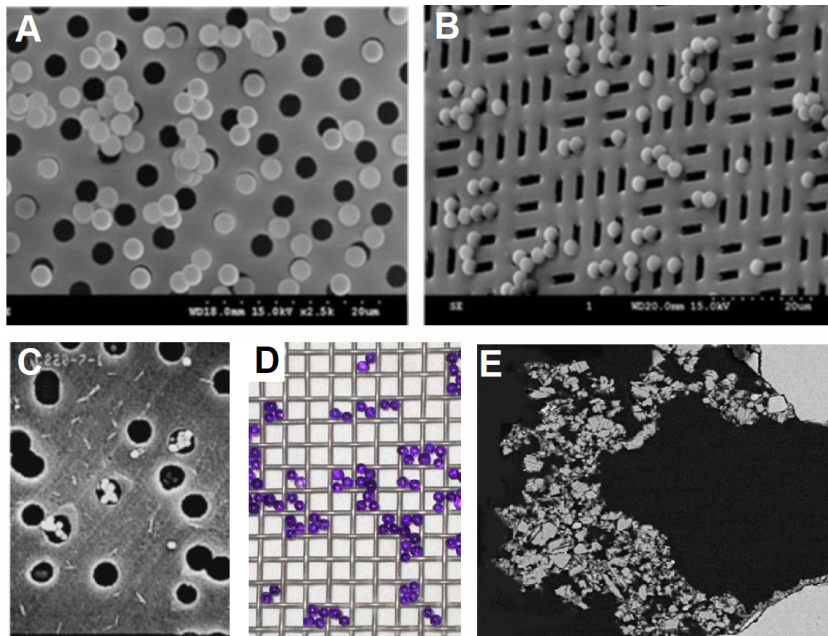


Figure 1.5: Sieving with spherical particles in spherical (a) and slotted pores (b), from Warkiani et al. (2015). Bridging with 200nm particles in 1-2 μ m pores, adapted from Ramachandran et al. (1999) (c), 3 μ m particles in 5 μ m pores, adapted from Roussel et al. (2007) (d), and fragments of clay, from Poesio et al. (2004) (e).

Bridging

If the suspensions are strongly concentrated and if the appropriate configuration in term of position and number of particles occurs, arch of particles can occurs (Marin et al., 2018). Figures 1.5c-e show several examples with colloid particles. These arches are quite fragile and can be destroyed by ultrasound (Poesio et al., 2004), or with the accumulation of particles. Several clogging and unclogging events can occur and their intermittence depends strongly on the confinement W/D (Souzy et al., 2020).

Progressive clogging

The progressive clogging is based on the successive deposition of particles. Two capture zones emerge from both side of the pore and grow until they merge to clog the pore (figure 1.6). This is the mechanism that is be studied during the thesis, we will detail later in the chapter on some properties of the progressive clog.

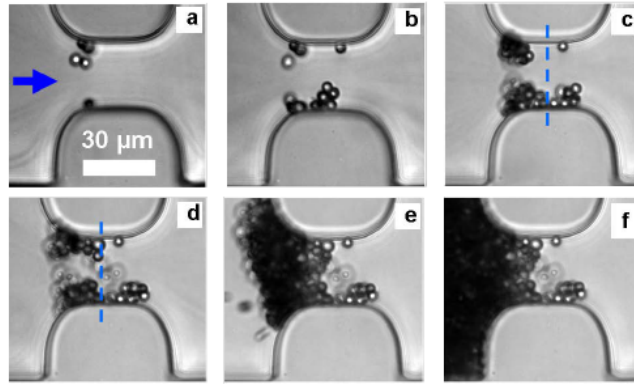


Figure 1.6: Clog formation with $4\mu\text{m}$ particles in a $30\mu\text{m}$ pores. Particle are deposited in the pore wall (a-b) and two captures zones appear and grow (c-d), until the clogging of the pore (e-f). The dash blue line is the center of the pores. From Dersoir et al. (2015).

Before discussing the different mechanisms that take place in progressive clogging, let us introduce some basics.

1.2 At the particle scale

This section presents the general description of the transport of a particle by the fluid, considering the main forces acting on the particle that cause it to collide other particles.

1.2.1 Particle transport

1.2.1.1 Hydrodynamics in microchannel

Navier-Stokes equation and characteristic numbers

The movement of an incompressible fluid with constant dynamic viscosity is described by the Navier-Stokes equation:

$$\rho \left(\frac{\partial \vec{v}}{\partial t} + (\vec{v} \cdot \nabla) \vec{v} \right) = \rho \vec{g} - \vec{\nabla} p + \eta \nabla^2 \vec{v} \quad (1.1)$$

With ρ and v are respectively the volume density and the velocity of the fluid. p is the pressure and g the gravity force.

- Reynolds number

In a fluid flow, there are two mechanisms for transporting momentum, convection and diffusion. Depending on the flow conditions, they do not have the same amplitude. The Reynolds number Re is the ratio of these two transports:

$$Re = \frac{\text{inertia}}{\text{viscosity}} = \frac{\rho(\vec{v} \cdot \vec{\nabla})\vec{v}}{\eta \nabla^2 \vec{v}} = \frac{UL}{\nu} \quad (1.2)$$

With U and L the characteristic velocity and length of the flow, η the fluid kinematic viscosity.

At low Reynolds $Re \ll 1$, the inertial term of the Navier-Stokes equation (1.1) is negligible and the flow is laminar and stable. At high Reynolds $Re \gg 1$, the inertial term dominates and the flow is unstable and turbulent.

- Stokes number

The importance of the local acceleration with the viscous term is measured with the Stokes number:

$$St = \frac{\text{acceleration}}{\text{viscosity}} = \frac{\partial \vec{v} / \partial t}{\eta \nabla^2 \vec{v}} = \frac{U^2}{T\nu} \quad (1.3)$$

T is the intrinsic time. If $St \ll 1$, the acceleration is neglected.

We work in laminar condition, with $Re \ll 1$ and $St \ll 1$ and thus the Navier-Stokes equation (1.1) is simplified by the Stokes equation:

$$\rho \vec{g} - \vec{\nabla} p + \eta \nabla^2 \vec{v} = 0 \quad (1.4)$$

Fluid in a microchannel : Hagen-Poiseuille flow

A Hagen-Poiseuille flow is a stationary laminar flow limited by walls, its profile is schematized on figure 1.7. From the Navier-Stokes equation (eq. 1.1) the fluid velocity through a rectangular section, the most common geometry in this thesis is thus (Bruus, 2008):

$$v_x(y, z) = \frac{4H^2 \Delta P}{\pi^3 \eta L} + \sum_{n, \text{odd}} \frac{1}{n^3} \left[1 - \frac{\cosh(n\pi \frac{y}{H})}{\cosh(n\pi \frac{w}{2H})} \right] \sin(n\pi \frac{z}{H}) \quad (1.5)$$

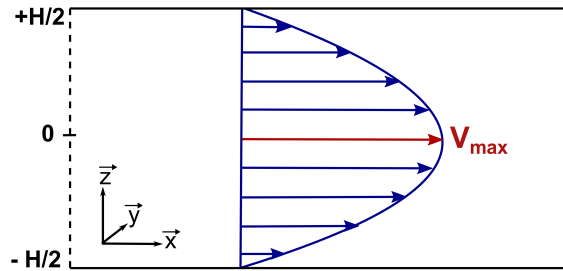


Figure 1.7: Velocity profile for $v_x(0, z)$ in a rectangular duct of height H . v_{max} is the maximal velocity in the center of the channel

In a porous packed bed medium, if pores are circular, the velocity becomes:

$$v_x(y, z) = \frac{\Delta P}{4\eta L} (R^2 - y^2 - z^2) \quad (1.6)$$

Fluid in porous media: Darcy and Kozeny-Carman

The Darcy law relates the pressure gradient ΔP and the flow rate Q , with S and L respectively the section and length of the pore and K the porous media permeability, knowing ΔP and the kinematic viscosity η :

$$Q = \frac{-KS \Delta P}{\eta L} \quad (1.7)$$

Considering ϵ the fraction of the porous media occupied by the pores, the velocity fluid v_f inside pores is then equal to:

$$v_f = \frac{Q}{S\epsilon} = \frac{v_s}{\epsilon} \quad (1.8)$$

Where $v_s = Q/A$ is an apparent velocity (also called seepage or superficial velocity) through the porous medium deduced from the Darcy's law, slightly lower than the actual velocity.

The permeability is an essential parameter for porous media models, but is empirical because of the difficulty to measure it in a porous media like a packed bed. To be more accurate, Kozeny (1927) has made the assumption that a porous medium as a packed bed can be considered as an assembly of capillaries of specific size and geometry:

$$v_s = \frac{D_{eq}^2}{36k\eta} \frac{\epsilon^3}{(1-\epsilon)^2} \frac{\Delta P}{\Delta L} \quad (1.9)$$

With η the fluid viscosity, D_{eq} the mean diameter of the particle composing the packed bed and k the constant depending of the capillaries geometries. Carman (1937) modified this constant to including the tortuosity $k = 2 \left(\frac{\pi}{2}\right)^2$. The Kozeny-Carman equation for a packed bed composed of spherical particles is then:

$$v_s = \frac{D_{eq}^2}{180\eta} \frac{\epsilon^3}{(1-\epsilon)^2} \frac{\Delta P}{\Delta L} \quad (1.10)$$

Hydrodynamic resistance

At low Reynolds $Re \ll 1$, it is possible to make an analogy between the Ohm's law $U = RI$ and the flow through a microchannel $\Delta P = R_{eq}Q$. The hydrodynamic resistance R_{eq} depends on the channel geometry and can be found from Hagen-Poiseuille equations 1.5 and 1.6 (Bruus, 2008):

$$\text{For a rectangular channel: } R_H = \frac{1}{1 - 0.63 \frac{h}{w}} \frac{12\eta L}{h^3 w} \quad (1.11a)$$

$$\text{For a cylindrical channel: } R_H = \frac{8\eta L}{\pi r^4} \quad (1.11b)$$

It is therefore possible to calculate simply R_{eq} from resistors in series or in parallel.

The R_{eq} example presented in figure 1.8 is then:

$$R_{eq} = 2R + \frac{2R_{res} + R_{pore}}{2} \quad (1.12)$$

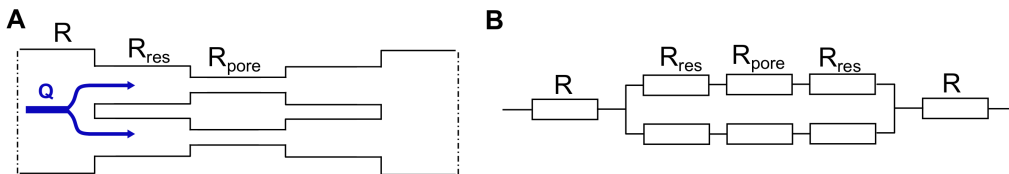


Figure 1.8: Example of microfluidic circuit (a) and its equivalent electrical diagram (b).

To solve more complicated cases, the Kirchoff laws are also compatible:

- For each node of the circuit : $\sum_i q_i = 0$, q_i the flow rate of the i^{th} resistance.
- For each closed loop of the circuit : $\sum_i P_i = 0$.

1.2.1.2 Forces acting on particles

Buoyancy, gravity and Drag forces

The motion of a particle suspended in a static fluid of density ρ_f is subjected to the gravity \vec{P} and the buoyancy \vec{F}_b , based on the Archimedes principle and equal to the weight of the displaced volume by a sphere of radius R and density ρ_p :

$$\vec{P} = m_p \vec{g} = \frac{4}{3} \rho_p \pi R^3 \vec{g} \quad (1.13)$$

$$\vec{F}_b = m_f \vec{g} = \frac{4}{3} \rho_f \pi R^3 \vec{g} \quad (1.14)$$

At low Re , as the particles moves with a velocity U_p , it generates a shearing of the fluid of viscosity η , the force opposing to the motion:

$$\vec{F}_D = -6\pi\eta R \vec{U}_p \quad (1.15)$$

The balance between these forces gives:

$$\vec{U}_p = \frac{2}{9} \frac{\Delta\rho \vec{g} R^2}{\eta} \quad (1.16)$$

During ours experiments, $\Delta\rho = 0$ to avoid any sedimentation or creaming.

Particles diffusion and Péclet number

Brownian motion

Suspended particles have a random motion associated to thermal agitation and due to the collision of fluid particles which generates a particle displacement (Einstein, 1905). This alternation between straight lines and sudden changes of direction is called a random walk or Brownian motion. The trajectory of a single particle can not be predicted since its move in any direction with the same probability $\langle x(t) \rangle = 0$ but rescaled at the origin, spreads in space and over time. The quadratic displacement of a particle $\langle x^2(t) \rangle = 2Dt$ depends both of the elapsed time t and a diffusion coefficient D . The smaller the particles, the greater their diffusion (figure 1.9). This diffusion coefficient is defined by $D = mk_bT$, with k_b the Boltzmann constant and m the mobility of the particle, defined as the ratio of the particle velocity and Drag force (equation 1.15). For a spherical particle, the coefficient diffusion is known from the Stokes-Einstein equation:

$$D = \frac{k_b T}{6\pi R \eta} \quad (1.17)$$

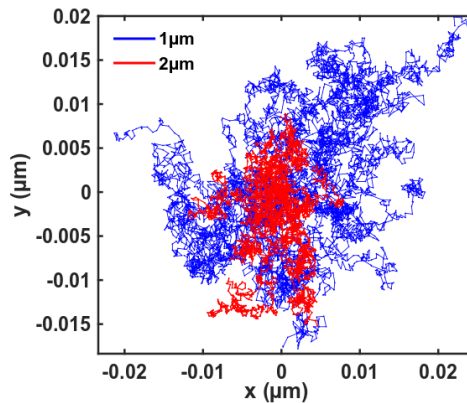


Figure 1.9: Experimental diffusion trajectories of 1µm and 2µm particles over 180 seconds.

- Péclet number

Diffusion and convection lead to the particle transport in a fluid. The Péclet number characterizes the importance of diffusive transport on convection:

$$Pe = \frac{\text{convection}}{\text{diffusion}} = \frac{U_f L}{D} \quad (1.18)$$

We work in conditions where the diffusion is negligible $Pe \gg 1$ and where particles remain on their fluid streamlines. However when streamlines are compress, which is our case when fluid enters into a pore of the membrane, particles can migrate on others streamline.

Particles near contact

Modified Drag force

When a particle comes close to a wall, the Drag force is modified. Theoretically, the greatest F_D exerted on the particle is when the particle is in contact with the wall and decreases quickly with distance. However, because of a thin layer of fluid between the particle and the wall, the particle does not touch the wall. The fluid layer offers a strong resistance when the particle shears or squeezes it. Several studies have investigated theoretically the hydrodynamic interactions considering different configurations like a sphere toward a plane surface (Brenner, 1961), in a Stokes flow (Cox et al., 1967) or with a translation and a rotation (Goldman et al., 1967; Kim et al., 2013).

1.2.2 Attachment mechanisms

For colloidal particles, the most widely used approach to describe the interactions between a particle and a wall or between particles is the DLVO theory that takes into account the long range electrostatic repulsion, the short range attraction and even the shorter range Born repulsion.

1.2.2.1 Electrostatic interactions

The surface of a colloidal particle suspending in a polar liquid can be charged according to several mechanisms like ionization, ion adsorption or dissolution. In our work, particles and wall surfaces are generally negative.

Under Coulomb interactions, the charged surface of the particles influences the ions in the surrounding liquid since the counterions are attracted by the surface and coions repelled into the bulk. This mechanism leads to the formation of a double layer around the particle.

1. In the first layer, called the Stern or Helmholtz layer, the counterions are adsorbed and are immobilized strongly enough to overcome thermal agitation. This layer δ is only a few nanometers, or a thickness of a layer of adsorbed counterions, until the stern takes place (figure 1.10a).
2. In the second layer, called the diffuse layer, the ions are distributed according to the importance of the electrical forces and the random walk and are mobile. Its thickness is known as the Debye length κ^{-1} below which the electrostatic interactions take place:

$$\kappa^{-1} = \left(\frac{\epsilon_0 \epsilon k_B T}{e^2 \sum_i (z_i c_i)} \right)^{\frac{1}{2}} \quad (1.19)$$

With k_B the Boltzmann constant, T the temperature, e the charge of an electron, z_i the valence of the i^{th} ion and c_i its concentration. For NaCl, $z_i = 1$.

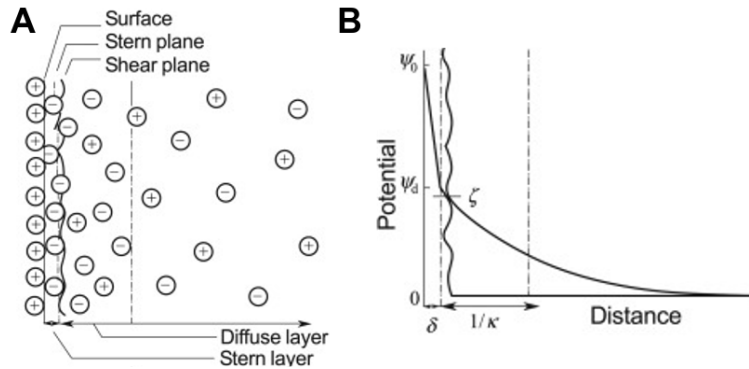


Figure 1.10: (a) Schematic representation of the electrical double layer from Stern theory. The shear plane is the junction between the mobile and not-mobile zone. From Shaw (1980). (b) Potential decrease with the distance from ψ_0 the electrical potential at the surface to ψ_d the Stern potential and starting from a distance ζ from ψ_d to 0. From Shaw (1980).

Debye's length depends only on the properties of the solution and describes how the charges of the solution are screened. The smaller this length, the more the charges are screened and the closer the two surfaces can get to each other (figure 1.10b). Adding electrolytes in the suspension can thus decrease κ^{-1} and favours the aggregation between particles or deposition onto surfaces.

In the event of diffuse layer overlapping for two spheres or a sphere and a plane, we can calculate the interaction energy V_R . No exact analytical expression exists, but several studies have proposed numerical or approximate solution (Hogg et al., 1966; Reerink et al., 1954; Sader et al., 1995):

- For two spheres of radius a_1 and a_2 , separated by a distance H :

$$V_R = \frac{64\pi\epsilon k_B^2 T^2 \gamma_1 \gamma_2}{e^2 z^2} \frac{a_1 a_2}{(a_1 + a_2)} \exp(-\kappa H) \quad (1.20)$$

With

$$\gamma = \tanh\left(\frac{ze\psi_d}{4k_B T}\right) \quad (1.21)$$

In the limit of the Debye-Hückel approximation where $ze\psi_d/k_B T \ll 1$ either when the interaction potential is less than 25mV, the equation 1.20 is simplified:

$$V_R = 2\pi\epsilon\psi_d^2 a \exp(-\kappa H) \quad (1.22)$$

- For a sphere of radius a and a plane, separated by a distance H :

$$V_R = \frac{64\pi\epsilon k_B^2 T^2 \gamma^2}{e^2 z^2} a \exp(-\kappa H) \quad (1.23)$$

1.2.2.2 Van der Waals

The Van der Waals forces arise from interdipole interactions. Several types of interactions compose the Van der Waals forces but for non-polar objects they are dominated by the induced dipole-induced dipole interaction. This interaction is called the London force or dispersion force and is the product of the Hamaker constant A depending on the polarization and refractive index of materials with a geometrical term. Between two identical atoms, London (1930) described the Hamaker constant as:

$$A = \pi^2 C \rho_1 \rho_2 \quad (1.24)$$

with ρ_i the number density for each material and C a coefficient of dispersion interaction:

$$C = \frac{-3}{4} \alpha^2 \frac{h\nu}{(4\pi\epsilon_0)^2} \quad (1.25)$$

where ν is the orbiting frequency of an electron, h the Planck constant and α the electron polarizability.

For two bodies 1 and 2 separated by a thin layer of fluid 3 (Israelachvili, 2015):

$$A = \frac{3}{4} k_B T \left(\frac{\epsilon_1 - \epsilon_3}{\epsilon_1 + \epsilon_3} \right) \left(\frac{\epsilon_2 - \epsilon_3}{\epsilon_2 + \epsilon_3} \right) + \frac{3h\pi\nu}{8\sqrt{2}} \frac{(n_1^2 - n_3^2)(n_2^2 - n_3^2)}{(n_1^2 + n_3^2)^{1/2}(n_2^2 + n_3^2)^{1/2} [(n_1^2 + n_3^2)^{1/2} + (n_2^2 + n_3^2)^{1/2}]} \quad (1.26)$$

n_i is the material refractive index of materials. For two spheres, the Hamaker constant is reduced to:

$$A = \frac{3}{4} k_B T \left(\frac{\epsilon_1 - \epsilon_3}{\epsilon_1 + \epsilon_3} \right)^2 + \frac{3h\nu}{16\sqrt{2}} \frac{(n_1^2 - n_3^2)^2}{(n_1^2 + n_3^2)^{3/2}} \quad (1.27)$$

Hamaker (1937) derived the interaction energies V_A of the London force between different objects:

- For two spheres of radius a_1 and a_2 , separated by a distance H and considering the Derjaguin approximation $H \ll a_i$:

$$V_A = \frac{A a_1 a_2}{6H(a_1 + a_2)} \quad (1.28)$$

- For a sphere of radius a and a plane separated by a distance H and with $H \ll a$:

$$V_A = \frac{A}{6} \left(\frac{a}{H} + \frac{a}{H+2a} + \ln\left(\frac{H}{H+a}\right) \right) \quad (1.29)$$

London forces are subject to retardation effects since the propagation time is limited and can reduce the correlation between the charges as well as the interaction when the distance is equal or larger than 0.1λ with λ the wavelength of the intrinsic electronic oscillations. There are several expressions for delayed

interactions between two spheres (Gregory, 1981; Ho et al., 1968; Schenkel et al., 1960) and between a sphere and a plane (Gregory, 1981).

- For two spheres of radius a_i separated by a distance H with $H \ll a_i$ and $H \ll \lambda/\pi$ (Schenkel et al., 1960) :

$$V_A = -\frac{Aa_1a_2}{6(a_1 + a_2)h} \left(\frac{1}{1 + 11.12h/\lambda} \right) \quad (1.30)$$

- For a sphere a and a plane, separated by a distance H with $H \ll a$, (Gregory, 1981)

$$V_A = -\frac{Aa}{6h} \left(1 - \frac{5.32H}{\lambda} \ln \left(1 + \frac{\lambda}{5.32H} \right) \right) \quad (1.31)$$

1.2.2.3 Born repulsion

A short distance, 0.1 to 0.2 nm, a repulsive force called the Born repulsion emerges from the strong repulsive between atoms, when their electron clouds overlap, similar to a hard sphere interaction. Feke et al. (1984) found the potential between two macroscopic spheres. For two identical spheres of radius a separated of h :

$$V_B = 4A \left(\frac{\sigma}{a} \right)^{n-6} \frac{(n-8)!}{(n-6)!} \frac{1}{R} \left(\frac{-R^2 - (n-6)(n+7)}{R^{n-5}} + \frac{R^2 + (n-6)(n+7)}{(R+2)^{n-5}} \right) \quad (1.32)$$

With $R = h/2a + 1$. Generally, $n = 12$:

$$V_B = \frac{A}{3700} \left(\frac{\sigma}{a} \right)^6 \frac{1}{R} \left(\frac{-Ra^2 + 30}{R^7} - \frac{R^2 - 54}{(R+2)^7} \right) \quad (1.33)$$

1.2.2.4 The DLVO theory

By summing the electrical double layers (EDL) and the Van der Waals interactions we obtain the so called DLVO (Derjaguin-Landau-Verwey-Overbeek):

$$V_{TOT} = V_A + V_R \quad (1.34)$$

The total interaction V_{TOT} is composed of a first infinite minimum, a maximum also called the energy barrier and a second minimum indicated on figure 1.11. Note that Born interaction can be added to avoid an infinitely attraction in the first minimum which is physically impossible.

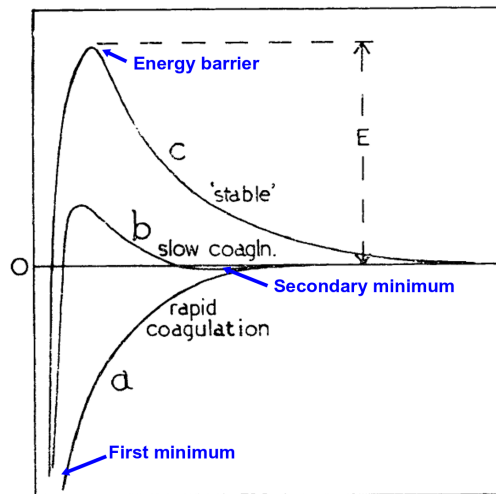


Figure 1.11: DLVO profile for a stable suspension (c), a suspension with a slow coagulation (b) and an unstable suspension (a). Adapted from Schenkel et al. (1960).

The amplitude of the minima and energy barrier depends on the suspension and are stability criteria. An important energy barrier prevents the particles aggregation and the suspension is stable (figure 1.11c).

When it is lower, the particles are destabilized and any collision between particles can generate an aggregate. The transition between a stable suspension with a high energy barrier and an unstable suspension (figure 1.11a) is sudden and is called the critical coagulation of concentration (CCC).

1.2.3 Particle adsorption

We describe here the particle capture, from the first deposited ones to the growth of the deposit at the wall. We discuss about the competition between the DLVO and hydrodynamic forces which can promote either the deposition or the erosion of particles.

1.2.3.1 Surface roughness: the first deposited particle

The combination of DLVO effects and the lubrication forces makes it difficult to understand the capture of the first objects of a deposit on the walls since with these forces acting the particles they should not be captured on the surface. Numerical models must therefore often impose the position of these first objects (Agbangla et al., 2014; Trofa et al., 2019). However, the channel or particle surface roughness is often invoked to explain the capture of the first particles. On a layer of PDMS, Bongaerts et al. (2007) measured some surface roughness about 10 nm with peaks even going to several hundred of nanometers.

Henry et al. (2012) presented a scenario of attachment or detachment of particles based on the surface inhomogeneity. When particles roll on the surface of the wall because of the hydrodynamic torque, they can meet an asperity that creates one or more contact points. Depending on the kinetic energy of the particle, this asperity allows their attachment or detachment (figure 1.12a). Prakash et al. (2021) have observed that the surface asperities could favour the particles deposit. Duru et al. (2015) also presented a three steps scenario for a particle entering a pore which undergoes a torque close the pore (figure 1.12b). This torque comes from the symmetry breaking of the Van der Waals forces between the particle and the membrane, where the particle asperities can either help to the deposition or removal of the particle.

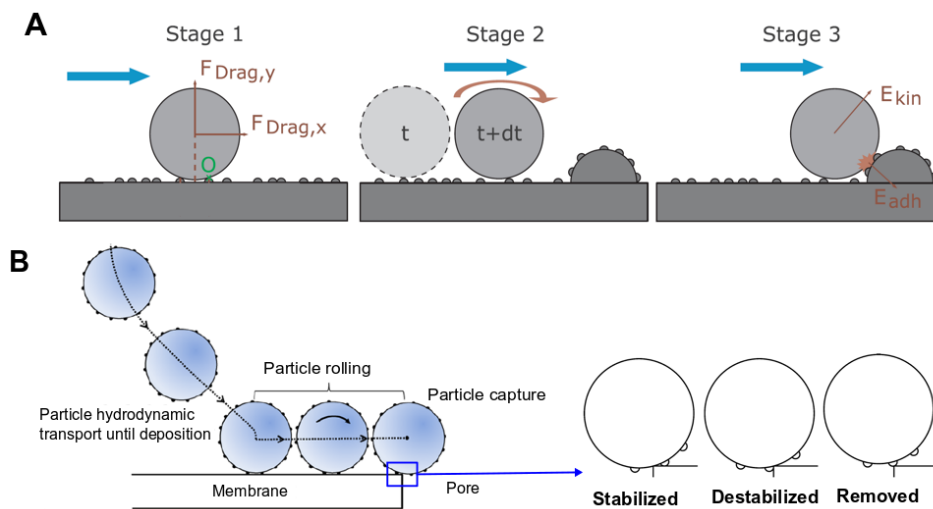


Figure 1.12: (a) Henry et al. (2012)'s scenario. Particles are set in motion with the hydrodynamic force in step n°1, and roll on the surface in step n°2 before be attached or resuspended by some plane asperities in step n°3. (b) Duru et al. (2015)'s scenario. When the particle is close to the pore, the particle asperities stabilized, destabilized or removed the particle.

1.2.3.2 From the monolayer to the growth of the deposit

In our experimental conditions, particles and walls are negatively charged and without adding electrolytes in the suspension and the barrier energy between particles is higher than between a particle and a wall (figure 1.13). A particle is more likely to be captured by a wall than by a deposited one. To form multilayer, it is necessary to screen the charges on the particle surface or to increase the particle kinetic energy to overcome the energy barrier.

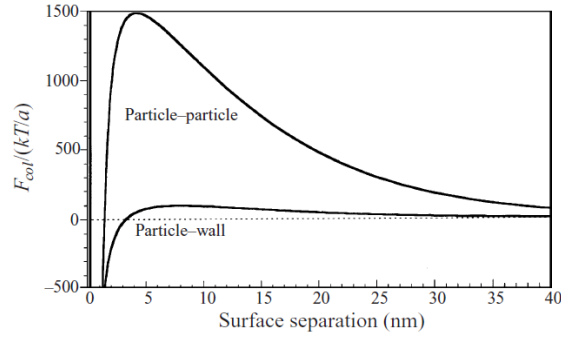


Figure 1.13: DLVO estimation for the interaction between two particles and a particle-wall, where a is the particle radius. From Ramachandran et al. (1999).

The monolayer

A deposited particle prevents another particle deposit in its closed vicinity. This blocking effect is due to the repulsion between the particles and limits the maximum coverage rate of the walls (figure 1.14a). A compression of the electrostatic double-layer by adding salt leads to an high coverage (Adamczyk et al., 1992). The coupling of particle interactions and hydrodynamics forces a flowing particle that approaches another deposited one to flow around it. Because of the flow, a deposited particle has an asymmetrical "shadow zone" (figure 1.14b) where the probability of deposition is reduced. This excluded region increased with the size and velocity of the particle (Ko et al., 2000).

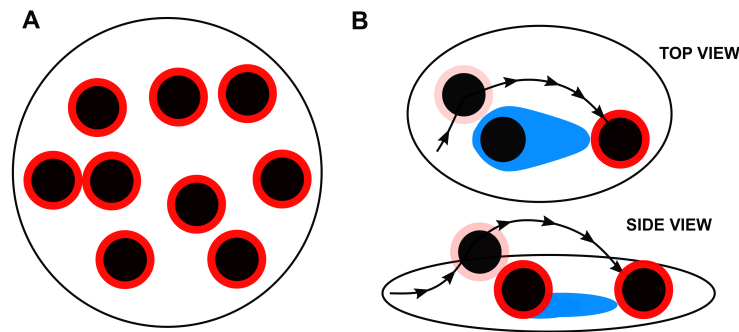


Figure 1.14: (a) Illustration of the blocking effect. The red zone is the surface blocked by the particle that limits the coverage rate. Inspired from Adamczyk et al. (1992). (b) Illustration of the shadow effect. Blue part is the shadow zone, red part the blocking effect. Inspired from Ko et al. (2000).

The growth of the deposit

The formation of multilayer or growth deposit of particles depends strongly of the interparticle interactions. Ryde et al. (1991) showed that an increase of the ionic strength could allow the transition from a monolayer to a multilayer by screening the surface charges of nanoparticles. The particle-fluid interaction is also an important parameter since Ramachandran et al. (1998) showed experimentally that increasing the particle velocity i.e. their kinetic energy, can increasing the number of deposited particles (figure 1.15b). They calculated the particles trajectories for different conditions of flow rate and ionic strength (figure 1.15c), and showed that the particle deposition is dependent of both a critical flow rate and an ionic strength.

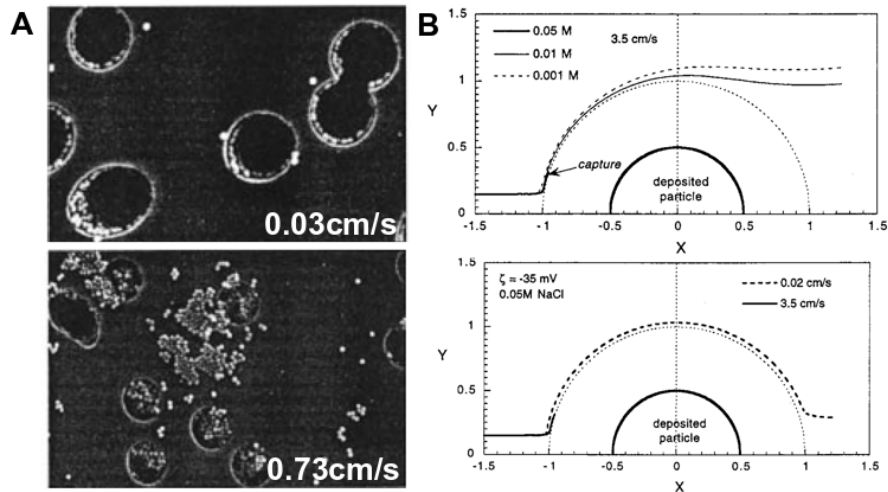


Figure 1.15: (a) SEM images of particle deposition for two particle velocities. From Ramachandran et al. (1998). (b) Calculated trajectories for flowing particles near a deposited one. (top) Different ionic strengths at the same flow rate. (bottom) Different flow rates at the same ionic strength. From Ramachandran et al. (1998).

The growth deposit is localized around a previously deposited particle and is called cluster in this configuration. Gudipaty et al. (2011) noticed that the particle-cluster interactions were privileged against the particle-wall interactions and the number of cluster remain limited. Trofa et al. (2019) confirmed with a numerical simulation the observation of Gudipaty et al. and noticed that the fluid modifies the morphology of the cluster with erosion (figure 1.16).

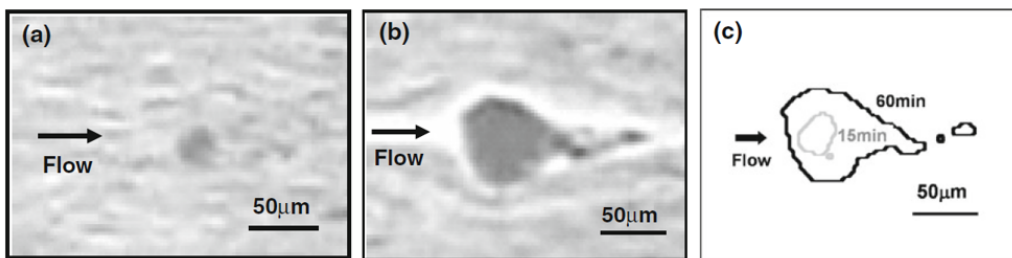


Figure 1.16: Evolution of the cluster size after 15min (a) and 60min (b). The cluster outlines are overlap in (c). Adapted from Gudipaty et al. (2011).

If charges are strongly screened, the deposit can grow in a single direction and form structures called dendrites. Agbangla et al. (2012) noted that the direction of the flow could strongly influence the formation of dendrites (figure 1.17a). de Saint Vincent et al. (2016) provided a phase diagram including different dendrite shapes, depending on the flow rate and the ionic strength (figure 1.17b). There is a coexistence of labile zone where fluid just holds together on the deposit, and cohesive one when the fluid shape the deposit. These particular structures can have an important impact in clogging.

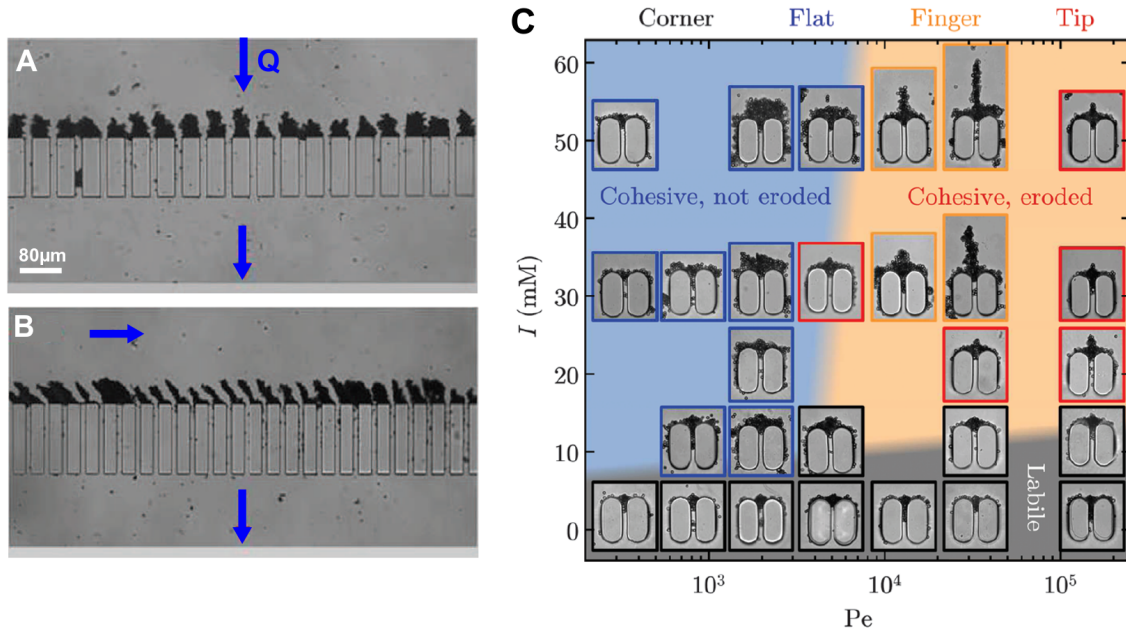


Figure 1.17: Dendrites formation with cross-flow (a) and dead-end (b) filtration. Adapted from Agbangla et al. (2012). (c) Phase diagram according to the ionic strength and the flow rate. From de Saint Vincent et al. (2016).

1.2.3.3 Deposition versus erosion

Increasing the flow rate initially favors the deposit but a too high shear may erode single particles or even part of the deposit. Actually, there is a competition between the two torques generated by the Drag force T_D and by the attractive force T_A (Bergendahl et al., 2000; Torkzaban et al., 2007) (figure 1.18):

$$T_D = l_D F_D \quad (1.35)$$

$$T_A = F_A l_n \quad (1.36)$$

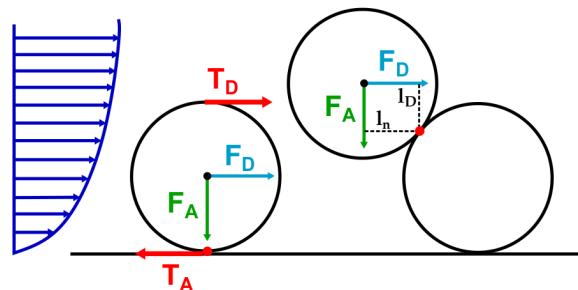


Figure 1.18: The torques acting on a deposited particle over a plane surface or over another particles.

The favourable attachment condition with no energy barrier corresponds then to $T_{VDW} > T_D$ and the unfavourable attachment condition to $T_D > T_{VDW}$. In the first case, whatever the flow condition, a particle remains attached to the surface while in the second case a sufficiently low velocity enables locally favourable attachment.

Chequer et al. (2021) observed that particles deposited on a plane surface are swept off while the flow velocity increases (figure 1.19) and Whittle et al. (2000) studied the formation of doublet of particles, composed of a deposited particle and a mobile one, which rotates around the immobile one under flow.

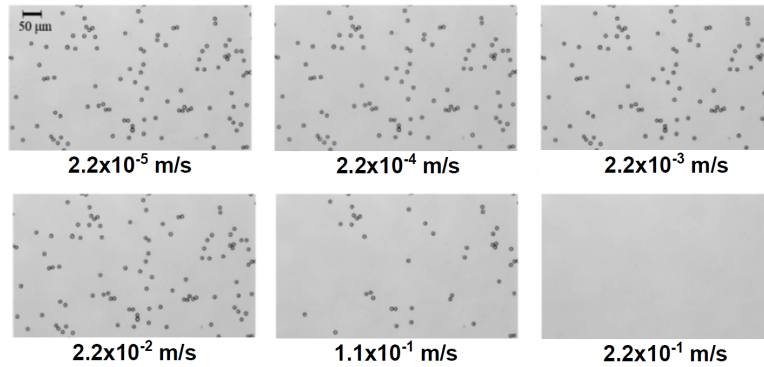


Figure 1.19: Particles of $10\mu\text{m}$ are swept off a plane surface while the flow velocity increases, with no repulsive barrier and $I=0.3M$. From Chequer et al. (2021).

When the hydrodynamic torque overcomes the attractive torque, it is mainly a rolling mechanism that allows the particle detachment under laminar conditions. This detachment can limit the formation of the deposit, but also induces the detachment of parts of the deposit (figure 1.20a-b), as observed by Gudipaty et al. (2011). In some cases, deposit detachments can have an impact in the clogging of porous media (figure 1.20c) (Bizmark et al., 2020; Gerber et al., 2019). Jung et al. (2021) performed simulation to understand these erosions by considering an aggregate that collides the deposit and is eroded or not, confirming how hydrodynamic force, the shear and the collision probability are important.

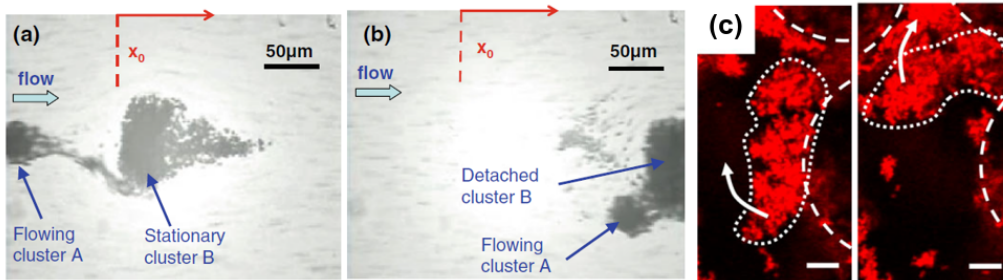


Figure 1.20: (a-b) Detachment of a cluster by another. From Gudipaty et al. (2011). (c) Deposit detachment and movement on a more stable position in a porous media composed of glass spheres (represented by the dashed circles). Scale bar: $10\mu\text{m}$. Adapted from Gerber et al. (2019).

1.3 From the single pore to the porous media clogging

We detailed in the previous section the main phenomena at the basis of clogging, the DLVO and hydrodynamic forces. Here, we present the state of the art of the progressive clogging. With the advent of the microfluidics, several studies have proposed to describe the clogging with *in-situ* method.

1.3.1 Clogging of a single pore

The first *in-situ* study on clogging at the pore scale of Wyss et al. (2006) showed that a fixed number of particles has to pass through the pore before it is clogged. They found a simple relationship between the average clogging time t^* , the flow rate Q and the particle volume fraction Φ , $t^* \propto 1/(Q\Phi)$, and related this equation to a number of particles N^* passing through the pore before its clogging:

$$N^* \propto \frac{t^* Q \Phi}{V_p} \quad (1.37)$$

These experiments show that t^* is strongly dependent of the volume fraction Φ (figure 1.21a). N^* seems to be independent of the flow rate Q and Φ (figure 1.21a) and on the contrary strongly depends on the confinement, described by a steep power law (figure 1.21b). Wyss et al. (2006) proposed a model to express the dependence between N^* and W/D :

$$N^* \propto (W/D)^m \text{ with } m = 4 \pm 0.1. \quad (1.38)$$

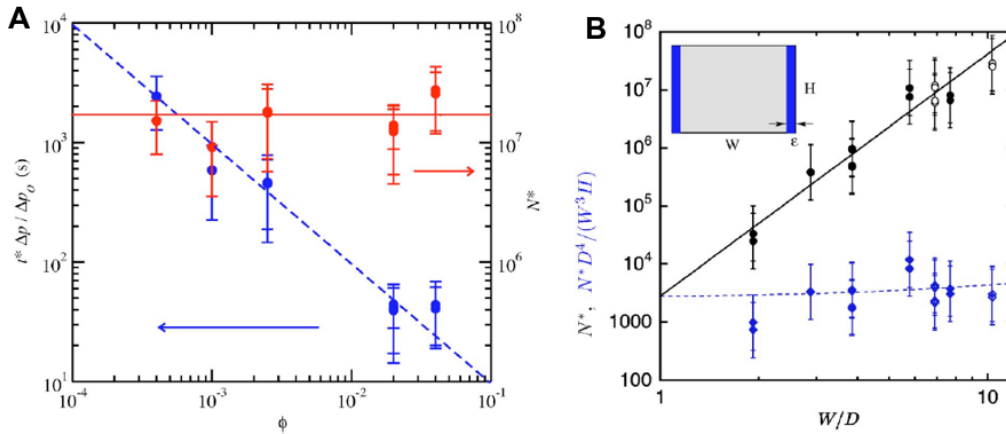


Figure 1.21: (a) Dependence of the average time clogging t^* and the number of particles N^* passing through the pore before its clogging. The clogging times are normalized with the flow rate. The blue dotted line is an inverse power law and the straight red line a constant value. From Wyss et al. (2006). (b) N^* number of particles as a function of W/D . In black, experimental data (open symbols: $2.9\mu\text{m}$ and solids symbol: $5.2\mu\text{m}$). In blue, model (equation 1.37). Adapted from Wyss et al. (2006).

Dersoir et al. (2015) verified that N^* follows a power law for particles from $2\mu\text{m}$ to $10\mu\text{m}$ (figure 1.22a), but unlike Wyss et al. (2006), the power law follows an index $m = 7$. This difference could be explained by the fact that the Wyss suspension is not perfectly monodisperse and would contain larger particles than the size distribution peak, leading to a more rapid clogging. More importantly in Dersoir's experiments, the N^* evolution is divided into two regimes (figure 1.22b), a constant N^* at low pressure and an increasing N^* at high pressure. The authors supposed a constant clog structure in the first regime while in the second the particle adhesion is modified, which delays the clog formation.

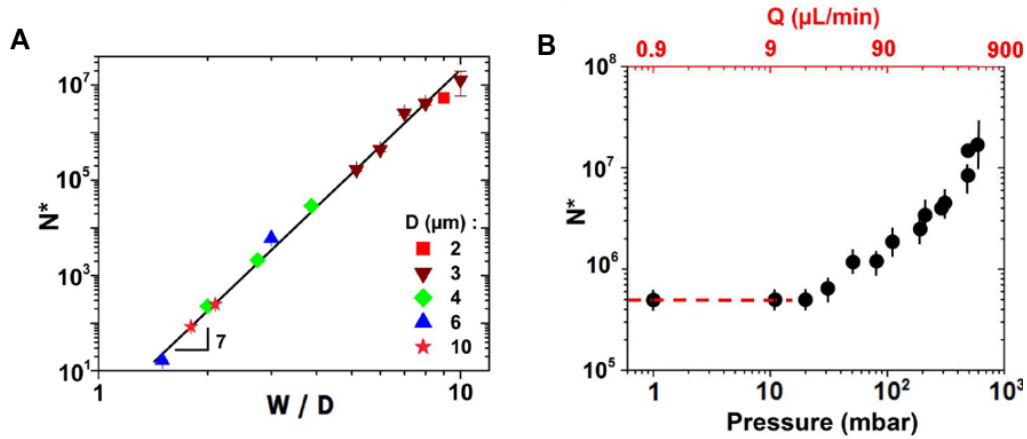


Figure 1.22: (a) Variation of N^* with the confinement W/D . The continuous line is a power law. From Dersoir et al. (2015). (b) Variation of N^* in function of the flow rate with an imposed flow rate, for $3\mu\text{m}$ particles. The dashed is a guide for the eyes. From Dersoir et al. (2015)

Both studies Dersoir et al. (2015) and Wyss et al. (2006) observed a strong dependence of the clogging with the NaCl concentration. Wyss et al. showed that t^* decreases when increase the ionic strength (figure 1.23a), making the assumption that a spontaneous aggregation between particles speeds up the clogging process. Dersoir et al. (2015) found that N^* is inversely proportional to the ionic strength (figure 1.23b), but without observing spontaneous particles aggregation in the bulk. Numerical studies also noticed a clog delaying thanks to the repulsion between the objects (Chen et al., 2016).

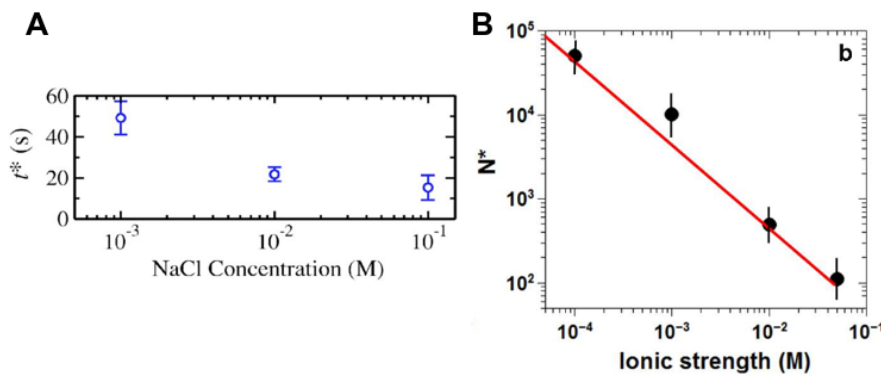


Figure 1.23: (a) Variation of t^* with the NaCl concentration. From Wyss et al. (2006). (b) Variation of N^* with the ionic strength for $4\mu\text{m}$ particles. From Dersoir et al. (2015)

The dependence of ionic strength, flow rate, and volume fraction not only impacts the clogging time, but also the deposit and its morphology. Agbangla et al. (2012) illustrated the existence or even the coexistence of different mechanisms such as dendrites, arches or clusters (merging of cakes layers of several clogged pores) under different conditions of formation (figure 1.24a). They showed that clog formation is more important when the particle volume fraction and the flow are higher when no salt was added to the suspension. When the salt content is high dendrites are systematically observed whatever the volume fraction. Sendekie et al. (2016) highlighted the link between hydrodynamic conditions and physiochemical interactions for clogs. At low and high moderate ionic strength, they found no clogging at high flow rate and an important clogging delay at moderate ionic strength (figure 1.24b). By considering the collective interaction of particles, different behaviour of clogs emerge. At low flow rates, the repulsion between objects prevents the clogging while high flow rate wipe particle off or even lead to the resuspension of part of the deposit.

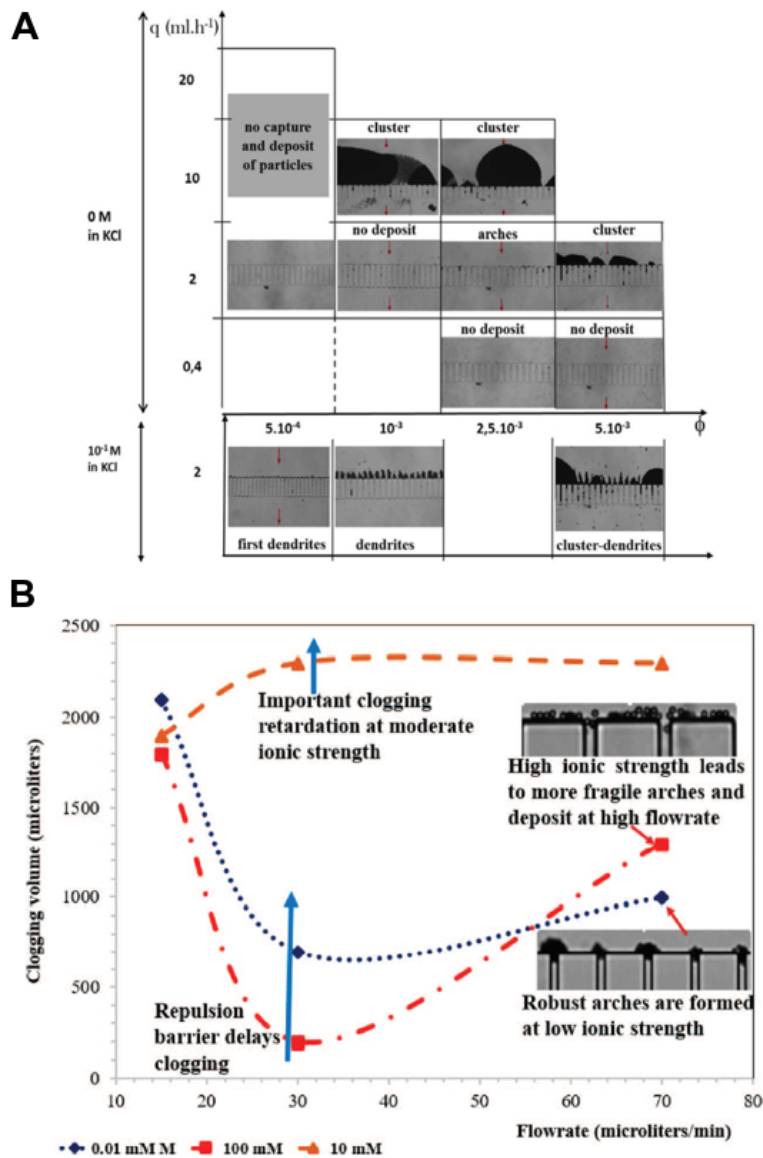


Figure 1.24: (a) Different clog structures for 5µm particles, depending on the flow rate, the ionic strength and volume fraction. Zones without clogs have been observed during 90min while zones with $q=10$ mL/h have been for 40min. From Agbangla et al. (2012). (b) Filtered volume leading to clogging according flow rates and for different ionic strengths (KCl), with 5µm particles and a volume fraction $\Phi = 10^{-5}$. From Sendekie et al. (2016).

Dersoir et al. (2019) obtained more detailed information of the clog structure with confocal imaging (figure 1.25). They imaged the pore in such a way that only two particles flow through the pore at the same time and observed that the first particles are preferentially deposited on the pore corners, the more stable position considering hydrodynamic forces. These deposited particles helped for the capture of other particles, since the new deposited are very often near an already deposited particles. The growing particles clusters finally merge and completely clog the pore in this way.

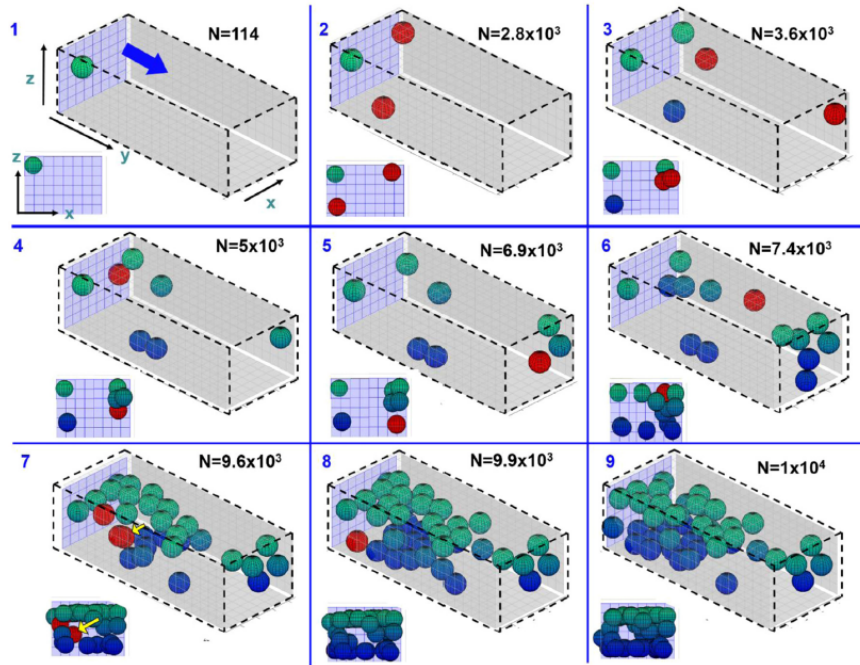


Figure 1.25: The clog build-up, with the blue plane the cross-section entrance. Red particles are the new deposited particles and the blue-green gradient positions particles from the top (blue) to the bottom (green). The yellow arrow shows the first particle stopped by others particles and not the wall. From Dersoir et al. (2019)

Clogging with some polydisperse suspensions

The vast majority of the works on clogging with microfluidic channels have used model suspensions that were supposed to be monodisperse, i.e. their size distribution is well peaked around a mean value. Several studies have shown that these monodisperse suspensions may contain minute quantities of larger objects that directly impact the clogging time. Mustin et al. (2010) observed that after an object deposition on the channel walls, a particle as large as the diameter of the pore is captured, the pore being soon after clogged (figure 1.26a). They showed that the clogging time was directly related to these objects. Hence when we remove them there is significant increase of the clogging time (figure 1.26b).

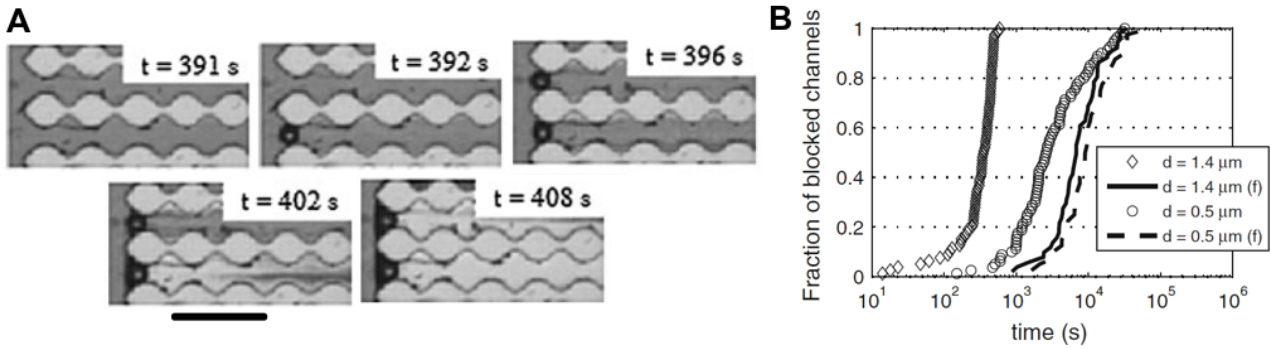


Figure 1.26: (a) Constriction blocked with a large particle. Scale bar: 100μm. From Mustin et al. (2010). (b) Evolution of the clogging time depending on the presence of large objects. From Mustin et al. (2010)

Still considering the presence of large particles in the suspensions, Sauret et al. (2014) proposed a method to estimate their concentration c based on the clogging time. t^* no longer depends on the volume fraction of the particles but on the concentration of the large objects: $t^* = 1/cQ$. Since the probability of clogging depends on t^* and follows a Poisson distribution, the distribution of clogging time provides the concentration c .

The clogging of membranes by polydisperse suspensions is the rule more than the exception in industrial applications. In addition, the objects composing the suspensions can be deformable, like monoclonal aggregates used by Duchêne et al. (2020). These authors showed that the sieving of such objects is far more complex than for non-deformable ones, since aggregates larger than the pore can enter in it and may even be flow through it after having underwent very large deformations (figure 1.27).

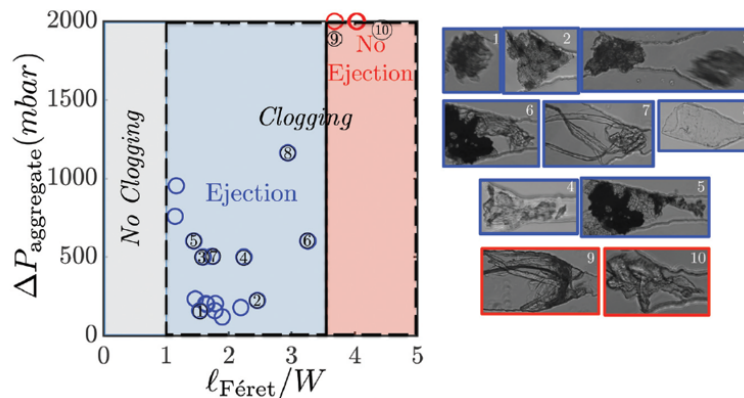


Figure 1.27: (left) Behavior of deformable aggregates when they encounter a constriction. For l_{feret}/W aggregates are larger than the pore. (right) Picture of some aggregates in the constriction. Adapted from Duchêne et al. (2020).

1.3.1.1 Particles accumulation behind the clog

After the formation of clogs, particles keep accumulating and may form a thick or long porous medium composed of particle behind the clog head (figure 1.28).

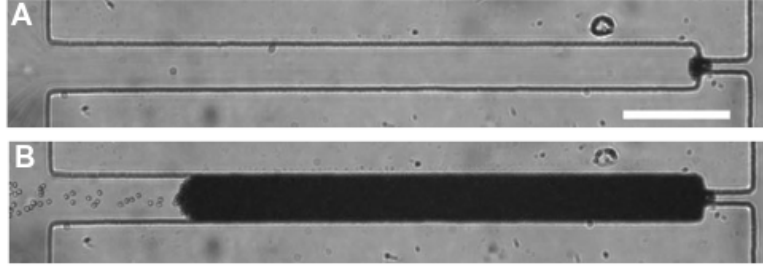


Figure 1.28: The clog head (a) and the important particle accumulation behind it (b). Adapted from Sauret et al. (2018). Scale bar: 100 μm .

Sauret et al. (2018) studied the time evolution of both the clogging dynamics and the flow rate. Taking into account of the resistance of each part of the channel, empty or filled with particles, they found the expression of the accumulation length over time:

$$l(t) = \left(\frac{2\alpha\Delta pk}{\eta\phi} t \right)^{1/2} \quad (1.39)$$

With α the volume fraction of particles, η the viscosity, k the permeability and ϕ the compacity of the packed bed, expressed with the Carman-Kozeny relation. By comparing the model with the experimental $l(t)$, they found a master curve for different pressures or particles concentration (figure 1.29a). They expressed the temporal evolution of the flow rate depending on the number of channels that remain open over the total number one N :

$$Q(t) = Nqe^{-t/\langle t \rangle} \quad (1.40)$$

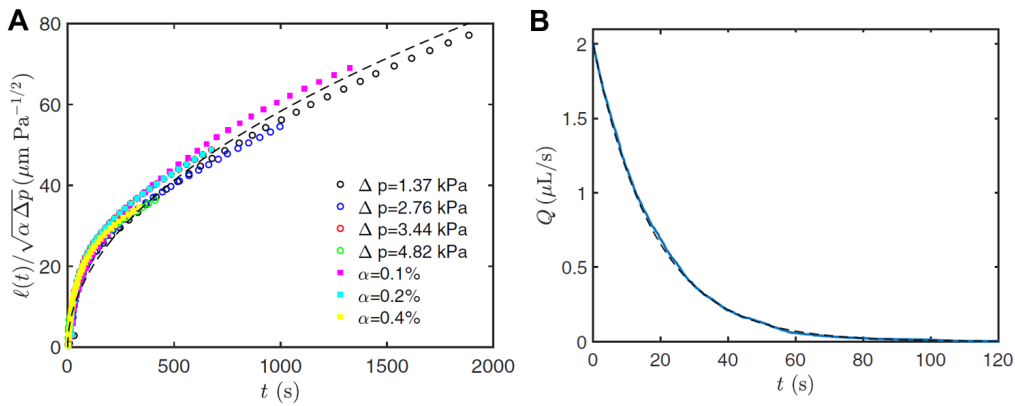


Figure 1.29: (a) Evolution of $l(t)/\sqrt{\alpha\Delta p}$ with particles concentrations and pressures. The dotted line is the analytical expression of $l(t)$ (eq 1.39). From Sauret et al. (2018). (b) Time evolution of the flow rate from numerical simulations (blue line). Dotted line, the equation 1.40. Adapted from Sauret et al. (2018)

Behind the particle accumulation and the flow decline, the structure of the packed bed can also impact the fluid transport. Linkhorst et al. (2016) observed the transport of rigid fluorescent nanoparticles through a packed microgels particles, with amorphous and crystalline zones. They noticed that despite smaller pores in crystalline zones, particles passed faster through it (figure 1.30b), because of the void alignment in microgels packing. Between two crystalline zones, the particle slows down before reaching another crystalline zone (figure 1.30a).

Concerning the structure arrangement for very low confinement, Mokrane et al. (2020) observed some differences by varying the formation conditions of the particle accumulation behind a clog. By fitting the radial distribution function, they noticed a parameter describing the local spatial organisation and depending on the ionic strength and on the distance from the pore. The more salt there is or the further away from the pore, the more disordered the structure is (figure 1.30b).

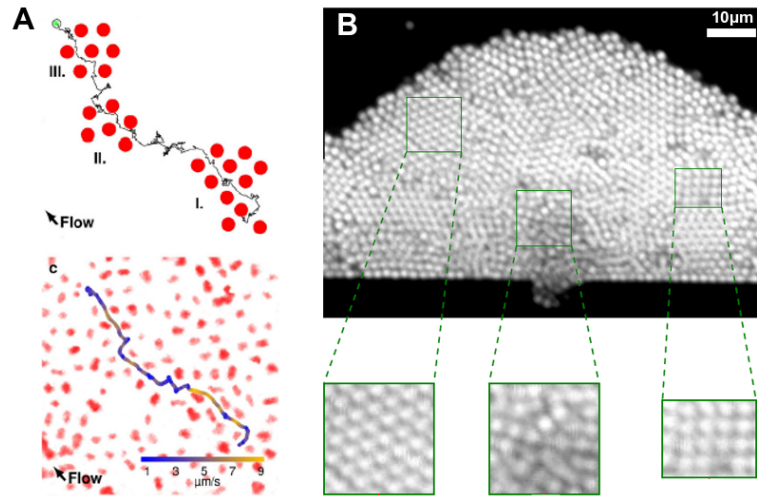


Figure 1.30: (a) Transport of a nanoparticles in a packed bed. (top) Trajectory through crystallines zones (I-III). (bottom) Particle velocity. Adapted from Linkhorst et al. (2016). (b) Different structures inside an accumulation of $1\mu\text{m}$ particles. Adapted from Mokrane et al. (2020).

1.3.1.2 Backwashing of the pore

Several experimental studies have focused on the improvement of the backwashing process, once the clog or accumulation behind are formed. Lohaus et al. (2020) studied the microscopic aspect by comparing experiment and numerical simulation, at different flow rates. They identified three mechanisms of backwashing as i) the erosion of individual particles, ii) the breakage of cluster (figure 1.31a) and iii) the cluster fragmentation and resuspension (figure 1.31b). The last two mechanisms are dominant, the first one being mainly observed at the beginning of the backwashing process since the particles have less contact points with the others in the cake layer rather than near the clog. This indicates a greater importance of particle-cluster interactions rather than particle-particle interactions as during the formation of the clog that explains why the flow rate of the backwashing is higher than that for clog formation.

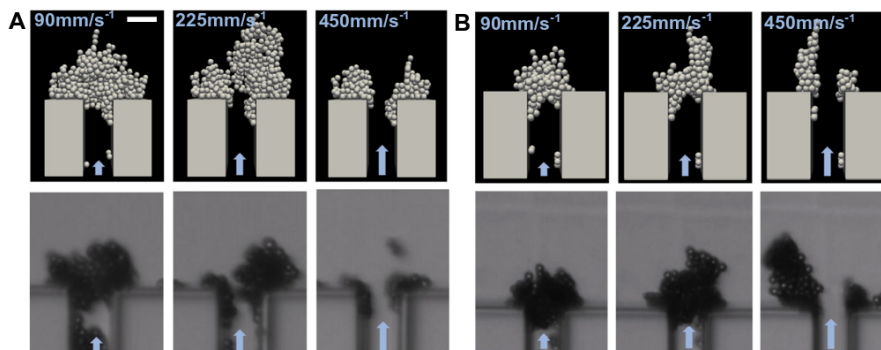


Figure 1.31: The two dominant mechanisms of backwashing, the breakage of cluster (a) and the cluster fragmentation (b). (top) Numerical simulation of the backwashing at different inverse flow rate. (bottom) Experimental equivalent with a smaller backwashing flow rate, from $0.1\mu\text{L}/\text{s}$ to $10\mu\text{L}/\text{s}$. Scale bar: $20\mu\text{m}$. Adapted from Lohaus et al. (2020).

1.3.2 Clogging of porous media

The main feature with a porous medium is the connection between pores, called cross-talk, which induces strong modification on the flow and particle distributions inside the medium.

1.3.2.1 Pore cross-talk

The filtration through a membrane involves a large number of pores close to each other. Hence the clogging of a pore is expected to have an impact on its neighbours. Liot et al. (2018) compared the growth rate v_N^*/v_0^* of the particle accumulation behind clog, in a single row of pore, as a function of the number of clogged pores N (figure 1.32). They proposed a model with the number of neighbouring pores as a parameter to fit the growth rate of the accumulation. Their model shows a strong cross-talk between pores. Liu et al. (2019b) also observed a strong dependence in the formation of clog in a 2D porous media with interconnected pores.

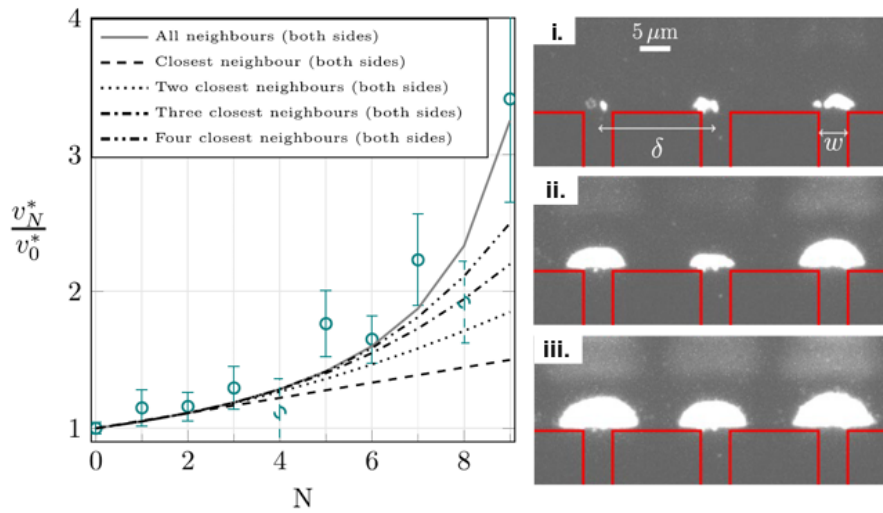


Figure 1.32: (left) The normalized growth rate v_N^*/v_0^* over the number N of clogged pores. Blue point are experimental data and different lines the model considering more or less neighbours. (right) Images of the growth particles accumulation behind clogs after 22min (i), 44min (ii) and 66min (iii). Adapted from Liot et al. (2018)

1.3.2.2 Clog front at the entrance of 2D and 3D porous media

Column packed bed and breakthrough curves are largely used to explain colloid adsorption, erosion or even clogging. Most of the studies were interested in the study of clogging in packed beds and highlighted the importance of the fluid velocity and the physico-chemistry of the suspension on the morphology deposit, without being able to verify with due to the lack of direct visualization of the mechanisms (Elimelech et al., 1990; Mays et al., 2005, 2007).

Several studies using *in-situ* imaging techniques of 2D and 3D porous media have subsequently observed concentrated clogging at the entrance of the media. Gerber et al. (2018) and Bizmark et al. (2020) observed the signature of nanoparticle deposition in a 3D packing bed, composing of transparent spheres. They both noticed that the clogging is concentrate at the entrance of porous media, with respectively NMR and confocal experiments.

Auset et al. (2006) imaged for the first time the filtration of colloid in a 2D transparent porous medium, with shape of collector mimicking grains. They injected several size of colloid and observed a clog concentration at the very entrance of porous media (figure 1.33). For larger sizes, sieving is the major mechanisms, and for smaller particle, porous are clogged with both sieving and particle deposition. Parvan et al. (2020) simulated clogging of a porous media with a lattice Boltzmann simulation and still noticed the clogging at the pore entrance.

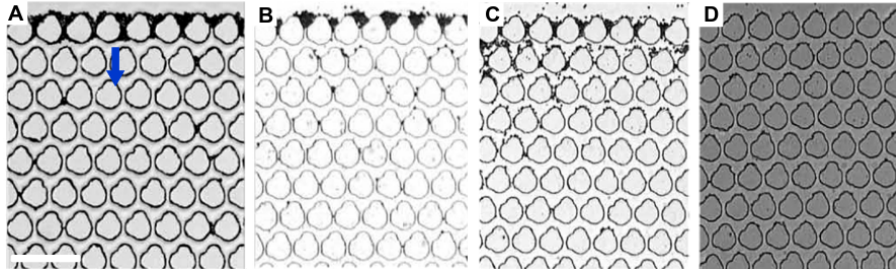


Figure 1.33: Filtration in a porous media by colloid $7\mu\text{m}$ (a), $5\mu\text{m}$ (b), $4\mu\text{m}$ (c) and $3\mu\text{m}$ (d). The blue arrow is the direction of the flow. Scale bar: $100\mu\text{m}$. Adapted from Auset et al. (2006).

If the clogging at the entrance of the porous media has been observed in several experimental conditions, there is no real explanation at the particle scale for this behavior.

1.3.2.3 Impact of internal tortuosity and connectivity within a porous medium

Bacchin et al. (2014) have investigated the impact of the connectivity but also the tortuosity of the medium on the clogging of porous media (figure 1.34a). They compared three types of geometry, straight pores for a single pore, connected pores and staggered pores to mimic a porous media, with a suspension containing KCl. They observed experimentally the formation of dendrites in the straight geometry, without internal clogging. For the connected medium, the volume of the medium is almost completely full, while for the staggered only limited deposition is observed on the collector tops. Lohaus et al. (2018) simulated the experimental condition of Bacchin et al., by taking into account repulsion between particles, short range interactions, or re-entrainment of particles or parts of the deposit, and obtained results close to the experiments of Bacchin et al (figure 1.34b) except for the straight geometry with intern deposition and dendrites downstream instead of upstream.

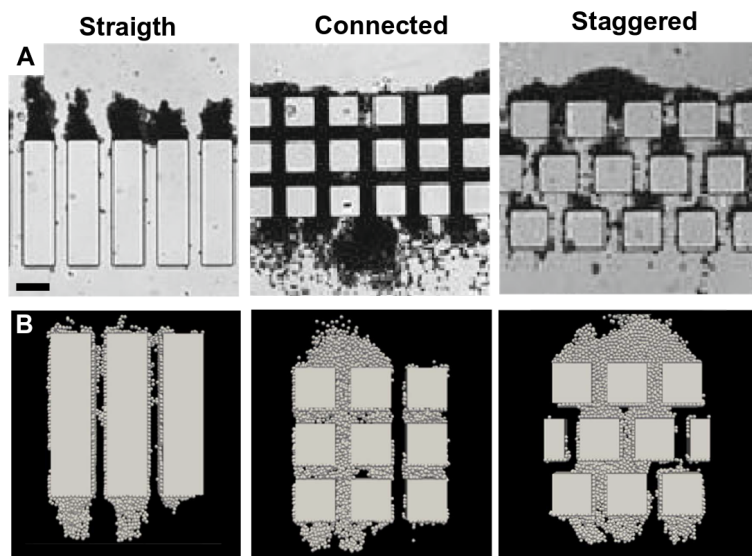


Figure 1.34: Comparison between the experimental clogging of Bacchin et al. (2014) (a) and the simulations from Lohaus et al. (2018) (b), for different geometries of porous media. Scale bar: $50\mu\text{m}$.

One may wonder if the clogging process they observed can be transposed to larger porous media since there is a very limited number of rows inside the porous medium. The proximity of large reservoirs before and after the three rows of collectors can greatly impact the behavior of particle inside the medium and disturb the interaction between the pores.

1.3.2.4 Cake layer

The pore cross-talk in porous media can also impact the growth of the cake layer. Van De Laar et al. (2016) and Zwieten et al. (2018) have observed different evolutions of the cake layer considering either a dead-end filtration or a cross flow filtration. In the former case, the cake layer is so important that it overflows on both side and help to the clogging of neighbouring pores (figure 1.35a). In the latter case, the cake layer is completely non existent or is very thin since particles are immediately re-suspended by the flow if they are not part of the clog (figure 1.35b).

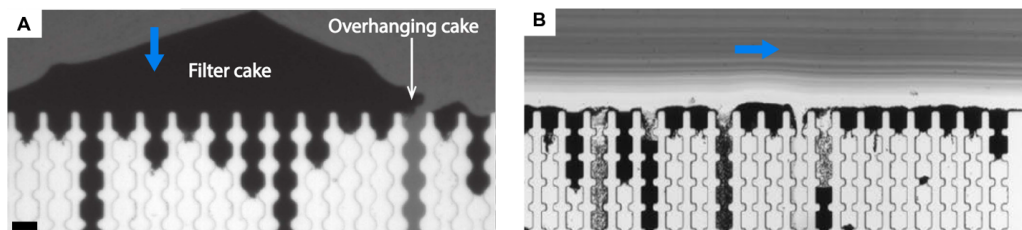


Figure 1.35: (a) Cake growth and impacts neighbouring pores with dead-end filtration (flow parallel to the pores). From Van De Laar et al. (2016). (b) Limitation of the cake growth with cross-flow filtration. Adapted from Zwieten et al. (2018). Blue arrows indicated the flow direction. Scale bar: 50 μ m.

1.4 Thesis objectives

The progressive clogging mechanisms is a complex process that depends on several physico-chemical parameters such as inter-particle and particle-wall interactions, hydrodynamic interactions that can promote or limit the deposition of particles, as well as the degree of confinement, corresponding to the pore size to particle size ratio W/D . In addition, the fouling and the clogging of a pore or a membrane induces a sudden and important flow decline. Several studies investigate the role of these parameters, however none of them shows the complete dynamics of pore clogging or relates the flow decline to the fouling, while the understanding of these two phenomena is crucial for industrial membranes. In this thesis, we try to answer to these two main questions:

- How does the progressive clogging occur within a pore?
- What are the consequences of the pore clogging on the flow conditions across the porous medium?

Based on these questions, the thesis is naturally split into two parts.

Part 1 - Clogging of a single pore

We first focus on a single pore to monitor the formation of the deposit, particle by particle, until the pore is clogged and a large accumulation grows behind it. We link the progressive clogging to the flux decline by measuring the particle velocity thanks to particle tracking. This first part is divided into three chapters.

Chapter 3 - The impact of aggregates on clogging

We describe the clogging history in a single pore, particle by particle. We show that aggregates are systematically present inside clogs, despite they are very rare in a monodisperse suspension we used. We determine how their probability of capture is modified with the particle stabilisation, the flow rate, the ionic strength and the confinement.

Chapter 4 - The flow decline during the pore clogging

We couple experiments and flow simulations to understand how flow across the pore is impacted by its fouling. We also determine the flow within the clog already formed.

Chapter 5 - Structure and flow conditions through a colloidal packed bed formed under confinement

We measure the main features of the particles accumulation behind the clog, i.e. the permeability with particle tracking and the volume fraction by counting the objects, by varying the flow rate and the ionic strength. We also performed unclogging experiments.

Part 2 - Clogging of a porous medium

We use the same methodology to study the clogging of porous media with interconnected pores. We describe the phenomenology of the medium clogging, taking into account the cross talk between the pores and we try to understand the impact of the pore clogging process on the flow conditions .

Chapter 6 - The clogging of interconnected pores by colloidal particles

We study the clogging in an ordered porous medium by strongly repulsive particles. We present a model only based on the tail of the size distribution and the capture probability of the objects to describe the

pore clogging process.

Chapter 7 - Impact of interaction potentials on the clogging of porous media

We perform the same experiment as in chapter 6 but adding salt to work in favourable deposition conditions, i.e. with no electrostatic repulsion at the collector's surface.

Chapter 8 - Flow decline during the clogging of porous media

We establish the relationship between the flow decline and the degree of fouling of a porous media. We propose a model to rationalize our data, considering the porous medium as a matrix of hydrodynamic resistance.

Chapter 9 - Clogging with fragmented colloid plastics

We perform clogging experience in an heterogeneous medium with fragmented nanoplastics with different size distributions.

Chapter 2

Materials and methods

The experimental work of this thesis deals with clogging experiments at the pore and particles scales. The originality of the thesis lies in the systematic use of (i) high speed image capture to be able to monitor the consecutive particle deposition inside a pore and (ii) dedicated image analysis routines to track the particle motion and the development of the fouling layer. This chapter presents the imaging tools used to monitor particles passage and the microfluidic chip fabrication protocol. Then we present the features of the different suspensions of particles used a characterisation *in-situ* and under flow thanks to image analysis during stop and go experiments. Finally, we expose the different image analysis tools and programs created during the thesis, at the pore scale up to the porous media scale.

Contents

2.1	Description of a typical microfluidic experiment	48
2.1.1	Camera	48
2.1.2	Microscopy and micrometric particle	49
2.1.3	Microfluidic technique	52
2.1.4	Injection of the suspension in the microfluidic system	55
2.2	Particle suspension	56
2.2.1	Particle stabilization	56
2.2.2	Monodisperse suspensions and aggregates	58
2.2.3	Fast Radial Symmetry (FRS)	58
2.2.4	Detection of aggregates dimensions	62
2.3	Image analysis	65
2.3.1	Particle tracking	65
2.3.2	Automated detection of clogged pores in a porous medium	68

2.1 Description of a typical microfluidic experiment

This section presents the tools used for a typical microfluidic experiment, which consists in the pressurisation of a particle suspension through a transparent microfluidic system imaged by a camera and a microscope (figure 2.1).

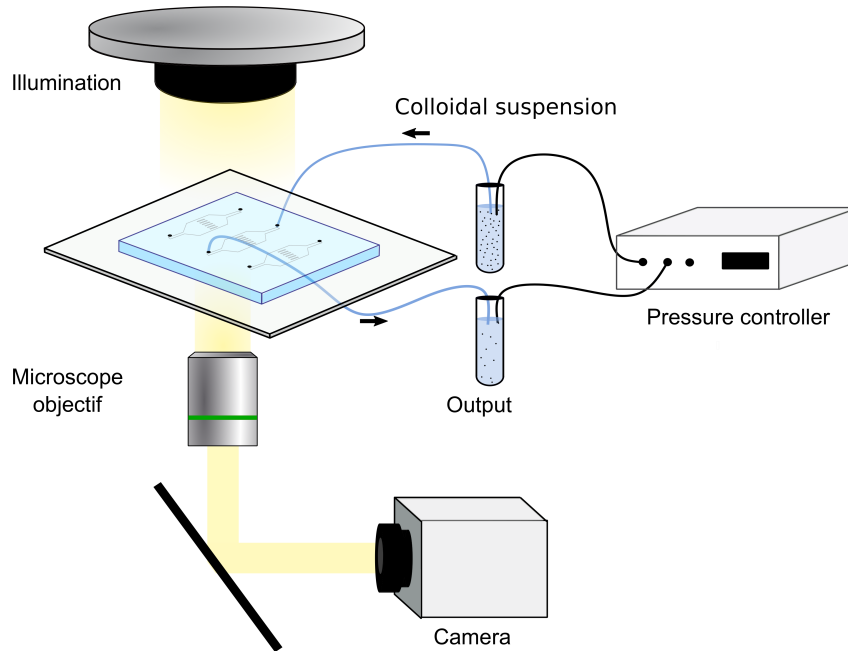


Figure 2.1: Sketch of the experimental setup

2.1.1 Camera

Experiments are performed with a Hammamatsu Orca Flash 4.0. On this camera, the sensor is separated into two zones and the pixels reading is done in parallel (figure 2.2). The initial frame rate for a sensor zone of 2048x2048 pixels is 100 fps (frame per second) but reducing the number of line from either side of the sensor center increases the fps. For example, a reduced sensor zone of 2048x128 pixels can reach 1600 fps.

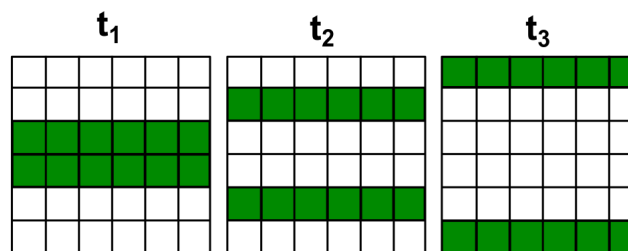


Figure 2.2: Shutter operation for Hammamatsu Orca Flash

2.1.2 Microscopy and micrometric particle

We used microparticles which can be correctly resolved with conventional microscopy methods, such as brightfield or fluorescence microscopy.

2.1.2.1 Brightfield microscopy

The brightfield microscopy is the simplest microscopy technique. The sample is illuminated with a white light creating a contrast between the denser areas where light is more absorbed and areas where light is more transmitted. The illumination path (figure 2.3a) starts from a light source before passing through two lenses. First the collector lens collects the light to focus it in the plane of the aperture of the condenser. Then the condenser lens projects the light onto the object and through the objective which magnifies the image. The light is finally projected by a photo-ocular onto the camera sensor. We used the Köhler protocol to obtain an optimal lighting, by differencing the illumination path from the image path (figure 2.3a-b) and obtain a perfectly homogeneous image without the image of the filament.

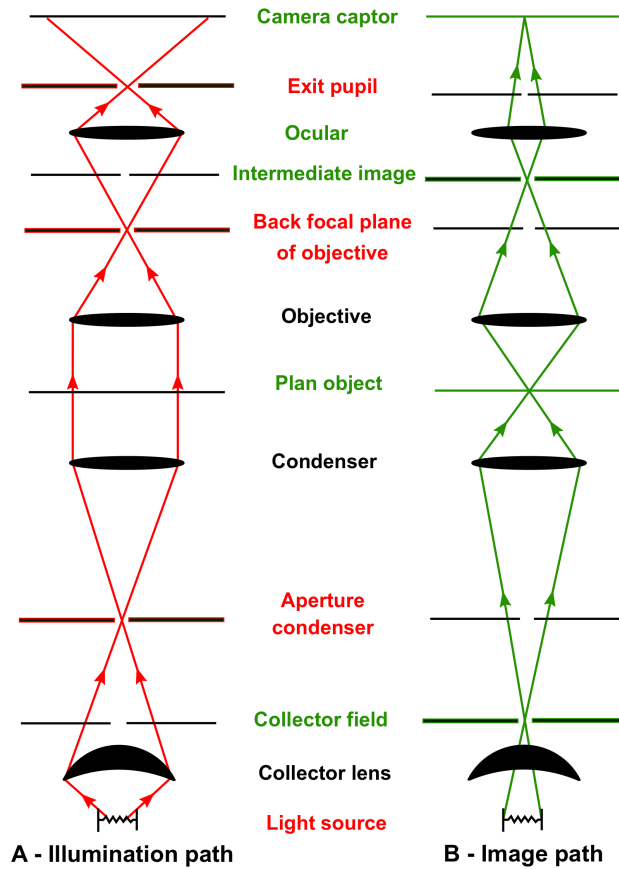


Figure 2.3: Principle of brightfield microscopy. The illumination path is composed of the lamp filament, aperture condenser, focal plan and exit pupil (a). The image path is composed of the collector field, object plane, intermediate image plane and the camera captor (b). Adapted from Elliot et al. (2001)

2.1.2.2 Fluorescent microscopy

Some particles we used are synthesized with a fluorophore inside. A source of light is sent to a filter which transmits only the part of the light containing the wavelength necessary for the excitation of the fluorophore. A dichroic mirror reflects the excitation light on the sample (figure 2.4). To return to its fundamental state, the fluorophore emits a light which passes through the dichroic mirror again. An emission filter eliminates the rest of the excitation light before reaching the camera sensor.

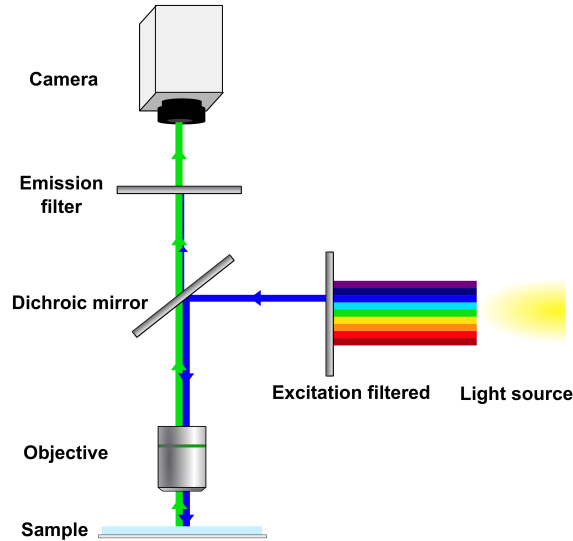


Figure 2.4: Fluorescence microscopy

2.1.2.3 Diffraction and focal plane

Microparticles can be well resolved, but the size of the objects is impacted by the diffraction. Due to the wave-like nature of the light, the maximum resolution of a microscope is limited by diffraction through a finite aperture (figure 2.5a). The smaller the object, the greater the diffraction. The numerical aperture A is the ability of an objective to receive light and transmit the details of the sample (figure 2.5b):

$$NA = n \sin \sigma \approx n \frac{D}{2f} \quad (2.1)$$

with n the refractive index in the medium between the object and the system, f the focal length, D the entrance pupil and σ the maximal half-angle of the cone of light. A larger numerical aperture lets more rays going towards the object and provides a better resolved image. For this purpose, a condenser is placed before the object to concentrate the oblique rays (figure 2.5b).

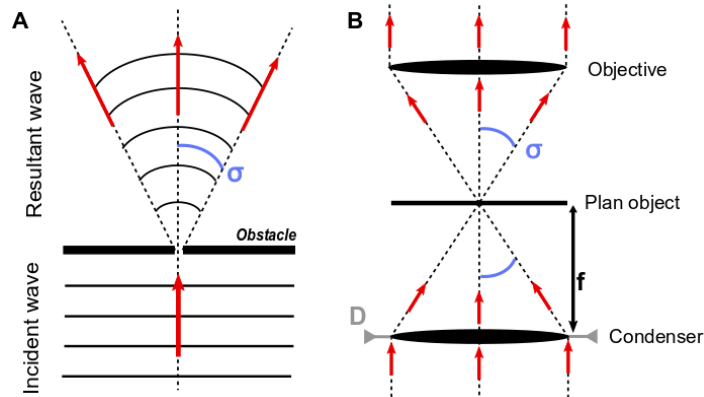


Figure 2.5: Diffraction by a finite aperture (a), by a microscope (b)

The diffraction limits the resolution of the imaging system, the image of a point is not a point but a diffracted figure, called the Point Spread Function (PSF). The diffraction pattern of a particle is an Airy disk that presents several rings. Figure 2.6 shows the PSF amplitude of a fluorescent particle.

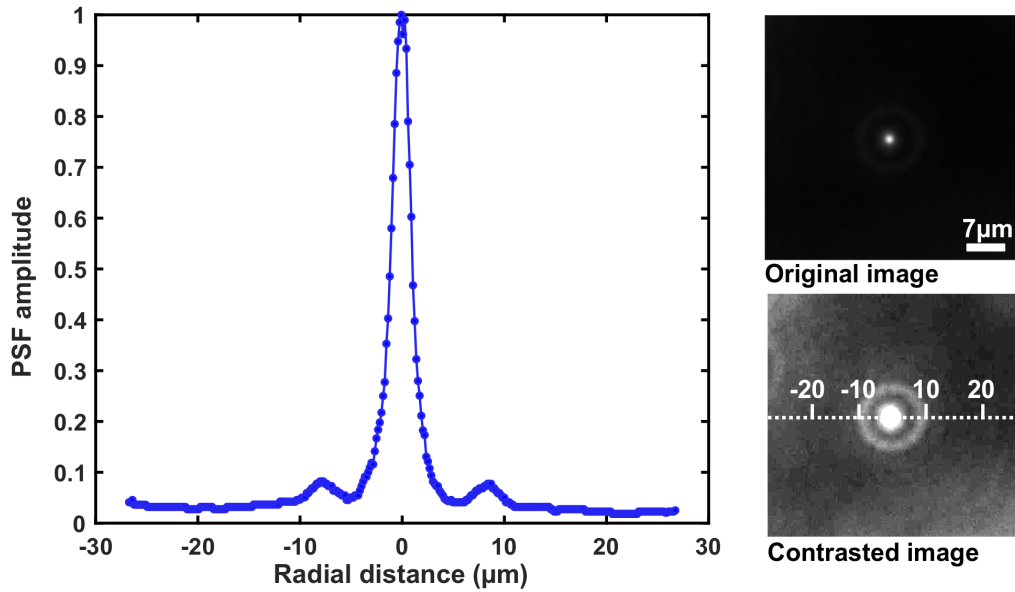


Figure 2.6: PSF amplitude and Airy pattern of a 1.8 μm PMMA particle.

The rings of the Airy pattern expand as the particles move away from the focal plane (figure 2.7). Therefore it is not possible to define accurately the size of particles with a microscope since the diameter of the size of rings depends on the z-position. Another consequence is that the average intensity over the whole particle will depend on its position in the focal plane, which we will take advantage of in particle tracking algorithm.

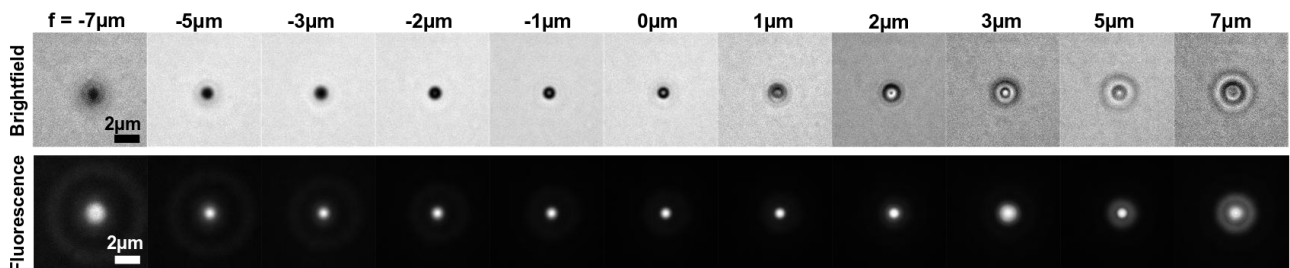


Figure 2.7: Airy patterns for brightfield and fluorescence images of a 2 μm particles for different z-positions.

2.1.3 Microfluidic technique

To control small volumes of fluid between the nanoliter and the microliter, we use microfluidic systems. Over the past twenty years, the use of soft lithography techniques has allowed fabricating such microfluidics channels, mainly in a low elastic modulus elastomer like PDMS (Polydimethylsiloxane).

2.1.3.1 Softlithography and microfabrication

The microfabrication consists in making a master from photolithography which can be moulded or replicated several times. We use the method described in Xia et al. (1998). The entire process of photolithography is illustrated on figure 2.9a. To manufacture the mould, we use a silicon wafer, on which a thin layer of SU8, a negative photoresist, is spin-coated. The height of this layer varies as a function of the viscosity of the resin and of the rotation speed of the spin-coater. For each resin the manufacturer provides a graph of the rotation speed versus the height of the film. The film deposited on the wafer is heated to 95°C, this step is called soft bake and allows the evaporation of the solvent before the UV exposure through a photomask, plastic or chrome. The transparent parts of the mask allows UV rays to pass through and reticulate the resin underneath while the opaque parts in chrome block them. The time of UV exposure depends on the film thickness. After the exposure another heating step is used called the post exposure bake, where the wafer is heated to 95°C. Thereafter, the non-UV exposed zones are removed by a PGMEA developer and the wafer is rinsed with isopropanol to stop the development process. There is a final baking step around 120-150°C.

Once the master is made, it can be moulded (figure 2.9b) several times with an elastomer, the most commonly used being the PDMS that can be easily peeled off. We use Dow Corning's Sylgard 184 PDMS, in which reticulate agent is mixed with the liquid polymer matrix in a 1:10 ratio. This reticulated silicone-based elastomer is homogeneous, isotropic and optically transparent. The mixture is poured over the master in a petri dish, degassed and put in the oven for 2 hours at 65°C. Once cured, the replica is a soft solid that is cut from the mould with a scalpel, and holes for the inlets and outlets are punched. To close the microsystem, we use glass slides coated with PDMS to obtain a channel where all the walls have the same surfaces properties. The PDMS coated glass slide and the PDMS channel are plasmatized for one minute before being irreversibly assembled. The plasma treatment modifies the surfaces and transforms the groups $-\text{OSi}(\text{CH}_3)_2\text{O}-$ at the surface of the PDMS into $-\text{O}_n\text{Si}(\text{OH})_{(4-n)}$ (figure 2.8). Duffy et al. (1998) assumed that the formation of covalent siloxane (O-Si-O) bridges by condensation reaction explains the very strong contact between the two substrates. The silanol (-OH) groups are polar and make the surfaces strongly hydrophilic for 48 hours. To work in hydrophobic conditions, the chip is placed in an oven at 120°C for 2h.

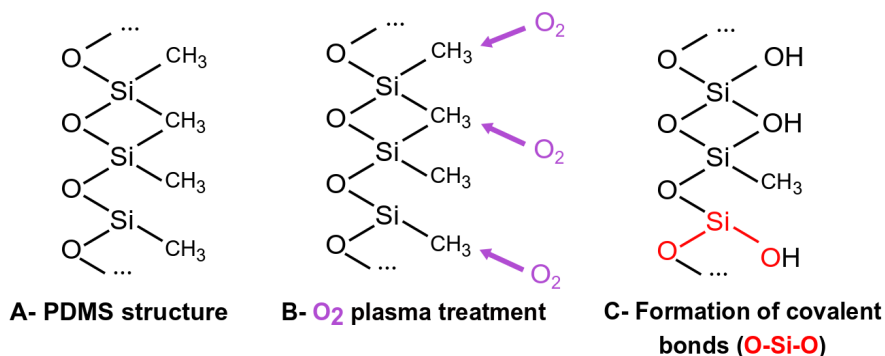


Figure 2.8: Plasma treatment

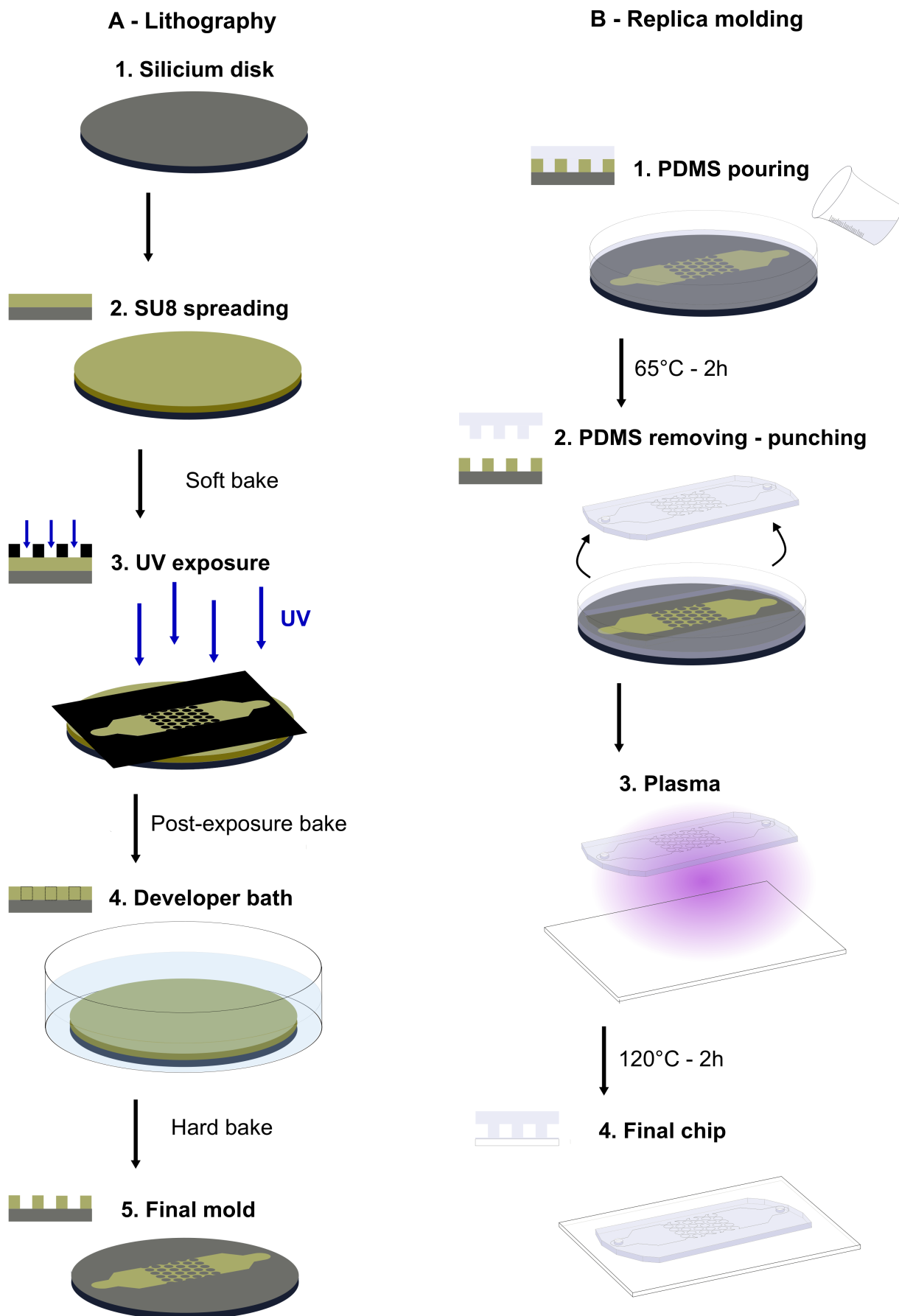


Figure 2.9: Softlithography process.

2.1.3.2 Hydrodynamic resistance characterization of microfluidic chips

To be able to fix the same flow conditions in microfluidic channels with different geometries, we determine their hydrodynamic resistance. We flow pure water through a flow sensor (Fluigent), connected in series with the microfluidic channel. The measure has an accuracy of 5% and is adapted with the corresponding viscosity of the used fluids. We impose different pressures and measure the flow to obtain the hydrodynamic resistance for each geometry.

A second method consists in flowing directly the liquid and weighting the mass passing through the channel. We measure on a scale with an accuracy of 0.2 mg every 10 minutes for one hour. As the scale is very sensitive, the weighing should be done without contact of the outlet tubing and takes 2 to 3 seconds to be stabilized. we have 10% uncertainty with this technique.

2.1.3.3 PDMS microchannel deformation

Gervais et al. (2006) performed a characterization of this deformation of PDMS channels with a low Young's modulus between 1 and 4MPa depending on the curing agent concentration (Johnston et al., 2014). According to their study, the channel deformation is non-uniform throughout the channel and decreases along the flow (figure 2.10), which was experimentally verified by Hardy et al. (2009), using fluorescent fluid.

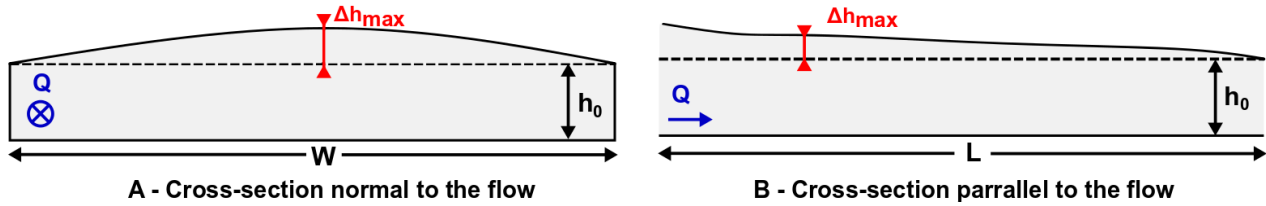


Figure 2.10: Schematic representation of polymer channel deformation under an imposed flow rate. Adapted from Gervais et al. (2006)

Using the relation $\delta P = R_H Q$ and the hydrodynamic resistance R_H for a rectangular channel:

$$R_H = \frac{12\mu L}{h^3 W} \quad (2.2)$$

We obtain a flow-pressure relation dependent on the deformation in height:

$$-\frac{\partial p(z)}{\partial z} = \frac{12\mu}{h^3 W} Q \quad (2.3)$$

The resolution of this equation is too complex to obtain an analytical solution, thus Gervais et al. proposed a scaling approximation with Hook's law $\epsilon = \sigma/E$ where ϵ the strain, σ the stress and E the Young's modulus or the elastic modulus:

$$\epsilon_{vertical} \sim \frac{\Delta h}{W} \sim \frac{p}{E} \quad (2.4a)$$

$$\epsilon_{lateral} \sim \frac{\Delta W}{h} \sim \frac{p}{E} \quad (2.4b)$$

Gervais et al. considered the conditions where $W \gg h$, for which the lateral deformations are negligible:

$$\frac{\Delta h_{max}}{h_0} = c_1 \frac{pW}{Eh_0} \quad (2.5)$$

with c_1 a geometry constant of order 1. If $W \sim h$, the scaling approximation still works, but the deformation will take place for the top and the two lateral walls, the bottom one being not deformed, due to the stiffness of the glass slide on which there is the thin layer of PDMS.

Our most deformable channels are constrictions with a cross section of $8\mu\text{m}\times 8\mu\text{m}$ and the pressures used for this geometry are in the range 5-270mbar, for which the deformation is around a tenth of a micron (figure 2.11a). Within this pressure range the increase of the hydrodynamic resistance, due to the very slight widening the cross section, is small and the linear relationship between the pressure and flow rate is still valid (figure 2.11b).

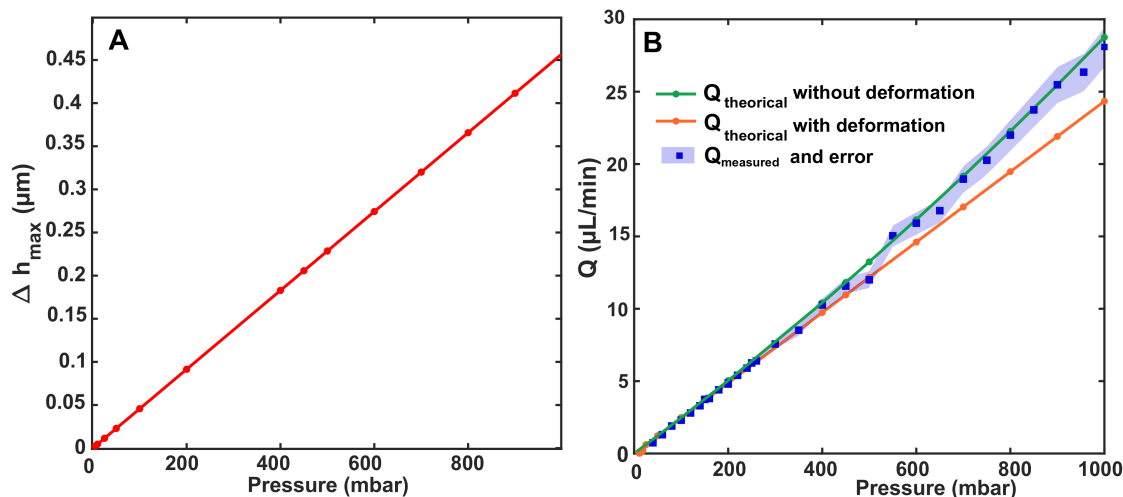


Figure 2.11: The maximal deformation under pressure of a $8\times 8\mu\text{m}$ channel (a) and the associated modification of the flow rate (b).

2.1.4 Injection of the suspension in the microfluidic system

Suspension

The dispersing medium, which composition is detailed later on, is always composed of water in which we add 0.3g/L EDTA (ethylenediaminetetraacetic acid) to prevent the growth of biofilm. This medium is systematically filtered (PTFE filter, 0.2mm) before adding particles, to avoid contamination, dust and other fibers. Colloidal suspensions are changed every day to avoid coagulation of particles or contamination and are systematically sonicated for half an hour before their injection in the microchannels.

Tubbing

The tube containing the colloidal suspension is connected to the microfluidic channel with a PTFE tubing, of different internal diameters, 0.38mm or 0.8mm. The larger diameter has the advantage of allowing more rapid homogenization of the particles across the entire width of the channel and it avoids an excessive deposition inside the tubing. For the most unstable suspensions, the injection tubing is systematically changed between each experiment to minimize this effect and it is changed on a daily basis. The injection is performed by applying a pressure drop between the inlet and the outlet. The inlet and outlet are pressurized via a pressure controller (OB1 Elveflow, MFCS Fluigent or flow EZ Fluigent). Before the passage of the particles in the pore at the middle of our chip, we immobilize them in order to quantify the impact of the hydrostatic pressure, due to the differences of height of the liquids in the tubes containing the suspensions at both ends.

2.2 Particle suspension

2.2.1 Particle stabilization

We use two types of particles in this thesis, their main difference being the way they are stabilized.

2.2.1.1 Stabilization by surface charges

The latex particles are provided by Invitrogen and microParticle GmbH, and their surface are stabilized by sulfate group. As seen in the previous chapter, the addition of salt can however screen the charges at the surface of the particles and allows them to come closer to each other or even to form spontaneously aggregates (figure 2.12).

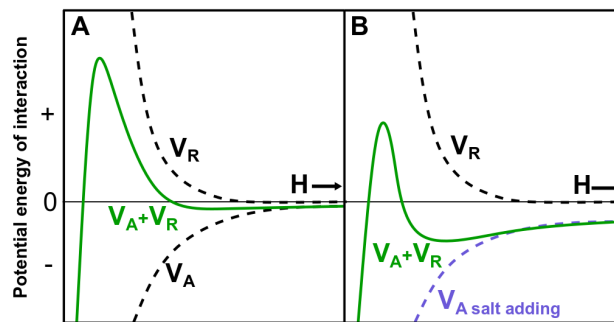


Figure 2.12: Potential energy of interaction between colloidal particles (a) and evolution by adding salt (b). H is the distance between the surface of the objects, V_A the attractive potential and V_R the repulsive potential.

2.2.1.2 Steric stabilization

Steric repulsion relies on the grafting of polymer chains on the particles surface (figure 2.13). This type of stabilization is not impacted by the variation of the ionic strength (Fritz et al., 2002).

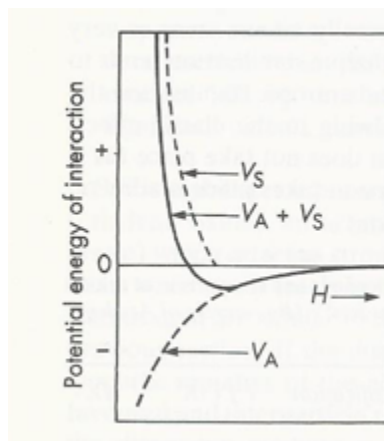


Figure 2.13: Potential energy of interaction between steric particles. H is the distance between the objects, V_A the attractive potential, V_R the repulsive potential and V_S is the steric potential. From Shaw (1992).

We used PMMA particles synthesized by A. Schofield (University of Edinburgh) by a emulsion polymer described by Shen et al. (1993). These particles are made in the presence of a steric stabilizer (PVP), a monomer (MMA) and an initiator (Aibn) in a liquid medium (methanol). The whole mixture is heated up and the initiator dissolves in the medium. Free radicals are generated and react with the monomers to form polymer that precipitate to generate nuclei. These unstable nuclei aggregates with each other then adsorb stabilizers on their surface and become stable particles. At the end of the chemical process, the particles are supposed to be stabilized to prevent their aggregation. However, by characterizing the suspensions, we observed a fairly small amount of aggregates. We assume these aggregates may have formed during the synthesis of the particles. Some studies have proved a deformation of the particles according to the volume of cosolvent (Zhang et al., 2010), a small variation of the concentration of polymer increases the polydispersity in size of the suspension (Almog et al., 1982) or an excess of monomers can desorb the stabilizer during the nuclei phase and thus promotes the formation of particles aggregate. The measure of these small modifications of components during the synthesis are complex to measure since the reaction process can not be stopped easily, however the presence of aggregates is therefore unavoidable in monodisperse suspensions, at least for this synthesis protocol.

We also use coated PS particles, onto which a polymer brush is grafted, synthesized according to a similar protocol to Shen et al. (1993) but with different polymers like TFEMA (trifluoroethyl methacrylate) and tBMA (tert-butyl methacrylate)(Kodger et al., 2015). These particles were provided by Thomas Kodger (University of Wageningen).

2.2.1.3 Summary of the properties of materials and particles

To prevent sedimentation or creaming, the particles are suspended in a density match fluid. Table 2.1 summarizes the properties of the main materials of the particles and the liquid suspension.

Type	Density (g/cm ³)	Refractive index	Charge (mV)	Suspension fluid
Sulfate latex	1.055	1.59	30-35	Water - Glycerol (23.2%)
PS coated	1.066	1.59	-	Water - Glycerol (27.5%)
PMMA	1.18	1.42	70	Water - Urea (37%) - Glycerol (30%)

Table 2.1: Particles material used

The following table 2.2 summarizes the different particles used in the thesis.

Type	Origin	Size (μm)
Sulfate latex	microParticle GmbH	0.97, 1.5, 1.85, 3 and 5
Sulfate latex	Invitrogen	2
PS coated	T. Kodger	2.4
PMMA	A. Schofield	1.8

Table 2.2: Particles used in the thesis

2.2.2 Monodisperse suspensions and aggregates

We develop here a method to characterize colloidal suspensions and quantify their size distribution that includes the aggregates.

Stop and go method

To quantify the amount of aggregates, as well as their geometrical features inside the suspension, we have set up a characterization method called stop and go. To characterize the size distribution considering the different objects, we inject a suspension with a very low volume fraction of $5 \cdot 10^4$ into a rectangular channel (1cm long, 0.5mm wide and $20 \mu\text{m}$ high). During this experiment, we stop the injection for 6–7s and image the particles in one part of the channel. Thereafter we flush the channel with a large pressure for 3–4s, high enough to get new particles in the field of view. In this way, we obtain typical pictures with around 1200–1400 objects and after 7–8h of experiment, we obtain a total amount around $3 \cdot 5 \cdot 10^6$ objects. For each image we detect the position of each object and determine whether if they are single particle or an aggregate. In the later case, we counted the number of particles composing the aggregates thanks to the fast radial symmetry algorithm (FRS), detailed on the next paragraph. We also extract several morphological parameters like the perimeter, the area or the maximal length.

2.2.3 Fast Radial Symmetry (FRS)

2.2.3.1 Why the FRS ?

We want to characterize the suspension according to the size of the objects, but also on their type, single or aggregate. If they are aggregates, we count the number of particle composing them. To locate and detect fluorescent particles, the most commonly used method is the gaussian fitting. However, due to their proximity of neighbouring particles in an aggregate there is an overlapping or their respective gaussian fits, which makes it difficult to distinguish each particle. In addition, when particles are well packed inside an aggregate the intensity distribution can be so smoothed that the algorithm eventually detects only one particle. Figure 2.14 shows some wrong aggregates detection with the gaussian method. For this comparison, we use an algorithm based first on a threshold on the image before a spatial bandpass suppressed the individual pixel value fluctuations and then smooth information on the picture (Crocker et al., 1996). Each local maxima is then a center particle. We choose the Fast Radial Symmetry (FRS) a method developed by (Loy et al., 2003). Initially, this method was used by the computer vision community, to find circles deformed into ellipses by perspective in an image. The FRS is based on a weight image since each pixel has a value, lies to its contribution at the symmetry considering the objects around it and not considering the pixel as central.

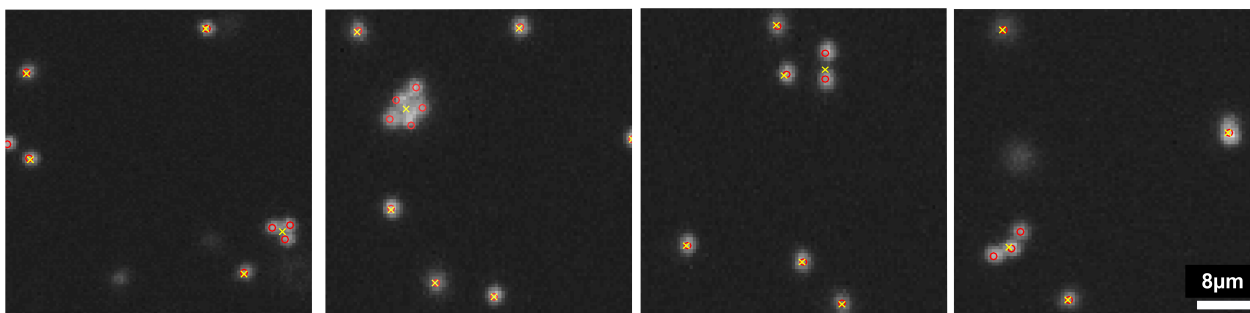


Figure 2.14: Detection of the particle center with the gaussian method (yellow crosses) and the FRS method (red circles). Each cross or circle corresponds to a detected particles or aggregate.

It is more interesting to use the FRS rather than an algorithm based on the commonly used hough transform, due to its computational cost. The most common circular hough transform (CHT) algorithm find a circle of center (a,b) with three parameters, the pixel position (x,y) and the radius of the circle. The complexity for an image of $N \times N$ pixels is about $O(N^3)$ (Kimme et al., 1975). Several algorithms based on the CHT have lower complexity, but at the moment the FRS is the most efficient and simple with a complexity of $O(N)$, generated by a single operation of convolution.

2.2.3.2 Definition of the FRS transform

For each pixel $\mathbf{p} = (x,y)$ of the original image, a Sobel gradient $g(\mathbf{p})$ is calculated:

$$g(\mathbf{p}) = \sqrt{g_x^2(\mathbf{p}) + g_y^2(\mathbf{p})} \quad (2.6)$$

with $g_x(\mathbf{p})$ and $g_y(\mathbf{p})$, the values of horizontal and vertical gradient at the point (\mathbf{p}) .

The transform is calculated for many radii $n \in \mathbb{N}$, a set of radii of symmetry, and gives the contribution to the radial symmetry at a distance n from each point. The set of radii is not necessarily continuous and the more complete it is, the less the error increases with a larger impact on computing time.

For each radius n , the positively-affected pixels $\mathbf{p}_{+ve}(\mathbf{p})$ and the negatively-affected pixel $\mathbf{p}_{-ve}(\mathbf{p})$ are calculated. They correspond to points pointing toward and away from the center respectively at (\mathbf{p}) , represented in figure 2.15.

$$\mathbf{p}_{+ve}(\mathbf{p}) = \mathbf{p} + \text{round} \left(\frac{\mathbf{g}(\mathbf{p})}{\|\mathbf{g}(\mathbf{p})\|} n \right) \quad (2.7a)$$

$$\mathbf{p}_{-ve}(\mathbf{p}) = \mathbf{p} - \text{round} \left(\frac{\mathbf{g}(\mathbf{p})}{\|\mathbf{g}(\mathbf{p})\|} n \right) \quad (2.7b)$$

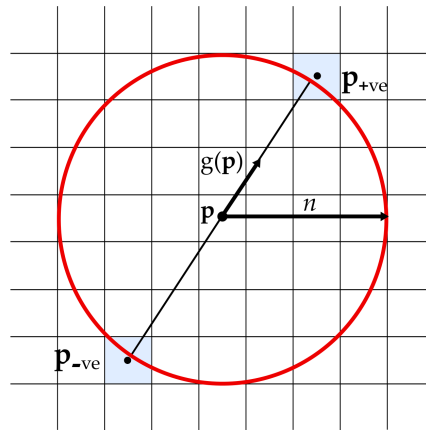


Figure 2.15: Location of $\mathbf{p}_{+ve}(\mathbf{p})$ and $\mathbf{p}_{-ve}(\mathbf{p})$ pixels affected by the gradient element $g(\mathbf{p})$ centered at \mathbf{p} and around a circle of radius $n=3.5$. Adapted from Loy et al. (2003).

These affected points generate an orientation projection image O_n and a magnitude projection image M_n . Initially empty, these images are incremented for each pair of affected pixels:

$$O_n(\mathbf{p}_{+ve}(\mathbf{p})) = O_n(\mathbf{p}_{+ve}(\mathbf{p})) + 1 \quad (2.8a)$$

$$O_n(\mathbf{p}_{-ve}(\mathbf{p})) = O_n(\mathbf{p}_{-ve}(\mathbf{p})) - 1 \quad (2.8b)$$

$$M_n(\mathbf{p}_{+ve}(\mathbf{p})) = M_n(\mathbf{p}_{+ve}(\mathbf{p})) + \|\mathbf{g}(\mathbf{p})\| \quad (2.9a)$$

$$M_n(\mathbf{p}_{-ve}(\mathbf{p})) = M_n(\mathbf{p}_{-ve}(\mathbf{p})) - \|\mathbf{g}(\mathbf{p})\| \quad (2.9b)$$

Then a convolution is performed at radius n :

$$S_n = F_n * A_n \quad (2.10)$$

Where

$$F_n(\mathbf{p}) = \frac{M_n(\mathbf{p})}{k_n} \left(\frac{|\tilde{O}_n(\mathbf{p})|}{k_n} \right)^\alpha \quad (2.11)$$

And

$$\tilde{O}_n(\mathbf{p}) = \begin{cases} O_n(\mathbf{p}) & \text{if } O_n(\mathbf{p}) < k_n \\ k_n & \text{otherwise} \end{cases} \quad (2.12)$$

α is the radial strictness. A too low value highlights point without radial symmetry such as line, but a too high value can also attenuate point of interest. A_n is a 2D gaussian and k_n a scaling factor.

The images S_n are calculated for all radius $n \in \mathbb{N}$ and a weight image S is formed:

$$S = \frac{1}{|N|} \sum_{n \in N} S_n \quad (2.13)$$

Before applying the FRS algorithm, we binarized the picture. The figure 2.16 illustrates all the steps of the FRS for $2\mu\text{m}$ particles.

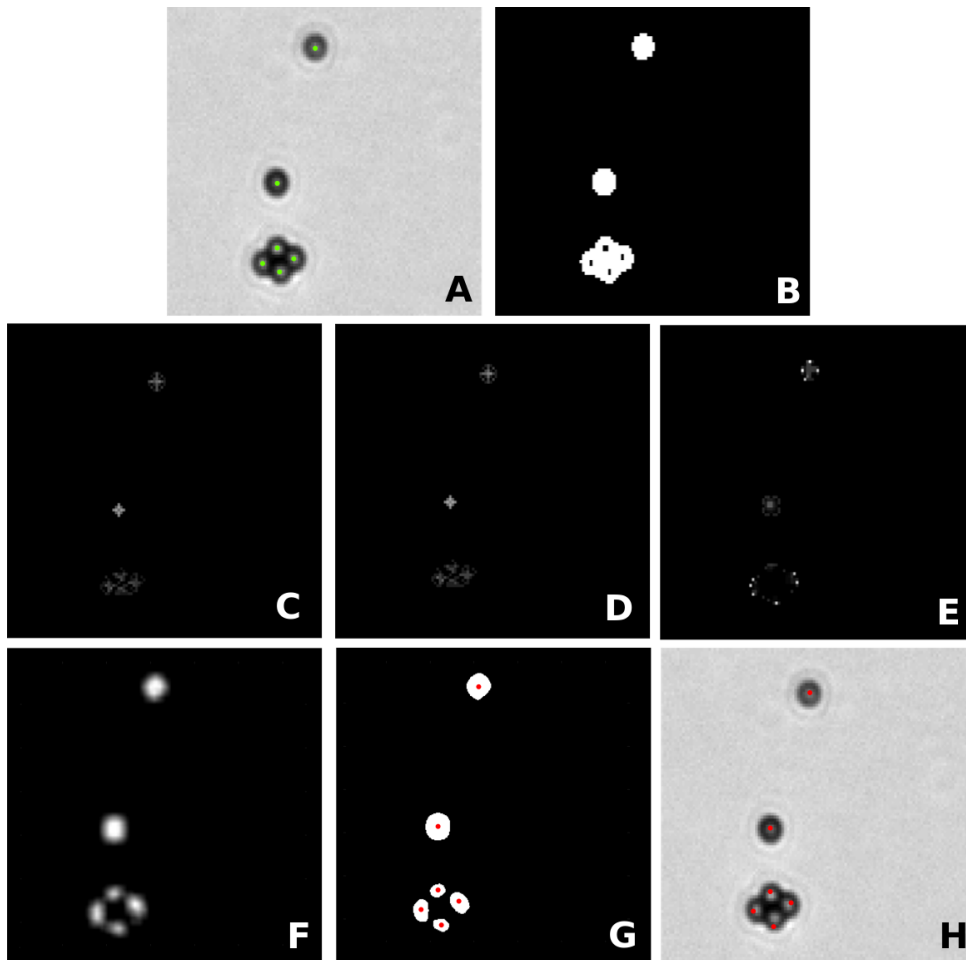


Figure 2.16: Different steps of the FRS transform. We seek the particle center indicated by green dots in the original image (a). The first operation is to binarize the image (b). From the FRS, we obtain O_n the orientation image (b) and M_n the magnitude image (d). These matrices are convoluted S_n (e) to formed a weighted image S , smoothed (f). After threshold to highlight the interest points (g), we extract the positions of particles (red dots) (h).

The points obtained do not indicate the center of mass of the particles composing the aggregate (figure 2.16h), but rather the areas where local symmetries have been detected. The counting of these points allows to obtain the type of aggregate considered (see examples figure 2.17). The FRS transform works well for both brightfield and fluorescence microscopy (figure 2.17).

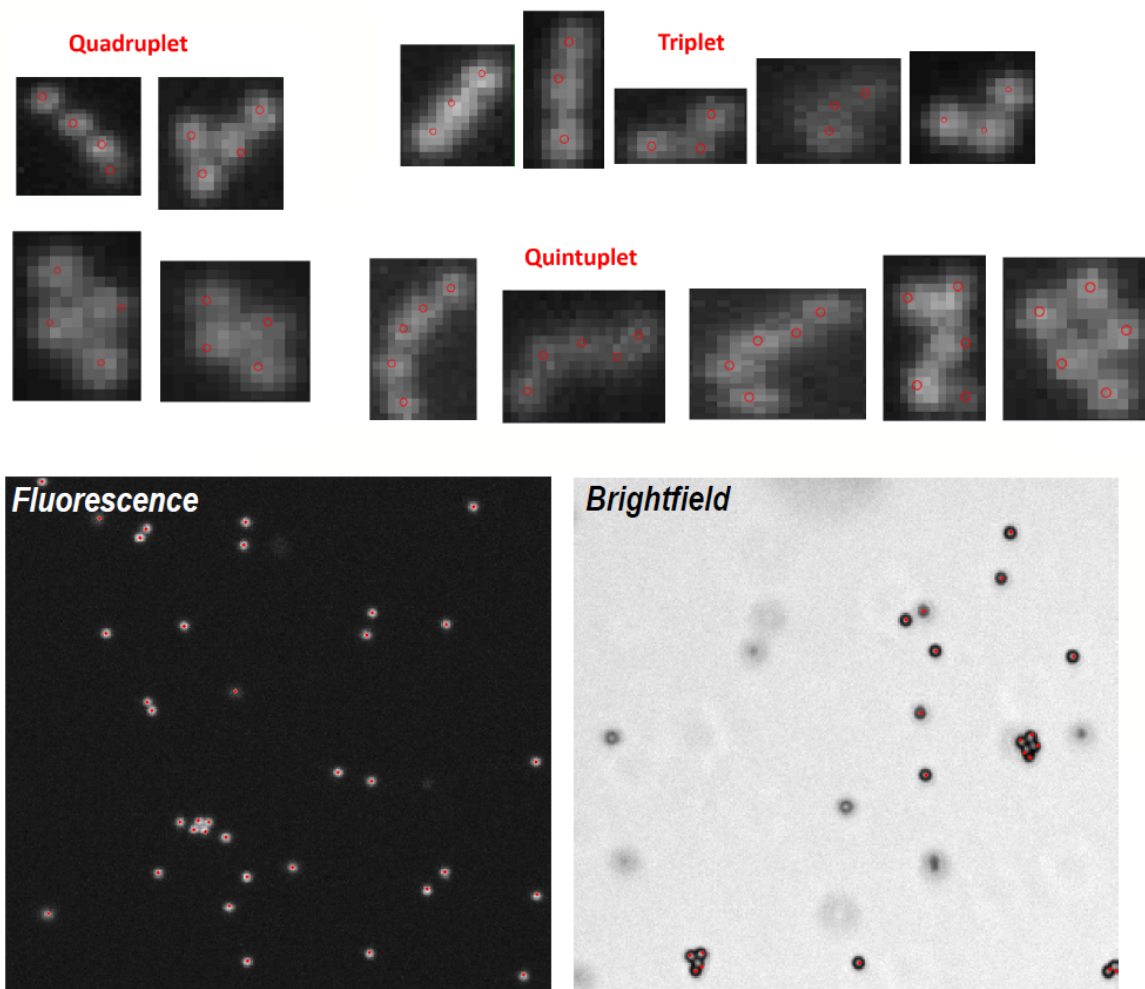


Figure 2.17: (top) Examples of triplet, quadruplet and quintuplet with the FRS method. (bottom) Detection of particles with fluorescence and brightfield microscopy with the FRS algorithm. Red dots or circles indicate a particle.

2.2.4 Detection of aggregates dimensions

To extract more geometrical features about the objects, we couple FRS with other algorithms. Here, we are interested to obtain the maximal dimension of aggregate L_{min} and L_{max} an equivalent to the maximum diameter of F eret. To find these dimensions, we measure the distance d between two parallel planes for a couple of points as a caliper measurement (figure 2.18) and we select the largest value between these couple of points.

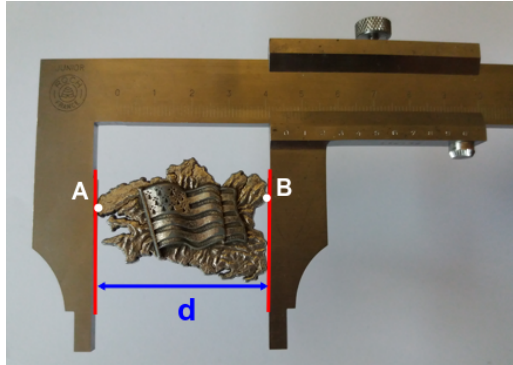


Figure 2.18: Example of a measure of the distance d between two parallel planes (red lines) for a couple of points $[A,B]$ on a complex shape.

First, the image is thresholded and binarized to obtain the shape of the object. We search for each pixel of this object all its vertices, which form several convex sets in the object. A set is convex when a segment $[A, B]$ connecting any two points a and b , in the object is contained in the object (figure 2.19).

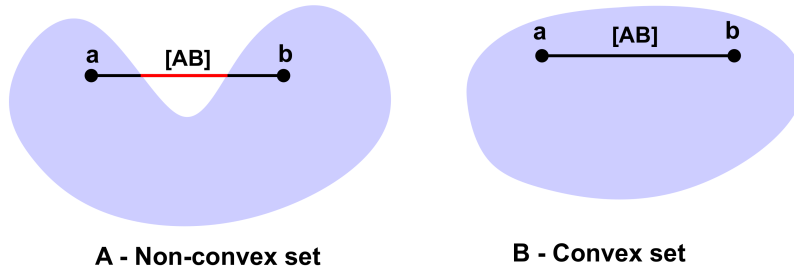


Figure 2.19: Definition of a convex set

The convex sets formed by the vertices have a convex hull, which is quite simple to conceptualize. Let us consider that a rubber band is stretched around all the points. When it is released, the band contains the set of points and represents the convex hull (figure 2.20).

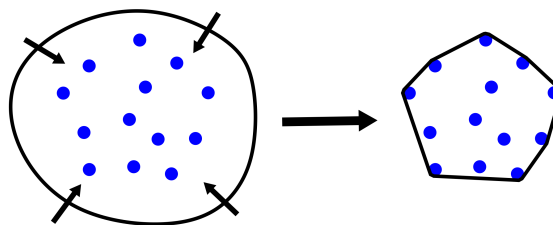


Figure 2.20: Concept of the convex hull

This concept is a little more complicated to set up algorithmically, and is the most expensive step of the processing. We have chosen the Quickhull algorithm, which is simple and efficient to set up for 2D objects (Barber et al., 1996). It is a Divide and Conquer type of algorithm:

1. For a set of points we connect the most distant points possible in x (red line figure 2.21a). The points on either side of this line form two sets, which is treated recursively.

2. In the first set, we look for the point the furthest from the line (isolated red dot figure 2.21a) and form a triangle. All the points contained within this triangle are not considered as extreme and are thus eliminated (figure 2.21b).
3. This process continues until there are no points left on either sides of the line (figure 2.21c-d).

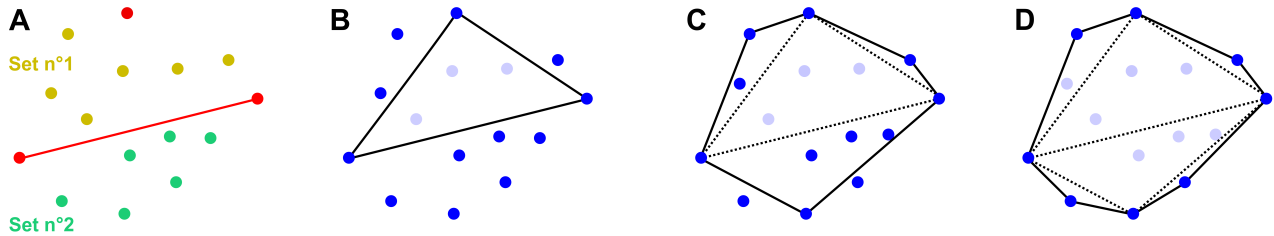


Figure 2.21: Concept of the Quickhull algorithm

The two most time consuming operations of this algorithm are adding a point to the hull and partitioning to find the extreme points. Figure 2.22 presents an example of vertex and convex hull detection on a aggregate.

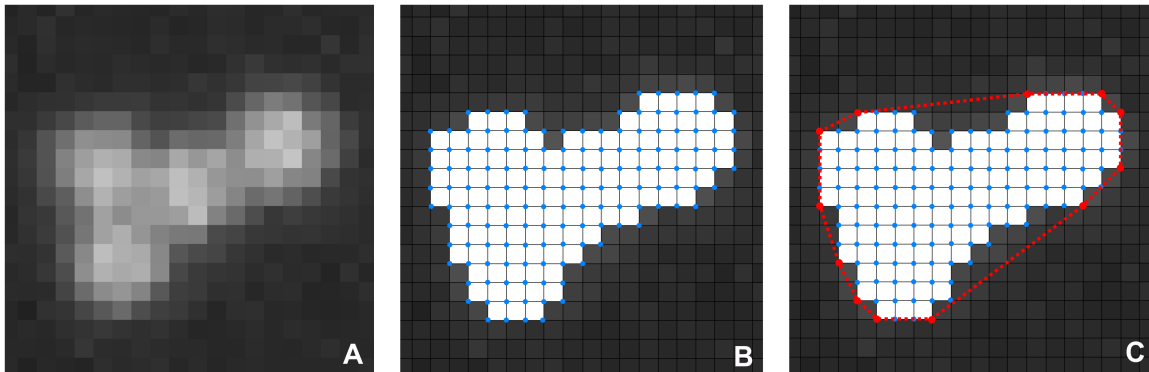


Figure 2.22: From an original image (a), the vertices of the pixels are detected (blue dots) (b) and after the quickhull algorithm we obtain the convex hull (red line) of the aggregate shape (c).

Once the hull is defined, the dimensions of the object can be calculated. For that, it is necessary to calculate for each pair of points the distance separating them. For N points, there are $N(N - 1)/2$ pairs, i.e. an important computation time of $O(N^2)$. To reduce this cost, Preparata et al. (2012) proposed to use the following theorem (Yaglom et al., 1961): "The diameter of a convex figure is the greatest distance between parallel lines of support". Rather than calculating the distances between all the points, Shamos (1978) created an algorithm that identifies the antipodal point pairs, i.e. the pairs of points admitting parallel support lines. A polygon support line is a line that passes through a point of the polygon contour such that the entire polygon is on the same side of the line (figure 2.23). This algorithm makes it possible to reduce the points considered to less than $3N/2$, a linear complexity $O(N)$ in time.

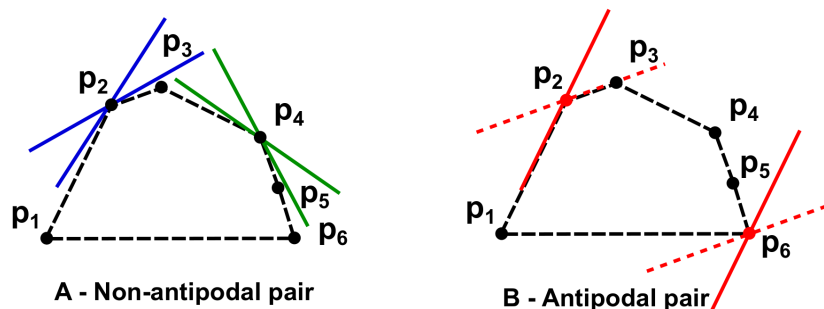


Figure 2.23: Antipodal points

L_{max} is the greatest distance between two antipodal pairs of the hull and L_{min} the smallest (see the example on figure 2.24). We reference only to these lengths to define the aggregate dimensions in the thesis.

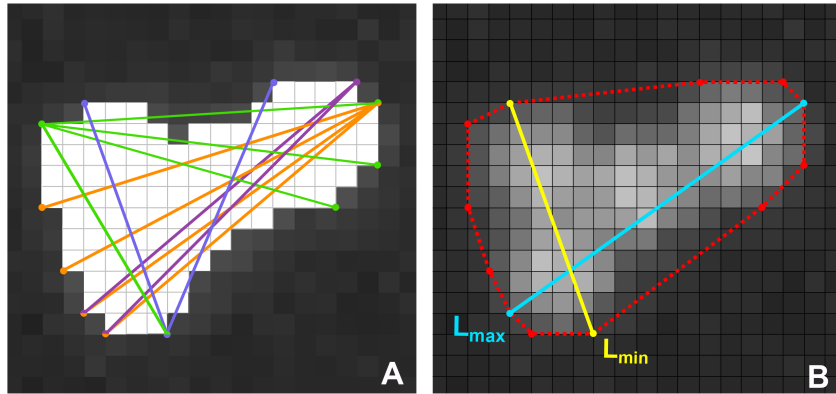


Figure 2.24: Continuation of the example 2.22 with the detection of some antipodal pairs (a) and the determination of L_{max} (blue line) and L_{min} (yellow line) (b).

2.3 Image analysis

This section presents the detection algorithms developed to analyse the various and diverse images obtained during the experiments.

2.3.1 Particle tracking

We use image analysis to determine the *in-situ* variations of the flow conditions. Other techniques like the weighing of the liquid that flow out of the chip is too slow to capture the fast variations of the flow decline corresponding to the progressive fouling of a pore. Indeed, a precision balance needs 5-10s to give a stabilize value of the mass, making it impossible to continuously measure the outgoing mass, especially since the last part of the clogging process is around 1s. We choose to monitor the variation of velocity of the particles that are transported by the fluid, thanks to a particle tracking algorithm. In addition, this algorithm can be coupled to others like FRS to determine at the same time the type of flowing objects and their velocity. At the pore scale, particle tracking is performed in the reservoir part upstream of the pore (figure 2.25), which allows acquiring a sufficient number of images to obtain a reliable measurement of the particle velocity.

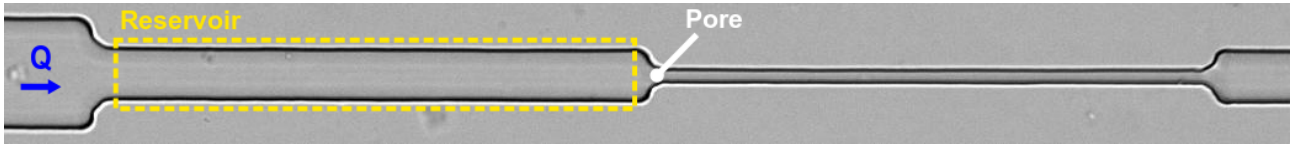


Figure 2.25: Zone of the particle tracking (red rectangle)

According to the flow conservation, we link the particles velocity in the reservoir to the flow:

$$Q = v_{pore}S_{pore} = v_{reservoir}S_{reservoir} \quad (2.14)$$

The fluorescent or brightfield images are thresholded and binarized to limit the noise. The particles coordinates correspond to their mass center that consider the lateral deformation of the image of the particle under flow (figure 2.26). This processing can generate errors on the center of the particles, but once the number of pixels per particles is higher than 20 we are able to accurately find it. A shift of one pixel induces for example an error of $0.32\mu\text{m}$. These errors are often systematic and are erased in the calculation of the velocity, which are averaged over at least fifteen positions. However, if the frame rate is not high enough or the particle velocities too high, particle image can be deformed and we have fewer particle positions in the reservoir.

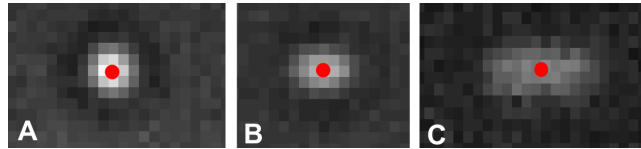


Figure 2.26: Particle deformation with $v = 100\mu\text{m/s}$ (a), $200\mu\text{m/s}$ (b) and $500\mu\text{m/s}$ (c).

With a constant ratio between the sections of the reservoir and the pore for all used channels, the difference of particles velocity is:

$$v_{pore} = 3v_{reservoir} \quad (2.15)$$

The particles suspension is sufficiently diluted and the frame rate sufficiently high to be able to distinguish each object for the others. Since the reservoir section is straight our particle tracking algorithm is based on three criteria resumed on the figure 2.27.

A rectangular research zone

The particle at time $t+1$ is searched only in a rectangular research area in front of the particle at time t (figure 2.27a). The length of this search box depends on the speed of the particle and the frame rate. The height is only a few pixels and allows to anticipate positions slightly outside of the streamline of the particle (figure 2.27b).

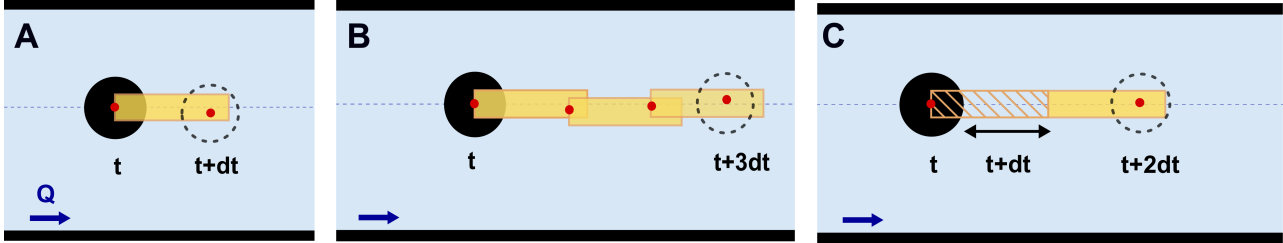


Figure 2.27: The three criteria of our particle tracking: a research zone limited to a rectangle (a), considering small variation of the particle trajectory (b) and recovery of possible lost positions (c).

Lost position

If the particle is lost at time $t + dt$, the particle tracking searches the particle on the rectangle zone at the next time (figure 2.27c). Such a situation occurs if two flowing particles overlap (figure 2.28), or if the particle passes over a deposited particle (figure 2.29).

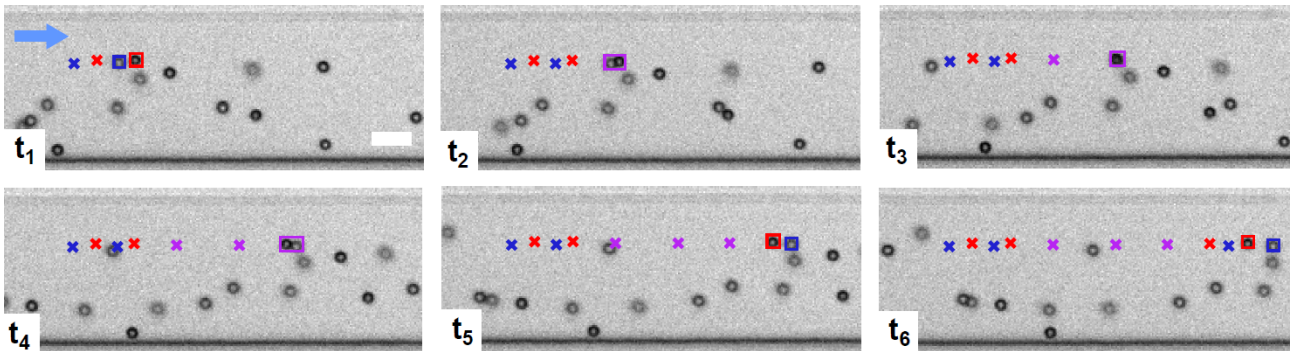


Figure 2.28: Overlapping of two flowing particles. The blue particle is faster than the red one and they collapse (purple symbols) from t_2 to t_4 before being discernible. Rectangles are current positions and crosses the previous positions. Scale bar: $10\mu\text{m}$.

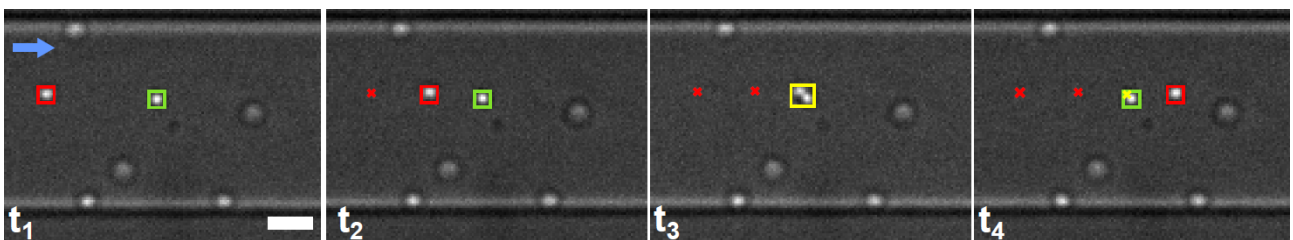


Figure 2.29: Overlapping of a flowing particle (red symbols) and a deposited one (green symbols). They collapse (yellow symbols) at t_3 before being found individually. Rectangles are current positions and crosses the previous positions. Scale bar: $10\mu\text{m}$.

Overlapping of particles

Because of the Poiseuille flow, not all the particles flow at the same velocity in the channel. Particles can surpass each other, and several candidates can be found in the particle tracking search area. In this case, the particles are not in the same focal plane (figure 2.7) and can be discriminated according to their intensity (figure 2.30).

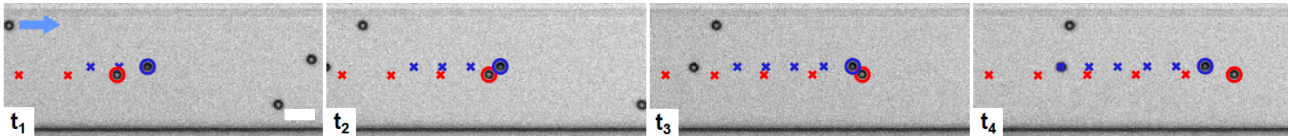


Figure 2.30: Detection of two very close particles. The red particle is faster than the blue one but both can be discriminated from t_2 to t_3 thanks to their intensity profile.

2.3.1.1 Information from particle tracking

The particle velocity provides additional information.

1. N^* the number of particle tracking passing through the pore before clogging (defined section 1.3.1).

2. The probability capture of each object.

We systematically determine the type and size of the objects that flow through the microfluidic filter during the clogging, with an acquisition frame rate sufficiently high to be able to monitor separately each object that deposits. The type of captured aggregate is determined manually and the capture probability is calculated from the number of flowing particle through the pore and the distribution obtained from the stop and go experiments. The composition of the clog is thus known, as well as the dimension of the objects.

3. The volume fraction into the pore and into the reservoir.

The particles that accumulate over a given length of the medium are counted, which allows us to obtain a volume fraction with an error of 4 to 5%.

4. The rotation of the object

By mixing object characterization methods like FRS or objects dimension with particle tracking, we are able to monitor the temporal variation of the orientation of an object (figure 2.31) considering only ϕ , one of the two angles characterizing the rotation of an object since we image with a microscope.

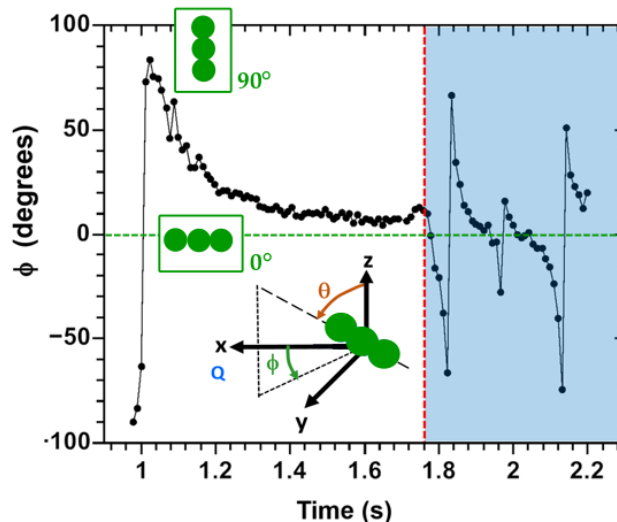


Figure 2.31: Rotation Φ of a line-shaped triplet with particle tracking, into the reservoir (white part) and inside the pore (blue part). For 0° position, the triplet is perfectly aligned in the flow direction. The rotation of such an object is very slow and the rotation period is not finished when it enters in the pore, in which is greatly modified its rotation.

2.3.2 Automated detection of clogged pores in a porous medium

This section provides a method for the automatic detection of clogs in a porous medium composed of cylindrical plots we called thereafter collectors. From this detection, we obtain the clogging time and the position of each new clogged pore. This detection is decomposed in two phases, first the detection of the pore center whether or not they are clogged.

Initialization of the porous media

Before studying the deposition and clogging in a porous medium, the area occupied by the collectors must be removed. We build from the image of the empty porous medium I_0 , a binary mask image M whose area collectors are equal to 0. The images I_m are systematically multiplied by M to remove the area of the collectors. First, I_0 is binarized (figure 2.32a-b) and the center of the collector are recovered with the FRS method (figure 2.32c), and the final image reverse to obtain M (figure 2.32d).

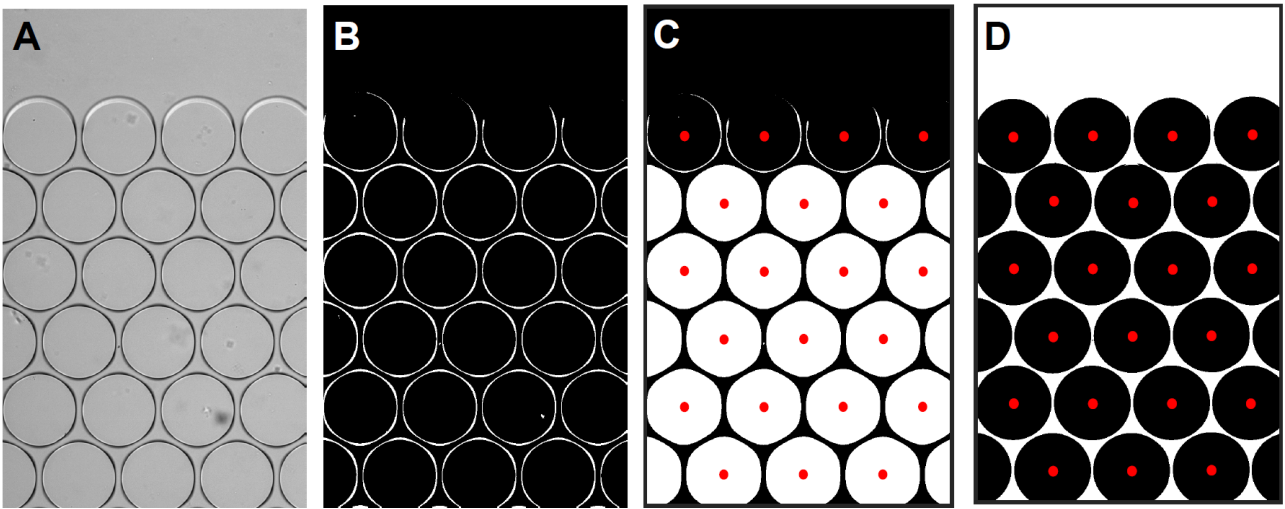


Figure 2.32: Formation of the mask M . The image of the empty porous medium I_0 (a) is binarized (b) and the center of collector recovered even with a sparse circle with FRS (c). Finally, we reverse the image to obtain M (d).

Pore center detection

Between each pair of collectors center, there is a pore center. To recover the pores center, we first use a Delaunay triangulation to detect all pairs of collector center. This triangulation is such that for a set of points (here the collectors center), no one is outside the circumscribed circle of one of the triangles of the triangulation (figure 2.33).

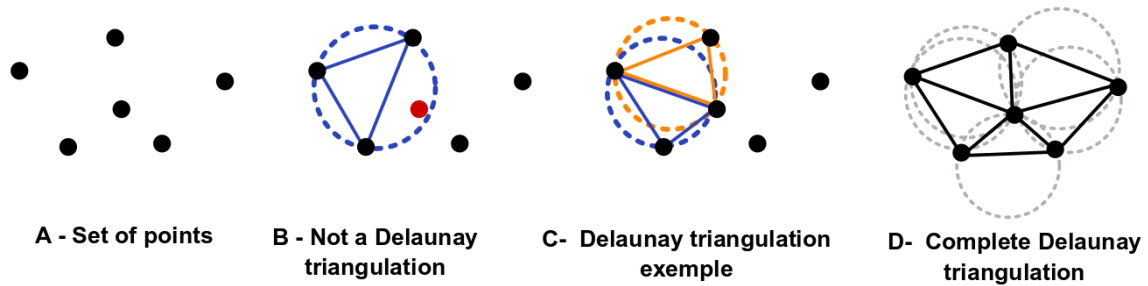


Figure 2.33: Delaunay triangulation

The center of the pores corresponds to the middle of the segments composing the triangulation (figure 2.34).

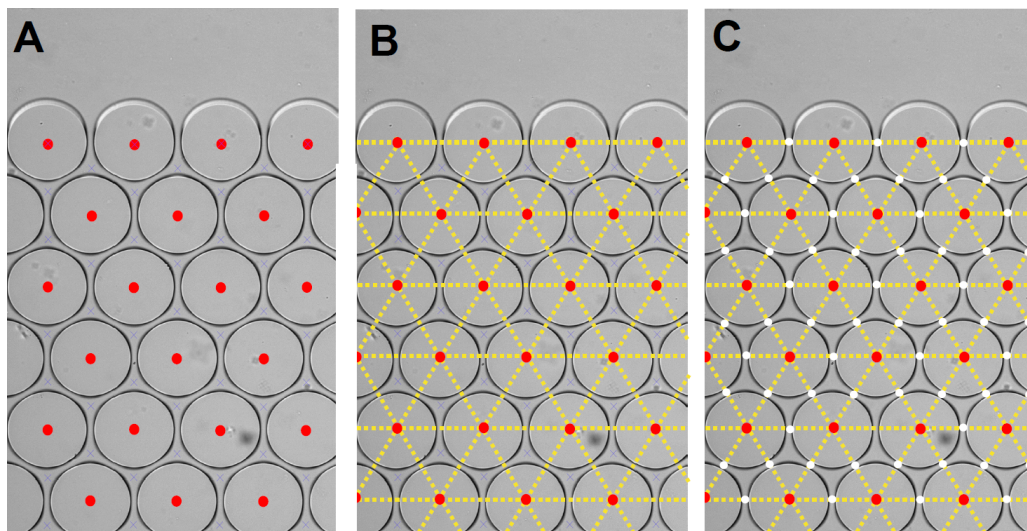


Figure 2.34: Pores center detection. From the collectors center (a) with a Delaunay triangulation (b) we identify the pores center (c).

Clog detection

Once the pores center are detected, we search for clogs themselves according to five criteria illustrated in figure 2.35, since no single criterion is satisfactory. For each image $I_m \times M$, we detect several thousand of deposits around the collectors. If a deposit validates the five criteria, it is considered as a true clog. This method allows us to eliminate partial clogging or deposits that do not partake to the clogging.

A. A minimal area

The clog area can not be too small. The area of the deposit is firstly discriminated by its size and smaller area are eliminated. However, some partial clog that spread along the flow direction may be detected as clog (figure 2.35a).

B. Contact with two collectors

The clog must fill the entire width of the pore, and thus be in contact with two different collectors. The deposit is placed in a rectangle as small as possible, and if two of the corners of the box are in contact with different collectors, this criteria is validated (figure 2.35b).

C. Proximity with center pores

Clog formed in a pore, thus close to its center. If the deposit center is close enough of a pore center, then this criteria is validated (figure 2.35c).

D. Clog intensity

Partial clogs can validate the three previous criteria, simply because wall are covered of particles. To discriminated these partial clogs, we fixed a threshold on their average velocity. If the clog is dark enough, this criteria is validated (figure 2.35d).

E. Intensity profile after the clog

When clog is formed, no more particle can pass through it. The intensity behind the clog is then constant, however since a particle passes, the intensity profile varies. This criterion is obviously not sufficient in itself since a pore would be considered as clogged if the particles no longer arrive in the medium (figure 2.35e).

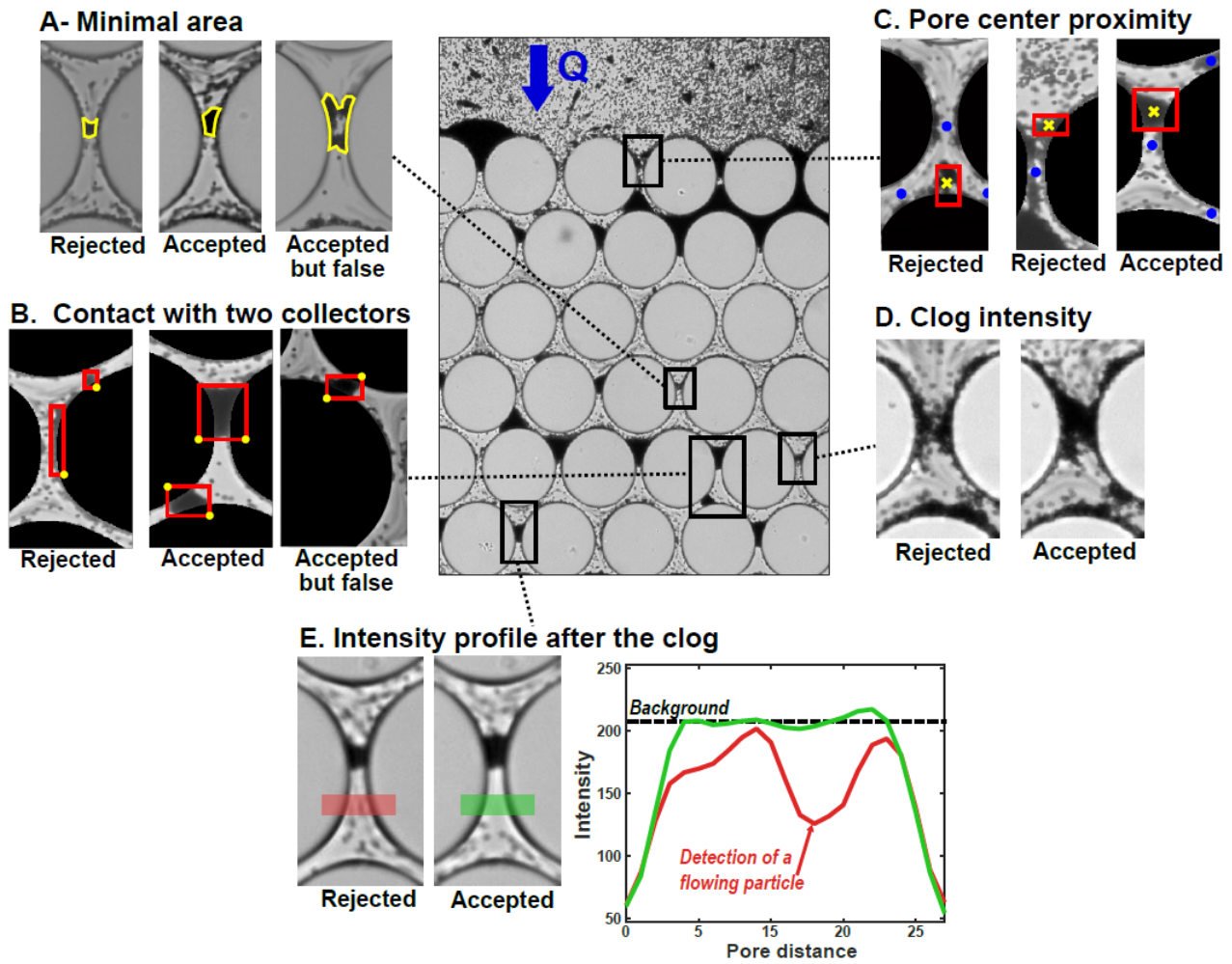


Figure 2.35: Criteria to detect clogs in porous media. For each criterion is presented a deposit considered as a true clog (Accepted) or not (Rejected). Considering only one criteria can lead to false clog detection (Accepted but false) (a) The deposit must have a minimum area. In yellow the outline of the area deposit. (b) The deposit must be in contact with two collectors. Red rectangle are the limit of the deposit, at least two extremities (yellow dots) have to be in contact with 2 collectors. (c) The deposit center must be close to that of a pore. Blue dot are the pores center, yellow cross the deposit center and red rectangle the limit of the deposit. (d) The deposit must reach a minimum average intensity. (e) No flowing particle has to be detected in the area behind the clog. The graph shows the intensity of a clogged pore, and an open pore with a flowing particle detected. Rectangles are the area where intensity is measured, with intensity represented in the graph, with color respect. Scale bar: 100 μ m.

All together, these five criteria make it possible to determine the moment when a pore is clogged and the number of automatically detected clogged pores is very close to that of we can manually determine by checking the images (figure 2.36). The porous media are imaged every 3-5s, allowing us to monitor the growth of the deposits, the clogging and the accumulation behind a clog for each pore.

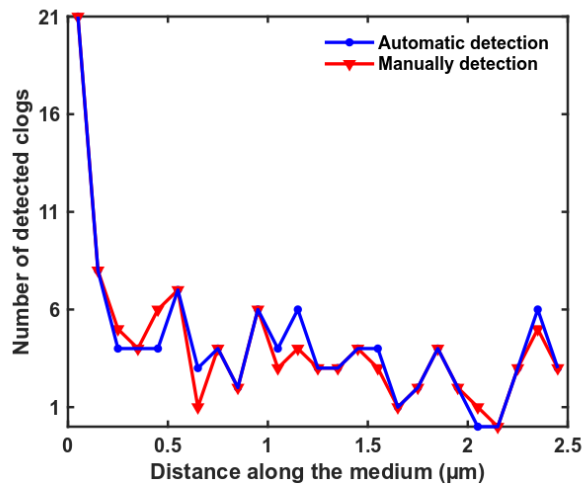


Figure 2.36: Comparison of the number of clogs along a porous medium between automated detected clogs and manually detected clogs.

This method works only for the stable suspensions. In case of large deposits or even dendrites (see chapter 7) in the whole medium formed with unstable suspensions, the detection of clogs has to be done manually.

Part I - At the particle scale

Chapter 3

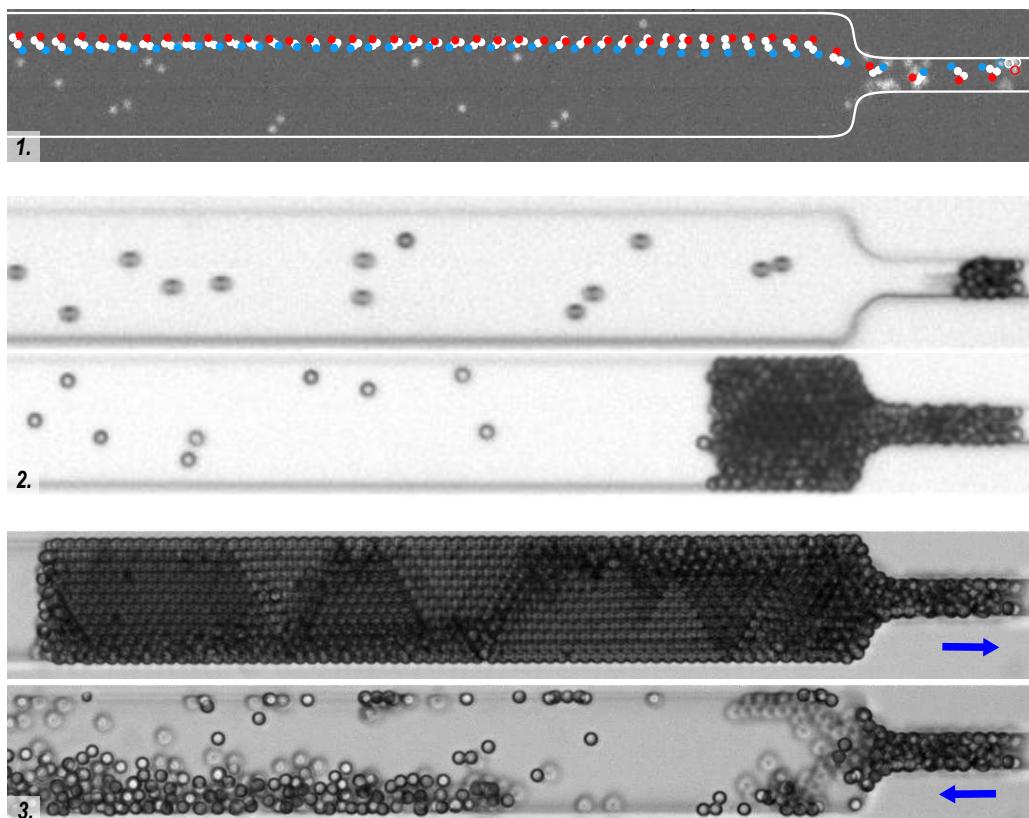
The impact of aggregates on clogging

Chapter 4

The flow decline during the pore clogging

Chapter 5

Structure and flow conditions through a colloidal packed bed formed under confinement



Fouling (1), clogging and accumulation (2), unclogging (3).

Chapter 3

The impact of aggregates on clogging

The so-called progressive clogging has often been studied in various conditions, mainly with monodisperse suspensions. Some studies have investigated the role of polydispersity of the objects in the clogging with mixtures composed of large or small particles. However, up to now nobody has monitored the dynamics of the clogging process by colloidal particles. The objective of this chapter is to fill this gap by characterizing the objects that form the clogs and by providing the dynamics of their capture. We clearly show that despite the use of monodisperse suspensions, aggregates composed of several particles, initially present in the suspension, are responsible of the progressive clogging of the pores, regardless of the flow rate, the confinement, the DLVO interactions or the type of particles. The results of this chapter have been published in *Soft Matter* (2020) and *Journal of Membrane Science* (2021).

Contents

3.1	There is no perfectly monodisperse suspension	76
3.2	Aggregates are responsible for clogs, whatever the conditions	76
3.3	The more relevant parameters impacting the clogging	78
3.3.1	The capture probability is strongly dependent of the flow rate	78
3.3.2	Ionic strength	79
3.4	Brief summary of the papers	80

3.1 There is no perfectly monodisperse suspension

We used in this work several types of monodisperse microparticle suspensions, stabilized against aggregation sterically or electrostatically. Despite this stabilization, we detected the presence of aggregates composed of several particles and corresponding typically to a few percent of the population, whatever the nature of the suspension. Figure 3.1 shows the PDF of the size distributions for two types of stabilization for particles with the same size. Both distributions are centered at the particles diameters expected, but also with a tail for the larger particles (inset).

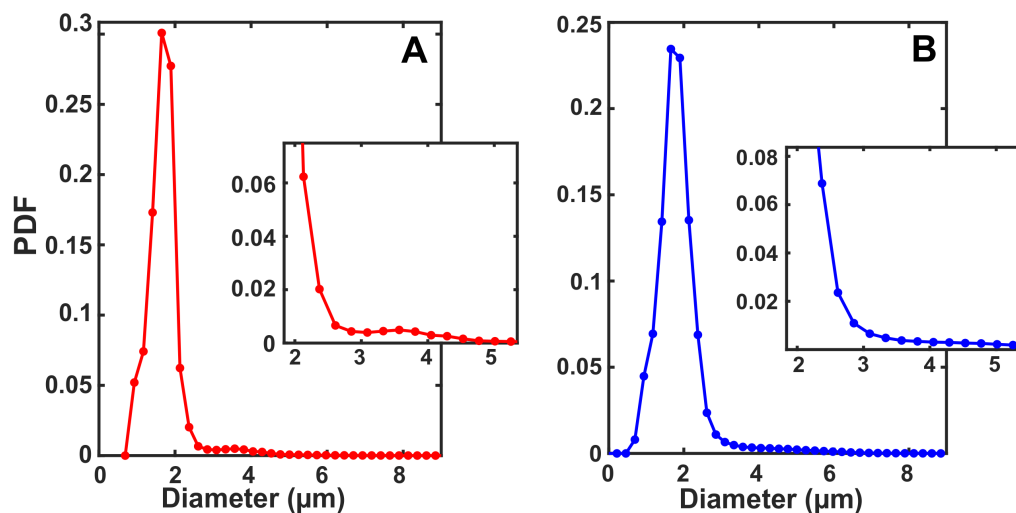


Figure 3.1: Size distribution of 1.8µm particles suspension with a steric stabilisation (PMMA) (a) and electrostatically stabilisation (PS) (b). Inset: zoom in on the tail of the distributions.

3.2 Aggregates are responsible for clogs, whatever the conditions

Whatever the flow conditions, DLVO interactions or geometry, the physical interception of aggregates is the main cause of pore clogging, even though there are few aggregates in the suspension. We have never observed the formation of clogs by successive deposition of single particles, as it was supposed to be so far. We monitored the formation of several hundred of clogs which allowed us to obtain reliable statistics on the size and shape of the aggregates and to determine their probability to be captured that increases rapidly with their size (figure 3.2a).

This higher probability of capture is actually not only related to the size of the object but also to its shape. Aggregates as well as spherical particles rotate around their centre of mass but the rotations are more or less complex for the aggregates, depending on their shape and their position relative to the pore walls (figure 3.2c). For spherical particles, this rotation does not have any impact on their capture. On the contrary, the rotation of aggregates favours their physical interception. For example, when entering in a constriction, aggregates underwent brutal modification of the orientation of their major axis while trying to align along the flow direction. This change in rotation favours the capture of the aggregate, which is not the case for spherical particles (figure 3.2b). Similarly, when aggregates navigate inside a partially clogged pore it is easily captured by the particles of the deposit.

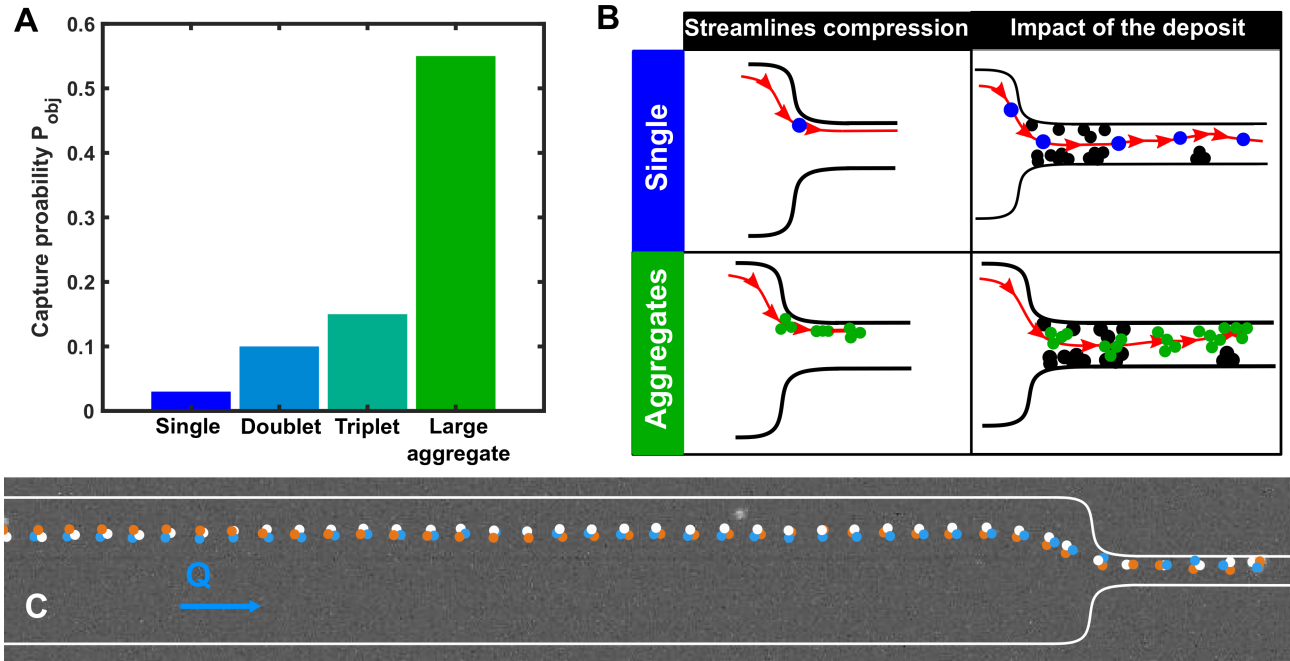


Figure 3.2: (a) Capture probability for different types of object in a $1.8\mu\text{m}$ PMMA suspension. (b) Scheme of single and aggregates trajectories when streamlines are compressed and when deposit can modify the object trajectories. (c) Rotation and deposition of a triangular-shaped triplet, disturbed near the pore entrance.

The typical formation of a clog is shown in figure 3.3. Single particles do not form more than monolayers (a), but they facilitate the capture by physical interception of a quadruplet (b). This quadruplet significantly reduces the cross-section of the pore which allows the capture of a triplet (c) and a doublet (d). The pore is then clogged with a few additional single particles (e).

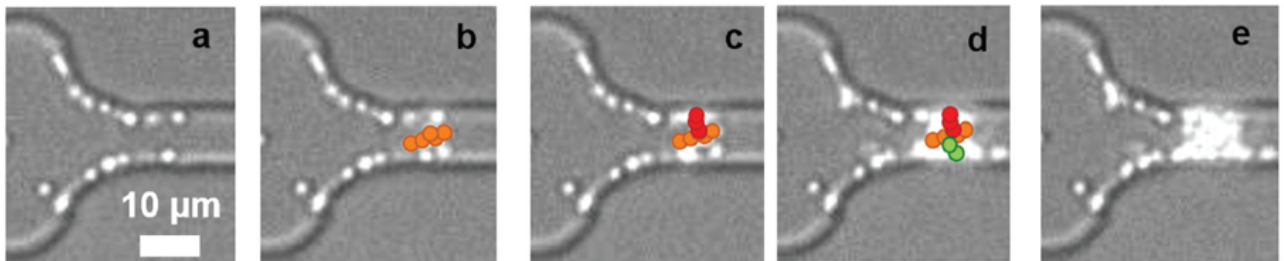


Figure 3.3: Successive images of pore clogging with $1.8\mu\text{m}$ PMMA particles. Formation of a monolayer (a) then successive capture of quadruplet (b), triplet (c) and doublet (d) before the pore is clogged (e).

3.3 The more relevant parameters impacting the clogging

Previously, a study of Wyss et al. (2006) (see on section 1.3.1) found that the clogging time t^* of a pore was strongly dependent on the volume fraction Φ of the suspension and the flow rate Q . This relationship means that there is a certain number of particles N^* that passes through a pore before it is clogged:

$$N^* = t^* Q \frac{\Phi}{V_p} \quad (3.1)$$

In the context of our study, the meaning of N^* is slightly modified since enough single particles must pass through the pore before aggregates arrive and clog the pore. Thus, the more the aggregates there are, the lower N^* is. With this new definition of N^* and the knowledge of the distribution of aggregate sizes inside a suspension we are able to determine their impact on clogging in function of different parameters (flow rate, confinement or ionic strength).

3.3.1 The capture probability is strongly dependent of the flow rate

When we increase the flow rate, we observed that N^* remains constant until suddenly it increases for a critical flow rate (black dotted line figure 3.4a). As we come closer to this critical flow rate, the number of aggregates that partakes to the clog decreases while their size increases (figure 3.4b-c). This trend is mainly due to the fact that a higher flow rate increases the hydrodynamic torque, which is able to wipe objects off from the pore walls. However, due to their shape aggregates are more easily captured and they are not detached by the flow since they share a higher number of contact points with the deposit or the pore walls. The capture of these large aggregates is very unlikely since they are very rare. Therefore, many particles have to pass through the pores before these objects show up, corresponding to the sharp increase of N^* in figure 3.4a).

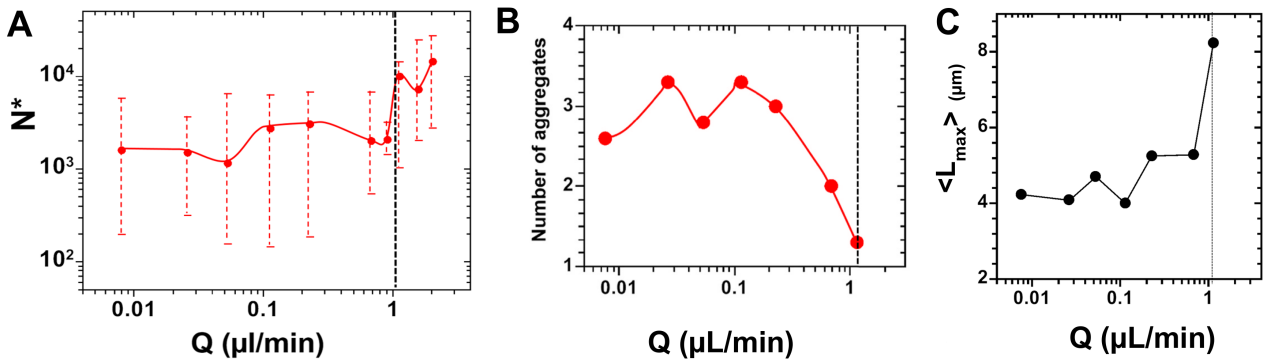


Figure 3.4: Evolution of N^* the number of particles passing through the pore before its clogging (a), the average number of aggregate in a clog (b) and the average maximal length of aggregate in a clog (c) for a $1.8\mu\text{m}$ PMMA suspension.

3.3.2 Ionic strength

Adding salt increases the number of aggregates

Classically, adding NaCl to a colloidal suspension modifies the DLVO forces. The addition of salt has two consequences i) particles more easily stick to the walls and ii) screening of the surface charges promotes the formation of aggregates. Thus when the ionic strength increases there are more aggregates and hence N^* decreases (figure 3.5a).

Changing the surface charges does not change the clogging

To modify the surface charges of the particles without modifying the ionic strength we used sterically particles with different surface charges, anionic, cationic and neutral. Under these conditions, it was expected that clogs with cationic particles would form very quickly since the channel surface is negatively charged. However, N^* (figure 3.5b) is constant for all the suspension, which proves once again that the physical interception of aggregates dominates over the other parameters.

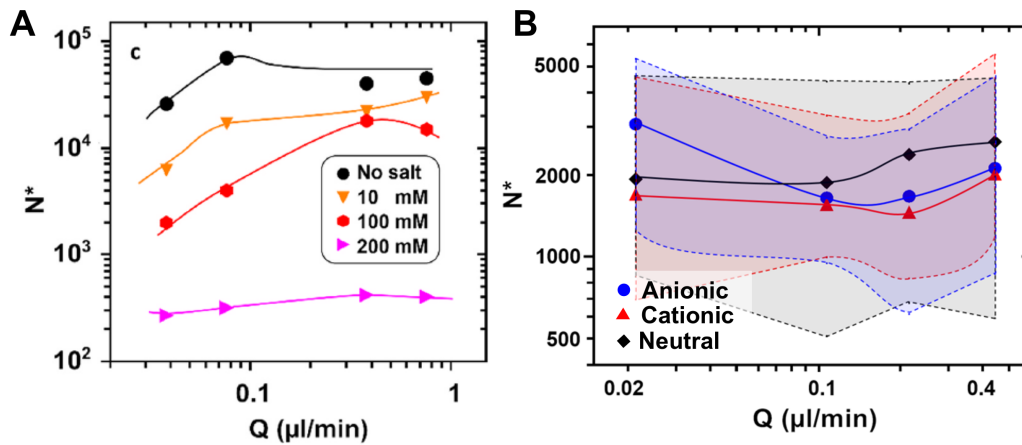


Figure 3.5: Evolution of N^* for 1.8 μm PS particles at different ionic strength (a) and 2.4 μm PS particles for three states of charges (b).

3.4 Brief summary of the papers

Dynamics of progressive pore clogging by colloidal aggregates

Objective: imaging the progressive clogging of a pore by stable and dilute monodisperse suspension. During this process we determine for each object that deposits its shape and size.

- Aggregates are systematically found in 90 clogs while they represents 2.3% of the population.
- The capture probability of aggregates is directly dependent on their size. The larger they are, the higher their capture probability, even though their relative proportion in the suspension decreases with their size.
- The flow rate impacts the capture probabilities of objects. The size of the aggregates that are wiped off by the flow increases with the flow rate. For the highest flow conditions there are only large aggregates in the clogs.
- The objects rotate around their center of mass, which favour their contact at the walls when passing through the constriction or avoid the deposit inside the pore. Objects with complex shapes have a higher radius of gyration and hence are more likely to come into contact with the wall than spherical particles with the same radius.

The contribution of colloidal aggregates to the clogging dynamics at the pore scale

Objective: verification of the major role of aggregates in clog formation by modifying the flow rate, DLVO interactions, confinement and the particle size distribution of the suspensions.

- Even though the formation of each clog is unique we can sort them into two categories based the ratio of their size of the largest aggregates in the clog over the width of the pore:
 - $L_{\max} < W$: there are no more than two aggregates composed of 4-9 particles.
 - $L_{\max} > W$: there is a least on aggregate larger than the pore width.
- N^* , the number of particles passing through the pore before it is clogged is constant until a critical value, from which it increases.
- The main effect of the addition of salt to the suspensions is the increase of the number of aggregates. There is a limited impact of the surfaces charges of the particle on the clogging process.



Cite this: DOI: 10.1039/d0sm01403f

Dynamics of progressive pore clogging by colloidal aggregates†

 N. Delouche,^a A. B. Schofield ^b and H. Tabuteau ^{*a}

The flow of a suspension through a bottleneck often leads to its obstruction. Such a continuous flow to clogging transition has been well characterized when the constriction width to particle size ratio, W/D , is smaller than 3–4. In such cases, the constriction is either blocked by a single particle that is larger than the constriction width ($W/D < 1$), or there is an arch formed by several particles that try to enter it together ($2 < W/D < 4$). For larger W/D ratios, $4 < W/D < 10$, the blockage of the constriction is presumed to be due to the successive accumulations of particles. Such a clogging mechanism may also apply to wider pores. The dynamics of this progressive obstruction remains largely unexplored since it is difficult to see through the forming clog and we still do not know how particles accumulate inside the constriction. In this paper, we use particle tracking and image analysis to study the clogging of a constriction/pore by stable colloidal particles. These techniques allow us to determine the shape and the size of all the objects, be they single particles or aggregates, captured inside the pore. We show that even with the rather monodisperse colloidal suspension we used individual particles cannot clog a pore alone. These individual particles can only partially cover the pore surface whilst it is the very small fraction of aggregates present in the suspension that can pile up and clog the pore. We analyzed the dynamics of aggregate motion up to the point of capture within the pore, which helps us to elucidate why the probability of aggregate capture inside the pore is high.

 Received 4th August 2020,
 Accepted 28th September 2020

DOI: 10.1039/d0sm01403f

rsc.li/soft-matter-journal

Introduction

The flow of colloidal suspensions in confined environments often leads to partial or complete clogging in various contexts including natural flows inside soils and rocks,¹ filtration through a membrane,² during chemical synthesis³ or transport in micro-engineered channels,⁴ porous networks⁵ and reactors.⁶ Three main mechanisms have been identified to explain pore clogging by spherical particles, which depend on the width to particle size ratio, W/D .⁴ Firstly, there is clogging by sieving for particles bigger than the mean pore/channel size^{7,8} or for pores whose dimensions are 2–3 diameters of the particles, $W/D < 2-3$, hydrodynamic bridging occurs when several particles try to enter the pore together.^{9–11} Finally for even larger pores the clogging process is progressive and there is an accumulation of particles until pore blocking happens.^{12–16}

Microfluidic experiments have largely helped to quantify and better understand the way clogs are formed. This technology, that emerged twenty years ago, gives access to various geometric

features in 2D¹⁷ and more recently in 3D¹⁸ such as those encountered in membranes used in the filtration processes inside industrial equipment. The transparent model filters made by this technique enable us to follow and track particles up to the point of their capture by the surface of the pores.^{14,19,20} Most of the previous clogging studies have focused on the impact of the geometry of the pore,^{13,14,21–23} focusing particularly on the influence of the confinement,^{12–14} as discussed above. Others have looked at the influence of the particles' properties like the interparticle interactions or the interactions between the particle and pore surface^{12,13,21,24–26} and the effect of the polydispersity of the suspension.^{7,8,27} More recently, studies on the clogging of model filters have been performed with deformable particles like microgels.^{28–30} Finally, microfluidics has been used to determine under which conditions a pore blocked by colloidal particles can be de-clogged by reversing the flow.³¹ Among this growing set of publications most of them provide images of the pore either partially or completely clogged,^{21,28,32–35} but only few have gone further and considered the behavior of the particle inside a clog or in a deposit.^{14,15,29} The dynamics of particle deposition have been monitored only in very confined situations for both non Brownian^{36,37} and colloidal particles.¹⁴ No such dynamics have been provided at the particle level for progressive fouling since it requires challenging imaging conditions to see through the

^a Univ Rennes, CNRS, IPR (Institut de Physique de Rennes)-UMR 6251, F-35000 Rennes, France. E-mail: herve.tabuteau@univ-rennes1.fr

^b School of Physics and Astronomy, The University of Edinburgh, The James ClerkMaxwell Building, The King's Buildings, Mayfield Road, Edinburgh, UK

† Electronic supplementary information (ESI) available. See DOI: 10.1039/d0sm01403f

forming clog.¹⁵ In such mild confinement, for $4 < W/D < 10$, with W and D respectively the pore width and the particle diameter, particles partly cover the pore surface and at some point, they are supposed to start accumulating on top of this first layer until the pore is finally blocked. However, several works have pointed out that in such confinement the fouling process may be not due to the progressive accumulation of monodisperse particles. Gerber *et al.*,³⁸ show that particles can form only a monolayer on glass beads in a 3D packed bed when the ionic strength is low compared to the critical coagulation concentration. Others experiments in transparent model filters have shown that frequently particles of different sizes are involved in the clogging process. Even though they worked with monodisperse suspensions, they found that a few particles in the suspension, larger than the mean size, are mainly responsible for pore blocking. Either their size is bigger than the pore size leading directly to pore blocking; the particle being arrested at the pore entrance, or smaller particles first deposit on the pore surface, forming a monolayer, and then a larger one blocks the remaining part of the pore cross section.^{7,8,27} Such pore blocking is often seen when one uses natural and engineered suspensions that are composed of aggregates and are polydisperse in shape and size. For instance, injections of therapeutic proteins like monoclonal antibodies often contain aggregates so large that they lead to clogging of the needle or infusion catheters³⁹ and flocculated clay particles form large aggregates that are responsible of the clogging of membrane filters⁴⁰ and drippers in microirrigation.⁴¹

When there is a salt gradient and colloidal particles flowing through a porous network we also observe pore clogging as in a reverse osmosis membrane.⁴² Microfluidics has also helped to better understand how aluminium salts used in antiperspirants gels lead to the aggregation of sweat proteins which block eccrine sweat pores.⁴³ Shin *et al.*, show that flows in porous media can induce strong diffusiophoretic focusing at fluid junctions where particles spontaneously accumulate until their concentration is high enough to cause a blockage.⁴⁴ This localized salt gradient can lead to irreversible blocking by particles two orders of magnitude smaller than the pore width.

Clogging issues are also often encountered when solid particles are formed under flow either by mixing different species⁴⁵ as for instance during the formation of kidney stones⁴⁶ or as a product of chemical reactions. During flow chemistry, the solid particles and aggregates produced are transported by the flow and deposited inside the processing equipment.^{47,48} These aggregates grow continuously due to the constant supply of reactants and also help to capture other flowing aggregates or isolated particles.³ The growth under different flow conditions leads to different shapes and morphologies of aggregates, which can also be fragmented by the flow.^{49,50}

As far as we know nobody has determined the different features of the clogging dynamics at the pore scale by such particle aggregates even though they make up most of the natural and industrial colloidal suspensions. In this paper we describe clogging experiments with a dilute, stable against aggregation, mostly monodisperse colloidal suspension inside

a microfluidics model porous medium over a wide range of applied pressures. During these experiments we systematically monitor the deposition history of colloidal particles within a pore and the mean size and shape of each deposited object. These observations allow us to show that there is a major influence from a minute quantity of aggregates present in our monodisperse suspension. There is no progressive accumulation of single particles alone leading to the pore clogging. These particles can only form a monolayer on top of the pore surface onto which a small number of aggregates deposit and eventually block the pore. The higher deposition rate of aggregates directly on the pore walls or on the colloidal monolayer deposit is due to their rotation around their center of mass that increases significantly their physical capture at a higher distance from the pore/deposit surface than is seen for single particles.

Materials and methods

Microfluidics filter and image analysis

We used standard methods of soft lithography and PDMS molding⁵¹ to build our microfluidic device. We followed the same protocol used by Dersoir *et al.*,¹⁵ to obtain a model filter completely made of PDMS in order to have the same colloidal interactions between the particles and the lateral and horizontal walls of the device. The device is 12 μm high and composed of two large channels on both sides of a model filter made of 26 identical and independent channels in parallel (Fig. 1a and b). Each channel is composed of two consecutive reservoirs connected to a pore, which corresponds to the narrowest part of the filter with a width W equal to 7 μm , which corresponds to a pore width-mean particle size ratio equal to 3.9 (Fig. 1c). When the pore is clogged, the two reservoirs are never completely filled by particles which avoids the premature clogging of the two

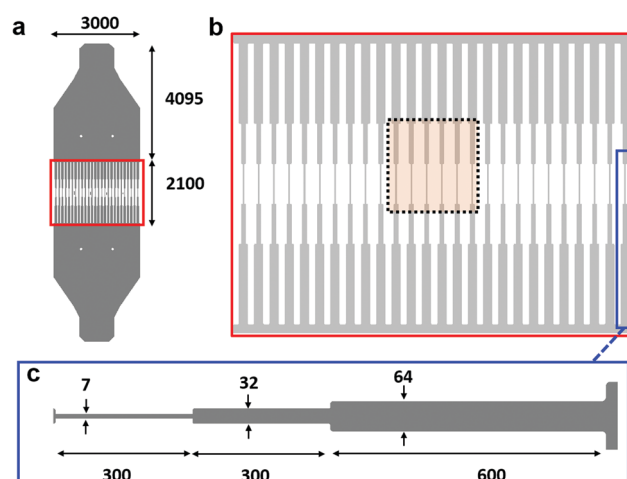


Fig. 1 (a) Model filter with inlet and outlet and the filtering zone in the middle, highlighted by the red rectangle (colour online). (b) Zoom of the filtering zone composed of 26 identical channels. The dotted rectangle corresponds to the zone which is imaged by the camera. (c) Details of the channel geometry with the thinnest part corresponding to the pore, on the left, and the two reservoirs on the right. All the dimensions are given in μm .

adjacent channels. During the experiments we image only the six channels in the middle of the filter (Fig. 1b, dotted rectangle), which allows us to use an acquisition frame rate high enough to perform particle tracking (PT) on all the particles that flow through both the pore and the reservoir just upstream. The experiment is stopped when these six channels are clogged. We image the transport of fluorescent particles with a sCMOS camera (Hamamatsu Orca Flash 4.0).

To flow the suspension, we used a precise microfluidics pressure control system (Elveflow OB1 Mk2 or Fluigent MSFC) to impose a constant pressure gradient between the pore inlet and the outlet. We work with a wide pressure range (0.5 mbar to 120 mbar) corresponding to a flow rate Q at the beginning of the experiment, between 0.008 and 0.9 $\mu\text{L min}^{-1}$. There is an increase of W is lower than 0.5 μm for the highest applied pressure. We measure this flow rate by weighing the mass of water flowing through the device for one hour with an analytical scale, with an accuracy of 0.2 mg, connected to the device outlet. Since we work with a pressure gradient the clogging of several pores does not significantly change the flow rate in the other pores. The Reynolds number is always smaller than 10^{-3} and the Péclet number is high and between 1.6×10^4 to 5.2×10^6 . Under these conditions inertia and particle Brownian diffusion are negligible.

The particles with a diameter $D = 1.8 \mu\text{m}$ were synthesized following the procedure detailed in Shen *et al.*⁵² They are made of PMMA in which a NBD (7-nitrobenzo-2-oxa-1,3-diazole) dye is incorporated. These particles use a polymer brush coating, composed of polyvinylpyrrolidone chains that bear negative charges, to stabilize themselves against aggregation. The resulting zeta-potential is equal to -70 mV . We used a mixture of water (33% by weight), urea (37%) and glycerol (30%) in order to obtain an isodense suspension to negate particle sedimentation over the course of the entire experiment.

Suspension characterization

Characterization of aggregates. The monodisperse suspensions are characterized by a size distribution with a peak around the mean diameter of the particles. However, like all monodisperse suspensions, we also find contaminants, mainly particle aggregates and to a lesser extent large particles. The aggregates are likely formed at the beginning of the particle synthesis when the semi-stable PMMA particles are rapidly growing and by random chance encounter other such particles.⁵³ This may lead to the formation of few stabilized aggregates. Those aggregates are composed of 1.8 μm particles which seems to be linked permanently to each other. Examples of such aggregates are shown in Fig. 2. We checked that the distributions of aggregate shape and size do not change when these aggregates flow through the different parts of the model filter where they experience various levels of shear. From this we conclude that the aggregates of our suspensions are stable against shear flow and their distribution does not evolve as they flow through the model filter. We also added various amount of salt and determined the aggregate size distribution and found no difference even for salt concentrations where the surface charge of the polymer brush is completely screened. This confirms that both particles and aggregates are stabilized by the polymer brush

grafted on their surface. This means there is a steric stabilization of all the types of particles which prevent them from adhering to each other.

To characterize the size distribution of the different objects that compose the suspension we inject a suspension with a very low volume fraction of 5×10^{-4} into a rectangular channel (1 cm long, 0.5 mm wide and 20 μm high). During this experiment, we stop the injection for 6–7 s and image the particles in one part of the channel. Thereafter we flush the channel with a large pressure for 3–4 s, high enough to get new particles in the image. In this way, we obtain typical pictures with around 1200–1400 objects and after 7–8 h of experiment, we obtain a total amount of roughly 3.3×10^6 objects. In each image we start by detecting the particle position and determine whether it is in an aggregate or not. To locate and characterize fluorescent particles, the most commonly used method is Gaussian fitting. Due to the proximity of neighbouring particles within an aggregate there is an overlapping of their respective Gaussian fits, which makes it difficult to distinguish each particle (triplet in Fig. S1a, left, ESI[†]). In addition, when particles are well packed inside an aggregate the intensity distribution can be so smoothed that the algorithm eventually detects only one particle (quintuplet in Fig. S1b, left, ESI[†]). To overcome these difficulties, we use fast radial symmetry⁵⁴ which detects zones with a high radial symmetry from gradients in the images. Rather than looking at the contribution of the pixels around a central one, the FRS algorithm quantifies the contribution each pixel makes to the symmetry of pixels around it. Thanks to this method, we are able to determine the particle centre of overlapping particles inside the aggregates (Fig. 2). Secondly, we determine the centroid of the projected areas of the aggregates. The coupling of this second step with the FRS method gives us access to the number of particles within an aggregate and also the geometrical descriptors of the aggregates (Fig. S1 and S2, ESI[†]).

We use a particle tracking method at 100 frames per second to capture the aggregate dynamics under flow, with a flow rate of 0.05 $\mu\text{L min}^{-1}$ and a low particle concentration of 5×10^{-3} . This method is able to discriminate adjacent flowing particles and also those which are deposited in the reservoir. Using the FRS method and the centroid detection, we get various useful features of the flowing aggregates (orientation, shape and number of particles inside an aggregate).

We systematically determine the type and size of the objects that flow through the microfluidic filter during the clogging experiments, with an acquisition frame rate sufficiently high, between 3 to 30 fps, to be able to monitor separately each object that deposits. The type of captured aggregate is determined manually and the capture probability is calculated from the number of flowing particles through the pore and the distribution obtained from the stop and go experiments.

Results and discussion

We have previously performed clogging experiments with 4 μm particles in two confined situations ($1.5 < H/D < 3$) where

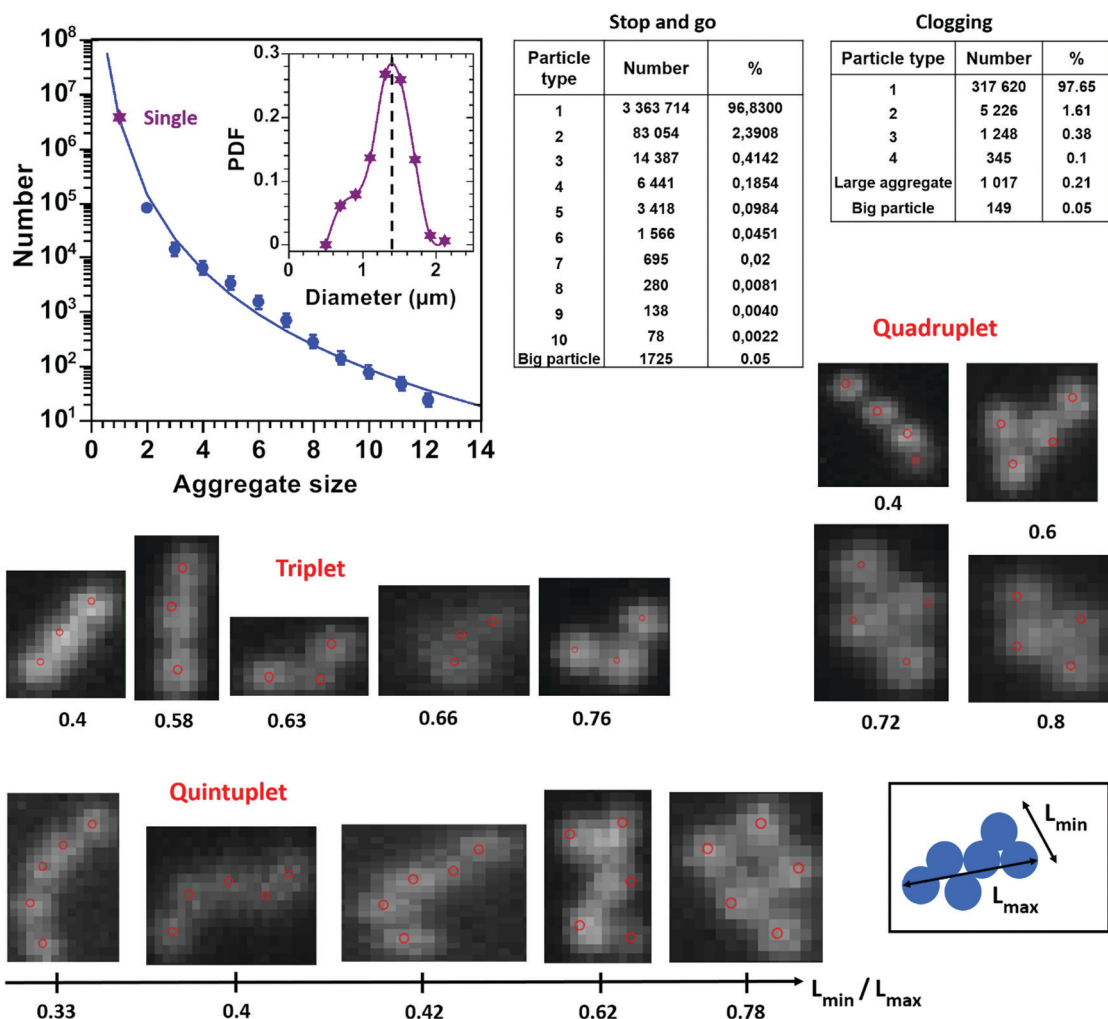


Fig. 2 (top-left) Distribution of aggregate sizes inside the PMMA suspension. The size of aggregates corresponds to the number of particles within an aggregate. The continuous line is a power law fit of the data with power index of -4.4 . (inset) Particle size distribution of the single particles determined from image analysis, which is centred on $1.4 \mu\text{m}$. More accurate size measurements from MEB images lead to a greater mean particle size of $1.8 \mu\text{m}$. (right) Proportion of the different types of particles that composed the PMMA suspension from the “stop and go” and the “pore clogging” experiments. (bottom) Examples of images of triplets, quadruplets and quintuplets with different shapes characterized by the ratio L_{\min}/L_{\max} , defined in the scheme in the bottom right corner.

particles captured by the pore walls lead directly to the clogging of the pore.^{14,15} More precisely, there is no need to accumulate particle on each other to block the pore, *i.e.*, the formation of particle monolayers on the different pore surfaces lead to the pore blocking. Thanks to confocal microscopy we were able to monitor the clog formation at the particle scale by following the particle deposition individually. We show in both studies that self-filtration is the main mechanism of pore clogging since the confinement is rather high. After the deposition of a few particles inside the pore by direct interception by the pore walls, the following deposition events are due to hydrodynamic interactions between those immobile objects and those about to be captured. The influence of aggregates was rather limited since we observed very few aggregates larger than doublets being captured within the pores. Even though confocal imaging is a very powerful tool to get the structure of the clog it does not give access to the dynamics of particle deposition, which is the goal of the present work.

Here, we perform clogging experiments in long pores but in a less confined configuration where we flow smaller, $1.8 \mu\text{m}$ PMMA particles through $8 \mu\text{m}$ wide and $12 \mu\text{m}$ high pores. In this case there must be particle accumulation over several layers in addition to the initial particle monolayer in contact with the pore walls to completely obstruct the pore. Rather than using confocal microscopy we use a sCMOS camera able to track particles when they flow through the pore which means that, in contrast to our previous studies,^{14,15} we do not have access to the structure within the forming clog. Instead, we are able to determine the dynamics of the particles as they get captured, and also their size and shape, which allows us to determine the aggregate size distribution as the aggregates flow through the pore.

Major contribution of aggregates to pore clogging

We first count the number of particles deposited inside the pore for flow rates, Q , between 0.008 and $0.9 \mu\text{L min}^{-1}$. The

clogging process is not due to the progressive deposition of single particles alone, as is presupposed,^{12,13,25} even though the suspension is rather monodisperse with around 97% of the particles having the same size (Fig. 2, left table). Single particles are mainly captured on the pore walls by physical interception, but they are then unable to pile up on that initial monolayer to progressively clog the pore (Fig. 3a). It turns out that particle aggregates, which corresponds to 3% of the particle population, are mainly responsible of the pore clogging. Whatever the flow rate there are three to five aggregates, from doublets up to aggregates composed of 10–12 particles, that deposit inside the pore in each experiment (Fig. 3b–d). The capture of these aggregates also facilitates the deposition of isolated single particles as these capture events lead to the formation of a porous deposit through which fluid can still flow and individual particles that follow these fluid paths can get trapped.

Since we have enough aggregates, (Fig. 2, right table), we are able to determine their probability of capture, which is the ratio of the number of aggregates deposited over the total number that flow through the pore, for each aggregate type. Note that there are large variations of this probability from one experiment to another since the history of the clogging formation for a given pore, *i.e.*, the successive particle–aggregate deposition process, is unique. However, since we have performed an important number of trials clear trends emerge from the variation of the capture probability with Q (Fig. 4).

The capture of aggregates, irrespective of their size, is much higher than the deposition of single particles for the full range of Q . For $0.02 < Q < 0.24 \mu\text{L min}^{-1}$ there is a sharp decrease in the capture probability corresponding to a lower particle deposition by physical interception by the pore walls,¹⁴ for all

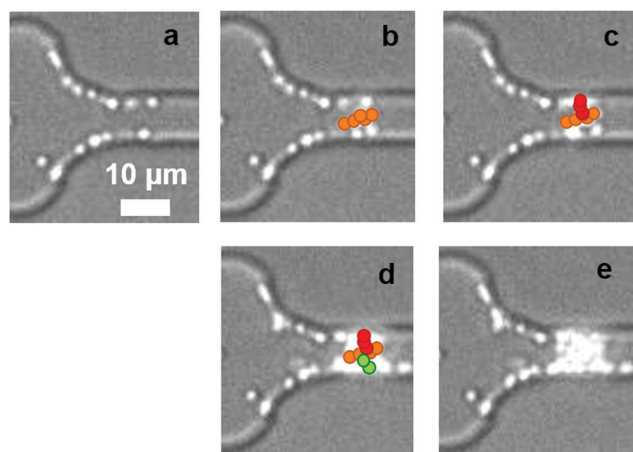


Fig. 3 Successive images for pore clogging by single particles alone (a) and aggregates, a quintuplet in (b), a triplet in (c) and a doublet in (d). The pore is completely obstructed by few additional single particles in each step. All the deposited aggregates were identified as they flowed through the reservoir zone prior their deposition. The position of these captured aggregates in the pore is approximate since this is a 2d view of the pore constructed to show that the aggregates were effectively immobilized in the forming clog. Note that individual particles are also captured by the deposited aggregates but we do not highlight their position in the clog so as not to overload the images.

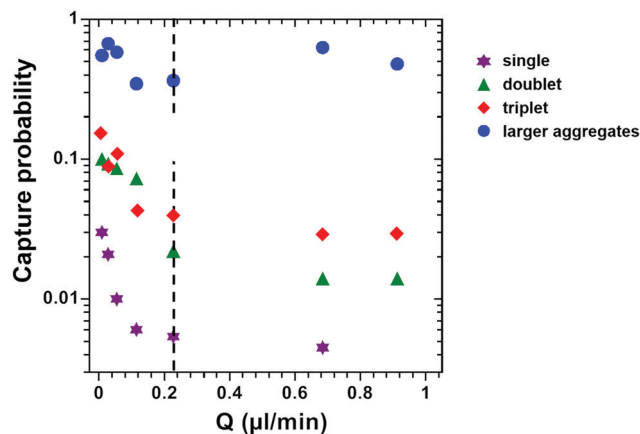


Fig. 4 Variation of the capture probability of single and aggregate particles with the flow rate Q . The dashed line corresponds to the limit between the two flow regimes.

particle types. From $Q > 0.2\text{--}0.4 \mu\text{L min}^{-1}$ the capture probability does not change with Q for aggregates while there is a very slight decrease for single particles. In this flow regime the physical interception of particles by the pore walls is the smallest while capture by the deposit, *i.e.*, by particles already stuck in the pore, remains constant. It is worth noting that the capture probability increases rapidly with the number of particles within an aggregate, irrespective of the flow rate. This is intuitively related to the aggregate's dimensions, the bigger the aggregate the more they are confined and the closer to the pore walls they are, enhancing their capture. However it is not just a question of size since particles bigger than the mean size are also present in the suspension and these have a very limited contribution to the pore clogging even though they quite numerous (Fig. 2, left table). Indeed, big particles, with a diameter smaller than the width of the pore, can be easily wiped off the pore walls by the flow since they experience high shear variations. In the case of aggregates they can withstand higher shear stresses as their structures are more open, reducing the torque due to the shear, since the fluid can pass through them.⁵⁵ In addition, aggregates have multi-contact with either the pore wall and/or the deposit that increases significantly their stability against removal by the flow. This is particularly true for the aggregates formed from four or more particles for which we observe that their capture probability remains high and varies between 0.3 and 0.7 over the range of Q we used.

To identify the underlying physical processes that are responsible for the capture of aggregates we look at their dynamics near the pore entrance, following their motion from the reservoir zone up to their capture by the pore walls or the deposit inside the pore. In this way we will be able to determine the features of the physical interception of aggregates. The interception of spherical particles by the pore walls is well known.^{12,56} In our filter geometry spherical particles flow through the reservoir and follow a given straight streamline along its path. When the particle get closer to the pore entrance, the width of the channel is narrower leading to a compression of the streamlines, which allows the particle to

move from its original streamline to another that is closer to the surface of the pore wall. At some point the particle cannot avoid the pore surface, due to its finite size, and comes sufficiently close to the surface, below tens of nanometer from it, and falls in the attractive part of the interaction potential between the particle and the pore surface and thus becomes stuck.¹²

Whatever their size and shape aggregates rotate periodically during their transport through the microchannel (Fig. 5a–c and

Fig. S3, ESI†), like a rod that exhibits Jeffery orbits in pure shear flow.^{57,58} This means that even though the center of mass of an aggregate remains located on the same streamline in the reservoir, just upstream of the pore, their edges come periodically closer to the nearby pore walls. However, contrary to the simple case of rods, in our experiments there are large variations in the dynamics of the aggregate spinning process due to the flow conditions in high confinement and there are

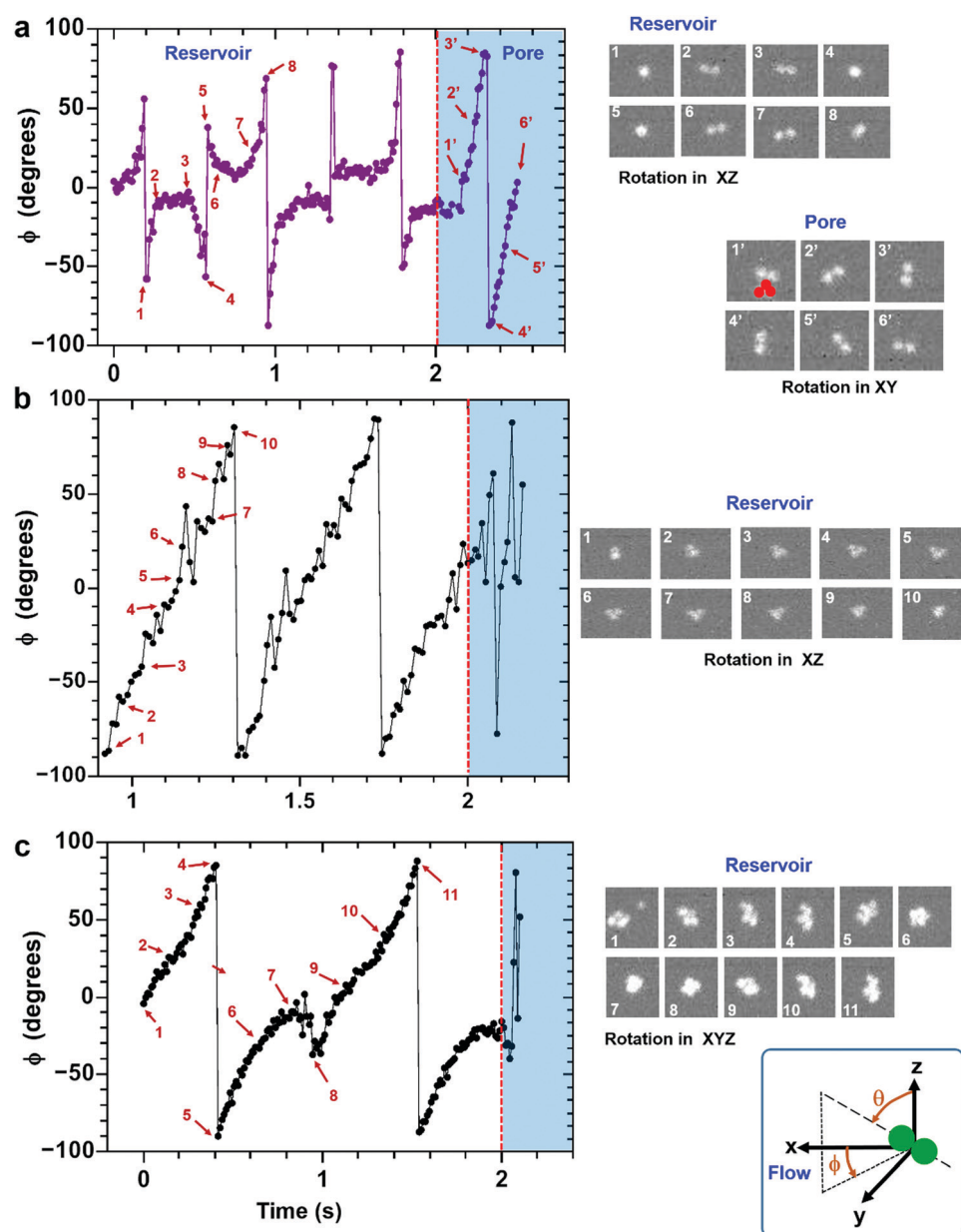


Fig. 5 (a) Variation of the orientation ϕ in the XY plane (see sketch on the bottom left corner), parallel to the top and bottom surfaces of the pore and corresponding to the observation plane of the microscope, for a doublet that flows consecutively in the reservoir and then in the pore. The numbers refer to the images on the left. The long axis of the doublet is in the z-direction at the beginning and the end of each period (images 1, 4, 5 and 8). Inside the pore the trajectory of the doublet is modified by the deposit (the red triplet is in contact with the pore wall) in image 1'. (b) Variation of the orientation for a flat triangular shaped triplet until it gets captured inside the pore. At the beginning of each period the triplet lies completely in the YZ plane, perpendicular to the flow direction (images 1 and 10), while at the middle of the period it lies in the XY plane, parallel to the top and bottom surface of the channel (image 5). (c) Variation of the orientation for a large aggregate with a complex shape and composed of at least of 6 particles. The dynamics of deposition inside the pore for the triplet (b) and the large aggregate (c) are shown in Fig. 6a and b, respectively.

especially important variations of the shear along the height of the channel. These lead to additional hydrodynamic interactions of the aggregates with the pore walls, modifying the spinning process especially at the transition between the reservoir and the pore. For instance, for the doublet in Fig. 6, upstream of the pore, it rotates along the flow direction in XZ plane, the plane perpendicular to the lateral walls of the pore, *i.e.*, it has a tumbling motion in the reservoir. We observe an important change in the doublet's rotation dynamics at the pore entrance (red dashed line in Fig. 5a). At this position the channel becomes more confined along the width ($8\ \mu\text{m}$) than along the height ($12\ \mu\text{m}$) leading first to an increase of the local fluid velocity and more importantly, to a modification of the orientation of the aggregate.

In less than $30\ \mu\text{m}$, corresponding to the distance over which the channel is progressively narrowed, the doublet rotates in all planes and then becomes stabilized when the pore section no longer changes, rotating only in the XY plane, parallel to the top and bottom walls as it travels along the pore (see also Fig. 6a for the case of a triplet that deposits and Fig. S3 for other examples, ESI[†]). This means that when the pore cross section becomes constant the doublet finds an equilibrium position relative to the pore surfaces and performs periodic rotations, while at the pore entrance the edges of the doublet can come closer to the lateral walls of the channel increasing its

probability of being captured at this point. Such modifications of both the rotation planes and the trajectory also occur when aggregates encounter a particle/aggregate attached to the pore surface (Fig. 6c). We suggest that this rather fast modification of the aggregate orientation leads to their capture mainly near the pore entrance and no further than $30\text{--}40\ \mu\text{m}$ inside the pore, as illustrated in Fig. 6a–c, where various aggregate types encounter new flow conditions as they either enter a pore or come across the surface of the deposit inside the pore. During that short moment one of their edges cannot avoid touching the pore walls (Fig. 6a and b). This is also true when aggregates come across particles/aggregates already deposited at the pore surface (Fig. 6c). An important observation, which confirms our hypothesis, is that almost no aggregate deposition occurs inside the pore far downstream of the entrance. Most of the time aggregates find a new equilibrium position around which they rotate without any possibility of touching the pore walls as they flow through the pore. However aggregates can still be stopped anywhere within the pore if they encounter other particles/aggregates or a channel defect; events which are rare in our set of experiments.

As already mentioned above, similarly to spherical particles, aggregates have to flow near the lateral walls of the reservoir, upstream of the pore, to be captured by physical interception by the pore walls. Aggregates that are closer to the lateral walls of the reservoir zone have more chance of being captured further downstream at the pore entrance since they have to flow very close to the walls at that location (Fig. 6a, b and Fig. S2, ESI[†]). After the capture of several particles and aggregates inside the pore there is also physical interception of flowing aggregates but this time by these immobile particles that compose the deposit (Fig. 6c). In such a case, there is no dependence on the position in the reservoir of the aggregates about to be captured. Thus aggregates that flow in the middle part of the reservoir can be captured by the colloidal deposit, in contrast to direct interception by the lateral walls. This also suggests that the probability to capture aggregates is increased when the surface of the pore becomes crowded.

In the following, we focus on the influence that the geometrical features and shape of the aggregates has on their capture. It turns out that aggregates that deposit in the pore have no preferential shape whatever their size. Actually, the distribution of the shape of the captured aggregates during clogging experiments is identical to that obtained from the stop and go experiment, simply meaning that it is a matter of probability (Fig. S4, ESI[†]). Nevertheless, we can go a bit further on the influence of the aggregate shape by considering that the probability of capturing aggregates is related to their maximum length or major axis, called here L_{max} , since the two opposite edges along L_{max} are the closest points to the pore walls during the aggregate rotation. We found that the capture probability increases and scales with the third power of L_{max} (Fig. 7). This suggests that aggregates act as “effective spheres” with a diameter equal to their long axes L_{max} as they enter into the pore. In other words, aggregates spin around their center of mass in such a way that their two edges along their greater dimension describes the surface of a sphere of diameter L_{max} .

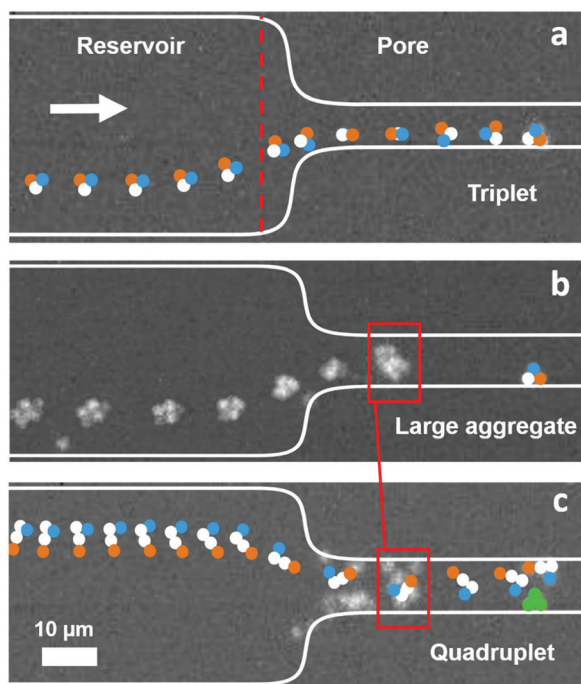


Fig. 6 Deposition dynamics of various aggregates inside the same pore for $Q = 0.05\ \mu\text{L}\ \text{min}^{-1}$. The different colors in (a) and (c) help to see the abrupt variation of rotation of the aggregates as they enter the pore. The arrow points in the flow direction while the dashed line in (a) corresponds to the transition between the reservoir and the pore. The red squares in (b) and (c) outline the final position of the large aggregate deposited in (b), around which the quadruplet performs an abrupt rotation, while the green triplet corresponds to the first deposition event in this pore that takes place in (a).

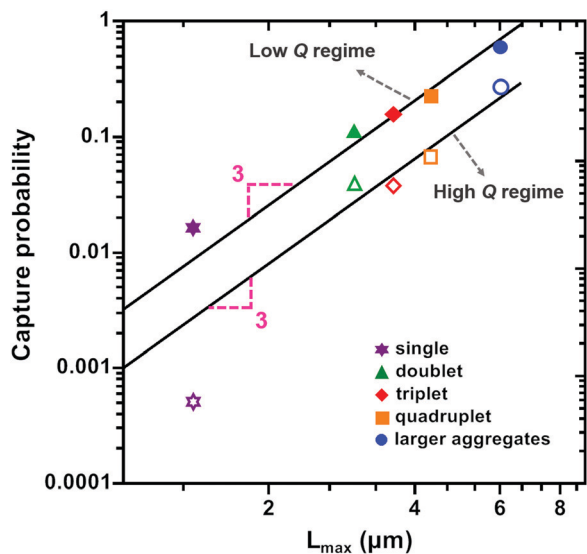


Fig. 7 Variation of the capture probability of aggregates with L_{\max} for $Q = 0.017$ (top curve with full symbols) and $0.228 \mu\text{L min}^{-1}$ (bottom curve with empty symbols). The continuous lines are power law fits of the data with an exponent equal to 3. The value of L_{\max} corresponds to the value of the median of the L_{\max} distribution for the different aggregate sizes.

This evolution of the capture probability with diameter, L_{\max} , is the same for both high and low flow regimes, but it appears to be greater in the low Q regime. We suppose that the higher rotation speed of the aggregates in this low flow regime⁵⁷ is responsible for such a behavior as this will mean that the edges of the aggregates will encounter the pore surface more frequently and thus increases their probability to be captured.

Summary and conclusions

In this paper we show that pores are mainly clogged by aggregates coming from the particle synthesis, when a predominantly monodisperse suspension of colloidal particles flows through a transparent model filter. In addition, we have determined the dynamics of aggregate particle deposition within a pore. Contrary to the work of Sauret *et al.*, the contaminant particles in our suspension are smaller than the pore size and thus pore clogging mainly results from the progressive accumulation of these aggregates and not from sieving a large aggregate. The analysis of the particle motion enables us to know what the shape and the size of the particles eventually captured are. We systematically found that aggregates, corresponding to a very small fraction of the suspension, *i.e.*, few percent, are actually responsible for the pore blocking. Unlike single particles, aggregates are able to deposit on the pore surface and on top of each other without being wiped off by the flow, since they can have multi contact points with the pore/colloidal deposit surface. The capture mechanism of aggregates is similar to that of single spherical particles, but in the former case there is physical interception of one of the two edges of the aggregates. As they flow through the channel, aggregates rotate around their center of mass, and thus behave

as effective spheres with a diameter corresponding to their maximum length L_{\max} , especially when they first enter in the constriction. Such a rotation enables the aggregates to get periodically closer to the pore or deposit surface and be captured, since the edges of the aggregates cannot always deviate from the deposit surface and avoid contact with it, unlike spherical particles that can more easily depart from the surface. The probability of aggregate capture is higher for low flow rates since the rotation speed of the aggregates is greater and thus increases their frequency of encountering the deposit/pore surface.⁵⁷

We performed clogging experiments with other suspensions, which were stabilized only by charge on their surface (for instance sulfate groups), obtained from different companies and also observed systematically that pore blocking results from aggregate accumulation. In each case there are between 0.5 and 2% of aggregates in the suspensions, before they are injected in the microfluidic devices. The geometrical features of these aggregates also remain unchanged until they deposit in the pores, *i.e.*, they are not broken by the flow while they are transported through the microfluidic channel.

We think that pore clogging by aggregates will also be observed in two other common situations in which aggregates are formed inside the porous structure. In a first situation, flow can induce particle aggregation in the bulk of the flowing suspension and also breaks up the aggregates. In a second one, colloidal particles can form a deposit on the pore walls but its growth can be limited by the flow that erodes its surface, releasing aggregates that may be captured further downstream. Generally speaking, this experimental work clearly shows that in order to draw sound conclusions on the dynamics of clog formation one must have to (i) know precisely the distribution of size and shape of the particles/aggregates that compose the suspension about to be filtered and (ii) be able to capture the dynamics of particle deposition in the pore. This methodology has to be used with different colloidal suspensions to check whether or not aggregates are indeed the main objects that accumulate and eventually block the pores.

Conflicts of interest

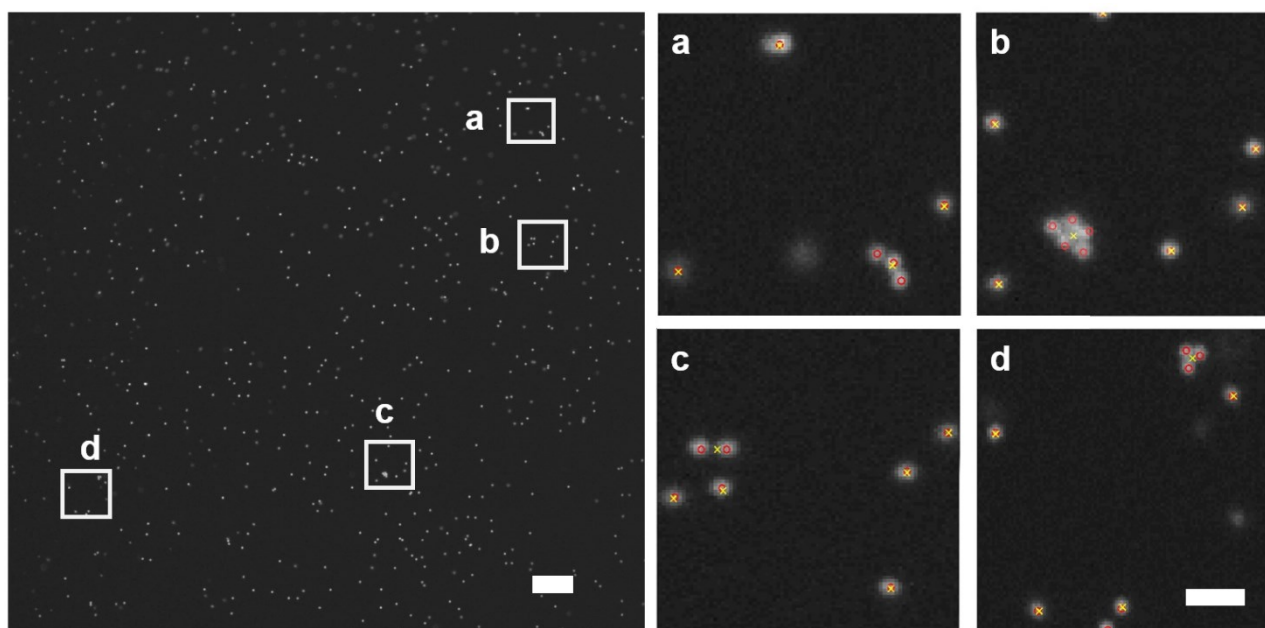
There are no conflicts of interest to declare.

References

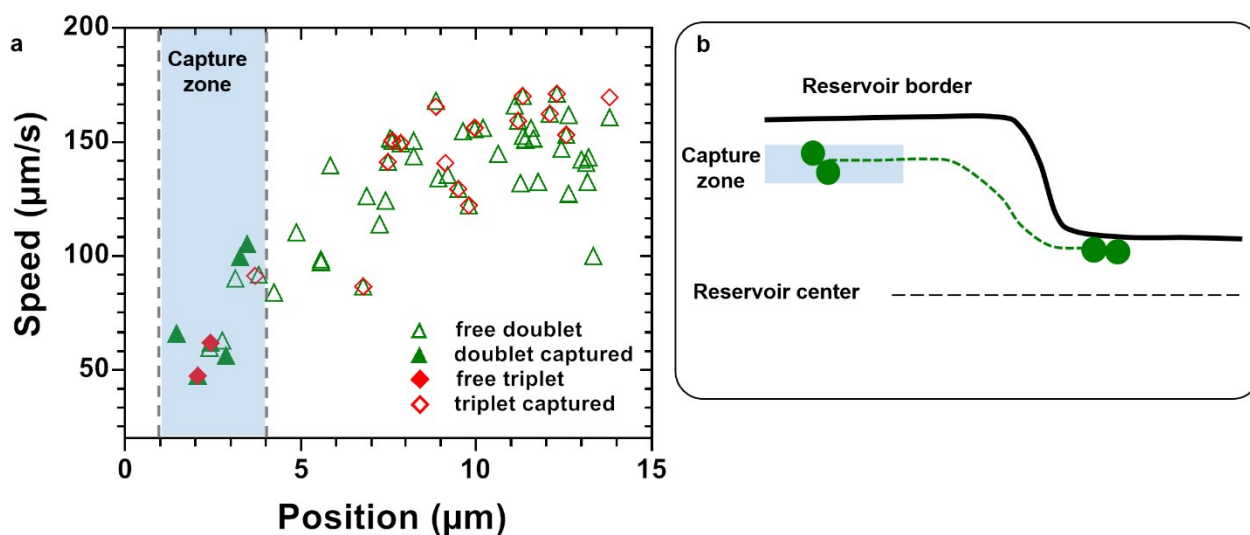
- 1 D. C. Mays and J. R. Hunt, *Environ. Sci. Technol.*, 2005, **39**, 577–584.
- 2 R. Gopal, S. Kaur, Z. Ma, C. Chan, S. Ramakrishna and T. Matsuura, *J. Membr. Sci.*, 2006, **281**, 581–586.
- 3 L. Sicignano, G. Tomaiuolo, A. Perazzo, S. P. Nolan, P. L. Maffettone and S. Guido, *Chem. Eng. J.*, 2018, **341**, 639–647.
- 4 E. Dressaire and A. Sauret, *Soft Matter*, 2017, **13**, 37–48.
- 5 Q. Liu, B. Zhao and J. C. Santamarina, *J. Geophys. Res.: Solid Earth*, 2019, **124**, 9495–9504.

- 6 Y. Chen, J. C. Sabio and R. L. Hartman, *J. Flow Chem.*, 2015, **5**, 166–171.
- 7 A. Sauret, E. C. Barney, A. Perro, E. Villiermaux, H. A. Stone and E. Dressaire, *Appl. Phys. Lett.*, 2014, **105**, 074101.
- 8 A. Sauret, K. Somszor, E. Villiermaux and E. Dressaire, *Phys. Rev. Fluids*, 2018, **3**, 104301.
- 9 V. Ramachandran and H. S. Fogler, *J. Fluid Mech.*, 1999, **385**, 129–156.
- 10 V. Ramachandran and H. S. Fogler, *Langmuir*, 1998, **14**, 4435–4444.
- 11 G. C. Agbangla, E. Climent and P. Bacchin, *Comput. Fluids*, 2014, **94**, 69–83.
- 12 H. M. Wyss, D. L. Blair, J. F. Morris, H. A. Stone and D. A. Weitz, *Phys. Rev. E: Stat., Nonlinear, Soft Matter Phys.*, 2006, **74**, 061402.
- 13 B. Dersoir, M. Robert de Saint Vincent, M. Abkarian and H. Tabuteau, *Microfluid. Nanofluid.*, 2015, **19**, 953–961.
- 14 B. Dersoir, A. B. Schofield and H. Tabuteau, *Soft Matter*, 2017, **13**, 2054–2066.
- 15 B. Dersoir, A. B. Schofield, M. Robert de Saint Vincent and H. Tabuteau, *J. Membr. Sci.*, 2019, **573**, 411–424.
- 16 T. van de Laar, S. ten Klooster, K. Schroën and J. Sprakel, *Sci. Rep.*, 2016, **6**, 28450.
- 17 D. C. Duffy, J. C. McDonald, O. J. A. Schueller and G. M. Whitesides, *Anal. Chem.*, 1998, **70**, 4974–4984.
- 18 A. Accardo, R. Courson, R. Riesco, V. Raimbault and L. Malaquin, *Addit. Manuf.*, 2018, **22**, 440–446.
- 19 C. M. Cejas, F. Monti, M. Truchet, J.-P. Burnouf and P. Tabeling, *Langmuir*, 2017, **33**, 6471–6480.
- 20 B. Mustin and B. Stoeber, *Langmuir*, 2016, **32**, 88–101.
- 21 P. Bacchin, A. Marty, P. Duru, M. Meireles and P. Aimar, *Adv. Colloid Interface Sci.*, 2011, **164**, 2–11.
- 22 Z. B. Sendekie, A. Gaveau, R. G. Lammertink and P. Bacchin, *Sci. Rep.*, 2016, **6**, 31471.
- 23 S. S. Massenburg, E. Amstad and D. A. Weitz, *Microfluid. Nanofluid.*, 2016, **20**, 94.
- 24 Z. B. Sendekie and P. Bacchin, *Langmuir*, 2016, **32**, 1478–1488.
- 25 T. van de Laar, S. ten Klooster, K. Schroën and J. Sprakel, *Sci. Rep.*, 2016, **6**, 28450.
- 26 R. van Zwieten, T. van de Laar, J. Sprakel and K. Schroën, *Sci. Rep.*, 2018, **8**, 5687.
- 27 B. Mustin and B. Stoeber, *Microfluid. Nanofluid.*, 2010, **9**, 905–913.
- 28 J. Linkhorst, T. Beckmann, D. Go, A. J. C. Kuehne and M. Wessling, *Sci. Rep.*, 2016, **6**, 22376.
- 29 J. Linkhorst, J. Rabe, L. T. Hirschwald, A. J. C. Kuehne and M. Wessling, *Sci. Rep.*, 2019, **9**, 18998.
- 30 I. Bouhid de Aguiar, M. Meireles, A. Bouchoux and K. Schroën, *Sci. Rep.*, 2019, **9**, 9241.
- 31 J. Lohaus, F. Stockmeier, P. Surray, J. Lölsberg and M. Wessling, *J. Membr. Sci.*, 2020, **602**, 117886.
- 32 G. Brans, A. van Dinther, B. Odum, C. G. P. H. Schroën and R. M. Boom, *J. Membr. Sci.*, 2007, **290**, 230–240.
- 33 M. E. Warkiani, F. Wicaksana, A. G. Fane and H.-Q. Gong, *Microfluid. Nanofluid.*, 2015, **19**, 307–315.
- 34 I. S. Ngene, R. G. H. Lammertink, M. Wessling and W. van der Meer, *J. Membr. Sci.*, 2010, **346**, 202–207.
- 35 I. S. Ngene, R. G. H. Lammertink, M. Wessling and W. G. J. Van der Meer, *J. Membr. Sci.*, 2011, **368**, 110–115.
- 36 A. Marin, H. Lhuissier, M. Rossi and C. J. Kähler, *Phys. Rev. E*, 2018, **97**, 021102.
- 37 M. Souzy, I. Zuriguel and A. Marin, *Phys. Rev. E*, 2020, **101**, 060901.
- 38 G. Gerber, M. Bensouda, D. A. Weitz and P. Coussot, *Phys. Rev. Lett.*, 2019, **123**, 158005.
- 39 C. Duchêne, V. Filipe, S. Huille and A. Lindner, *Soft Matter*, 2020, **16**, 921–928.
- 40 P. Bacchin, P. Aimar and V. Sanchez, *J. Membr. Sci.*, 1996, **115**, 49–63.
- 41 S. Bounoua, S. Tomas, J. Labille, B. Molle, J. Granier, P. Haldenwang and S. N. Izzati, *Irrig. Sci.*, 2016, **34**, 327–342.
- 42 R. Guha, X. Shang, A. L. Zydney, D. Velegol and M. Kumar, *J. Membr. Sci.*, 2015, **479**, 67–76.
- 43 A. Bretagne, F. Cotot, M. Arnaud-Roux, M. Sztucki, B. Cabane and J.-B. Galey, *Soft Matter*, 2017, **13**, 3812–3821.
- 44 S. Shin, J. T. Ault, P. B. Warren and H. A. Stone, *Phys. Rev. X*, 2017, **7**, 041038.
- 45 M. Emmanuel, D. Horváth and Á. Tóth, *CrystEngComm*, 2020, **22**, 4887–4893.
- 46 G. Laffite, C. Leroy, C. Bonhomme, L. Bonhomme-Coury, E. Letavernier, M. Daudon, V. Frochot, J. P. Haymann, S. Rouzière, I. T. Lucas, D. Bazin, F. Babonneau and A. Abou-Hassan, *Lab Chip*, 2016, **16**, 1157–1160.
- 47 R. L. Hartman, J. R. Naber, N. Zaborenko, S. L. Buchwald and K. F. Jensen, *Org. Process Res. Dev.*, 2010, **14**, 1347–1357.
- 48 R. L. Hartman, *Org. Process Res. Dev.*, 2012, **16**, 870–887.
- 49 A. Perazzo, L. Sicignano, G. Tomaiuolo, R. Marotta, R. Andreozzi and S. Guido, *Chem. Eng. Sci.*, 2019, **207**, 581–587.
- 50 M. Trofa, G. D'Avino, L. Sicignano, G. Tomaiuolo, F. Greco, P. L. Maffettone and S. Guido, *Chem. Eng. J.*, 2019, **358**, 91–100.
- 51 T. M. Squires and S. R. Quake, *Rev. Mod. Phys.*, 2005, **77**, 977.
- 52 S. Shen, E. D. Sudol and M. S. El-Aasser, *J. Polym. Sci., Part A: Polym. Chem.*, 1993, **31**, 1393–1402.
- 53 Y. Almog, S. Reich and M. Levy, *Br. Polym. J.*, 1982, **14**(4), 131–136.
- 54 G. Loy and A. Zelinsky, *IEEE Trans. Pattern Anal. Mach. Intell.*, 2003, **25**, 959–973.
- 55 S. Veerapaneni and M. R. Wiesner, *J. Colloid Interface Sci.*, 1996, **177**, 45–57.
- 56 L. A. Spielman, *Annu. Rev. Fluid Mech.*, 1977, **9**, 297–319.
- 57 K. Li and H. Ma, *Langmuir*, 2018, **34**, 2967–2980.
- 58 M. B. Salerno, M. Flamm, B. E. Logan and D. Velegol, *Environ. Sci. Technol.*, 2006, **40**, 6336–6340.

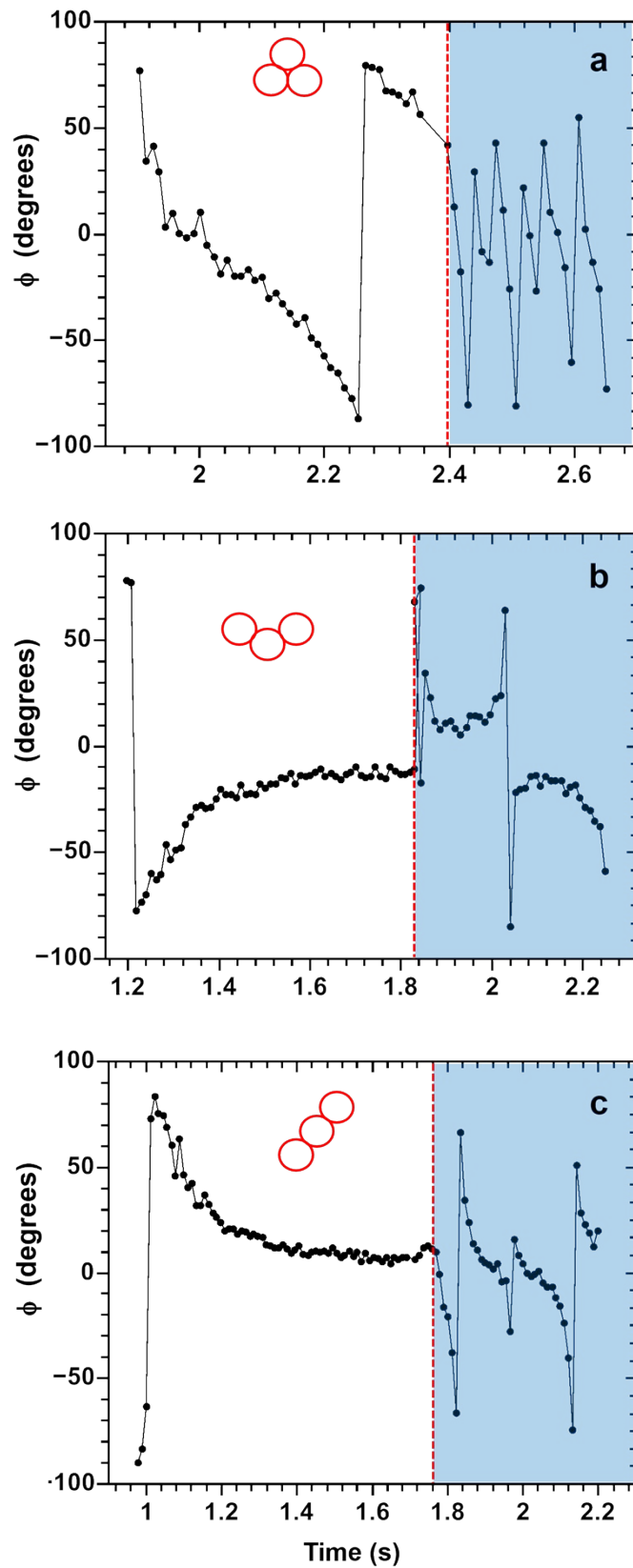
Supplementary figures



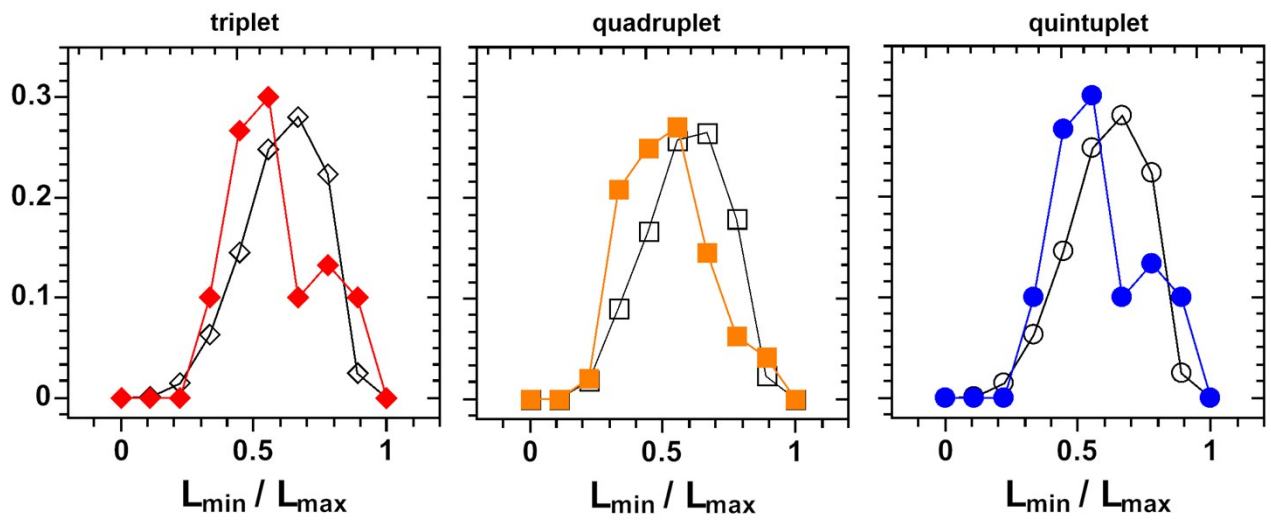
Sup. figure 1: (left) Image taken during the stop part of the stop and go experiment. Scale bar corresponds to $20\mu\text{m}$. (right) Zooms on the same image at various places to show the objects detected by the image analysis. The crosses and circles correspond respectively to the Gaussian and the fast radial symmetry methods. Scale bar corresponds to $10\mu\text{m}$.



Sup. figure 2: (a) Variation of the average speed of doublets and triplets in the reservoir zone. The origin of the position, $0\mu\text{m}$, corresponds to the reservoir border while the position equal to $15\mu\text{m}$ corresponds to its centre. (b) Sketch of the physical interception of aggregate particles by the pore walls.



Sup. figure 3: Variation of the orientation of triplets with different shapes as they are transported consecutively in the reservoir and in the pore. None of these aggregates eventually deposit in the pore.



Sup. figure 4: Probability distribution functions of the size ratio L_{\min} / L_{\max} for triplets, quadruplets and quintuplets measured in clogging experiments (full symbols) and during the stop and go experiments (open symbols).



Contents lists available at ScienceDirect

Journal of Membrane Science

journal homepage: www.elsevier.com/locate/memsci

The contribution of colloidal aggregates to the clogging dynamics at the pore scale

N. Delouche^a, J.M. van Doorn^c, T.E. Kodger^c, A.B. Schofield^b, J. Sprakel^c, H. Tabuteau^{a,*}

^a Univ Rennes, CNRS, IPR (Institut de Physique de Rennes)-UMR 6251, F-35000, Rennes, France

^b School of Physics and Astronomy, The University of Edinburgh, The James Clerk Maxwell Building, Peter Guthrie Tait Road, Edinburgh, EH9 3FD, UK

^c Physical Chemistry and Soft Matter, Wageningen University and Research, Stippeneng 4, 6708, WE Wageningen, the Netherlands

ARTICLE INFO

Keywords:

Colloidal particles
Aggregates
Pore clogging
Microfluidics
Particle size and type distributions

ABSTRACT

During the filtration of colloidal dispersions by a membrane, pores often get clogged by the suspended particles. Knowing the shape and size of the particles that cause this clog would be a great help to membrane users since they could then choose the ideal filtering device. Microfluidic technology enables the fabrication of model membranes or filters that are transparent, which allows for measuring the particle geometrical features that deposit either at the surface of the pores or on top of the fouling layer that has already formed. However, the use of microfluidic filters have been confined to the study of clog formation at the pore scale, overlooking the influence of the dynamics of the particle deposition on the clogging process. We have recently shown that looking precisely at what is deposited and how this is captured inside the pore provides new insight into the clogging process. In particular, we have found that a minute concentration of aggregates in a supposedly monodisperse dispersions are mainly responsible for pore fouling. In this paper, we use the same imaging technique to determine the entire clogging process for different types of monodisperse dispersions under various flow conditions, DLVO interactions with the pore walls, and confinements. We show that the way clogs form is appear complex but is also quite systematic in the fact that aggregates are the building blocks of the clog. Pores are clogged by progressive accumulation of aggregates with the average size of the aggregate required to cause the blockage increasing with increasing flow velocity. This work demonstrates that particle size and shape distributions of the feeding dispersion must be determined to understand which physical mechanisms are at play during the clogging process.

1. Introduction

Even though the consequences of membrane fouling on the flow conditions across a membrane are well documented, the precise underlying mechanisms remain poorly understood. We know that deposition of solids carried by a fluid at the surface of a membrane or inside its porous structure leads to a drop of pressure, but we have not yet determined the dynamics of particle deposition or capture by the membrane, up to the complete fouling of the membrane. This difficulty comes from the fact that it is rather challenging to see through a membrane as a suspension flows through it, since membranes are optically opaque. We can still monitor the deposit growth in situ using sophisticated techniques [1–3] but the temporal dynamics of the clogging formation remains inaccessible. We do not have access to the solid particle dynamics in the vicinity of a membrane except in model

situations, i.e., with model filters like micro-sieves or microfluidics channels [4–8]. For instance, Valencia et al. were able to determine the dynamics of the very first stages of the cake formation on the top of a membrane with particles bigger than the pore size. Only a few confocal studies have allowed imaging of the entire clogging process at the particle level inside a pore [9–11]. However, these works deal with very narrow pores where only the interaction between the particles and the pore surface are responsible for the fouling, i.e., the pore clogging resulted exclusively from the fouling of the pore surfaces. As far as we are aware, there is no experimental evidence at the pore scale of the clogging process that relies on the progressive accumulation of multi-layers of particles either inside a microfluidic model filter or membrane. This type of study is challenging to carry out since three advanced experimental conditions have to be met. Firstly, the particle deposit must be transparent to have access to the internal structure of the

* Corresponding author.

E-mail address: herve.tabuteau@univ-rennes1.fr (H. Tabuteau).

<https://doi.org/10.1016/j.memsci.2021.119509>

Received 27 January 2021; Received in revised form 29 May 2021; Accepted 4 June 2021

Available online 10 June 2021

0376-7388/© 2021 Elsevier B.V. All rights reserved.

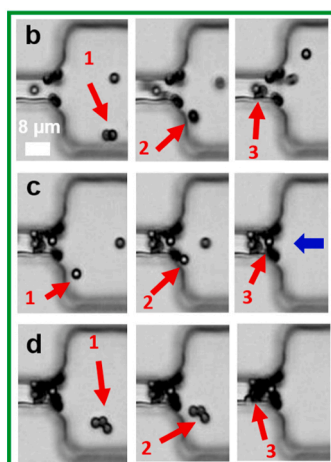
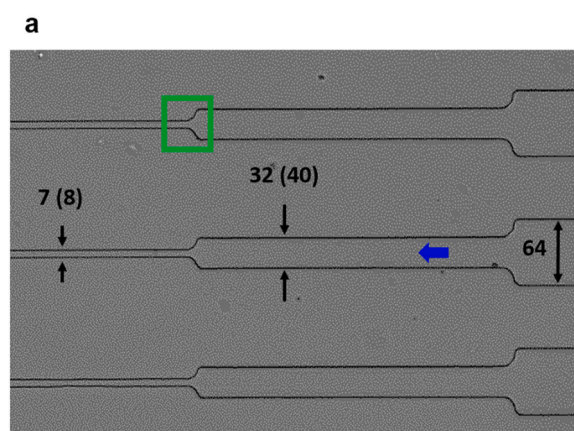
particle deposit as it grows unless one uses confocal microscopy with very restrictive conditions on the nature of the suspending liquid and particles [11]. Secondly, accessing the dynamics of the deposit growth requires high speed imaging, around ten thousand frames per second to be able to image the particle capture by the deposit [9]. Finally, measuring the variations of the flow conditions across the pore during fouling is required to determine the hydrodynamic resistance of the deposit. As a starting point to tackle these arduous issues, we have recently focused on the dynamics of the particles capture by the forming deposit [12]. We detect all the particles that go across a single pore. This configuration enables us to follow the trajectory of the particles about to be captured and also their size and shape. In addition, we can determine the probability of capture for the different type of particles, stabilized either by surface charges or polymer brushes.

We have discovered that when a rather monodisperse latex suspension flows through our model filter, the pores are clogged by an accumulation of aggregates and not by single particles, even though aggregates represent only small fraction of the suspension. In this paper, we use this new approach to determine the entire clogging formation for a wide range of flow conditions, using various monodisperse latex suspensions with different surface charges flowing through a model filter. During these experiments, we monitor the deposition history of colloidal particles within the pore and the mean size of each deposited object, which allows us to determine different clogging scenarios. We also determine different features of the deposit stability as it grows. In particular, we monitor detachment events of single particles or aggregates, which helps to quantify the erodibility of the deposits by the fluid flow. We show that for each type of dispersion that pore clogging always results from aggregate accumulation whatever the flow conditions. We distinguish two clogging regimes depending on the flow conditions. At low flow rates, pores are either clogged by an accumulation of small aggregates or by a mixture of small and large aggregates, while at higher flow rates, most of the clogs are formed with large aggregates. The transition between these two regimes is related to the detachment of small aggregates by the flow while the larger ones remain more firmly attached.

2. Materials and methods

2.1. Microfluidics filter and image analysis

We used the methodology developed in Delouche et al. [12] to make our model microfluidic filter. All pore walls are made of PDMS to obtain



the same particle-surface interactions everywhere on the pore surface [11]. During the filtration experiments particles flow through a main wide channel before entering the filter zone composed of long independent pores in parallel (Fig. 1). In this zone, there are two reservoirs upstream of the constriction/pore, which is the thinnest part of the filter and where clogging takes place. The two reservoirs are long and wide enough to ensure that the particle accumulation after the pore clogging event remains located in these reservoirs. Thus in such a configuration we can safely consider that the clogging process for each individual pore is independent of what happens in the surrounding pores. In addition, we can easily track particles over long distances in these two reservoir zones enabling a more accurate determination of their shape. The length of the reservoir also allows us proper tracking of the particles prior to their transport inside the pore. The experiment is stopped when the six pores at the center of the model filter clog. Most of the time not more than half of the pores are clogged when we stop the experiments. We image the transport of the different type of colloidal particles with a sensitive camera (Hamamatsu Orca Flash 4.0 v2). The suspension is injected in the filter by applying a difference of pressure with a regular pressure controller (Elveflow OB1 Mk2 or Fluigent MSFC). We determine the corresponding flow rate at the beginning of the experiment for each applied pressure with a sensor flow (Fluigent, 5% accuracy) located at the outlet of the filter. Particles follow fluid streamlines and their inertia is negligible since the Péclet and Reynolds numbers for the different flow conditions are respectively higher than 10^3 and smaller than 10^{-3} . In addition, we use different mixtures of liquid to match the particle density with that of the fluid mixture. We use homemade $1.8 \mu\text{m}$ PMMA and $2.4 \mu\text{m}$ PS particles coated by a polymer brush and commercial suspensions of $1 \mu\text{m}$ and $1.8 \mu\text{m}$ PS particles stabilized by sulfate groups on their surface, bought from Microparticles GmbH (Berlin). Details on the synthesis of $1.8 \mu\text{m}$ PMMA particles can be found in Delouche et al. [12]. PS coated particles were synthesized using a type of dispersion polymerization where the dispersant is formed *in-situ* [13]. During the formation of these particles, a reactive initiator-monomer, or *inimer*, is added which allows for a controlled growth of charged polymer brush by ATRP; the resulting particles have a well-defined charge density. Other $1.8 \mu\text{m}$ and $1 \mu\text{m}$ PS latex particles, stabilized by sulfate groups on their surface, were bought from Microparticles GmbH (Berlin).

2.2. Suspensions characterization

We use the stop and go method to obtain the particle size and shape

deposition. (For interpretation of the references to colour in this figure legend, the reader is referred to the Web version of this article.)

distribution for all the suspensions we used [12]. Briefly, each suspension is injected inside a straight channel (500 μm wide and 20 μm high) and we applied a rectangular wave pressure such that the suspension first does not move for few seconds allowing us to take non-blurred images of the suspended particles. Then the suspension flows for 3–4 s, to renew the particles in the field of view, and the flow is stopped again, and another image of the particles is taken. In this way, we obtain the size and the shape of thousands to millions of particles for each suspension. Such a high particle number counting enables us to easily detect the aggregates present in the suspension thanks to a Fast Radial Symmetry algorithm (FRS) [14]. Whether for the commercial or the synthesized monodisperse suspensions, aggregate particles represent but a few percent of the particle population (Fig. 2, top). Whatever their size, aggregates have very diverse shapes (Fig. 2a–b), and we define only two-dimensional features of each object, L_{max} and L_{min} (Fig. 2c). To obtain these lengths, we compute the convex hull of each object which can be simply conceptualized by a rubber band released around the aggregate. L_{max} also known as the Feret diameter, is the largest antipodal pair of the convex hull, and L_{min} the smallest [15,16].

We also determine the shape of the particles that get captured inside the pore during the clogging experiments with FRS. These size and shape characterizations are coupled with a particle tracking algorithm in the reservoir before entering the constriction (Fig. 1b–d). Due to the opacity of the deposit, the particle tracking does not directly allow knowledge of what object is deposited. Instead, we subtract the number of each type of deposited object manually from all objects in the reservoir. It is worth noting that we cannot get the precise 3D position of the particle center with this approach since we do not know at which height the particles are deposited, relative to the top or bottom part of the pore.

3. Results

3.1. Influence of particle type and confinement ratio W/D on the overall clogging dynamics

We have shown recently that minute quantities of aggregates inside a stable and highly monodisperse colloidal suspension deposit more frequently than the spherical particles [12]. In this previous article we focused on the dynamics of the capture of single aggregates directly on the pore walls or at the surface of the colloidal deposit. We also provided some qualitative information that explains why aggregates have such a high probability of capture. Here, we use the same experimental

approach to study the dynamics of successive deposition of single particles/aggregates leading to complete pore blocking for different types of particles, various flow conditions and two degrees of confinement defined as the ratio of the pore width, W , to the particle size, D , W/D . We first used monodisperse dispersions of 1.8 μm PMMA and PS particles and 1 μm PS particles and flow them in a microfluidic filter with a pore width $W = 8 \mu\text{m}$ and $H = 12 \mu\text{m}$. We begin by focusing on the global dynamics of pore clogging by looking at the evolution of the average number of particles that flow through the pore prior to clogging, N^* , with the flow rate Q [17–20] (Fig. 3). We determine N^* either by tracking all the particles that flow inside the pore, or from the knowledge of the clogging time and the volume fraction of the suspension [19]. For all the suspensions we used the average value of N^* is almost constant for low Q values while it increases for higher ones, as already observed with other particles [11,19]. In this new work, after careful inspection of the dynamics of all the particles that flow through the pore, we observe that there is indeed a progressive clogging of the pore, irrespective of the flow rate. However, most of the particles that form the clog are not single particles but rather aggregate particles, even though all the suspensions we used are primarily composed of individual particles (Fig. 2, top). The growth of the deposit up to complete pore blocking is mainly due to the progressive accumulation of aggregates, between two to six, irrespective of the flow rate and the particle type (Fig. 3, right). It is worth noting that for each suspension and flow condition there are large variations of N^* showing that pores are clogged in many different ways, involving aggregates with various shapes and sizes (Fig. 2, bottom).

Hereafter, we determine the different parameters that explain (i) such fluctuations for each Q value and (ii) the evolution of N^* with the flow rate. We consider separately regimes of high ($W/D = 4.5$) and low ($W/D = 8$) confinement for the 1.8 μm PMMA-PS and 1 μm PS particles, respectively. For the higher confinement, we mainly focus on PMMA particles, since similar conclusions can be drawn for PS particles. Despite the high variability in the clog composition, it is still possible to define different categories of clogs, irrespective of the flow conditions, based on geometrical features of the deposited aggregates. We split our clogging experiments into two categories depending on the size of aggregate present within the clog, by considering the greatest dimension of the aggregates, the length L_{max} that rules out the probability of aggregate capture [12]. Since aggregates have an anisotropic shape they rotate around their center of mass as they flow through our model filter. During this rotation, their two opposite edges along L_{max} come closer to either

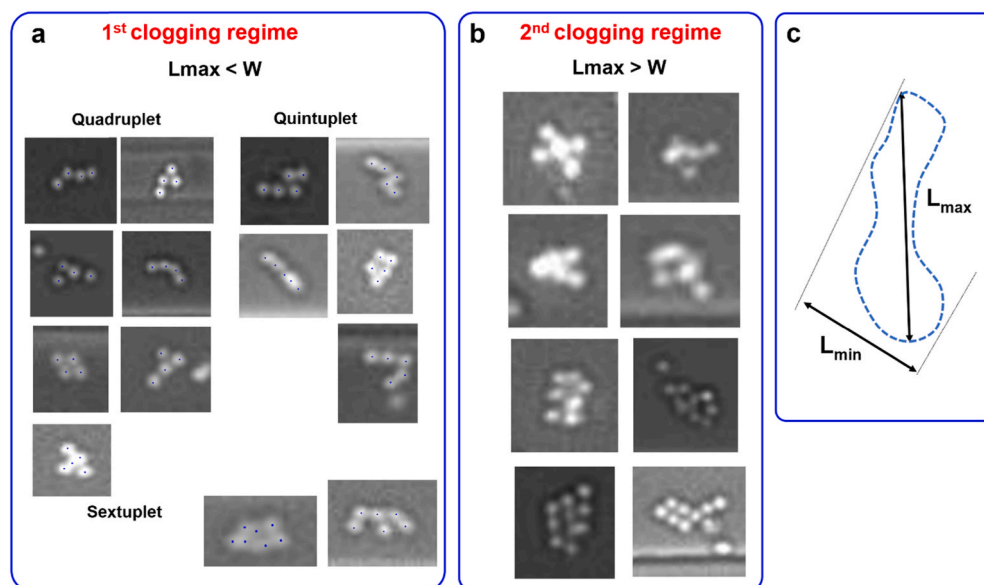


Fig. 2. (Top) Composition of the different suspensions and relative proportion of single particles and aggregates. We work with 6 suspensions of 1.8 μm PS particles containing different amount of added NaCl salt (top) while we work with three suspensions of 2.4 μm PS coated particles exhibiting different surface charges with no addition of salt (bottom right). (Bottom) (a–b) Various fluorescent images of 1.8 μm PMMA aggregates in the two clogging regimes with specific conditions of the aggregates length L_{max} . (c) Definition of the length L_{max} and the width L_{min} of the aggregates.

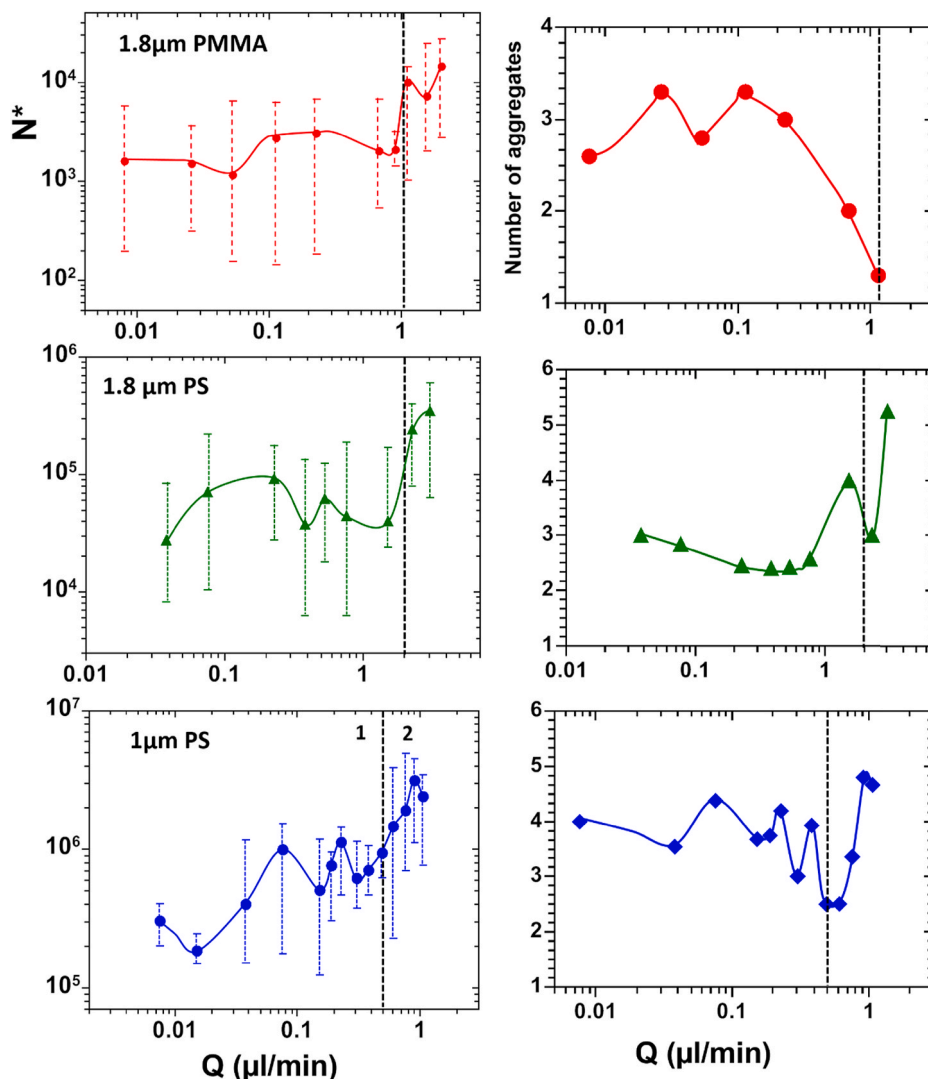


Fig. 3. (Left) Variation of the median value of N^* with the flow rate for 1.8 μm PMMA (top), 1.8 μm PS (middle) and 1 μm PS particles (bottom). The number of experiments for each flow rate are given in Fig. 2 of the supplementary. (Right) Evolution with Q of the average number of aggregates inside a clog when the pore is blocked. The continuous line on each plot are guides to the eyes. For each experiments the root mean square deviations is the same going from 2 to 7 particles.

the pore walls or the colloidal deposit and thus increase their probability to touch the surface, which eventually leads to the aggregate capture. We consider that aggregates larger than the pore width, $L_{\text{max}} \geq W$, have the greatest chance to be captured near the pore entrance, by the lateral sides of the pore. In our case this configuration corresponds to $L_{\text{max}} \approx 8 \mu\text{m}$. Note that aggregates with a length $L_{\text{max}} = 8 \mu\text{m}$ can be composed of 5–7 individual particles, depending on the shape of the aggregates. We found that in the first clog category, every deposited aggregate had its length $L_{\text{max}} < 8 \mu\text{m}$. In the second category, there is at least one aggregate with a $L_{\text{max}} > 8 \mu\text{m}$. Thus, we divide our results into two distinct regimes of clogging when $L_{\text{max}} < W$ and $L_{\text{max}} > W$.

Figs. 4 and 5 contain consecutive images of the entire clogging process for the 1st and the 2nd clog categories, respectively. Frequently single particles, the most numerous in the suspensions, start to be captured at the pore walls and are unable to form a thicker deposit (Fig. 4, image 1 to 4). It should be noted that aggregates are often captured by the pore walls as well. As discussed elsewhere [11,12,19], the presence of this monolayer of single or aggregate particles greatly enhances the capture of flowing particles. Aggregates, regardless of their dimension, can deposit at any time whatever the degree of fouling (sup. Fig. 1). In addition, not all captured particles belong to the clog, i.e. they are not inside the portion of the deposit that eventually blocks the pore.

Indeed, while most of the particles are captured near the pore entrance over a distance between 20 and 30 μm into the pore, the length over which clogs are built corresponds roughly to the pore width, W [19] (last image of Figs. 4 and 5). The final location of the clog and the entire dynamics of the clog formation are not predictable; the growth of the deposit being highly dependent on the local morphology of the deposit, the distance between the flowing aggregates from the deposit surface, and the shape and size of the aggregates [12]. Therefore, even if the deposit becomes important at a given location, reducing appreciably the pore cross section, the final position of the clog can be eventually located elsewhere (Fig. 5).

In the 1st category, $L_{\text{max}} < W$, there is often no more than two large aggregates from quadruplet to sextuplet, which partake in the clog build-up. Even with the deposition of such large aggregates, the pore remains partially clogged and then other smaller aggregates block the remaining pore space, leading to the complete obstruction of the pore (sup. Fig. 1a–b). In the 2nd category, even though the greatest aggregate dimension can be larger than the pore width, $L_{\text{max}} > W$, almost no clogging event is produced by the sieving of a single aggregate. More frequently an aggregate, larger than a quadruplet, is deposited and leads to an important reduction of the pore space, such that only a few objects are needed to terminate the clogging process. Other large aggregates can

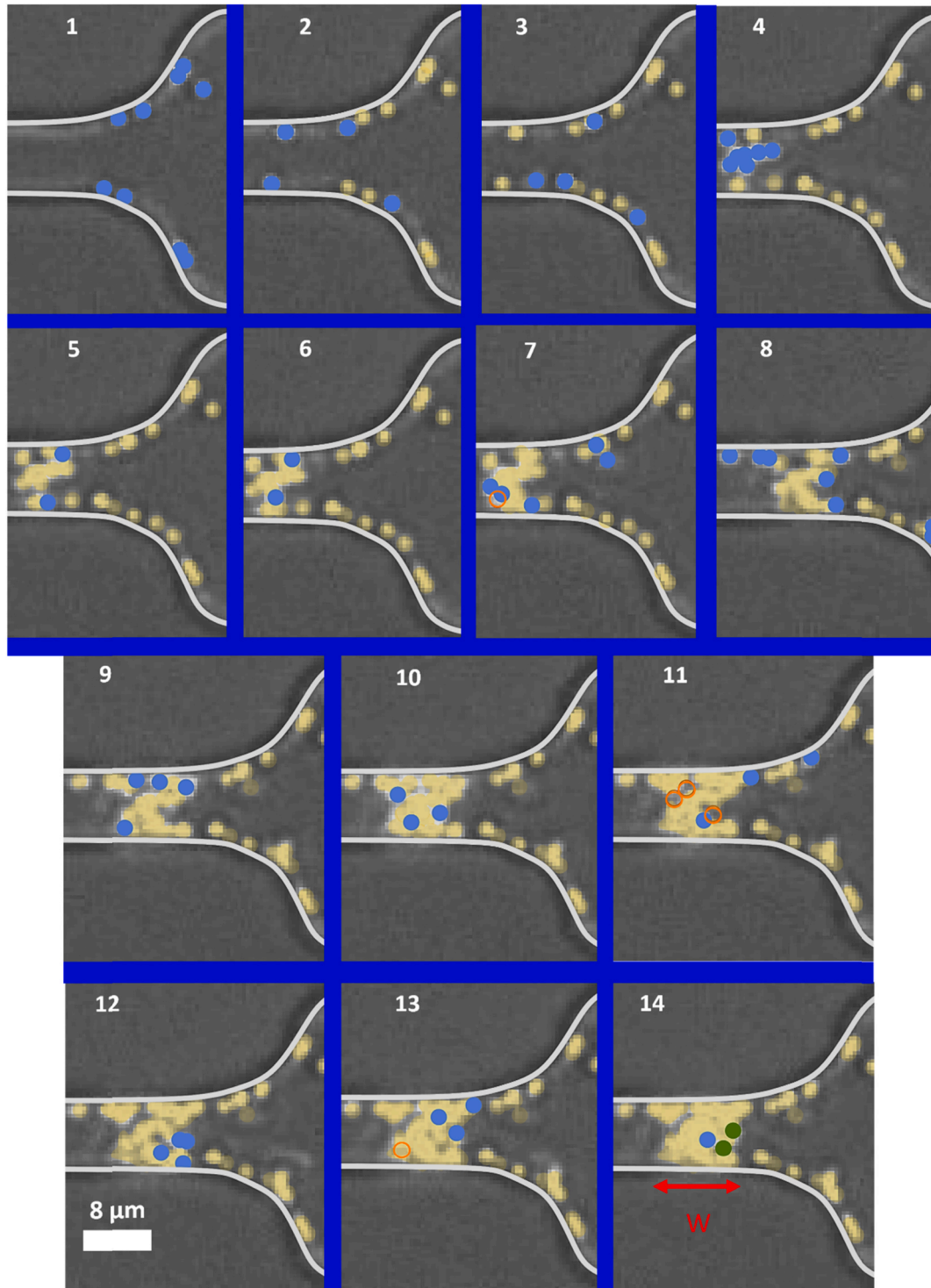


Fig. 4. Consecutive images of the clog formation for the 1st type of clogging corresponding to the data of sup. Fig. 1b. The blue objects correspond to particles that are just being captured while the yellow ones are already deposited. In images 11 and 13, the open circles denote particles detached by the flow. In image 14, the pore is finally blocked by the blue particle, the length of the clog being equal to W . Thereafter the accumulation of particles starts at the rear of the clog (two green particles). (For interpretation of the references to colour in this figure legend, the reader is referred to the Web version of this article.)

also pile up and completely block the pore in this way (sup. Fig. 1c–d).

In the following, we determine the relationship between the occurrences of the two clogging categories and the flow conditions. For the lower flow rates, $0.01 < Q < 1 \mu\text{l}/\text{min}$, N^* is constant, around 2000 particles, a value high enough to observe several dozens of doublets, a few triplets and larger aggregates that flow through the pore according to the particle size distribution (Fig. 2, top), confirming that the pore can

be blocked by aggregate deposition. For these low flow conditions, clogs mainly belong to the first category but as Q increases this trend is inverted (sup Fig. 2, top-left). For $Q > 1 \mu\text{l}/\text{min}$, there is an important increase of N^* with Q (Fig. 3, top left) and almost all the clogged pores belong to the 2nd category. This indicates that larger aggregates are more involved in the clogging process at higher flow rates. All together these results suggest that the mean size of deposited aggregates increases

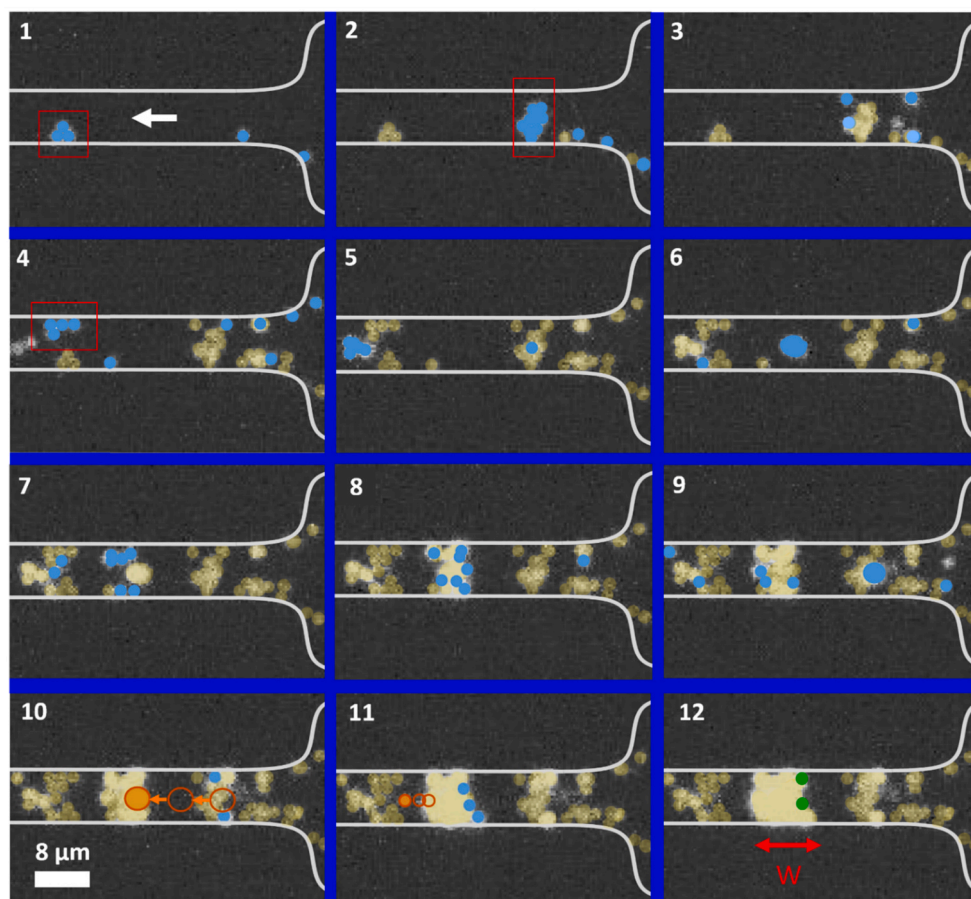


Fig. 5. Consecutive images of the clog formation for the 2nd type of clogging. The blue objects correspond to those particles which are just being captured while the yellow to green ones are already deposited. The rectangles in images 1–2 and 4 highlight the final position of various aggregates whose deposition dynamics can be found in Delouche et al. [12]. In image 9, a large particle is captured and remains static for 2 s before it again moves towards the location where the pore will eventually clog (image 10). In image 11, there are rearrangements within the clog that lead to the expulsion of particles at the clog front which do not seem to weaken the internal structure of the clog. In image 12, the pore is completely blocked; the length of the clog being equal to W and then the accumulation of particles starts at the rear of the clog (two green particles). (For interpretation of the references to colour in this figure legend, the reader is referred to the Web version of this article.)

with Q , evolution that can be understood if we consider the erosion by the fluid flow. At high flow rate the erosion prevents mainly the deposition of single particles and small aggregates, which thus leads to an increase of N^* since the clogging process mainly relies on large aggregates that are less numerous and thus requires that more particles flow through the pore prior to aggregate capture. A more detailed discussion is provided in the supplementary material (sup Fig. 3).

When we consider the PS particles, with the same size as the PMMA particles, we observe the same trend for the evolution of N^* with Q . However, the average value of N^* in the 1st clogging regime is 2.5 times higher than for PMMA particle, which can be explained mainly by the difference in distribution of particle size between the two suspensions. Indeed, for this suspension the total amount of aggregate number is only 0.56% while for the PMMA this is equal to 3.17% (Fig. 2, top) and hence more PS particles must flow through the pore to observe aggregate deposition. There is also an important variation of the particle size/object distribution. The proportion of large aggregates, which includes quadruplets, is equal to 0.37% for the PMMA while it is much smaller for PS, around to 0.01%. However, among this population of large aggregates for PS particles there are few very large objects that alone can plug the pore. These particles are responsible for 37% of the total clogging events at low flow rates, which increases significantly the number of clogs belonging to the 2nd clog category compared to the PMMA case (sup Fig. 2, top right). The increases of N^* with the flow rate starts from a higher Q value, presumably because PS particles have an increased adhesion on the pore walls and also with each other [19], and thus higher flow conditions are needed for particle detachment by the flow to occur.

The situation for the smaller 1 μm PS particles is similar despite the degree of confinement being seemingly less favorable to the formation of clogs since more particles being required to clog a pore. The average

number of aggregates to block the pore is slightly larger than for the two other types of particles, being around four (Fig. 3, bottom). Therefore, since the aggregates are formed with smaller particles there are more particles per aggregates, around 12–14 on average. Regardless of flow rate, all the clogs belong to the second category, which means that large aggregates are always involved in the clogging process (sup Fig. 2, bottom). The evolution of the average number of aggregates is similar to that of observed for the 1.8 μm PS (Fig. 3, bottom right). Since the particle size distribution is quite monodisperse (Fig. 2), the probability that such large aggregates flow through the pore is low, which explains why the average value of N^* at low flow rate is high, close to $7 \cdot 10^5$. (Fig. 3, bottom left).

3.2. Influence of the ionic strength

The clogging dynamics are modified by changing either the ionic strength of the suspension or the surface charge of the particles. In a first set of experiments involving 1.8 μm PS particles, the ionic strength of the suspension was modified by adding NaCl salt. In such a case, both particles and pore wall surface charges are modified simultaneously. In a second set of experiments, we worked with rather monodisperse polystyrene particles (PS) coated with a PVP brush which imparts steric stabilizations. In these experiments, another polymer is grown from the particle surface but with varying ratio of neutral, cationic and an anionic monomer to create particles of varying surface charge density [13].

3.3. Change of ionic strength of the suspensions by salt addition

We used the classical strategy to screen the surface charge the 1.8 μm PS particles, simply by adding NaCl salt to the particle suspension. Before each experiment the model filter is saturated by a salty solution

with the same salt concentration, C , as that of the colloidal suspension about to be injected. For C above 50 mM and 200 mM, respectively, the surface charge of the pore walls and that of the particles is completely screened. The particle size and type distribution in the various salty suspensions were determined thanks to the stop and go experiments previously described (Fig. 2, top). For $C \leq 100$ mM the population of aggregates are slightly modified, while above 100 mM it rises up significantly, with a steeper increase of the number of aggregates larger than quadruplets (Fig. 6a–b).

In the clogging experiments the salt addition has a direct impact on the evolution of N^* with flow rate (Fig. 6c–d). For the first clogging regime, $Q < 1 \mu\text{l}/\text{min}$, N^* decreases with C , with the sharpest decrease, found when the salt concentration comes closer to the critical coagulation concentration (CCC) of the suspension, $C = 200$ mM (Fig. 6d). While N^* does not vary with the flow conditions for the $C = 0$ mM dispersion, it first increases and then becomes constant for increasing Q for all the salty dispersion. These variations are far less pronounced for $C = 200$ mM. These evolutions of N^* are again directly related to the relative proportion of the aggregate population inside the suspensions (Fig. 2, top). The average number of aggregates required to clog a pore remains constant as long as the concentration of aggregates slightly increases, for C smaller than 100 mM (sup Fig. 4c). Even though the size of the aggregates involved in the clog formation significantly increases for $C > 100$ mM, the clogs are formed with more aggregates. The measure of the relative proportion of the two clogging categories defined previously indicates that the average size of the aggregates forming the clogs increases with both the flow rate and the salt concentration (see sup. Fig. 4 for a detailed description).

3.4. Influence of the surface charge of the particles

We performed clogging experiments with suspensions of $2.4 \mu\text{m}$ PS

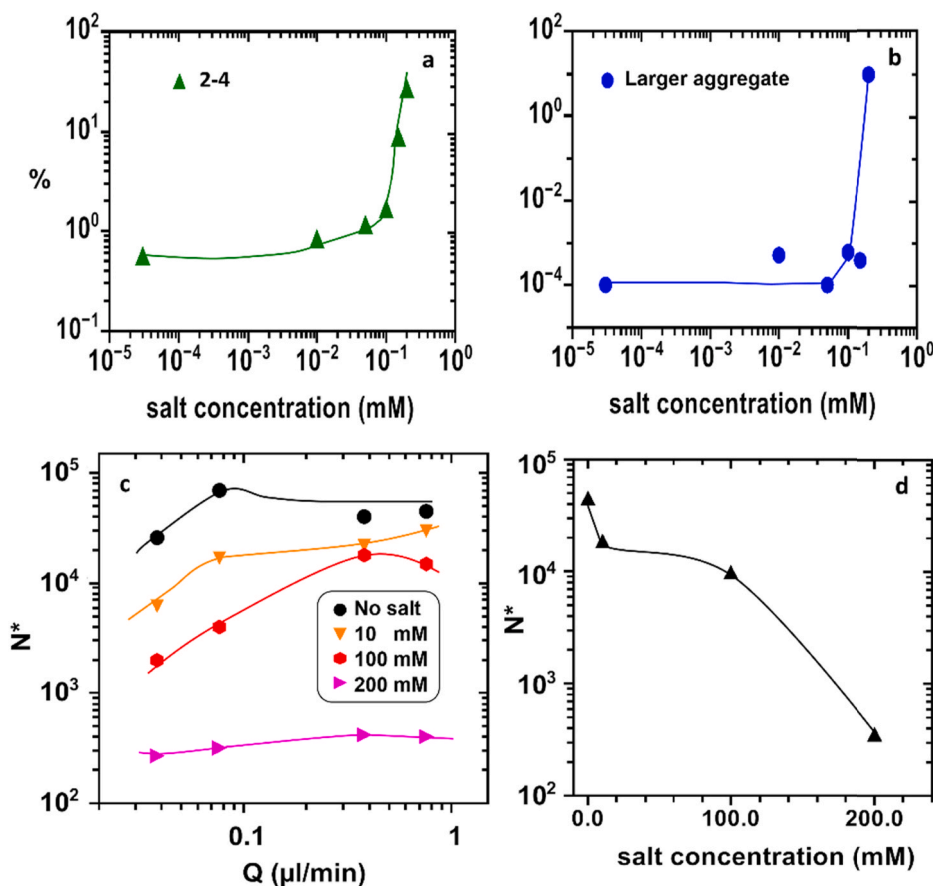


Fig. 6. Particle population percentage of doublet up to quadruplet (a) and larger aggregates bigger than quadruplets (b) measured during the stop and go experiments for suspensions of $1.8 \mu\text{m}$ PS with various amount of salt. (c) Variation of N^* with Q for suspensions with ionic strength. The data for the suspension with no salt added is identical to those shown in Fig. 3 (middle, left). (d) Evolution of N^* averaged for all Q values vs. the salt concentration. The continuous lines on all plots are guides to the eyes. (For interpretation of the references to colour in this figure legend, the reader is referred to the Web version of this article.)

particles with an anionic, cationic and neutral surface charges polymer coating for which the confinement ratio is higher than previously, $W/D = 3.3$ and with no salt addition. In such a high confinement the clog formation depends chiefly on the interactions between the surface of the particles and the pore walls rather than on the interparticle interactions [11]. In a given cross section only two monolayers need to deposit on both pore walls before only one extra layer of particle in between them is needed to block the pore almost completely. Thus, we may expect that the pores will be clogged more rapidly by the cationic particles since there is a net attraction between these particles and the negatively charged pore surface. Neutral particles should also rapidly clog the pores since they do not bear surface charges. We indeed observe that deposition of single particles directly on the pore surface is two times higher for the neutral and cationic particles than for the anionic ones. However, when we look at the overall clogging dynamics, the surface charge of the particles does not appear to play a role since the average number of particles needed to block the pore, N^* , is about the same, around 2000 particles for each particle type (Fig. 7a).

Looking at the particle level and the type of particles, we found again that aggregates play a dominant role in the clogging process. Since the confinement is higher, with $W/D = 3.3$, there is more particle capture by the pore walls and the average number of aggregates that deposit inside the pore, is also twice as high compared to other particles tested in section 2 of this paper (Fig. 7c). This can also come, in a lesser extent, from the higher aggregate concentration in the coated PS particles, around 7–8% of the total number of particles (Fig. 2, top). For the anionic particles, there are on average more than four large aggregates (quadruplets or larger) within each clog (Fig. 7c) which represent around 6% of the total amount of deposited particles within the clogs while they are the least numerous population of the suspension, less than 0.4% (Fig. 2, top). This is due to their high probability of capture (Fig. 7b). The situation is a bit different for the two other types of

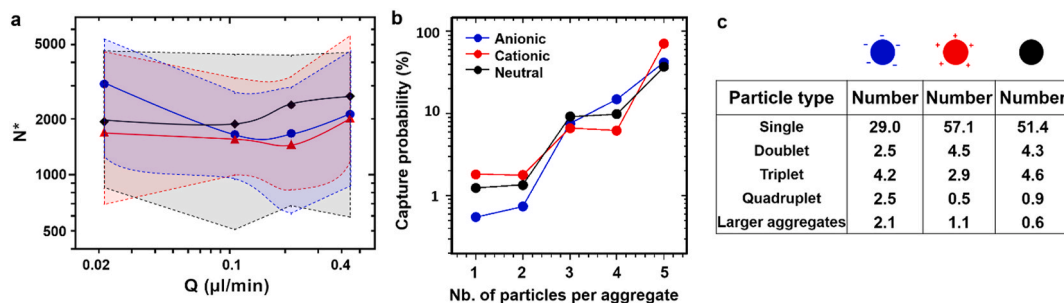


Fig. 7. (a) Variation of N^* with Q for the three types of PS coated particles (neutral in black, anionic in blue and cationic in red). Shaded areas correspond to the deviation between the extreme values of N^* . (b) Probability of capture for the various particle types. The last point of the graph on the right corresponds to the probability of capture for quintuplets and larger aggregates. (c). Average number of each particle/aggregate deposited inside a pore during the clogging experiments for all the flow rates. (For interpretation of the references to colour in this figure legend, the reader is referred to the Web version of this article.)

particles. For cationic and neutral particles there are only 1.5 aggregates larger than triplets in each clog on average (Fig. 7c). Note that significant part of the pores is clogged only by the accumulation of single particles and small aggregates, doublets and triplets. This is directly related to both the relative proportion of single particles and doublet in the suspensions and the surface charge properties of these suspensions. The population of single particles and doublets corresponds to 98.4% of the total amount of particles for both suspensions (Fig. 2, top) which increases their probability of capture. In addition, there is no electrostatic barrier between the pore surface and the neutral particles and even a net attraction for the cationic ones since the pore walls are negatively charged [21] promoting the particle deposition of both types of particles, since their capture probability is roughly 5 times higher than for the anionic particles (Fig. 7b). We supposed that neutral particles are captured only by physical interception, while the anionic and cationic particles are driven towards the pore surfaces due to very short-range electrostatic attractions, 30–50 nm from the pore surface. Therefore, cationic particles that are further away from the pore walls than the neutral ones can still deposit, which explains why the capture probability is slightly higher for cationic particles (Fig. 7b).

Surprisingly, these favorable conditions for particle deposition for the cationic and neutral particles do not play a role when we consider larger aggregates, starting from triplets. Indeed, the probability of capture for these aggregates are roughly the same, irrespective of the surface charge (Fig. 7b). This capture probability does not depend on the aggregate shape since aggregates have on average the same shape for the different particle types (sup Fig. 5). We suppose that the motion of large aggregates inside the pore is responsible of their capture. These aggregates are captured by physical interception as they rotate, when one of their edges come into contact with either the pore wall or the deposit [12]. Our results suggest that the nature of the surface charge does not modify the capture dynamics of large aggregates, since the capture probability is the same whatever the particle type. Therefore, the presence of large aggregates inside clogs formed by anionic particles is only due to the higher quantity of such aggregates in the anionic suspension injected in the model filter.

4. Discussion

In this work we considered fouling within the pore rather than on top of the membrane since the size of the particles of our suspensions are smaller than the pore size. We identified the different clogging mechanisms when the feeding suspensions contains aggregates and particles smaller and/or larger than the mean pore size of the filter. Pores can first be blocked by sieving a large particle or an aggregate. However, there are still some free spaces between the pore surface and this big object in which small particles can flow through and eventually block them. A second mechanism relies on successive accumulation of smaller aggregates, which is the more common case in our experiments. Whatever the

mechanism, even though single spherical particles can also be involved in the clogging process, they cannot alone block the pore by successive accumulation. They are mainly captured directly on the pore walls, by physical interception, or by the deposit, likely by sieving. Indeed, we have not observed physical interception of single particles by those which belong to the monolayer in contact with the pore walls or at the top of a deposit, while such a mechanism of particle capture is commonly used in numerical simulations of pore clogging [22,23]. However, from our experiments we cannot conclude definitively that there is no physical interception of a flowing particle by another immobile one, but rather that physical interception of aggregates is far more likely than physical interception of single particles. In the light of these results, it may be useful to have a new look at the results of almost all the works related to the clogging dynamics and mechanisms that used microfluidic channels as a model filter and monodisperse suspensions of spherical colloids [17,19,20,24–28] as the filtrate. Indeed, the results of these studies rely on the implicit hypothesis that single particles accumulate one after the other forming the deposit and thus they have not considered that aggregates could have played any role in the fouling process. In particular, we think that clogging of small pore sizes, not larger than two particle diameters, is more likely the result of doublet or larger aggregates capture rather than the hydrodynamic bridging of two single particles that enter simultaneously inside the pore [26,28–31]. Indeed, irrespective of the chemical synthesis of monodisperse particles, there are always small aggregates like doublets or even triplets in the suspensions. For instance in all the suspensions we used, the population of doublets is far from negligible since doublets represent between 0.5% and 8% of all the particles. This means that from a dozen up to 200 particles of these dispersions pass through a filter with pore sizes around two particle diameters doublets may statistically be present and can block the pores at their entrance. Therefore, even if there is only a tenth of a percent of aggregates in a suspension the probability to block the pore by aggregate sieving should be far more important than clogging the pore by hydrodynamic bridging. New experimental investigations involving the imaging of the particle capture inside or at the pore entrance have to be performed to confirm the sieving of aggregates in very confined situations.

5. Conclusion

By observing the dynamics of particle deposition within a pore, we show that for different types of monodisperse colloidal suspensions, under various flow conditions, confinements and electrostatic interactions, clogging proceeds mainly by successive depositions of aggregated particles. Therefore, even though these aggregates represent only few percent of the population they represent a major impact on the clogging process. We considered the clogging within the pore rather than on top of the membrane since the size of the particles of our feeding suspensions are smaller than the pore size. We identified two main

mechanisms of pore clogging. Pores can first be blocked by sieving a large particle or an aggregate. However, there are still some free spaces between the pore surface and this big object in which small particles can flow through and eventually block them. A second mechanism relies on successive accumulation of smaller aggregates, which is the more common case in our experiments.

We show that when an average number of particles N^* , or equivalently a Critical Volume of Suspension (CVS), passes through a pore it becomes clogged. Contrary to other works in dead end configurations [26,27] we found that there is always a CVS above which the pore will be completely fouled, irrespective of the flow conditions. We show that the CVS is directly related to the concentration of aggregates in the suspension. The CVS is constant for lower pressures while it increases with the pressure for higher pressures. Since we performed on average around fourteen replicates for each pressure, we can observe that for the range of pressure we used pores can be clogged either by accumulation of aggregates or by a partial fouling of the pore followed by the sieving of a large aggregate. The proportion of each category strongly depends on the aggregate size distribution of the different suspensions, however the average size of the aggregates involved in the clog formation always increases with increasing pressure. This trend is due to the detachment by flow of the smaller aggregates since they have less contact points with the deposit.

The role of aggregates in the clogging process has also to be confirmed in other pore geometries, especially for those encountered in industrial filters and membranes. Here the maximum average speed of the particles is not greater than 7 mm/s, a value which is comparable to those measured inside microfiltration membranes with the same pore size, around 10 mm/s [28]. Therefore, we expect that such membranes will be clogged mainly by the sieving of large aggregates rather than by the successive deposition of small aggregates which are smaller than the mean pore size.

Since our model filters are deformable, we cannot perform backwashing experiments to determine the mechanical resistance of the different types of clog. However, our results suggest that even if most of the particles forming the clog can be removed aggregates lying on the pore surface will rarely be detached by the flow. Finally, we believe that pore clogging by accumulation of aggregates should also be considered in cross flow conditions.

Author statement

N. Delouche: Conceptualization, Methodology, Investigation, Writing - Original Draft, Visualization, Writing - Review & Editing, Formal analysis. J.M. van Doorn, T.E. Kodger, A.B. Schofield and J. Sprakel: Methodology, Writing - Review & Editing, Formal analysis. H. Tabuteau: Conceptualization, Methodology, Investigation, Writing - Original Draft, Visualization, Writing - Review & Editing, Formal analysis. Supervision, Project administration, Funding acquisition.

Declaration of competing interest

The authors declare that they have no known competing financial interests or personal relationships that could have appeared to influence the work reported in this paper.

Acknowledgments

We acknowledge funding from the French Agence Nationale de la Recherche (ANR) (ANR-12-JS09-0003) and the CNES (Collmat).

Appendix A. Supplementary data

Supplementary data to this article can be found online at <https://doi.org/10.1016/j.memsci.2021.119509>.

References

- [1] Y. Gao, S. Haavisto, W. Li, C.Y. Tang, J. Salmela, A.G. Fane, Novel approach to characterizing the growth of a fouling layer during membrane filtration via optical coherence tomography, *Environ. Sci. Technol.* 48 (2014) 14273–14281, <https://doi.org/10.1021/es503326y>.
- [2] W. Luo, B. Arhatari, S.R. Gray, M. Xie, Seeing is believing: insights from synchrotron infrared mapping for membrane fouling in osmotic membrane bioreactors, *Water Res.* 137 (2018) 355–361, <https://doi.org/10.1016/j.watres.2018.03.011>.
- [3] I. Ben Hassan, C. Lafforgue, A. Ayadi, P. Schmitz, In situ 3D characterization of monodispersed spherical particle deposition on microsieve using confocal laser scanning microscopy, *J. Membr. Sci.* 454 (2014) 283–297, <https://doi.org/10.1016/j.memsci.2013.12.003>.
- [4] I.S. Ngene, R.G.H. Lammertink, M. Wessling, W. van der Meer, A microfluidic membrane chip for in situ fouling characterization, *J. Membr. Sci.* 346 (2010) 202–207, <https://doi.org/10.1016/j.memsci.2009.09.035>.
- [5] I.S. Ngene, R.G.H. Lammertink, M. Wessling, W.G.J. Van der Meer, Visual characterization of fouling with bidisperse solution, *J. Membr. Sci.* 368 (2011) 110–115, <https://doi.org/10.1016/j.memsci.2010.11.026>.
- [6] A. Valencia, C. Le Men, C. Ellero, C. Lafforgue-Baidas, P. Schmitz, J.F. Morris, Direct observation at the microscale of particle deposition during the first stage of the microfiltration process, *J. Membr. Sci.* 599 (2020) 117823, <https://doi.org/10.1016/j.memsci.2020.117823>.
- [7] J. Lin, D. Bourrier, M. Dilhan, P. Duru, Particle deposition onto a microsieve, *Phys. Fluids* 21 (1994–Present) (2009), 073301.
- [8] G. Brans, A. van Dinther, B. Odum, C.G.P.H. Schroën, R.M. Boom, Transmission and fractionation of micro-sized particle suspensions, *J. Membr. Sci.* 290 (2007) 230–240, <https://doi.org/10.1016/j.memsci.2006.12.045>.
- [9] B. Dersoir, A.B. Schofield, H. Tabuteau, Clogging transition induced by self-filtration in a slit pore, *Soft Matter* 13 (2017) 2054–2066, <https://doi.org/10.1039/C6SM02605B>.
- [10] J. Linkhorst, J. Rabe, L.T. Hirschwald, A.J.C. Kuehne, M. Wessling, Direct observation of deformation in microfluidic filtration, *Sci. Rep.* 9 (2019) 18998, <https://doi.org/10.1038/s41598-019-55516-w>.
- [11] B. Dersoir, A.B. Schofield, M. Robert de Saint Vincent, H. Tabuteau, Dynamics of pore fouling by colloidal particles at the particle level, *J. Membr. Sci.* 573 (2019) 411–424, <https://doi.org/10.1016/j.memsci.2018.12.025>.
- [12] N. Delouche, A.B. Schofield, H. Tabuteau, Dynamics of progressive pore clogging by colloidal aggregates, *Soft Matter* 16 (2020) 9899–9907, <https://doi.org/10.1039/D0SM01403F>.
- [13] T.E. Kodger, R.E. Guerra, J. Sprakel, Precise colloids with tunable interactions for confocal microscopy, *Sci. Rep.* 5 (2015) 14635.
- [14] G. Loy, A. Zelinsky, Fast radial symmetry for detecting points of interest, *IEEE Trans. Pattern Anal. Mach. Intell.* 25 (2003) 959–973, <https://doi.org/10.1109/TPAMI.2003.1217601>.
- [15] F.P. Preparata, M.I. Shamos, *Computational Geometry: an Introduction*, Springer Science & Business Media, 2012.
- [16] I.M. Yaglom, V.G. Boltyanskii, *Convex Figures* (Library of Mathematical Circle Volume 4), n.d. <https://www.biblio.com/book/convex-figures-library-mathematical-circle-volume-4/1034841221> (accessed December 19, 2020).
- [17] H.M. Wyss, D.L. Blair, J.F. Morris, H.A. Stone, D.A. Weitz, Mechanism for clogging of microchannels, *Phys. Rev.* 74 (2006), 061402.
- [18] A. Sauret, E.C. Barney, A. Perro, E. Villermaux, H.A. Stone, E. Dressaire, Clogging by sieving in microchannels: application to the detection of contaminants in colloidal suspensions, *Appl. Phys. Lett.* 105 (2014), 074101.
- [19] B. Dersoir, M.R. de S. Vincent, M. Abkarian, H. Tabuteau, Clogging of a single pore by colloidal particles, *Microfluid. Nanofluidics* 19 (2015) 953–961, <https://doi.org/10.1007/s10404-015-1624-y>.
- [20] S.S. Massenburg, E. Amstad, D.A. Weitz, Clogging in parallelized tapered microfluidic channels, *Microfluid. Nanofluidics* 20 (2016) 94, <https://doi.org/10.1007/s10404-016-1758-6>.
- [21] E. Spruijt, H.E. Bakker, T.E. Kodger, J. Sprakel, M.A.C. Stuart, J. van der Gucht, Reversible assembly of oppositely charged hairy colloids in water, *Soft Matter* 7 (2011) 8281–8290, <https://doi.org/10.1039/C1SM05881A>.
- [22] G.C. Agbanga, E. Climent, P. Bacchin, Numerical investigation of channel blockage by flowing microparticles, *Comput. Fluids* 94 (2014) 69–83.
- [23] J. Lohaus, Y.M. Perez, M. Wessling, What are the microscopic events of colloidal membrane fouling? *J. Membr. Sci.* 553 (2018) 90–98, <https://doi.org/10.1016/j.memsci.2018.02.023>.
- [24] T. van de Laar, S. ten Klooster, K. Schroën, J. Sprakel, Transition-state theory predicts clogging at the microscale, *Sci. Rep.* 6 (2016) 28450, <https://doi.org/10.1038/srep28450>.
- [25] R. van Zwieten, T. van de Laar, J. Sprakel, K. Schroën, From cooperative to uncorrelated clogging in cross-flow microfluidic membranes, *Sci. Rep.* 8 (2018) 5687, <https://doi.org/10.1038/s41598-018-24088-6>.
- [26] P. Bacchin, A. Marty, P. Duru, M. Meireles, P. Aimar, Colloidal surface interactions and membrane fouling: investigations at pore scale, *Adv. Colloid Interface Sci.* 164 (2011) 2–11.
- [27] G.C. Agbanga, É. Climent, P. Bacchin, Experimental investigation of pore clogging by microparticles: evidence for a critical flux density of particle yielding arches and deposits, *Separ. Purif. Technol.* 101 (2012) 42–48.
- [28] Z.B. Sendekie, P. Bacchin, Colloidal jamming dynamics in microchannel bottlenecks, *Langmuir* 32 (2016) 1478–1488.

- [29] V. Ramachandran, H.S. Fogler, Multilayer deposition of stable colloidal particles during flow within cylindrical pores, *Langmuir* 14 (1998) 4435–4444.
- [30] V. Ramachandran, H.S. Fogler, Plugging by hydrodynamic bridging during flow of stable colloidal particles within cylindrical pores, *J. Fluid Mech.* 385 (1999) 129–156, <https://doi.org/10.1017/S0022112098004121>.
- [31] G. Constant Agbangla, P. Bacchin, E. Climent, Collective dynamics of flowing colloids during pore clogging, *Soft Matter* 10 (2014) 6303–6315, <https://doi.org/10.1039/C4SM00869C>.

Supplementary

1-Deposition curves

We are able to provide deposition curves, i.e., the number of successive particles captured, singles or aggregates, against the number of particles that pass through the pore (Fig. 1) by counting each deposition event within the pore and determining the features of the deposited objects and also the number of particles that flow through the pore between each deposition event.

Clearly the shapes of the deposition curves are not the same. However, most of the time single particles are first captured by the pore wall even though very few aggregates can also deposit. During the clog formation, the rate of particles passing through the pore is not constant and there are moments where a considerable number of particles passes through the pore between two deposition events, while for other moments this number is much smaller and thus the clog formation is more “continuous”. This rate of deposition is directly linked to degree of local fouling of the pore cross section and also to the type of object that deposit.

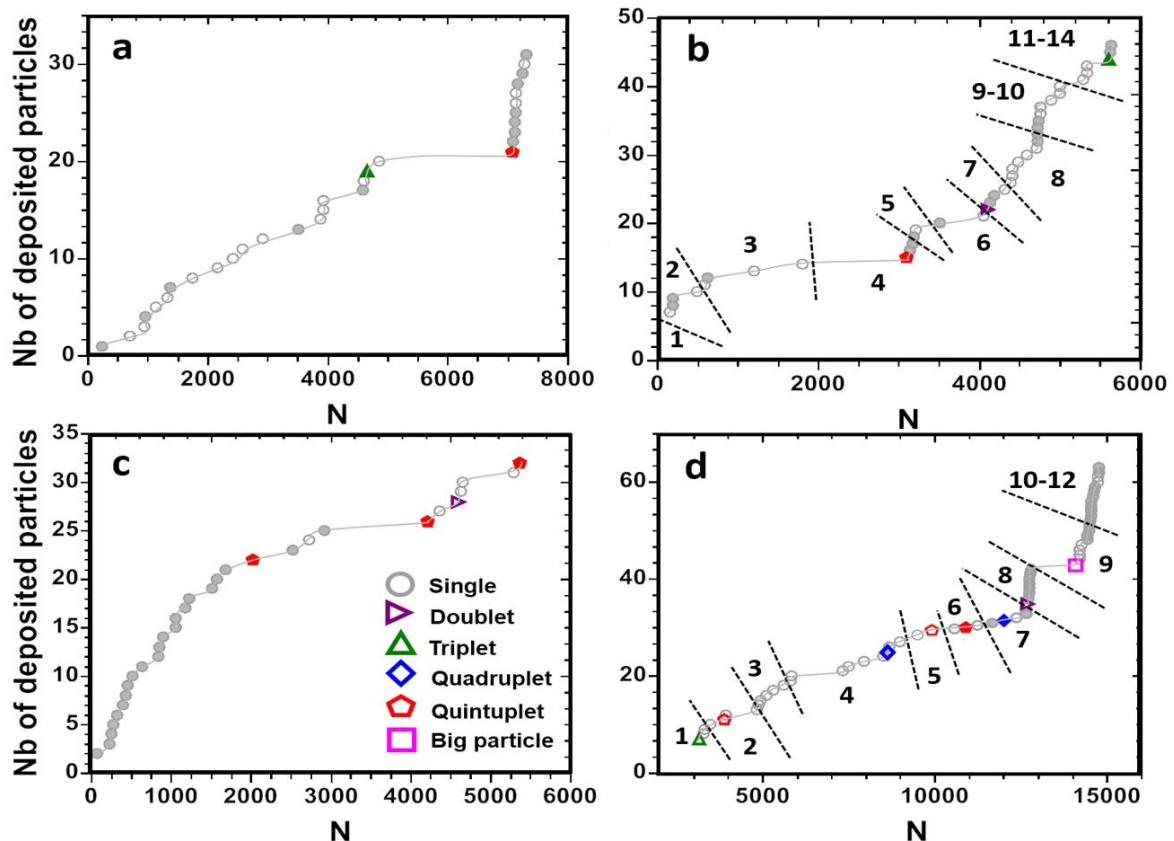


Fig. 1: Deposition curves for the 1st (a-b) and the 2nd clog scenario (c-d). The full symbols correspond to the objects that contribute to the clog since they are captured exactly where the clog eventually blocks the pore, while the open symbols are the objects that do not contribute directly to the clog, their deposition taking place elsewhere within the pore, where the growth of the deposit on the pore walls remains limited. The term “large aggregate” in the legend corresponds to aggregates composed of 6 particles or more. The images of the clog formation corresponding to the plots b and d are shown in figure 4 and 5, respectively. Each image number in these figures are related to the different zones of the deposition curves labelled by a number and delimited by oblique dashed lines. The continuous line on each plot are guides to the eyes.

In the 1st plot, (a), few single particles are captured when a triplet deposits. This aggregate helps capture a larger one whose deposition reduces the local pore cross section significantly enough to allow the capture of single particles up to the complete pore blocking. We observe a similar succession of deposition events in 3rd plot, (c), in which there is much deposition of single particles prior to the capture of the first aggregate, a quintuplet. In this case the pore is completely blocked by another quintuplet rather than by the successive deposition of single particles. Consecutive images in figures 4 and 5 in the main text help understand the deposition curves in the plots b and d respectively.

2-Evolution of the repartition between the two clogging categories with the flow conditions

We determine how the separation between the two clogging categories depends on the flow conditions for PMMA particles. We have seen that there are two clogging regimes when we look at the evolution of N^* with Q . In the 1st clogging regime, $0.008 < Q < 1 \mu\text{l}/\text{min}$, N^* is constant and roughly equal to 2000 particles, a value high enough to observe several aggregates flowing through the pore according to the particle size distribution (Fig. 2, top). In this first clogging regime clogs mainly belong to the first category (sup. Fig. 2, top-left). For $Q < 0.15 \mu\text{l}/\text{min}$ the average number of deposited aggregates is constant, irrespective of the aggregate size (sup Fig. 3a) and for $0.15 < Q < 1 \mu\text{l}/\text{min}$ the number of objects, larger than triplets, slightly increases while that of the smaller ones falls. In this later Q range, the detachment by the flow of doublets and triplets increases with Q while it does not affect larger aggregates (sup Fig. 3c). This means that the average size of the deposited aggregates increases with Q (sup Fig 3d). Note that there is often detachment of single particles from the pore wall in this first regime, more particularly at the end of the clogging process, where the remaining cross section of the pore is small and thus the local shear rate is high, which favors particle detachment (sup Fig. 3b and f).

In the 2nd regime, for $Q > 1 \mu\text{l}/\text{min}$, there is first a fivefold increase of N^* followed by a smoother increase of N^* with Q (Fig. 3a, top left). Almost all the clogged pores belong to the second category. The consecutive deposition of large aggregates involves less capture of smaller objects, from single up to triplet (sup Fig. 3a). It is worth mentioning that there is lower capture probability for all types of aggregate, still due to flow erosion. In addition to the lower capture probability, the number of detachment events of single particles or of part of the deposit increases with Q (sup Fig. 3f). Even if large aggregates have more contact points with the deposit the local shear rate is sufficient to detach them from $Q > 1 \mu\text{l}/\text{min}$.

Finally, we note that the clog formation is rather irreversible for both regimes since there is only a few percent of de-clogging events (sup Fig. 3e). Moreover, the structure of the deposit that accumulates on the pore walls does not evolve over time significantly since we observed local particle/aggregate rearrangements only for 15 to 20% of the clogs as they built-up (sup Fig. 3e). All together these results suggest that the main difference between the two clogging regimes is the influence of the erosion at higher flow rates which prevents the deposition of single particles and doublets-triplets and also to a lesser extent of larger aggregates. This erosion thus leads to an increase of N^* in the 2nd regime since the clogging process mainly relies on large aggregates that are less numerous. Indeed, to block the pore in this regime few large aggregates are needed which is confirmed by the increase of the aggregate dimension and also the number of particles per aggregate with Q (sup Fig. 3d and g).

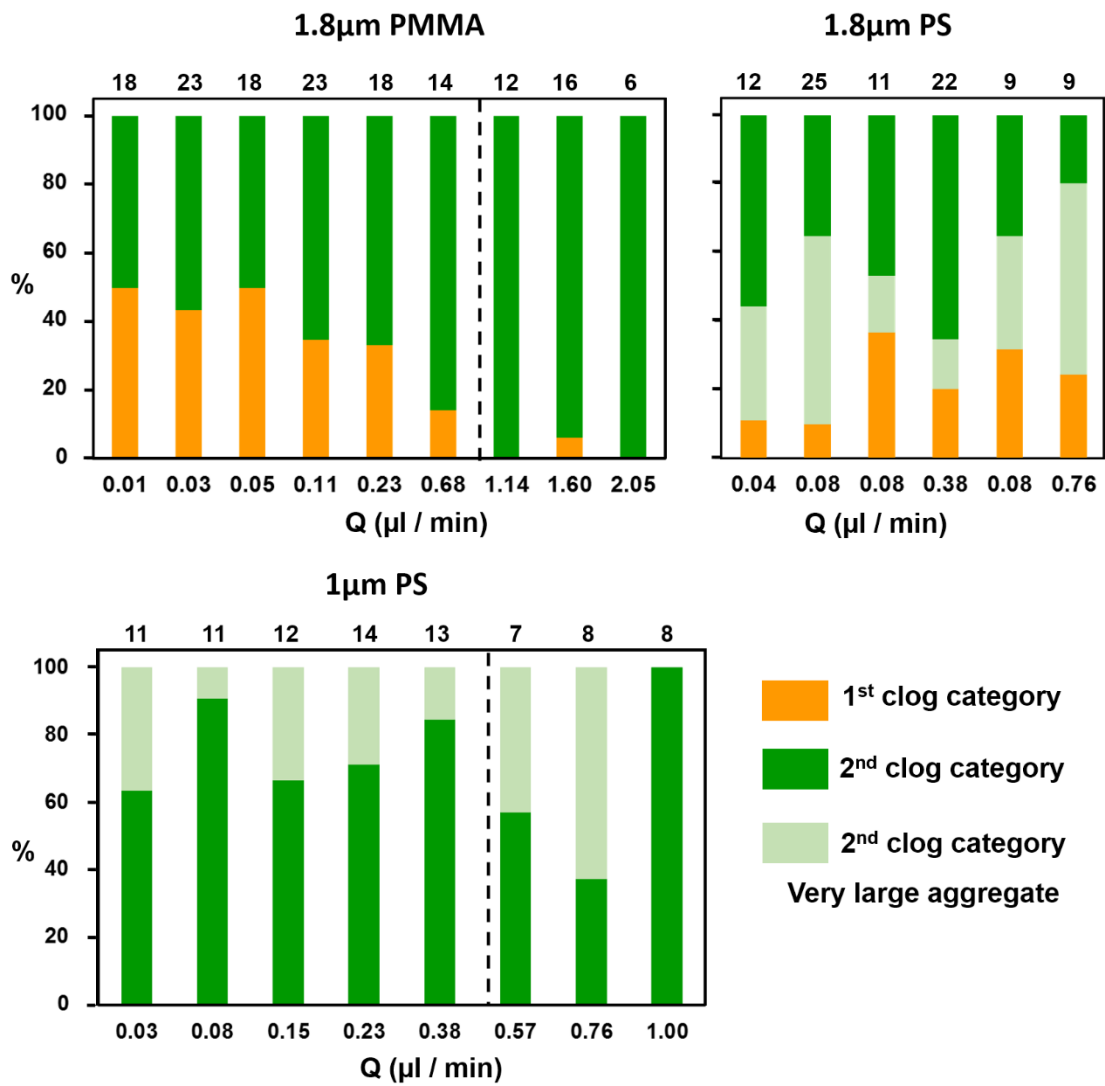


Fig. 2: Repartition of the clog experiments between the two categories for the 1µm PS (bottom), 1.8µm PMMA and PS particles (top) in the different flow conditions. The number of trials for each flow rate value is indicated at the top of the graphs. For 1µm and 1.8µm PS particles we make the distinction inside the 2nd category between the aggregates with $L_{max} > W$ and the very large aggregates that are sieved at the pore entrance.

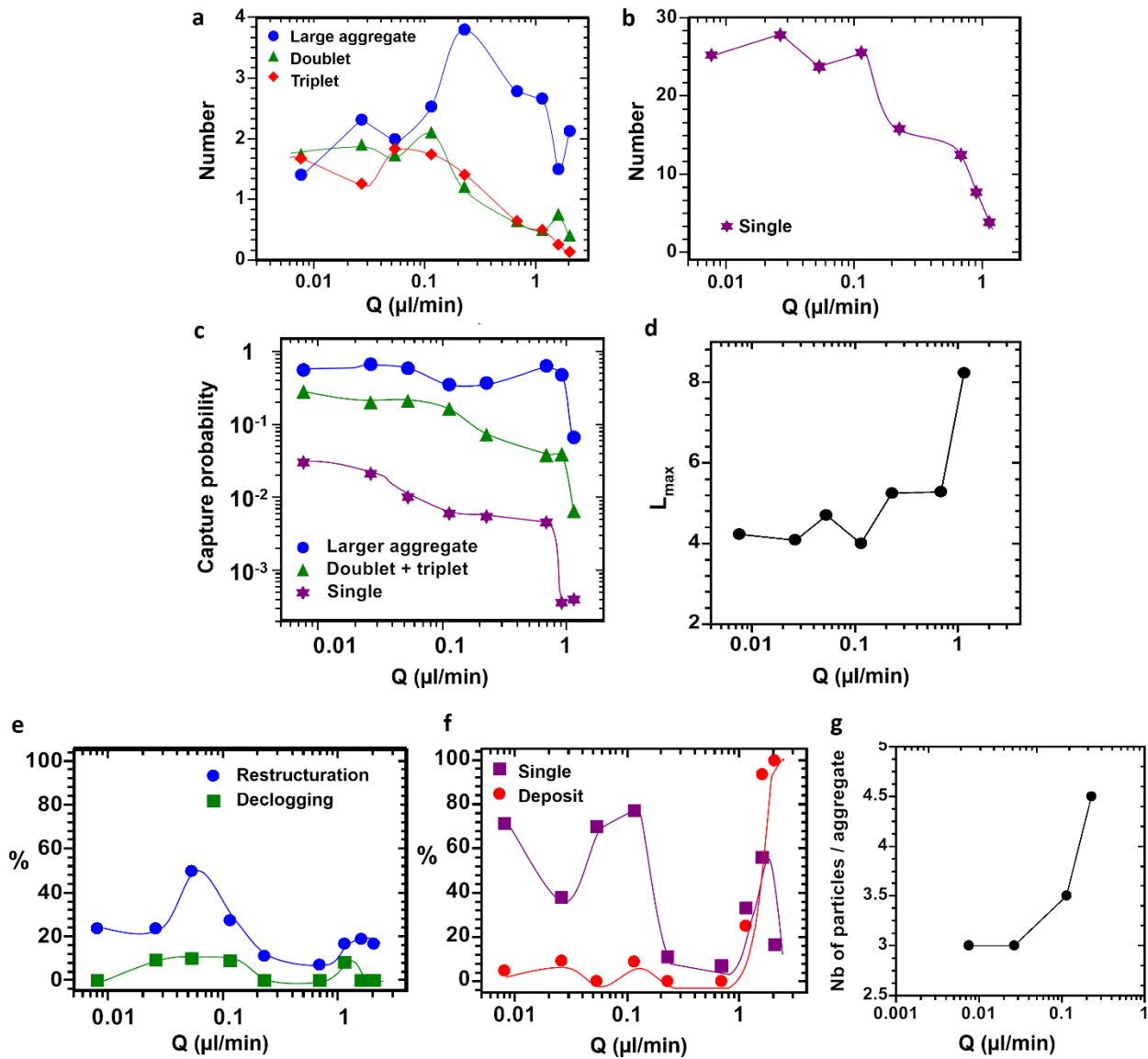


Fig. 3: (a) Average number of aggregates of the different types with different sizes that deposit in the pore during one experiment. (b) Average number of single PMMA particles that deposit in the 1st 20 μm of the pore during one experiment. (c) Capture probability of the different types of PMMA particles of the suspension with the flow rate. (d) Variation of L_{\max} with Q . (e) Percentage of experiments in which there is a detachment event of a single particle or of a part of the deposit. (f) Percentage of experiments in which there is a restructuring/rearrangement inside the deposit or a de-clogging of the pore. (g) Variation of the average number of particles per aggregate with Q . All the continuous lines on the plots are guides to the eyes.

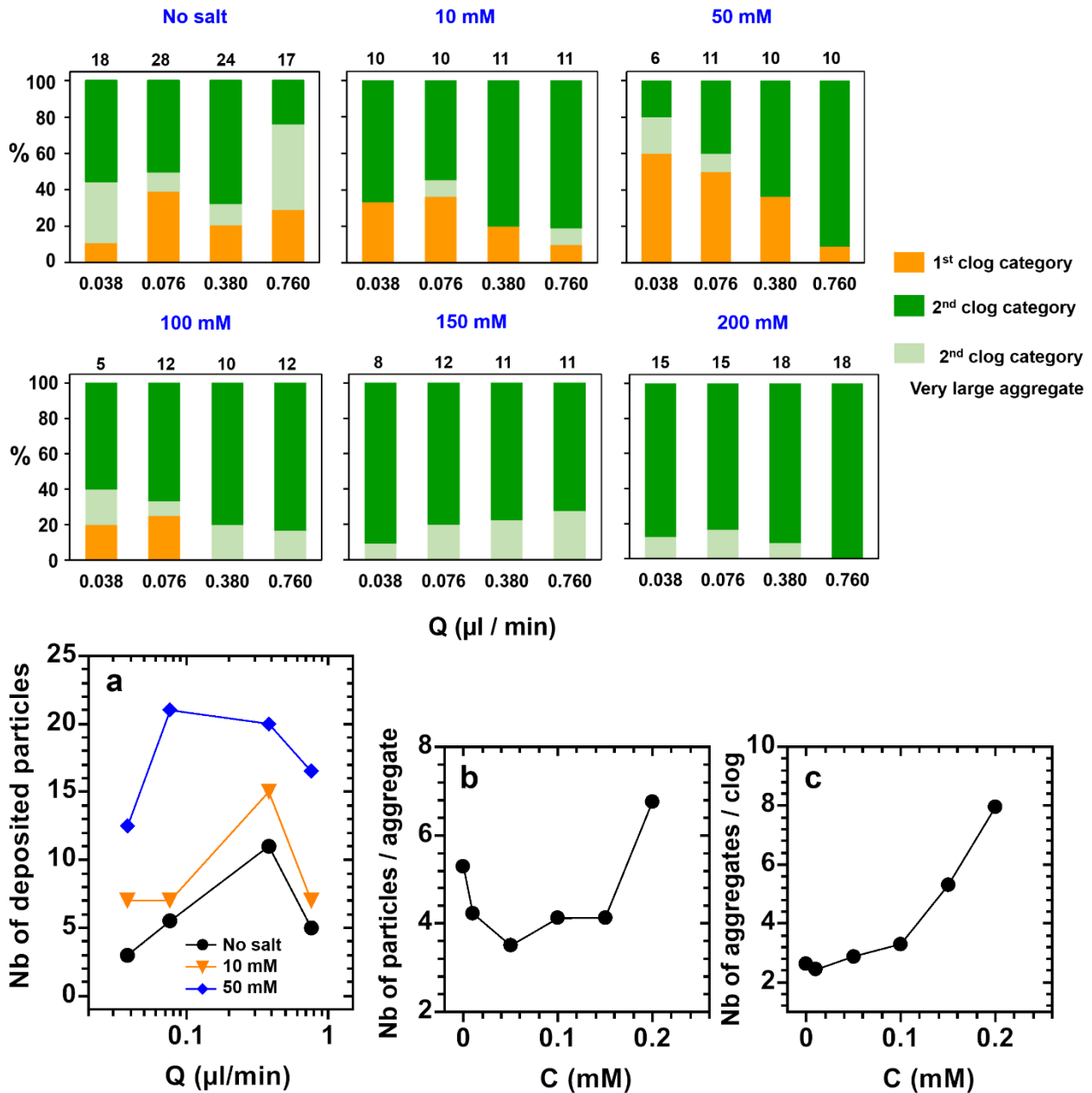


Fig. 4: (Top) Comparisons between the clog experiments for the two clog categories for the 1.8 μ m PS dispersed in solutions with various amount of NaCl salt. The number of trials for each flow rate value is indicated at the top of the graphs. With no salt added most of the clog belong to the second category (top left), with more than 70% of the clogs. For $C=10$ mM, even though the surface charges of the pore walls are not completely screened, the particle deposition is enhanced compared to the salt free case (a), favoring the formation of clog of the 1st category, (top middle). This trend is inverted when the flow rate increases and the 2nd clog category becomes the dominant one. This is due to the lower probability of deposition for the smaller aggregates, with these being more easily wiped off by the flow. A similar decrease of the population of the 1st clog category with Q is observed for $C=50$ mM, concentration for which the surface charge of the PDMS is totally screened (top right). However, for this salt concentration the second clog category remains dominant for the overall range of Q . The 1st clog category becomes even more restricted to the lower flow rates for $C=100$ mM (bottom left). The decrease of the number of clogs of the first category with Q is mainly due to the erosion of the smaller aggregates by the flow while the larger ones are less eroded (a). Closer to the CCC of the suspension from $C=150$ mM, clogs belong to the 2nd category (bottom middle and right), indicating that there are always large aggregates within the clogs. The number of clogs that involve aggregates larger the pore width, also increases with the salt concentration. From $C=100$ mM up to 200mM, around 20% of the clogs are mainly composed of one of these large objects, whatever the flow rate (b). (Bottom) (a) Average Number of single particles deposited in a pore for suspensions of 1.8 μ m PS particles with various amount of NaCl salt. (b) Average number of particles inside the aggregates that form the clogs with the salt concentration C . (c) Average number of aggregates inside a clog vs. C .

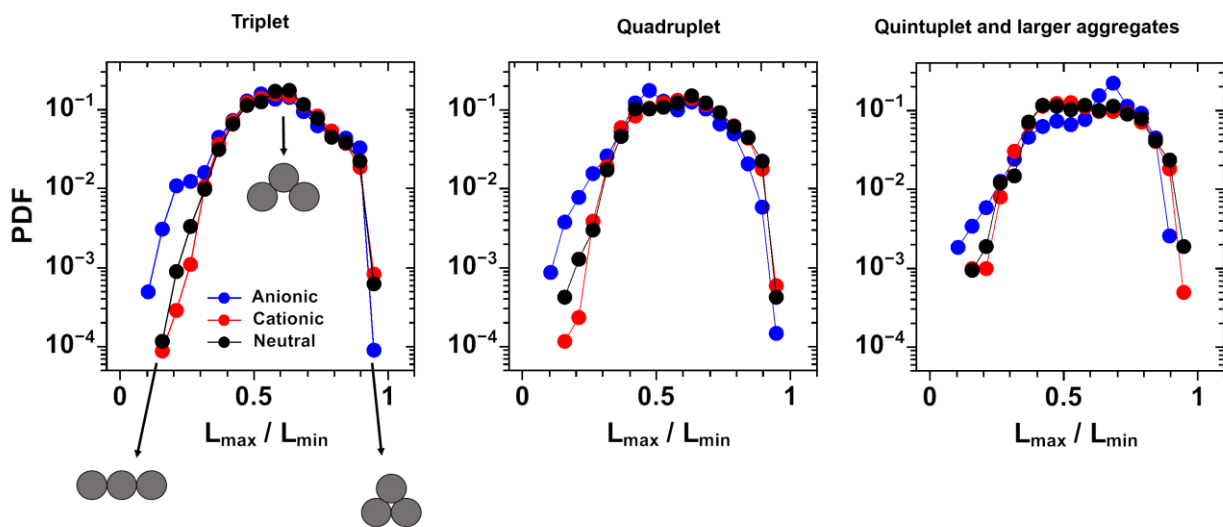


Fig. 5: Probability density functions of the aspect ratio L_{max}/L_{min} for triplet (left), quadruplet (middle) and quintuplet and larger aggregates (right) for the different PS coated dispersions. Shapes of triplet corresponding to various aspect ratios (left). The median value of the aspect ratio is equal to 0.6, irrespective of the aggregate and suspension type.

Chapter 4

The flow decline during the pore clogging

It has long been recognized that during the filtration process with a membrane, a large flow decline occurs if the membrane becomes fouled. There is currently no *in-situ* study based on images and deposition history of the membrane, even though access to these information could increase the efficiency of filtration operations by optimizing membrane backwashing or membrane replacement. With microfluidics, it has become possible to study individual pores of a membrane. However, no flow rate sensor can measure with a high acquisition rate and enough accuracy the small flow variations that take place when particles deposit in the pore. Here, we propose an *in-situ* measurement based on particle tracking, with which we determine the variations of flow conditions from particle velocities while simultaneously visualizing formation of the deposit. We monitor the variation of the flow conditions for particles of different types and natures, taking into account the presence of aggregates in the clogs. From experimental data, we perform numerical simulations to determine the flow inside a clog during its formation. We show that two phenomena are at the origin of the velocity decline i) the pore obstruction which induces a strong velocity drop and an accumulation on a few particles behind the clog head which also induces an important velocity drop and ii) followed by an important accumulation of particles that has a small contribution to the decline. The results of this chapter have been submitted for publication to Physical Review Fluids.

Contents

4.1	Two phases during the flow decline	110
4.2	A section reduction plus a progressive flow paths closure	110
4.3	From a heterogeneous to a homogeneous flow	112
4.4	Brief summary of the paper	112

4.1 Two phases during the flow decline

We measured the instantaneous velocity drops for particles of different sizes. The flow decline can be separated into two consecutive phases, for all the suspensions and the experimental conditions we have tested. In the phase I, as the pore cross-section is reduced up to its complete obstruction and later on when a few particles accumulate over about $10\mu\text{m}$ behind the clog head, we observed a sharp velocity decline (figure 4.1 green rectangle). The shape and amplitude of this velocity drop depends on how the particles are deposited or stacked. In the phase II, the flow rate keeps up decreasing as particles accumulate behind the clog, but much less rapidly (figure 4.1 blue rectangle). At this stage the particle velocity is inversely proportional to the length of the clog corresponding to a Darcy's flow inside the clog.

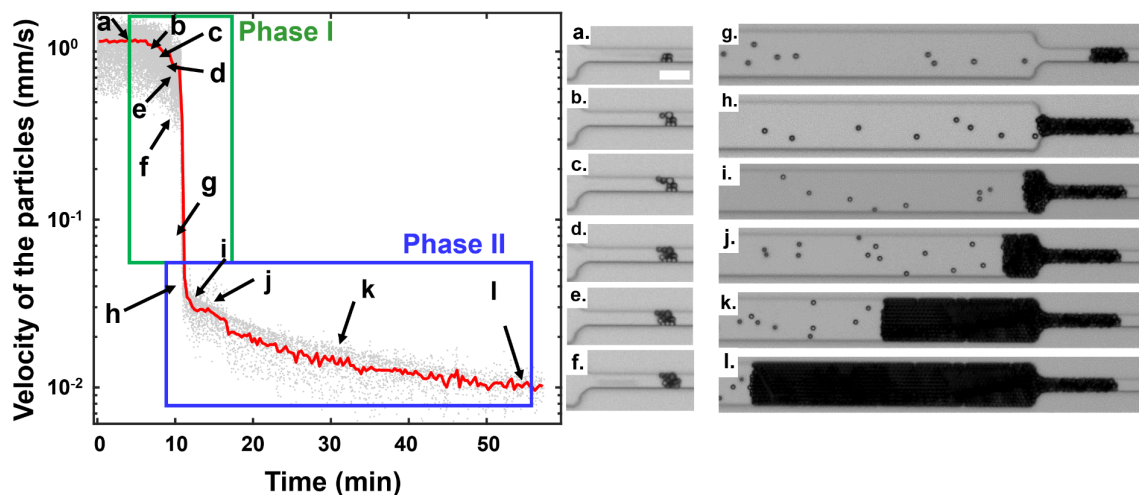


Figure 4.1: (left) Variation the particles velocity for $2\mu\text{m}$ PS particles over time. Gray dots and the red line correspond to the instantaneous particle velocities and the mean velocity, respectively. Each alphabetic label corresponds to an image on the right panel. (right) Serie of images in the two phases. Scale bar: $10\mu\text{m}$

4.2 A section reduction plus a progressive flow paths closure

To better understand how the accumulation of particle impacts the flow inside the clog and how emerge those two phases, we simulated the flow at each step of the clogging. From clogging experiments with $3\mu\text{m}$ PS particles and thanks to the low channel height ($8\mu\text{m}$), we find the position (x,y,z) of the particles during their accumulation. With these positions, we simulated with Comsol the flow in the clog structure each time a new particle deposits. As in the experiments, there are two distinct phases during the flow decline (figure 4.2). In phase I, the reduction of cross section and the obstruction of the pore take place with 4 particles and induce a strong flow decline. Thereafter, particles continue to accumulate and significantly decrease the flow rate, as much as during the obstruction process. In the phase II, the velocity drop is very low.

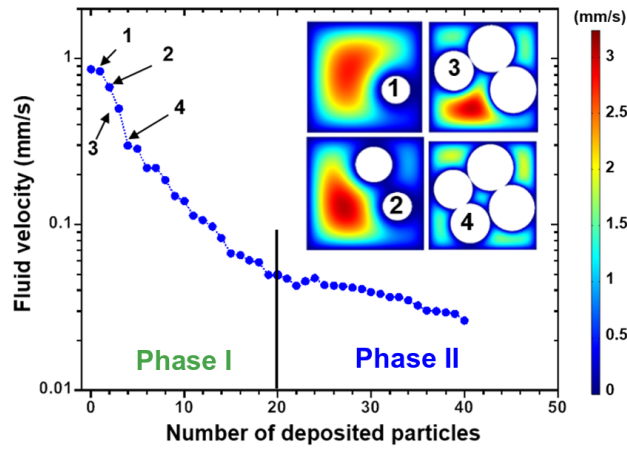


Figure 4.2: The drop in velocity of a clog formed with $3\mu\text{m}$ PS particles reconstructed with Comsol, with the two phases. The images correspond to the four consecutive particle deposition leading to the complete obstruction of the pore.

To understand the difference between the accumulation in phases I and II, one must take into account the evolution of the preferential flow paths. Just after the clogging, when a particle come, its block one of the 5 paths (figure 4.3 left). The particle increases the tortuosity of the accumulation and thus the local hydrodynamic resistance (Phase I on figure 4.3 right). Since all flow paths have a different hydrodynamic resistance, there is a partial redistribution of the flow inside the accumulation and the creation of one or more flow paths. During the accumulation in phase II, all the flow paths have almost the same hydrodynamic resistance. Now, when a new particle is deposited, the velocity drop is homogeneously distributed in all the pores of the section (Phase II on figure 4.3 right).

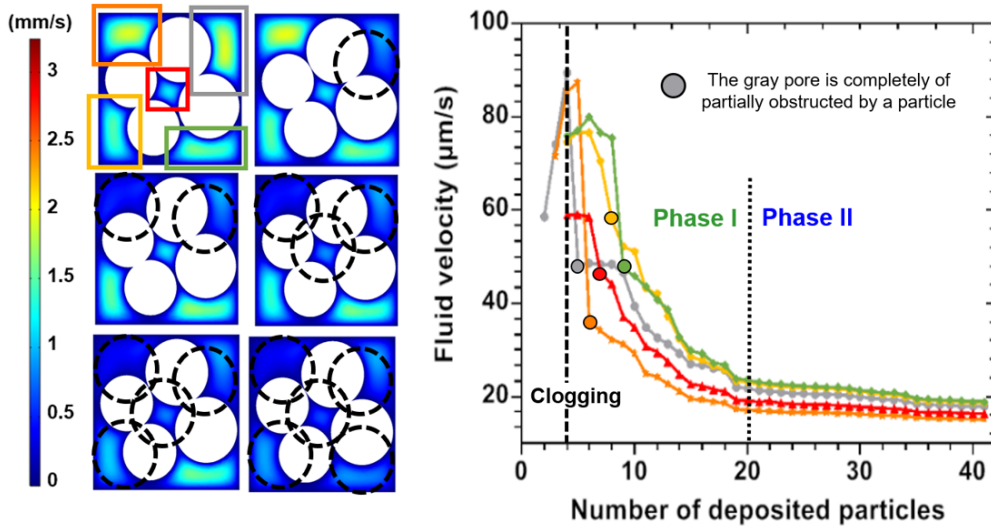


Figure 4.3: (left) Blockage of the 5 preferential flow paths just after the obstruction of the pore. The dotted black circle indicated the position of new particles, deeper in the channel. (right) Flow decline inside the 5 pores. The coloured circles indicate when a pore is partially or completely blocked with a new particle.

4.3 From a heterogeneous to a homogeneous flow

For a lower confinement than in the previous part, more particles are involved and lead to a more complicated clogging process. We reconstructed a $1.8\mu\text{m}$ PMMA particle clog from data obtained from confocal imaging provided by Benjamin Dersoir. It is not possible to have dynamic data but the confocal allows to obtain the structure of a clog composed by 400 particles and to simulate the flow through it, from which we are able to determine the local particle volume fraction, the number of pores per cross section and their average diameter.

Beyond the clog head (6-7 μm), we observe a decrease in the average pore diameter and an increase in the number of pores. This leads to an increase in hydrodynamic resistance and causes a the sharp decline in phase I. The composition of the clog head is very heterogeneous because of the presence of aggregates and 50% of the flow follows between 1 and 3 different paths (figure 4.4). The particle volume fraction inside the clog is low, about 32%, indicating that the pore is far from being filled. After 20 μm of accumulation, the flow distribution becomes constant: 50% of the flow is contained in a wide single path (figure 4.4), corresponding to the phase II, which still has a small contribution to the overall flow decline.

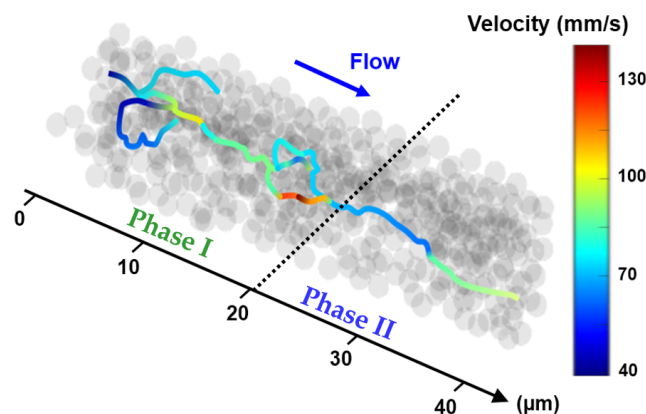


Figure 4.4: Flow paths inside the clog inside which 50% of the fluid flows.

4.4 Brief summary of the paper

Flow decline during pore clogging by colloidal particles

Objective: monitor the flow decline inside a pore, from the partial fouling up to the complete clogging, coupling the dynamics of clogging with particle tracking and the structure of clog with pore imaging.

- Whatever the experimental conditions, the flow decline has two phases:
 - Phase I: a sharp decline due to the clog head formation and an accumulation of particles only over few layers.
 - Phase II: a small flow variation when the particle accumulation is significant.
- From the simulation of the flow inside the forming clog we were able to show that the redistribution of the flow paths is responsible of an important part of the flow decline.

Flow decline during pore clogging by colloidal particles

N. Delouche^a, B. Dersoir^a, A.B. Schofield^b and H. Tabuteau^{a,*}

^a Univ Rennes, CNRS, IPR (Institut de Physique de Rennes)-UMR 6251, F-35000 Rennes, France

^b School of Physics and Astronomy, The University of Edinburgh, The James Clerk Maxwell Building, Peter Guthrie Tait Road, Edinburgh, EH9 3FD, UK

(Dated: July 22, 2021)

Abstract

The flow of colloidal suspensions through porous media often leads to the deposition of particles inside the pores which increases the local hydrodynamic resistance by narrowing the pore space available and modifying the flow path of the transported particles. There is a significant flow decline in the extreme case when the entire porous medium becomes clogged. However, there are no experimental studies that determine directly the amplitude of this flow decline when compared with the dynamics of the formation of the particle deposit. This is mainly due to the great challenge of gaining experimental access to the features of the internal structure of the deposit as it grows and thus the ability to determine the flow inside it. In this paper, we show that it is possible to monitor the flow decline corresponding to the successive deposition of colloidal particles inside a constriction/pore, ending by its complete blocking. The variation of the flow is determined by the measurement of the velocity of the particles through our channel. Such a technique coupled to the precise knowledge of what is deposited inside the pore, thanks to image analysis, enables us to determine the different contributions to the flow decline. We also use numerical simulations to access the flow inside the porous structure of the deposit as it grows. Together, experiments and simulations demonstrate that the obstruction process and the subsequent limited growth of the clog, corresponding to a few layers of accumulated particles, have a higher impact on the amplitude of the flow decline than the extra growth of the clog.

* herve.tabuteau@univ-rennes1.fr

I. Introduction

Most of us have experienced the decline in flow associated with the clogging of kitchen and bathroom strainer sinks. As pieces of food, hairs, or other types of small debris are transported by water towards the grid that composes the strainer they start to accumulate and the flow rate suddenly decreases. This flow decline also occurs in many other situations when suspensions of smaller particles, i.e., colloidal particles, flow through porous structure like filters[1], nozzles of inkjet printers [2], irrigation drippers [3] microfluidic devices [4] , chemical reactors [5,6], soils [7,8] and fractured rocks [9] where they can also be coupled to seismic events [10,11]. The permeability reduction of a porous media due to particle deposition is highly dependent on the stability and the size of the colloidal suspension and can reach three orders of magnitude with nanoparticles [12–14]. However, from these previous works we cannot determine the relative contribution to the flow decline at the pore or the particle scales, since the pores are interconnected. Indeed, we do not know to what extent the progressive fouling of adjacent pores is coupled. In addition, we cannot follow the capture or deposition of colloidal particles over time inside these pores in order to monitor the growth of the clog. Microfluidic experiments with transparent model porous media, coupled with various imaging techniques, have provided important information on the dynamics of the clog formation in such conditions. Some of these experiments helped define for which pore geometries [15,19], degree of confinement [4,15–18] and flow [4,15,19] pore clogging occurs, while others focused on the geometrical features and size of particles that compose the clog [20–23]. Only a few studies have simultaneously monitored the dynamics of clog growth and the variation of the flow conditions [4,24]. Sauret *et al.* performed clogging experiments with a single pore and have determined the permeability of a forming clog after it was well developed, knowing the volume of the clog and the particle volume fraction, and using the Carman-Kozeny relationship [24]. With their measurements they were unable to capture the strong variation of the permeability at the very beginning of the clogging process, when the pore cross section is first completely blocked. They supposed that the permeability of the clog head is high and does not contribute significantly to the hydrodynamic resistance of clog as it grows. Thus, up to now, nobody has measured the flow decline associated with the early moment of the clog formation. This partly comes from the fact that such measurements require simultaneous imaging of the deposition of particles that compose the forming clog and monitoring of the flow variations inside the pore. While the former experimental constraint can be easily meet by using high frame rates [15,18] the latter is really challenging since there is no flow sensor accurate and fast enough to measure such important brief flow variations at the pore scale. It would be beneficial to perform such measurements to

detect the early stage of clog formation as this information may be used to prevent their subsequent growth. This is particularly important in industrial filtration operations where the amplitude of the flow decline directly impacts the stoppage of the filtration process by giving information about when the filter should be cleaned or replaced [25].

In this paper we describe the clogging transition in a single pore by imaging the forming clog and tracking the colloidal particles transported by the fluid through the pore. This enables us to determine the variation of the flow conditions and the nature and type of particles that compose the clog. We consider the influence of the confinement and the composition of the colloidal suspensions. We also perform numerical simulations of the flow within a forming clog and inside one that has stopped growing to better understand the flow variations corresponding to the clogging transition. We show that three consecutive phenomena contribute to the flow decline associated with the clogging transition. First, there is a sharp flow decline due to the progressive narrowing of the cross section of the pore/channel, up to its complete obstruction. The magnitude of this first flow decline increases when the particle size used to construct the clog decreases as the mean pore size between the particles is smaller. After this initial obstruction event, the subsequent accumulation of a few layers of particles causes the average fluid velocity to decrease significantly as some of the remaining preferential flow paths through the clog are progressively closed. This closure process forces the fluid to flow on average through narrower pores which increases the hydrodynamic resistance of the clog. Finally, further growth of the clog leads to the smallest contribution to the flow decline, even for long clogs, and the fluid velocity is proportional to the inverse of the clog length, a characteristic of Darcy's flow.

II. Materials and methods

The soft lithography methodology used to make our model microfluidic filter and their geometrical features are identical to those of used in Delouche *et al.* [21,22]. Briefly, we design two types of model filters with the same height and width equals to $8\mu\text{m}$ to determine experimental the flow decline thanks to the particle velocity. Particles first flow through a unique and wide channel before entering either in a single narrow zone or several identical ones in parallel with a width $W=8\mu\text{m}$. For each narrow zone there are two consecutive reservoirs followed by a $120\mu\text{m}$ long pore, the narrowest part of the filter in which clogs form (figure 1). The two reservoirs are long enough to perform particle tracking and obtain the particles velocity using a sensitive camera (Hamamatsu Orca Flash 4.0 v2). We also used another similar model filter for the confocal imaging with a rectangular cross section, the width and the height of pore

being equal to 9 and 11 μm , respectively. We bond the PDMS channel on a glass slide covered by a thin layer of PDMS to ensure that particle-surface colloidal interactions are identical everywhere on the pore surface. The suspension is injected in the filter by applying a difference of pressure with a regular pressure controller (Elveflow OB1 Mk2 or Fluigent MSFC). A flow sensor (Fluigent, 5% accuracy) is used to determine the corresponding flow rates at the beginning of the experiments. Fluid inertia is negligible with Reynolds numbers for the different flow conditions always smaller than 10^{-3} . We used either home synthesized fluorescent PMMA particles with a 1.8 μm diameter and stabilized by a polymer brush [21] or 1.6 μm and 3 μm PS particles with sulfate groups at their surface bought respectively from Thermofisher (Life, USA) and Microparticles GmbH (Germany). We used different aqueous mixture to obtain isodense suspension to negate particle sedimentation inside the channel. The distributions of particle size and particle type, single particles or aggregates of various sizes, for each suspension are determined during “stop and go” experiments [22]. Such experiments allow us to see that there is 6.7 10^{-3} % of large particles in the 1.6 μm PS suspension. The particle size and type distributions of the 1.8 μm PMMA are provided in Delouche *et al.* [21].

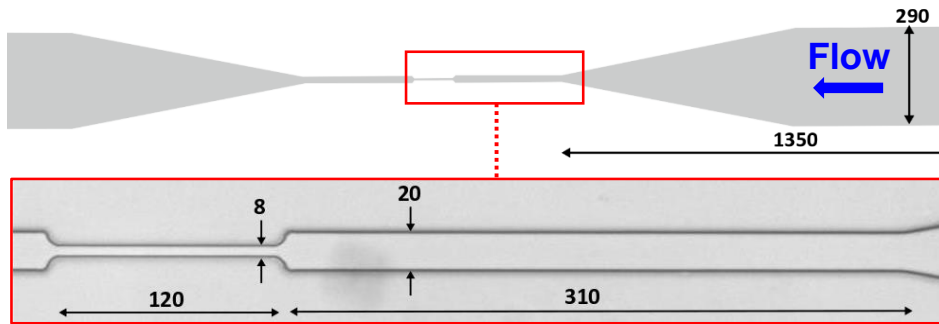


Figure 1: Geometrical features of the single channel experiment. All dimensions are in microns. The channel is generally clogged in its narrowest part and the particle velocities are determined in the long reservoir zone just upstream of this.

The flow decline corresponds to successive particle depositions within the pore zone. The deposition of particles leads to an increase of the hydrodynamic resistance of the channel, and since we work with a fixed pressure there is a flow rate decline and a decline in the particle velocity. Unfortunately, regular methods like flow meters or the weighing of the liquid that flows out of the filter, are not able to provide accurate measurements of such small variations of the flow conditions. To circumvent this issue we decided to perform in-silico measurements of the flow rate variation thanks to the velocity of the particles. In our flow conditions, with low Reynolds number smaller than 10^{-3} and Péclet Number between $4 \cdot 10^5$ and $1.8 \cdot 10^4$, particles follow fluid streamlines and act as flow tracers.

We are able to track all the particles that flow through the pore with a moderate frame rate of 100 frames per second. The determination of the particles velocity is made in the reservoir, upstream of the pore, thanks to particle tracking. We also capture the deposition of particles inside the pore by image analysis. We calculate the average particle velocity from the instantaneous velocity of 100-2000 particles, depending on the particle type, prior to the pore completely blocking while we use only 30-50 particles after the pore clogging with a particle volume fraction of the feeding suspension equal to $5 \cdot 10^{-4}$. In this latter condition, since we average over a lower number of particles we also have a lower precision on the average particles velocities. The variation of the imposed pressure, which is about 0.2mbar, also induces an uncertainty of the particles velocity. These two effects taken together lead to an error in the particle velocity of $10\mu\text{m/s}$. We determine the flow conditions inside the channel more or less filled with particles thanks to finite element software (Comsol). For the clog formed with $3\mu\text{m}$ PS particles we used the positions of the particles inside the clog as determined by bright field microscopy. We have a precision of $0.4\mu\text{m}$ for the particle center in the XY plan, i.e. along the flow direction. We are also able to determine the approximate position of the particles along the height of the channel due to the high confinement of the $3\mu\text{m}$ particles in $8\mu\text{m}$ by $8\mu\text{m}$ cross section. Indeed, there are only two to three particle layers along the height, a particle being either close to the top or the bottom horizontal surface or somewhere near the middle height. We end up with a maximum of $1\mu\text{m}$ for the particle center along the channel height. For the clog formed with $1.8\mu\text{m}$ PMMA particles we used confocal microscopy to obtain a more accurate 3D location of the particle centres with a precision of 50nm. For the $3\mu\text{m}$ PS and the $1.8\mu\text{m}$ PMMA particles we determine the flow condition each time a new particle deposits in the channel, using the steady-state Navier-Stokes model. No-slip boundary conditions are applied on the channel walls. We also impose the same pressure gradient used in the experiments and we take into account that the fluid viscosity is slightly higher than the water viscosity. We determine the flow rate over the entire clogging process in the same cross section, located downstream of the particle accumulation, and then calculate the corresponding mean velocity of the fluid in this section. We perform the same kind of simulation for the $1.8\mu\text{m}$ PMMA particles but we add ten particles at a time instead of one before determining the flow conditions across the clog

III. Results

A. Flow decline measurements

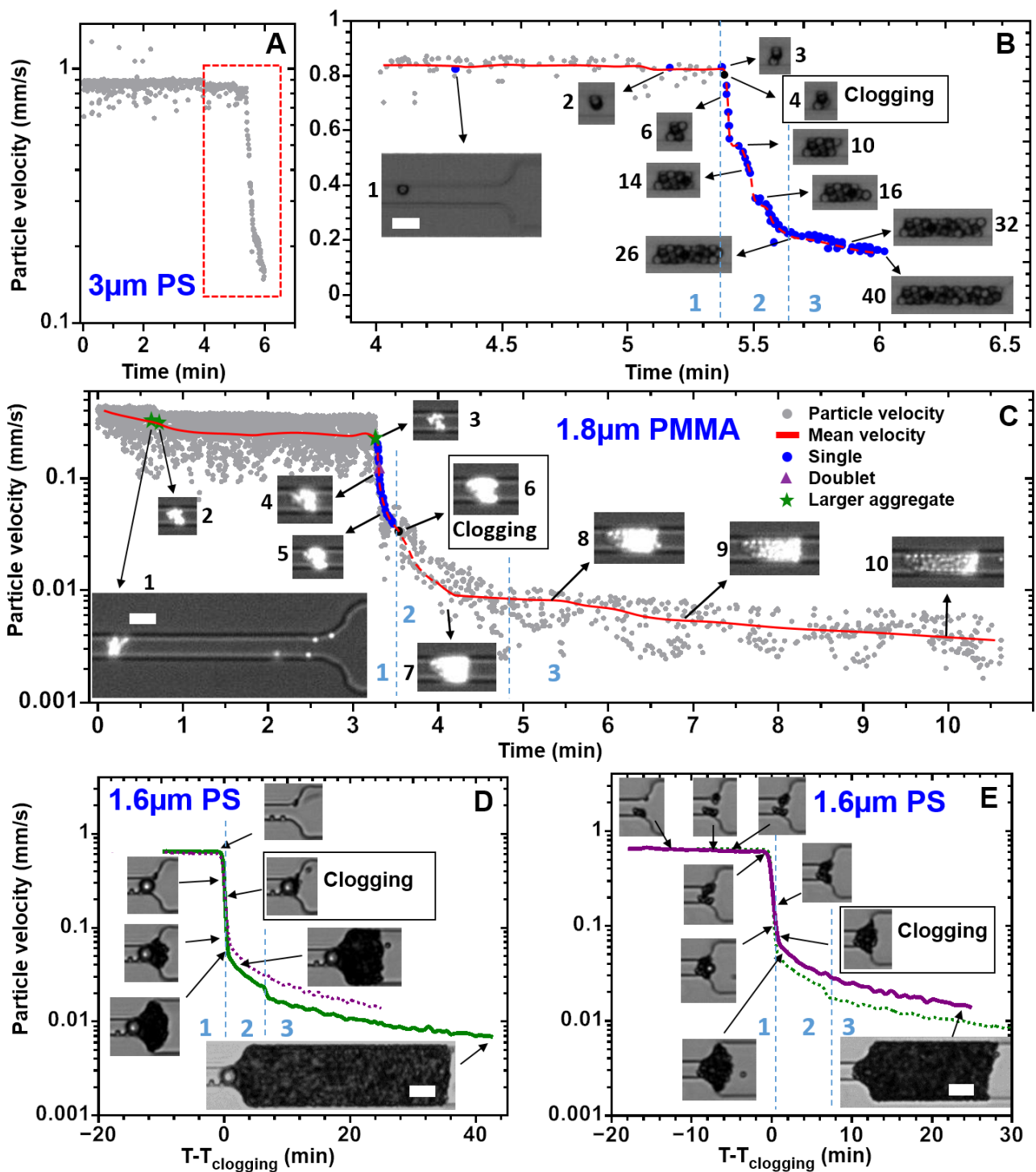


Figure 2: (A) Instantaneous velocity of all the 3 μm particles flowing towards the pore with an applied pressure of 7mbar. (B) Close-up on the clogging transition (dashed rectangle in the left graph). Blue dots correspond to the events of particle deposition while the continuous and dashed lines are respectively the average particle velocity and a guide of the eyes. The dark dot corresponds to the last particle that effectively blocks the pore. For each image we give the number of particles that compose the clog at that moment. (C) Variation of the instantaneous particle velocity for 1.8 μm particles over time, with the same definition for the symbols, the continuous and dashed lines. The applied pressure is equal to 3mbar. The first four images labelled with a number correspond to the deposition of an aggregate. The term “large aggregate” means that the aggregate is composed of at least three particle. Nineteen individual

particles are captured where the clog is formed in addition to a doublet and three large aggregates. (D-E) Evolution of the Mean particle velocity for 1.6 μm particle suspension also composed of few larger particles. The applied pressure is equal to 3mbar. For each graph the images are related to the continuous line. The dotted line in the left corner graph is the continuous line used in the right corner graph and vice and versa. All the scale bars correspond to 10 μm and the image of the complete obstruction of the pore is outlined by a black rectangle. The three stages of the flow decline are separated by two vertical dashed lines in B to E.

We first look at the general features of the flow decline during the clogging of a single pore with various types of colloidal suspensions. The variation of the flow decline over time is rather similar irrespective of the type of suspension and can be separated into three stages (Fig. 2). There is first a sharp decline of the flow corresponding to the complete obstruction. The shape of the flow decline curve in this step is highly dependent on the way the first particles pile up and clog the pore, particles that can be identical (Fig. 2A), be a mixture of aggregates and single particles (Fig. 2C) or a mixture of big and small ones (Fig. 2D-E), all these examples corresponding to most of the common cases of the pore clogging. In the highest confinement, for the 3 μm particles, the progressive narrowing of the pore relies massively on the particle capture by at least one wall of the pore, and thus depends mainly on the DLVO particle-pore wall interactions. For the 1.8 μm PMMA, spherical particles are first deposited on the pore surfaces, which help capturing several aggregates that enough obstruct the pore and allow the sieving of spherical particles [20–21]. During the pore narrowing some edges of the aggregates are in contact with the surfaces of the pore while other edges can be in contact with the particles already deposited. Therefore the stability of the growing deposits and the clog for 1.8 μm PMMA relies on both DLVO interactions among particles and between particles/aggregates and the pore surfaces. For 1.6 μm PS the pore is mainly blocked by either a big particle, followed by the sieving of smaller particles (Fig. 2D), or the successive deposition of particles and small aggregates before a big particle joins the deposit (Fig. 2E). Only in the latter case interparticle and particle-surface DLVO interactions are responsible of the cohesion of the deposits/clog. As for the 1.8 μm PMMA aggregates are mainly responsible of the pore clogging for the 1.6 μm PS since spherical particles also cannot form multilayers. In a second stage there is a limited accumulation of particles in the clog over a length, L_{clog} between 10 and 20 μm , corresponding to 1.2-2.5 W and that depends on the composition of suspension and the way the clog is formed, in particular the length along the pore over which the deposits grow to eventually clog the pore. Even though this limited accumulation corresponds to couple of layers of particles along the pore it has an important contribution to the flow decline. Finally, in the third step, the flow keeps decreasing but much less rapidly with the particle accumulation and the temporal evolution of the flow almost identical for different trials with the same suspension (Fig. 3A). During this step the velocity decrease is inversely proportional to L_{clog} (Fig. 3B), consistent with Darcy's law. For a given suspension and a fixed clog length, the

corresponding amplitude of the overall flow decline is almost constant (Fig. 2D-E), which is also the case when we change the applied pressure of the feeding suspension (Fig. 3C). We observe a substantial increase of this amplitude when we use feeding suspensions composed of smaller particles (Fig. 2).

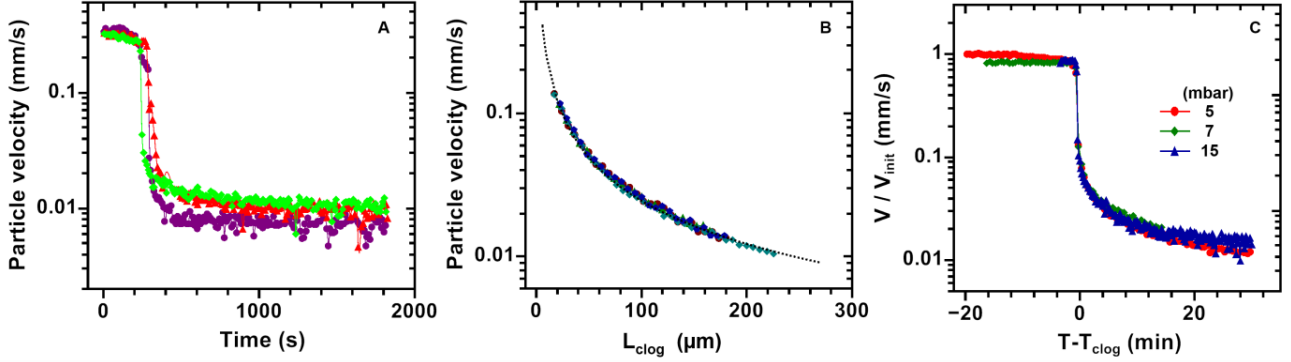


Figure 3: (A) Particle velocity decline over time during three clogging experiments with $1.8\mu\text{m}$ PMMA particles for an applied pressure of 15mbar. (B) Variation of the velocity of $2\mu\text{m}$ PS particles that accumulate at the rear of the clog with the L_{clog} for an applied pressure of 8mbar and in the same pore geometry. The dotted line is a fit of the data indicating that the particle velocity is inversely proportional to the length of the clog. (C) Variation of the velocity of $2\mu\text{m}$ PS particles scaled by their initial velocity prior to particle deposition in the constriction with time for various applied pressure. At $T-T_{\text{clog}}=0$ the pore is completely obstructed.

Note that the time scale of the clogging process is mainly fixed by the particle volume fraction of the suspension, i.e. the higher the particle concentration the faster the clogging process is for a given pore [22]. From all these observations we conclude that most of the flow decline corresponds to the blocking of the pore and the early stages of the clog growth while further accumulation of particles only leads to a small decrease of the flow conditions. In order to understand why there is such a sharp flow decline over the first tens of microns of the clog we use numerical simulations of the flow within the forming clog.

B. Numerical simulation of the flow in the forming clog

We perform flow simulation within the forming clog using Comsol to determine the flow variations each time a new particle is added to the clog. We use the approximate positions of the particles inside the pore obtained from the images of the deposited $3\mu\text{m}$ PS particle whose velocity decline over time is shown in figure 2B. We form progressively the clog, from the first deposited particles up to end of the accumulation process where the clog is composed of forty particles and about $30\mu\text{m}$ long. Here, we do not want to faithfully reproduce the flow conditions encountered in the experiment but rather study the flow inside a realistically structured clog. However, we check that slightly changing the position of the particles inside the clog, especially during the complete obstruction of the pore by the first four particles, does not significantly modify the flow decline. Once we add a new particle at the rear of the clog we

determine the flow velocity across the entire clog (Fig. 4), also the velocity mapping its porous structure, in several cross sections (Fig. 5). A comparison between the numerical and the experimental data is provided in figure 6. The overall shape of the fluid velocity decline across the clog as particles deposit inside the pore in the numerical simulation is similar to that of the particles velocity in the experiment. However, the velocity decline for the fluid is much greater than that of the particles, in particular for the complete pore obstruction by the first four particles (Fig. 6). The particle velocity is divided by only four while that of the fluid is divided by thirty on the overall accumulation. This difference comes from the fact that very few particles are used, sometime only one, to calculate the mean particle velocity in the experiment between each particle deposition event. The finite size of the particles is also responsible of this difference of the decline amplitude. Indeed, $3\mu\text{m}$ particles cannot move along streamlines close to the wall of the pore, and in average over a cross section they are going faster than the fluid.

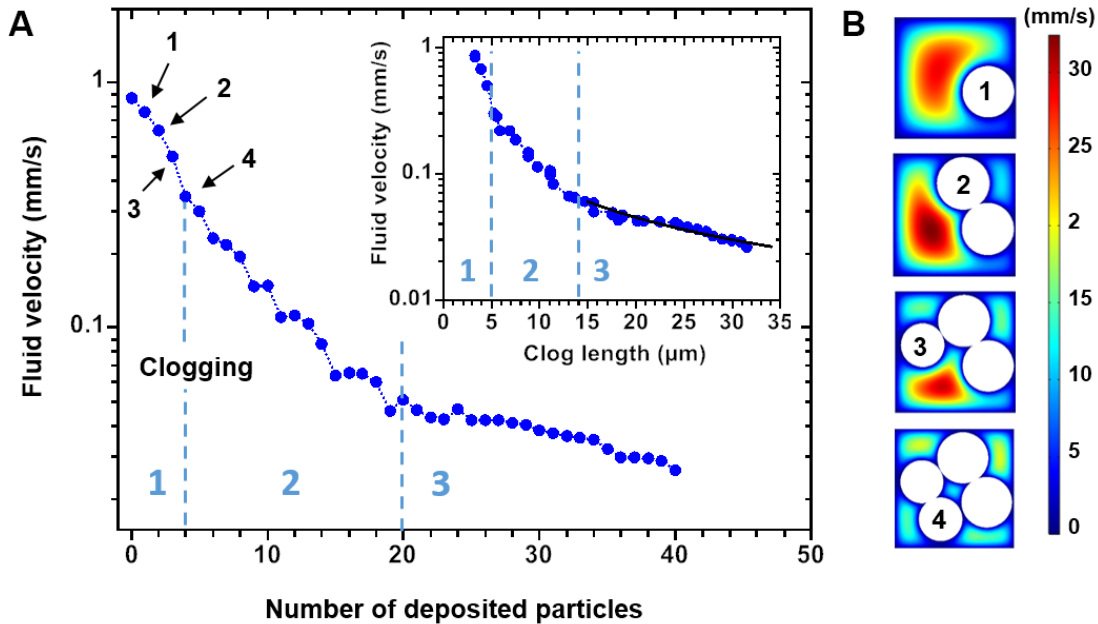


Figure 4: (A) Variation of the average fluid velocity through the clog as particles accumulate in a numerical simulation of the clog formation and the flow within it. The average fluid velocity in the pore without any particle inside corresponds to the first point of the graph. The pore is clogged when four particles successively deposit, the end of the process being outlined by the vertical dashed line. (Inset) Evolution of the fluid velocity with the clog length. The dotted lines correspond to the deposition of the twentieth particle from which the fluid velocity varies as the inverse of L_{clog} (continuous line). The three stages that contribute to the flow decline are separated by two dashed lines. (B) Velocity map in the 1st clogged cross section of the channel by the successive deposition of four particles, labelled with their arrival number.

The evolution of the flow decline in the numerical simulation can also be separated into three consecutive steps. There is first a sharp decrease of the velocity when the pore is completely obstructed by the successive deposition of four particles (Fig. 4B).

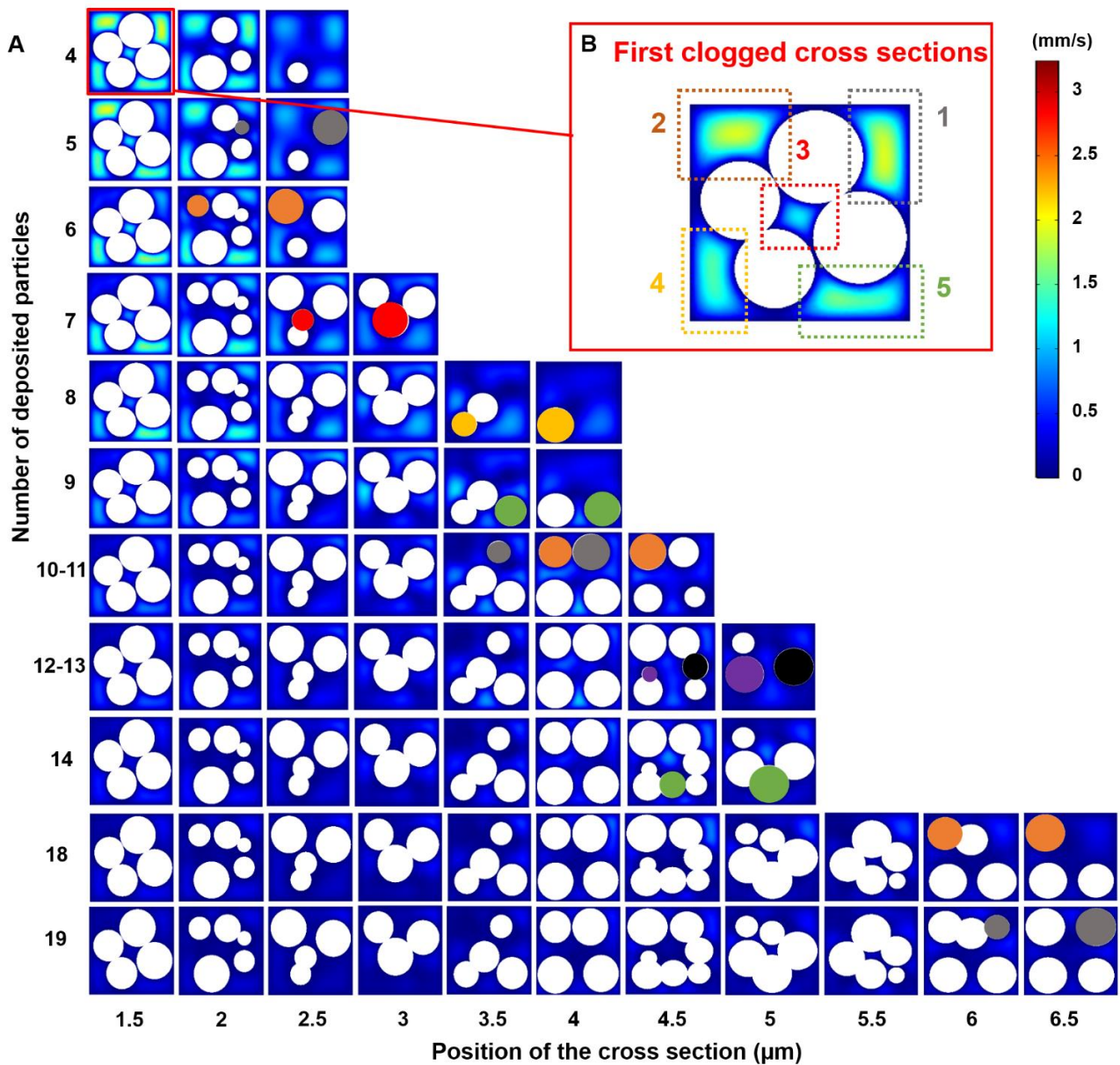


Figure 5: (A) Evolution of the flow velocity inside various cross sections (columns) of the entire clog for the deposition of the first nineteen particles that compose the clog. Each line corresponds to the deposition of one or two particles. (B) Close-up of the first cross section of the pore clogged by four particles. The five dotted rectangles outline the pores between the particles through which the fluid has to flow in the first clogged cross section (1st line and 1st column). We give the same colour to a pore and the particles that directly modify the flow condition in this pore when they deposit, i.e. particles N°5, 10 and 19 are in grey and induce a flow decline in the pore N°1 in A. The 12th and the 13th particles have different colours to show that do not contribute directly to the flow decline of any pore of the 1st cross section.

This step corresponds to an important reduction of the cross section available for the flow, since the fluid has to pass through five pores between the particles and the channel surfaces at the end of the complete obstruction of the pore (Fig. 4B). Later on, sixteen particles accumulate, adding 3-4 particles layers at the rear of the clog whose total length is equal to 8-9 μm . This very limited growth of the clog leads to an

even more important flow decline than the pore narrowing. Finally, the addition of another twenty particles at the rear of the clog results in the half reduction of Q , each particle deposition modifying only slightly the flow rate. In this last part of the flow decline, the fluid velocity decreases as the inverse of the clog length indicating that there is a Darcy flow across the clog, suggesting that the permeability of the clog is constant on average (Fig. 4A, inset). We can conclude that over a clog length equals to the width of the pore most of the flow decline takes place.

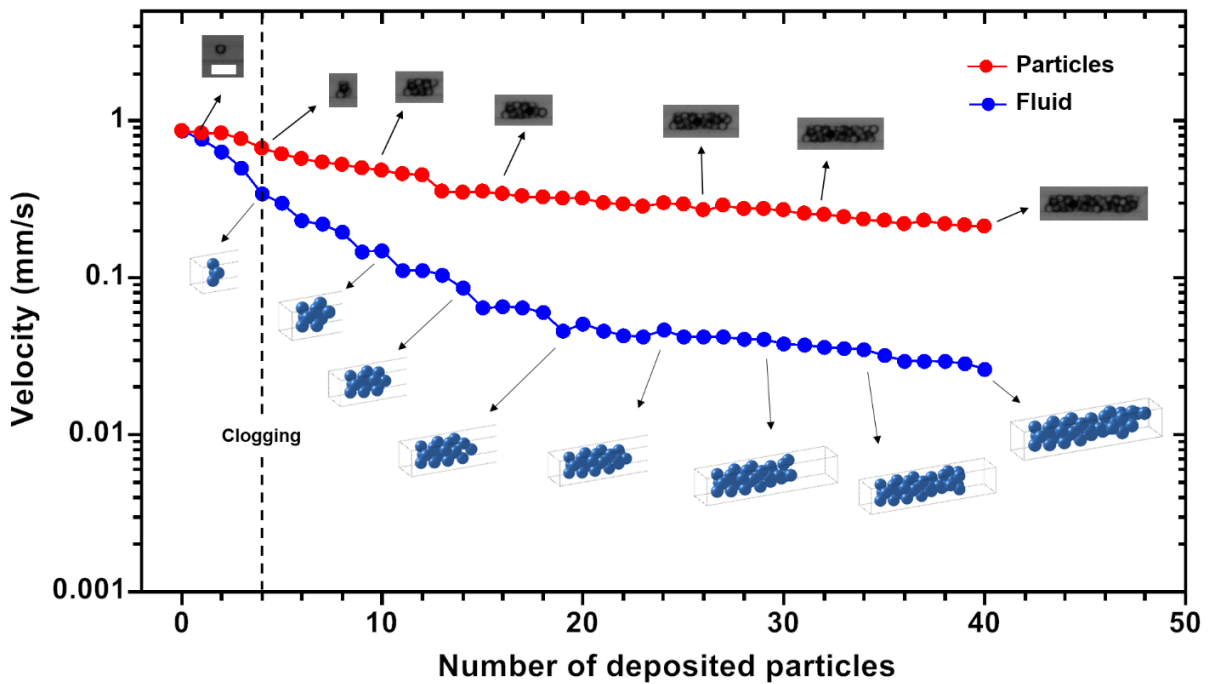


Figure 6: Variation of the particle velocity and the fluid velocity with the number of deposited particles, respectively from the experiments and the numerical simulations. The experimental data are those used in figure 2B. There is no deposited particle inside the pore for the first point of the two curves, which gives us the same value for both velocities. We also provided images or 3D views of the accumulation as the clog grows from the simulations and bright field images from the experiment. The scale bar corresponds to 10 μ m.

The evolution of the flow decline once the pore is blocked by the deposition of the first four particles can be understood by looking at the flow distribution within the forming clog (Fig. 7). As new particles accumulate, we hypothesize that a few flow paths that connect both ends of the clog are created with most of the fluid flowing through these preferential channels since they have a lower hydrodynamic resistance than the other narrower paths. However, at the same time the accumulation of a particle may also block one of these paths or modify their tortuosity, resulting in an increase of the local hydrodynamic resistance and also in a partial redistribution of the flow. To illustrate this process we consider the variation of mean fluid velocity at the head of the clog, inside the first blocked cross section when new particles accumulate. The fluid flows through five pores in this cross section, four of them being in the

corners while the last one is in the middle (Fig. 5B, inset). We suppose that if low preferential flow paths persist and connect both ends of the clog as particles accumulate then the flow will leave the clog head via one of these pores. As expected, each time a particle deposits and blocks more or less one of the five preferential flow paths the velocity decreases in the corresponding pore identified in this first blocked cross section (Fig. 5, first seven lines). Only a part of the flow upstream of the blocking particle, will follow the initial flow path, up to the clog head, while the other parts of the flow will be redirected in other directions [26] (Fig. 5, line “4” to “9”). Once around twenty particles accumulate, the fluid velocity is about the same in each cross section along the channel, meaning that there is no preferential flow path anymore at this stage of the clog formation (Fig. 5, line “19”).

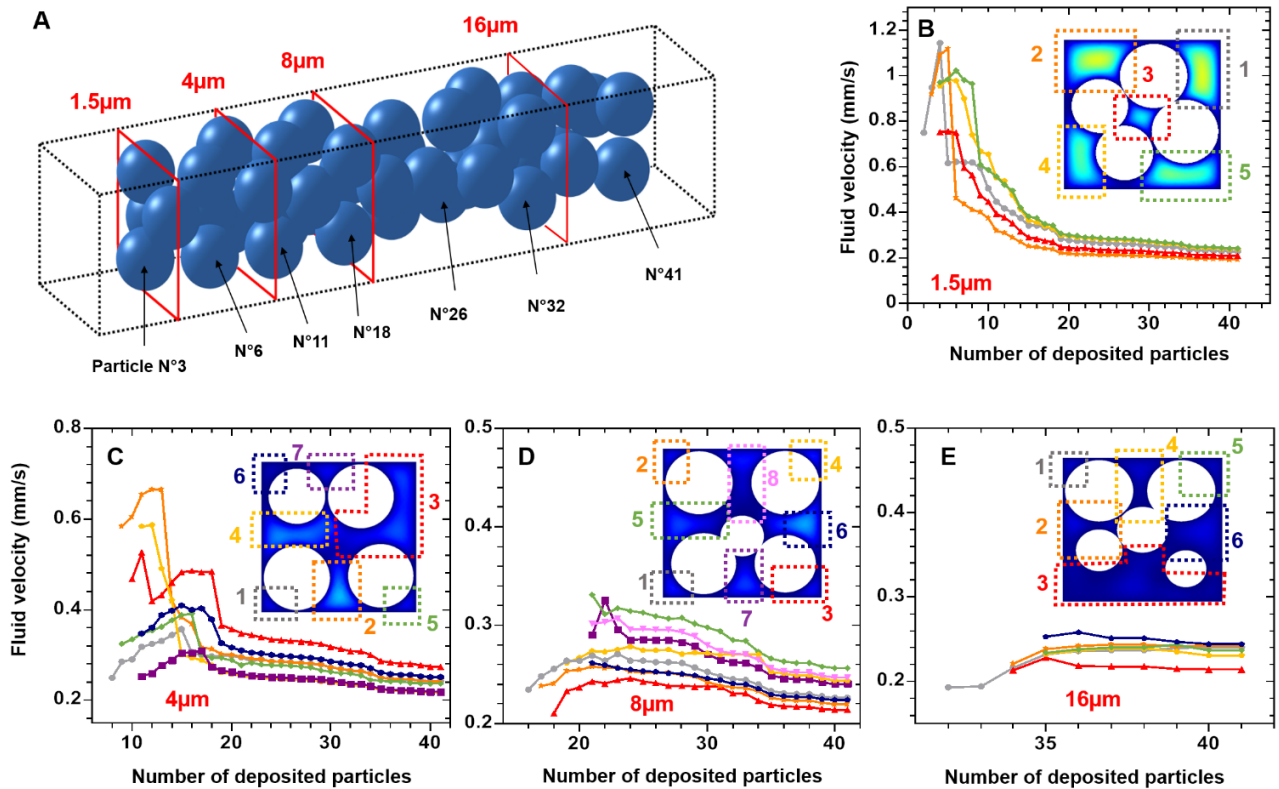


Figure 7: (A) 3D representation of a clog composed of 41 particles with a diameter $3\mu\text{m}$ in a Comsol simulation. The position of four slices used in the other parts of this figure (B-D) are outlined. For each of these slices, located at $1.5\mu\text{m}$ (B), $4\mu\text{m}$ (C), $8\mu\text{m}$ (D) and $16\mu\text{m}$ (E) from the clog head, we determine the variation of velocity within its pores as particle accumulate at the rear of the slice. We used the same colour in the image of each slice to outline the pores and the variation of the fluid velocity inside them in the graph.

To be more quantitative, we monitor the variations of the fluid velocity inside the pores belonging to four cross sections along the clog as particles pile-up (Fig. 7). As long as the number of particles that compose the clog is lower than 14-18, the flow inside the clog is rather heterogeneous with the fluid velocity being

different in each pore of the different cross sections (Fig. 7B-C). The sharp velocity decline in all the pores of the first two cross sections indicates an important redistribution of fluid in adjacent pores. In addition, the particle accumulation leads to a significant decrease of velocity in all the pores. When there are more than 20 particles inside the clog the velocity inside the pores of each cross section becomes similar and as more particles accumulate it still decreases but much more slowly (Fig. 7B-E). These measurements confirm that the accumulation of the first twenty particles leads to an important decay of the pore flow velocities due to the closure of the different preferential flow paths that connect both ends of the clog. As all these paths are closed there is a redistribution of the flow such that the fluid is forced to flow through narrower pores, before leaving the clog, increasing the viscous dissipation and leading to a higher flow decline across the entire clog.

C. Clogging transition with 1.8 μ m particles

The flow decline associated with the clogging transition is more complicated when the same pore is clogged by smaller particles like the 1.8 μ m PMMA since more particles are involved in the clogging process. While most of the flow decline takes place when around twenty particles accumulate inside the pore for the 3 μ m particles we need roughly the same number of objects with the 1.8 μ m particles just to completely block the pore for the first time (Fig. 2C). Thus, we suppose that there is a redistribution of flow and closure of low resistance flow paths inside the growing deposit before the channel is effectively clogged since there is a sharp velocity decline during this process (Fig. 2C). However, it is very challenging to observe such flow redistributions because it requires us to have access to the structure of the forming clog as particles deposit, as is seen in the 3 μ m particles. Instead, we determine the internal structure of the clog once it is formed and does not grow anymore, thanks to confocal imaging and image analysis [27,28], and determine the flow conditions within it. Note that we worked on images of a clogged pore from another model filter than the one we used up to now, the present pore being slightly wider (9 μ m) and higher (11 μ m) than in the previous case, which leads to a lower confinement with the ratio W/D , D being the particle size, two times greater. We distinguish two zones in the clog when we look at the variations of particle volume fraction (PVF) with the clog length that likely correspond to the pore obstruction and the subsequent growth of the clog due to the accumulation of particles. The PVF first increases over a distance L equal to 7-8 μ m that roughly corresponds to the width of the pore W (Fig. 8A), while for distance greater than L the PVF becomes constant at around 32% (Fig. 8A). We found such an evolution of the PVF along the pore for other clogs formed in the same conditions (Fig. 11).

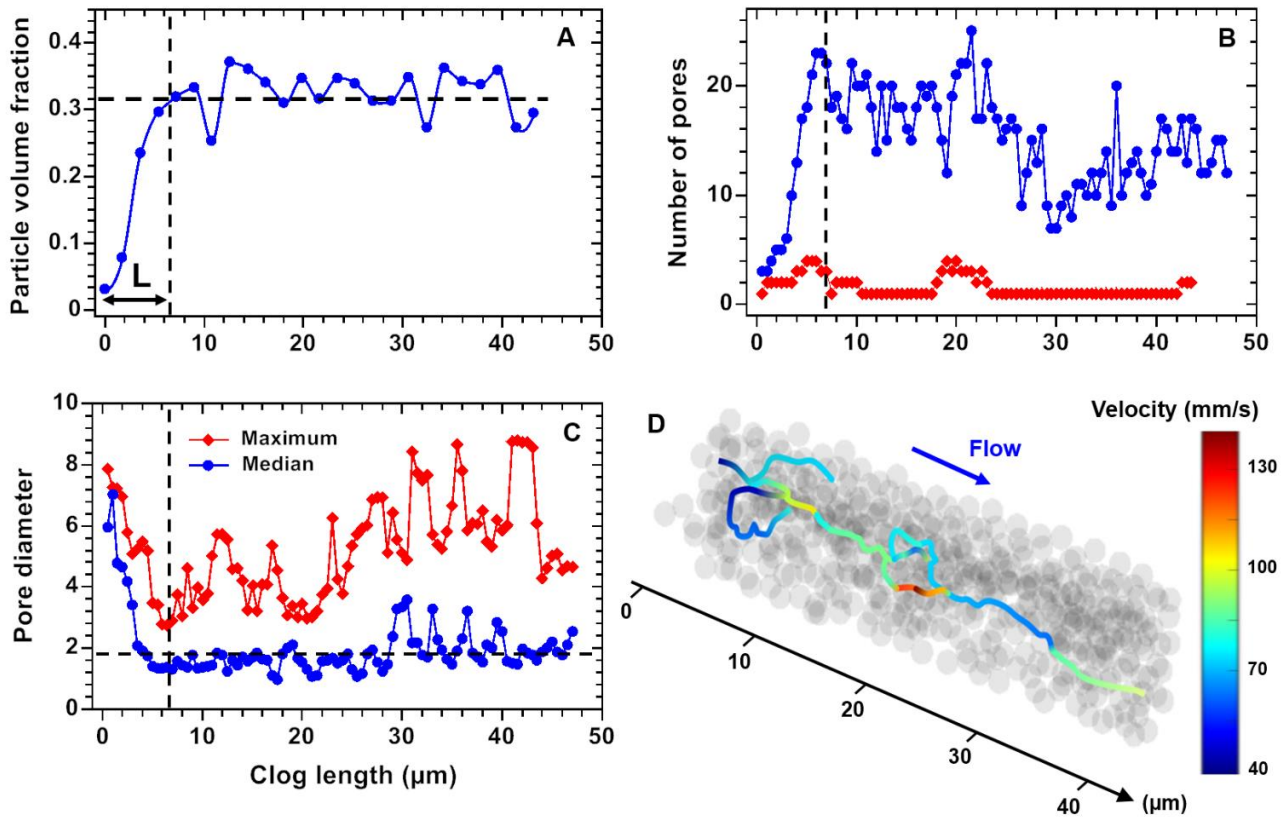


Figure 8: (A) Variation of particle volume fraction inside the clog along the length of the clog, L_{clog} . The Length L , equals to $6.5\mu\text{m}$, is the distance over which the particle volume fraction first increases, corresponding to the progressive obstruction of the pore until its complete clogging. The dashed line corresponds to the mean value of the volume fraction equals to 0.32. (B) Variation of the number of pores within the clog, in successive cross sections separated by $0.5\mu\text{m}$, through which all the fluid (top curve) or half of it flows (bottom curve). (C) Evolution of the median diameter of the pores formed by particle accumulation and that of the widest pore in cross sections every $0.5\mu\text{m}$ along the channel. (D) 3d Flow paths inside the clog through which half the fluid flows.

As the PVF increases the number of pores between the particles also becomes greater with their median size decreasing until they become a bit smaller than the mean particle size at the end of the first zone (Fig. 8A-C). The decrease of the mean pore size leads to an increase of the local hydrodynamic resistance, likely corresponding to the sharp velocity decline up to the channel obstruction reported in figure 2C. These results suggest that the channel is clogged at the cross section located at L since particles cannot flow through most of the pores of the deposit (Fig. 8B-C). However, even when the PVF reaches its maximum and becomes constant its value is low enough to have one wide zone in all the cross sections along the clog; a zone wide enough to let particles flow through it (Fig. 9A) and inside which, fluid flows faster than in the other pores (Fig. 9B). It turns out that these wide zones are not directly connected to each other, between adjacent cross sections, i.e., they are not located at the same position in each cross section, which ensures that there is no continuous path that the particles can follow to be transported across the growing clog (Fig. 9A). Therefore, the clogging process for the $1.8\mu\text{m}$ particles does not

correspond to the complete obstruction of a thin cross section of the channel, as it is the case for the $3\mu\text{m}$ particles, but rather to the partial fouling of the channel that spreads over a distance $L \approx W$, thus corresponding to the clog head. This partial fouling leads to the formation of three to four paths through which 50% of the fluid flows (Fig. 8D). The spatial heterogeneities in the head of the clogs likely comes from their composite nature, since they are systematically composed of a mixtures of aggregates, with various shapes and sizes, and spherical particles [21,22]. In the second part of the clog, for a clog length roughly equal W , corresponding to the zone where particles start accumulating, the structure of the clog is also heterogeneous with noticeable fluctuations in the number of pores and also of their mean size (Fig. 8B-C and Fig.9A). As a consequence, the flow in this part of the clog is heterogeneous with 50% of the fluid that flows mainly through one wide path while the other 50% flows through ten up to fifteen narrower pores (Fig. 8B-D and Fig. 9B, images 10 to 40). On average, this repartition of the flow between the pores remains the same all along the clog. We can consider that the permeability of the clog is constant and thus we have a Darcy flow through the clog, the flow rate decline being directly linked to the length of the clog, as already observed in a similar experiment [24]. The formation of this second part of the clog corresponds to the slowest velocity decline in figure 2 (Fig. 2C, from time greater than 4 min).

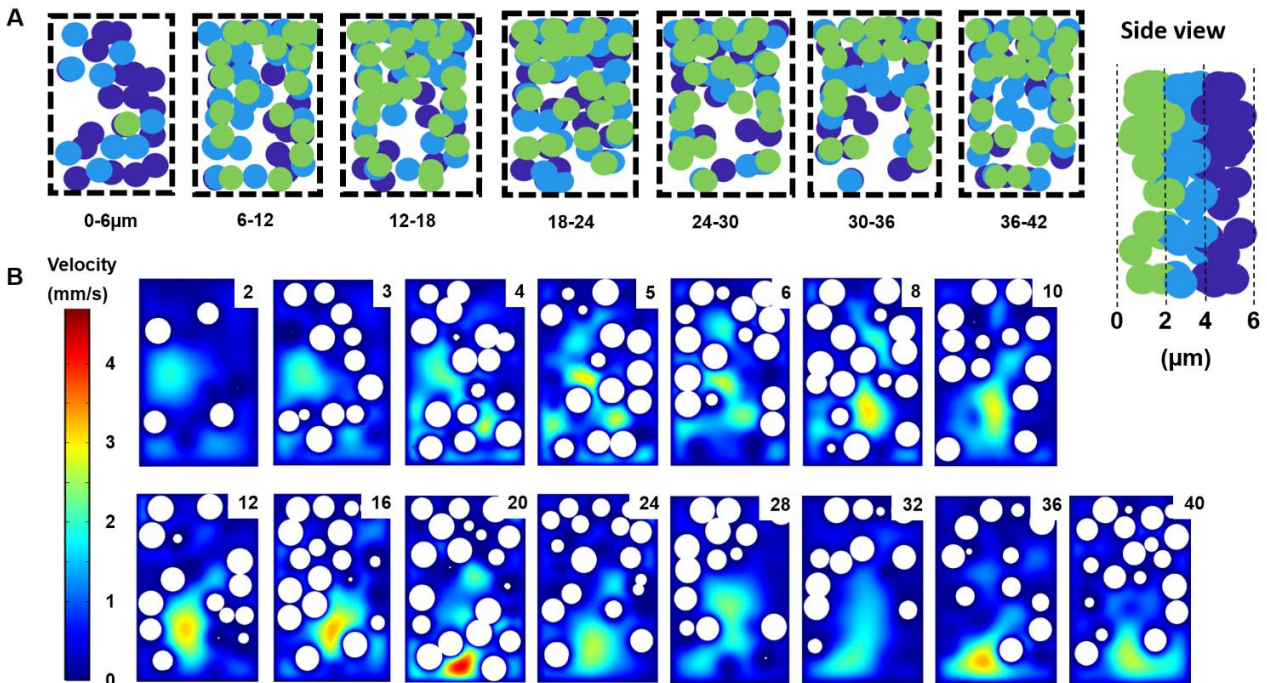


Figure 9: (A) $6\mu\text{m}$ thick cross section of the clog starting from the clog head. The side view on the right corner shows the colour code associated with the three cross sections that compose the wider cross sections. (B) Fluid velocity map in a different cross section of the clogged pore. The position of the cross section in microns from the entrance of the clog is reported on the top right corner.

We can perform numerical simulations of the flow across the clog, similar to what we did for the 3 μm particles even though we do not know how 1.8 μm particles accumulated. However, since we have the precise position of each particle within the clog and if we suppose that there is no rearrangement during the clog formation, we are able to reconstruct the whole clog by successive steps. At each step we add few particles to the clog and we determine the flow condition through the entire clog. However, we do not know when each particle deposits hence we decided to add 10 particles at the rear of the clog at each step, corresponding in average to a 1.4 μm thick cross section. The particles that belong to each added section are chosen such that their distances from the rear of the clog are the smallest. Therefore, we cannot determine accurately the evolution of fluid velocity in the pores between the particles as they deposit, as we did for the 3 μm particles in figure 5, but we still have access to the variations of the fluid velocity across the growing clog (Fig. 10). We found again that there are three contributions to the flow decline. The obstruction of the pores that requires the capture of about forty particles, which pile up non-uniformly along 7 μm corresponding to the clog head. In a second zone, further inside the clog, which spreads on 8-9 μm there is presumably an important redistribution of the flow paths with a slightly smaller contribution to the flow drop than the clog head. Finally, 16 μm from the very head of the clog, we obtain a Darcy like flow with the fluid velocity being inversely proportional to the clog length (Fig.10, inset), even though the flow is rather heterogeneous (Fig.8B and D).

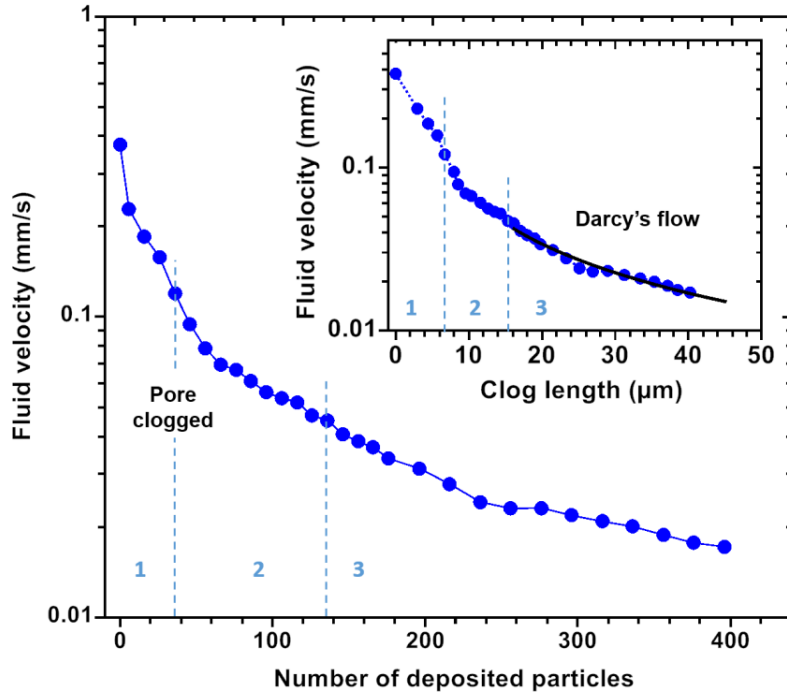


Figure 10: Variation of the average fluid velocity through the clog as 1.8 μm PMMA particles accumulate in a numerical simulation of the clog formation and the flow within it. The average fluid velocity in the channel without any particle deposited corresponds to the first point of the graph. The pore is clogged when 38 particles are deposited, the end of this process being outlined by the vertical dashed line. The beginning of the part of the clog in which there is a Darcy's flow is indicated by the vertical dotted line, when 138 particles have been accumulated in the channel. (Inset) Evolution of the fluid velocity with the clog length. The dashed and the dotted lines still indicate the length from which the pore is clogged and the beginning of the zone in which the fluid velocity varies as the inverse of the clog length (continuous line), respectively.

IV. Conclusion

We have determined the variation of the flow conditions corresponding to the clogging of a single straight pore/channel by colloidal particles, followed by the accumulation of particles at the rear of the clog. We have shown that there are three main contributions to the flow decline. Firstly, few particles accumulate and block a cross section of the channel which leads to a narrowing of the cross section of the channel through which the fluid flows. During this obstruction process the fluid is progressively forced to flow through the pores formed by the accumulation of the particles, which become more and more narrow. When the channel is completely clogged no particles can flow through it and the mean pore size has become smaller than the particle diameter. Such a reduction of the size of the flow cross section contributes significantly to the overall flow decline. As expected, the smaller the particles the greater the decline in flow as the pores of the clog are smaller [29]. Thereafter, there is a sieving process of the incoming particles. As these accumulate there is a progressive closure of low resistance flow paths that

connect the head and the rear of the growing clog. This limited growth of the clog also contributes significantly to the flow decline. This process takes place when the length of the clog is still small, around $10\ \mu\text{m}$, irrespective of the particle size and which corresponds to the width of the pore. The amplitude of the flow decline associated with the formation of these layers is highly dependent on the sizes and shapes of the particle that form the clog. The loss of some preferential flow paths forces the fluid to flow through more pores that are also narrower, resulting in a higher viscous dissipation and thus to lower flow conditions across the clog. More work has to be performed to better quantify the relationship between the flow redistribution and the flow drop in this second step. In the third and final step, for clog lengths greater than $W-2W$, depending on the particle diameter, the flow decline is only due to the increase of the clog length. The fluid velocity is inversely proportional to the clog length indicating that we have a Darcy like flow through this part of the clog, which thus has a constant permeability even though the flow can be quite heterogeneous with a broad distribution of the pore sizes formed by the accumulated particles. Therefore, when straight pores are clogged by colloidal particles, with a ratio $2 < W/D < 10$, we can safely consider that there is a Darcy's flow across the particle accumulation from a distance equal to $2W$ from the entrance of the clog. The contribution of this third step to the hydrodynamic resistance of the entire clog is much less important than the first two even for long clogs, which is confirmed by our detailed analysis of the flow conditions within the clog thanks to numerical simulations for two particle sizes. Consequently, these results show unambiguously that the early dynamics of pore clogging has a greater impact on the flow decline than the subsequent growth of the clog. We think that our results can be applied to real pores, like those that compose filtration membranes or found in natural porous environments, even though they do not look like simple straight channels. As expected there could be large variations of the amplitude of the flow decline for real pores whose size and the shape of the cross section are not constant. An interesting extension of this work would be to study the flow inside a growing clog when the flow rate rather than the pressure is fixed. In this case, there will be a great challenge for measuring the temporal variations of the pressure at the pore scale linked to the particle deposition. We also expect that the structure of the clogs partly composed of aggregates will be different, as well as its composition and the clogging time. Indeed, the available cross section of the pore available for the fluid flow will decrease as the deposits grow, which will require an increase of the pressure in order to keep the flow rate constant. Therefore, erosion or destabilization of the deposit may occur more often [30]. In such a case larger aggregates will be more involved in the clogging process since they are more stable under flow, i.e they are less detached by the flow than smaller aggregates [22].

Acknowledgement

We acknowledge the support of the Agence Nationale de la Recherche (ANR) (ANR-12-JS09-0003) and the CNES (Collmat).

Appendix

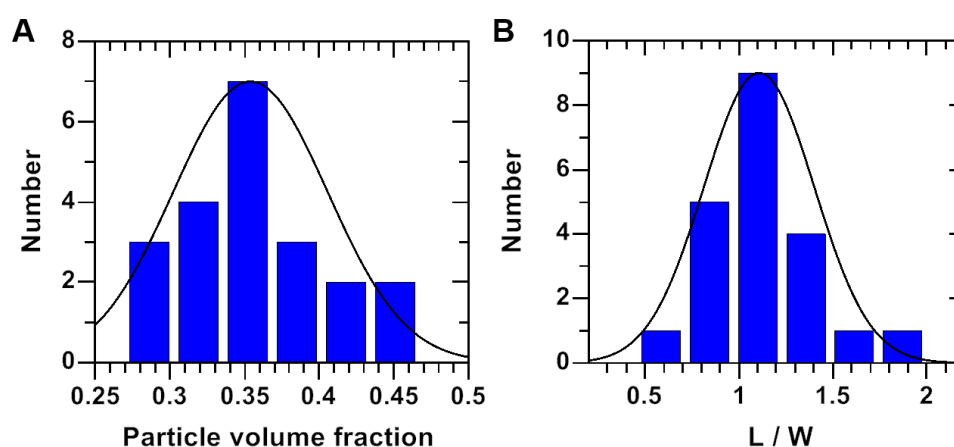


Figure 11: (A) Variation of the particle volume fraction for 20 clogs formed with 1.8 μ m PMMA particles in the same geometry with a width and a height of 9 and 11 μ m, respectively. (B) Histogram of the size of the head of the clog, L, scaled by the width W of the pore.

References

- [1] W. R. Bowen, J. I. Calvo, and A. Hernández, *Steps of Membrane Blocking in Flux Decline during Protein Microfiltration*, *J. Membr. Sci.* **101**, 153 (1995).
- [2] A. Lee, K. Sudau, K. H. Ahn, S. J. Lee, and N. Willenbacher, *Optimization of Experimental Parameters to Suppress Nozzle Clogging in Inkjet Printing*, *Ind. Eng. Chem. Res.* **51**, 13195 (2012).
- [3] S. Bounoua, S. Tomas, J. Labille, B. Molle, J. Granier, P. Haldenwang, and S. N. Izzati, *Understanding Physical Clogging in Drip Irrigation: In Situ, in-Lab and Numerical Approaches*, *Irrig. Sci.* **34**, 327 (2016).
- [4] Z. B. Sendekie and P. Bacchin, *Colloidal Jamming Dynamics in Microchannel Bottlenecks*, *Langmuir* **32**, 1478 (2016).
- [5] L. Sicignano, G. Tomaiuolo, A. Perazzo, S. P. Nolan, P. L. Maffettone, and S. Guido, *The Effect of Shear Flow on Microreactor Clogging*, *Chem. Eng. J.* **341**, 639 (2018).
- [6] R. L. Hartman, J. R. Naber, N. Zaborenko, S. L. Buchwald, and K. F. Jensen, *Overcoming the Challenges of Solid Bridging and Constriction during Pd-Catalyzed C- N Bond Formation in Microreactors*, *Org. Process Res. Dev.* **14**, 1347 (2010).

- [7] R. Blazejewski and S. Murat-Blazejewska, *Soil Clogging Phenomena in Constructed Wetlands with Subsurface Flow*, *Water Sci. Technol.* **35**, 183 (1997).
- [8] C. Mikutta, F. Lang, and M. Kaupenjohann, *Soil Organic Matter Clogs Mineral Pores*, *Soil Sci. Soc. Am. J.* **68**, 1853 (2004).
- [9] W. Zhang, X. Tang, N. Weisbrod, and Z. Guan, *A Review of Colloid Transport in Fractured Rocks*, *J. Mt. Sci.* **9**, 770 (2012).
- [10] M. Manga, I. Beresnev, E. E. Brodsky, J. E. Elkhoury, D. Elsworth, S. E. Ingebritsen, D. C. Mays, and C.-Y. Wang, *Changes in Permeability Caused by Transient Stresses: Field Observations, Experiments, and Mechanisms*, *Rev. Geophys.* **50**, (2012).
- [11] T. Candela, E. E. Brodsky, C. Marone, and D. Elsworth, *Laboratory Evidence for Particle Mobilization as a Mechanism for Permeability Enhancement via Dynamic Stressing*, *Earth Planet. Sci. Lett.* **392**, 279 (2014).
- [12] S. Veerapaneni and M. R. Wiesner, *Deposit Morphology and Head Loss Development in Porous Media*, *Environ. Sci. Technol.* **31**, 2738 (1997).
- [13] D. C. Mays and J. R. Hunt, *Hydrodynamic and Chemical Factors in Clogging by Montmorillonite in Porous Media*, *Environ. Sci. Technol.* **41**, 5666 (2007).
- [14] N. Bizmark, J. Schneider, R. D. Priestley, and S. S. Datta, *Multiscale Dynamics of Colloidal Deposition and Erosion in Porous Media*, *Sci. Adv.* **6**, eabc2530 (2020).
- [15] B. Dersoir, A. B. Schofield, and H. Tabuteau, *Clogging Transition Induced by Self Filtration in a Slit Pore*, *Soft Matter* **13**, 2054 (2017).
- [16] M. Auset and A. A. Keller, *Pore-Scale Processes That Control Dispersion of Colloids in Saturated Porous Media*, *Water Resour. Res.* **40**, (2004).
- [17] M. Auset and A. A. Keller, *Pore-Scale Visualization of Colloid Straining and Filtration in Saturated Porous Media Using Micromodels*, *Water Resour. Res.* **42**, (2006).
- [18] A. Marin, H. Lhuissier, M. Rossi, and C. J. Kähler, *Clogging in Constricted Suspension Flows*, *Phys. Rev. E* **97**, 021102 (2018).
- [19] B. Dersoir, M. R. de S. Vincent, M. Abkarian, and H. Tabuteau, *Clogging of a Single Pore by Colloidal Particles*, *Microfluid. Nanofluidics* **19**, 953 (2015).
- [20] A. Sauret, E. C. Barney, A. Perro, E. Villermaux, H. A. Stone, and E. Dressaire, *Clogging by Sieving in Microchannels: Application to the Detection of Contaminants in Colloidal Suspensions*, *Appl. Phys. Lett.* **105**, 074101 (2014).
- [21] N. Delouche, A. B. Schofield, and H. Tabuteau, *Dynamics of Progressive Pore Clogging by Colloidal Aggregates*, *Soft Matter* **16**, 9899 (2020).
- [22] N. Delouche, J. M. van Doorn, T. E. Kodger, A. B. Schofield, J. Sprakel, and H. Tabuteau, *The Contribution of Colloidal Aggregates to the Clogging Dynamics at the Pore Scale*, *J. Membr. Sci.* **635**, 119509 (2021).
- [23] C. Duchêne, V. Filipe, S. Huille, and A. Lindner, *Clogging of Microfluidic Constrictions by Monoclonal Antibody Aggregates: Role of Aggregate Shape and Deformability*, *Soft Matter* **16**, 921 (2020).
- [24] A. Sauret, K. Somszor, E. Villermaux, and E. Dressaire, *Growth of Clogs in Parallel Microchannels*, *Phys. Rev. Fluids* **3**, 104301 (2018).
- [25] J. Lohaus, F. Stockmeier, P. Surray, J. Lölsberg, and M. Wessling, *What Are the Microscopic Events during Membrane Backwashing?*, *J. Membr. Sci.* **602**, 117886 (2020).
- [26] K. Alim, S. Parsa, D. A. Weitz, and M. P. Brenner, *Local Pore Size Correlations Determine Flow Distributions in Porous Media*, *Phys. Rev. Lett.* **119**, 144501 (2017).
- [27] M. C. Jenkins and S. U. Egelhaaf, *Confocal Microscopy of Colloidal Particles: Towards Reliable, Optimum Coordinates*, *Adv. Colloid Interface Sci.* **136**, 65 (2008).

- [28] B. Dersoir, A. B. Schofield, M. Robert de Saint Vincent, and H. Tabuteau, *Dynamics of Pore Fouling by Colloidal Particles at the Particle Level*, *J. Membr. Sci.* **573**, 411 (2019).
- [29] S. Raha, K. C. Khilar, P. C. Kapur, and Pradip, *Regularities in Pressure Filtration of Fine and Colloidal Suspensions*, *Int. J. Miner. Process.* **84**, 348 (2007).
- [30] B. Dincau, C. Tang, E. Dressaire, and A. Sauret, *Clog Mitigation in a Microfluidic Array via Pulsatile Flows*, *Soft Matter* (2022).

Chapter 5

Structure and flow conditions through a colloidal packed bed formed under confinement

We propose a method to measure the permeability and volume fraction during the formation of the accumulation behind the clog using particle tracking and Darcy's law. We perform experiments of particle accumulations for different ionic strengths and pressures to observe the evolution of the accumulation features. Then we de-clog the channels to reproduce the backwashing experiments with clogs whose the deposit history and the accumulation features are controlled.

Contents

5.1	How to estimate the features of the particle accumulation?	136
5.1.1	Limitations of the Kozeny-Carman relation	136
5.1.2	Permeability and volume fraction from the particle tracking	136
5.2	Dependence of the particle accumulation with the ionic strength and the pressure .	137
5.2.1	Ionic strength	137
5.2.2	Pressure	138
5.3	Backwashing of the channel	138
5.4	Brief summary of the paper	139

5.1 How to estimate the features of the particle accumulation?

5.1.1 Limitations of the Kozeny-Carman relation

After the formation of the clog head, particles keep up accumulating and form an important packed bed of several hundred of micrometers. The two most interesting structural features are the permeability K of the accumulation and its volume fraction ϕ . For a packed bed of spherical particles, the best known relation to obtain the permeability is the Kozeny-Carman (KC) equation (defined in section 1.2.1.1):

$$v_s = \frac{D_{eq}^2}{180\mu} \frac{\epsilon^3}{(1-\epsilon)^2} \frac{\Delta P}{\Delta L} \quad (5.1)$$

Recently, Sauret et al. (2018) proposed an analytical description for the evolution of the accumulation length based on KC equation (more details in section 1.3.1.1), by estimating the volume fraction $\phi \approx 0.7$, that fits well their experimental data.

However in our case, particles accumulate in a very high confinement. In the chapter 4, we showed with confocal images provided by Benjamin Dersoir that the accumulation is very heterogeneous, with particles concentrated at the channel walls and a large flow path at its center. Since KC equation is based on pores of cylindrical sections more less sinuous, the heterogeneities of the pores in the cross section but also along the length of the accumulation invalids the use of this equation.

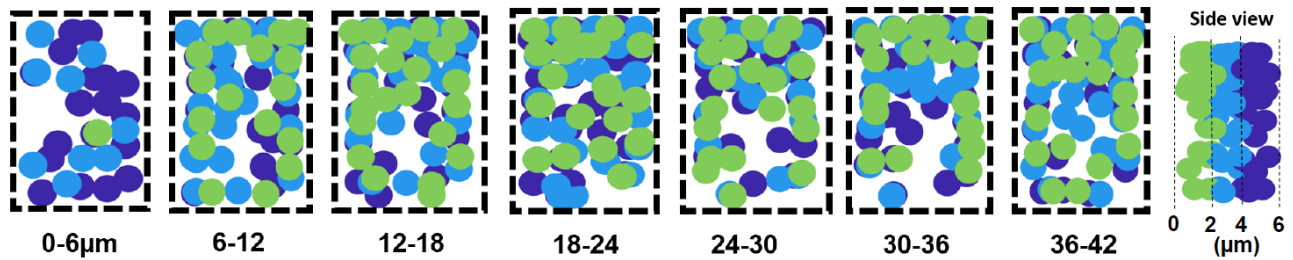


Figure 5.1: 6 μm thick cross section for a 1.8 μm particles accumulation in a 7 \times 14 μm pore, adapted from the chapter 4.

5.1.2 Permeability and volume fraction from the particle tracking

We compared the permeabilities K from different experiment conditions thanks to the particles velocities and the Darcy's law (defined in section 1.2.1.1):

$$\langle v_{part} \rangle = \frac{-K \Delta P}{\eta L} \quad (5.2)$$

We calculated the volume fraction ϕ along the accumulation length by counting the number of particles of diameter D that accumulate by slices of width $3.5D$. Decorrelate the volume fraction from the permeability measurement ensures the robustness of our results and gives an accurate value of the local volume fraction. According to the cross section of the channel where particles are accumulated, ϕ is either between $0.35 > \phi > 0.45$ in very confined channel or $0.5 > \phi > 0.65$ when the confinement is slightly higher, whatever the particle stabilization (figure 5.2).

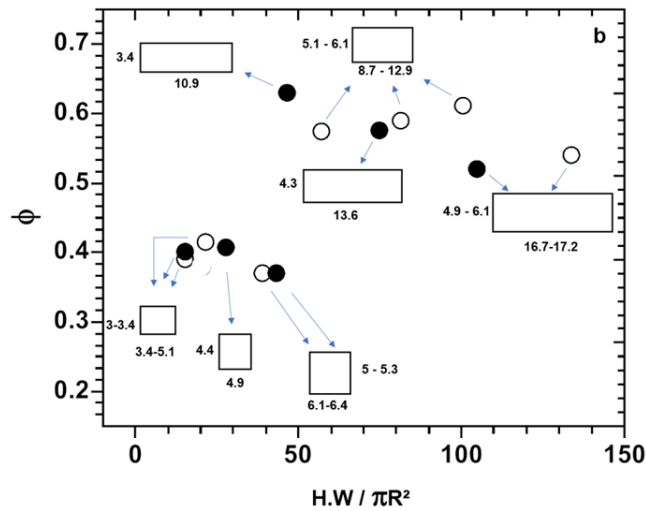


Figure 5.2: Variation of the averaged volume fraction with the ratio of the surface of the cross section over the projected surface of a particle $H.W/\pi R^2$. Filled and empty circles are particles stabilized sterically and electrostatically, respectively. Rectangles indicated the shape of the cross section, and the numbers near by correspond to the width and the height, scaled by the particle diameter.

5.2 Dependence of the particle accumulation with the ionic strength and the pressure

5.2.1 Ionic strength

We accumulate behind the clog head particles with various amounts of salt and changing both the particle and the cross section dimensions to obtain two different confinements. Most of the curves of the average velocity versus the clog length, obtained with different ionic strengths overlap, indicating that their permeability is the same since ΔP and η are constants (figure 5.3). We also confirmed that their volume fraction is constant. However, when the ionic strength approaches the CCC around 100-200mM, the number of aggregates increases and can represent 10 to 30% of the objects in the accumulation. The aggregates create defects in the accumulation and thus increase the permeability.

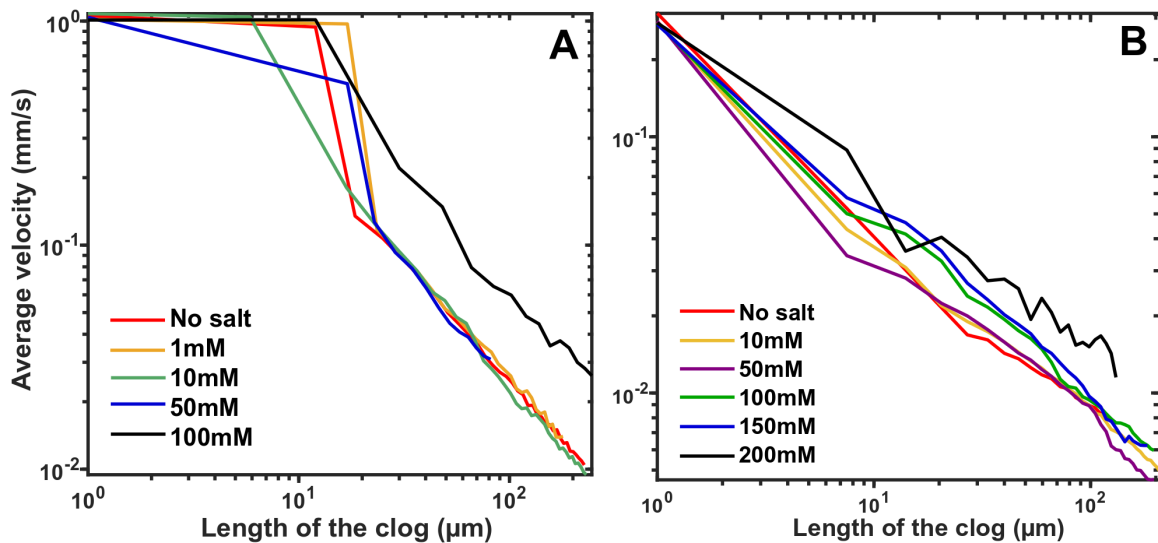


Figure 5.3: Flow declines with adding of salt for $H.W/\pi R^2 = 45$ (a) and $H.W/\pi R^2 = 113$ (b).

5.2.2 Pressure

In the same way, we performed experiments at different pressures to observe if increasing the arrival velocity of deposited particles could create defects in the accumulation such as aggregates with high ionic strength. After renormalization according to their reciprocal ΔP , all the curves fall on a master curve (figure 5.4) and this indicates that the feeding pressure has no impact on the permeability of the accumulation, which we later confirmed with the measurement of the volume fraction.

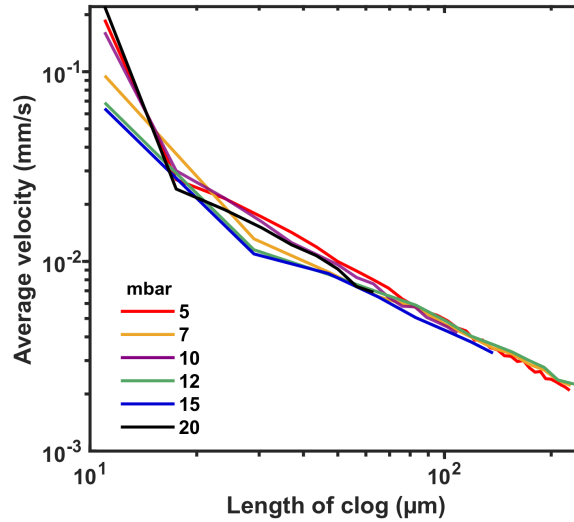


Figure 5.4: Normalized flow declines with the accumulation length for different pressure.

5.3 Backwashing of the channel

We performed de-clogging experiments like the backwashing process used to clean membrane, by reversing the pressure and we observed two zones. The first zone, closer to the rear of the clog is a labile zone where particles leave individually when they are no longer held together by the flow. In this zone, a hexagonal arrangement at the wall may appear (figure 5.5a) but this is not systematic and does not have any impact on the volume fraction of the clog. The second zone is closer to the clog head and is cohesive (red dotted line in figure 5.5b). We noticed that the length of the cohesive zone increased with the ionic strength but also with the pressure. We make the assumption that this is due, in the case of ionic strength, to the increase of the number of aggregates, while for the pressure to the creation of force chains along the height.

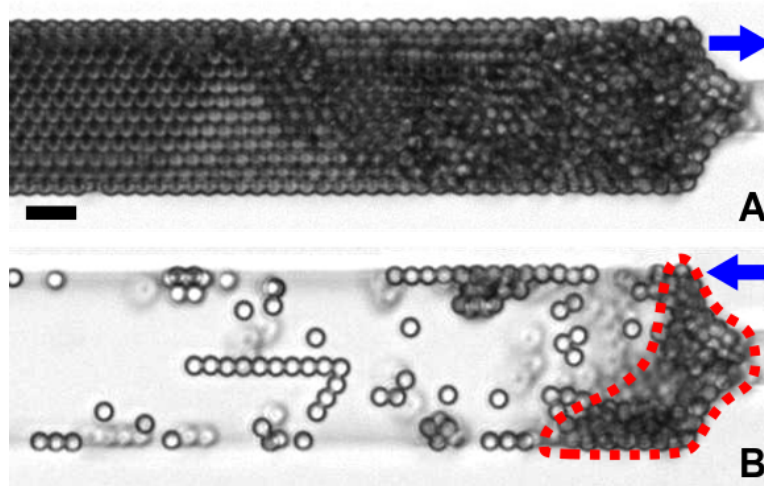


Figure 5.5: Accumulation of particles with an hexagonal arrangement at the wall (a) and its de-clogging (b). Red dotted line highlights the cohesive zone. Scale bar: $8\mu\text{m}$.

5.4 Brief summary of the paper

Coupling between the features of the particle accumulation and the flow conditions

Objective: observing the evolution of the particles accumulation features like the permeability and the volume fraction thanks to particle tracking and Darcy's law.

- The ionic strength I has no impact on the permeability and the volume fraction except when I reaches the CCC. The number of aggregates increases in the accumulation and thus increase the permeability.
- The pressure has no impact on both permeability and volume fraction.
- During the de-clogging of the channel, there are two zones:
 1. A labile zone at the rear of the accumulation, where particles form a dense repulsive suspension.
 2. A cohesive zone close to the clog head, whose remains compact even with strong flow reversal.

The more I or Q increases, the greater the length of the cohesive zone. This behavior, might be due to the presence of aggregate or the creation of chain of force across the height of the channel.

Structure and flow conditions through a colloidal packed bed formed under confinement

N. Delouche, B. Dersoir, AB. Schofield, H. Tabuteau*

Abstract

When a colloidal suspension flows in a constriction, particles deposit and are able to completely clog it. This fouling process is followed by an accumulation of particles corresponding to the growth of the clog. The knowledge of the dynamics of formation of such a dense particle assembly and its structural features is of primary importance in many industrial and environmental processes, and especially in filtration. While most studies concentrate on the conditions under which pore clogging occurs, this paper focuses on the accumulation of particles that follows pore obstruction. We determine the relative contribution of the confinement dimensions, the ionic strength and the flow conditions on the permeability and particle volume fraction of the resultant clog. We show that under high confinement the irreversible deposition of particles on the surfaces on the channel control the structure of the clog, irrespective of the other conditions. The accumulation of particles when the ionic strength reaches the critical coagulation concentration of the suspensions leads to a significant decrease of the permeability of the clog.

Introduction

The progressive formation of dense colloidal suspensions or colloidal gels near a surface/interface occurs in various natural and industrial processes. Colloidal particles sediment at the bottom of the ocean or river bed, they can also be driven by an evaporative flux near the contact line of a drying drop and form the so-called coffee ring pattern¹ or they accumulate on top of a filtration membrane in a filter cake^{2,3}. In all these examples the structure of the accumulated colloidal suspension results from the coupling between the advective flow, the confinement dimensions and the interparticle forces. For purely hard sphere like particles, dense deposits with an ordered structure are formed near the contact line of a drying drop, irrespective of the evaporation rate^{4,5}, or at the bottom of a tube under gravity, or ultracentrifugation conditions using 100 to 1000g⁶. Once a dense monodisperse hard sphere suspension is formed under high confinement, without any flow through it, Pieransky *et al.* observed the crystallization of the particle packing formed in between two plates separated by a distance not greater than 10 particle diameters⁷. Particles were alternatively arranged in a hexagonal and a square lattice as the separation between the two plates increased. It has been shown by Pansu *et al.*⁸ and later by Palberg

*et al.*⁹ that there are intermediate structures between the hexagonal and the square ones, which allow particles to pack more efficiently if a slight compression or a shear is exerted on the particle layers. The buckling of the layers leads to the formation of prisms periodically separated by stacking fault defects¹⁰. Dense packing of hard sphere can also be formed progressively, accumulating particles individually. Ortiz *et al.*¹¹ studied the formation of a deposit of polystyrene particles ($D=0.5\mu\text{m}$), transported by a fluid flow, over a porous obstacle in very high confinement (channel height H is around $0.9\mu\text{m}$ and $H/D=1.8$), for low Péclet number ($0.3 < Pe < 30$). They showed that the deposit behaved as a dense repulsive glass with the particles being held together on the porous obstacle by the flow. By varying periodically the flow rate they also showed that the deposit was slightly compressible^{12,13}. The structural features of particle accumulations are different when there is an attraction either between the particles or between the particles and the walls of the flow channel. For instance, the accumulation obtains a tenuous gel-like structure when there is a net attraction between the particles.¹⁴ More generally, the structure of the accumulation is either compact or tenuous depending on the DLVO interparticle potentials and the hydrodynamic conditions as shown by Saint Vincent *et al.* who performed experiments similar to that of Ortiz *et al.*¹¹ but in a less confined situation ($H/D=4$), in which they accumulated particles on a single pore¹⁵. By systematically varying the ionic strength, I , and the Pe number they observed various shapes of deposit. For low I , the particle accumulation formed at the entrance of pore is labile and has a limited growth, irrespective of the flow conditions. Larger and cohesive accumulations are observed when I increases such that particle surface charges are completely screened. Mokrane *et al.*¹⁶ have also considered the accumulation of particle at the entrance of a 2D model filter in a very low confinement ($H/D=18$). For various flow and ionic strength conditions they showed that a few particles are stuck near the pore entrance, on the pore surfaces while all the other particles form a dense assembly of repulsive spheres, maintained together by the fluid pressure. They determined the structural features of the monolayer in contact with one of the horizontal pore surface and from these measurements they showed that particles form an amorphous and more porous structure near the pore entrance while further away there is a crystal order, with a lower porosity. However, we do not know what the structure of the particles are in the bulk and if the evolution of this structure is influenced by the behavior of the particles in the monolayers close to the pore surface.

In this paper, we consider the evolution of the structural features of a dense colloidal suspension in a confined situation that is formed by particle accumulation in a channel upstream of an obstructed pore.

We determine the flow conditions through this accumulation in order to establish a relationship between its structure and the permeation flow through it. We determine the permeability in-situ of the growing clog from the variations of the particle velocity upstream of the accumulation. We look at the effect of the confinement, ionic strength and flow conditions on both the structural features of the clogs and the flow through them. We show that the degree of confinement and the shape of the channel cross section have the greatest impact on the mean structure of the clog. Under high confinement the structure of the clog is always heterogeneous and rather porous with a low particle volume fraction ϕ , around 0.3-0.35, while for slight modifications of the area of the channel cross section ϕ is closer to 0.5-0.6. The influence of the particle deposited on the channel surfaces and the nature of the objects (shape and size) that form the clogs are put forward to explain the variations of ϕ . Contrary to large and wide porous media composed of spherical particles, for which there is a direct relationship between ϕ and the flow conditions inside the porous structure, the Carman-Kozeny relationship cannot be used to predict the permeability of dense colloidal suspensions in high confinement since wall effects are not negligible. The flow within the particle accumulation is heterogeneous and mostly relies on a few preferential paths rather than exploring most the pore space between the particles. Nevertheless, we found that the permeability of the particle accumulation is constant, which corresponds to a Darcy flow. Finally we show that the permeation flow, through a compaction process, leads to the formation of cohesive zones inside the clogs.

Materials and methods

Details about the lithography, the pore geometry and imaging techniques used in this work can be found in previous papers [13-14]. Briefly, we employ a device with two long reservoirs followed by a constriction/pore in which the progressive obstruction by particle deposition takes place. The different part of channels are defined with a height H and a width W . 1.8 and $4.0 \pm 0.1 \mu\text{m}$. Fluorescent PMMA particles were synthesized by following the methods described in the paper of Shen *et al.*¹⁷, while PS particles coated by a polyelectrolyte brush were synthesized according to the protocol described in^{18,19}. PS particles with various diameters (1, 1.5, 1.8, 2 and $3 \mu\text{m}$) were supplied by Microparticle (GmbH, Berlin) or Life Technology (USA). We use a dilute suspension of these particles with a particle volume fraction of $5 \cdot 10^{-3}$, which enables us to track all the particles that flow through the channel and determine their shape and velocity. We estimated the volume fraction ϕ over the accumulation length by counting the number of particles of diameter D that accumulate in slices of width $3.5D$. We thus obtain an average ϕ over the whole accumulation, or local ϕ every $3.5D$ as the accumulation grows with maximum 5% of error. We also used high speed confocal microscopy (VT-Infinity III) to get the position of immobile particles within the channel for the 1.8 and $4 \mu\text{m}$ fluorescent PMMA particles. We work at low Reynolds

number, $Re < 10^{-4}$, and with a wide range of Péclet number ($1.6 \cdot 10^2 < Pe < 7 \cdot 10^5$). The de-clogging experiment is performed first by slowly decreasing the forward flow pressure, down to zero, followed by a slow increase of the pressure in the opposite direction with an increment of 0.05mbar every 10 seconds. A maximal pressure of 200mbar was imposed on the most cohesive zones, close to the clog head.

Results

Evolution of the particle volume fraction inside the clog formed in various confinements

The clogging dynamics of a pore is composed of three consecutive steps, regardless of the dimensions of the pore and the position of the head of the clog inside the pore (PRFluids when accepted)²⁰. The pore is first progressively fouled by particle deposition during which the mean particle volume fraction, ϕ (see methods), increases with the length of the clog, over a few tens of microns, depending on the cross section of the pore. This process continues until there is complete obstruction of the pore and this corresponds to the head of the clog. In this article, we focus on the subsequent steps during which particles accumulate at the rear of the clog head. We observed that ϕ always fluctuates around a mean value along the clog length, whatever the confinement used (figure 1a) as shown in Delouche *et al.* (PRFluids when accepted). There are two ranges of ϕ depending on the area and the shape of channel cross section (figure 1b). For smaller ratios of the area of the channel cross section over the projected surface of a particle, $H \cdot W / \pi R^2$, with R the radius of the particles, $0.35 < \phi < 0.45$, while for higher surface ratios $0.5 < \phi < 0.63$. These ranges are seen irrespective of the type of particle stabilization, (steric or surface charges). We note that while the area of the cross section does not change, there is an abrupt passage between the two regimes when the shape of the channel cross section goes from a nearly squared cross section to a rectangular one (at a surface ratio around 47, see figure 1b). In the lower range of ϕ , due to the high confinement along both the width and the height, the hydrodynamic interactions between the particles at the rear of the clog and those about to accumulate do not allow a dense packing to be obtained and most of the particles are in contact with the channel surface²⁰⁻²², leading to sudden and large fluctuations of ϕ along the pore length, up to 30% of the mean value, as the clog grows (figure 1a).

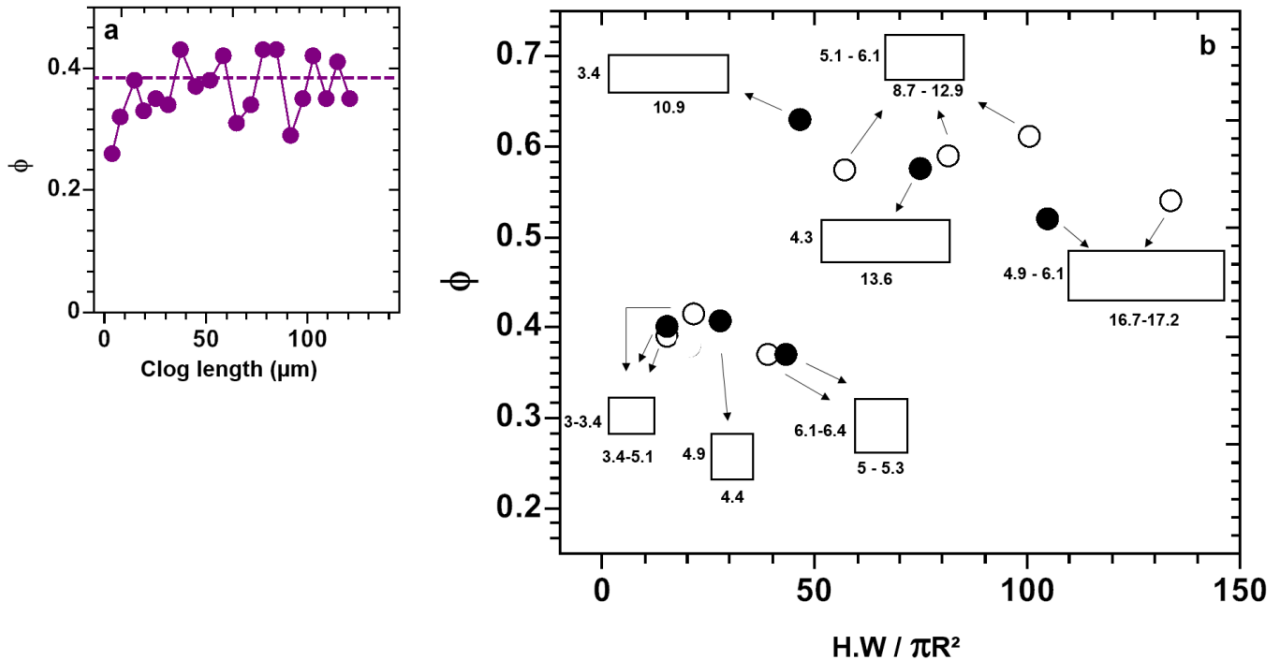


Figure 1: (a) Variation of ϕ along the clog length for $2\mu\text{m}$ PS in a pore with a cross section of $6.9 \times 8\mu\text{m}$. (b) Evolution of ϕ with the ratio of the surface of the channel cross section over the projected surface of the particles. Hollow and full circles correspond to particles stabilized by a polymer brush and surface charge, respectively. The diameter of particles is between 1 and $4\mu\text{m}$. The cross section for each test, with their height and width values scaled by the particle diameter, is indicated by an arrow.

There is also an important variation of ϕ between each clogging experiment since the dynamics of obstruction of each channel is unique. Therefore, in this lower range of ϕ , the spatial repartition of the particles on the channel surface rules the structure of the clog. Dersoir *et al.* (22) have observed in this confinement condition that the particles are preferentially captured in the corners of the channel and then at the pore wall. A slight shift of the position of a particle is able to prevent a compact stacking of particles on the surfaces. It is less the case with pores with rectangular section, even though the area of the cross section remains the same.

In the higher range of ϕ within the clog, all the cross sections of the channel are rectangular, with a wider than taller shape and we have various confinements along the height of the channels. The greatest mean value of ϕ , around 63%, is found for the highest confinement along H , for $H=3.4D$. In this condition, we suppose that most of the particles are in contact with one of the surfaces. This assumption is supported by the analysis of the evolution of ϕ as particles accumulate for two clogs formed under the same conditions (figure 2). In both cases the flow decline over time is almost identical even though the way the channel is obstructed is not the same, (figure 2 top right), nor are the structures of the growing clogs similar. For the 1st trial, from the beginning of the particle accumulation, ϕ is high, around 60%, and does

not change during the growth of the clog whose structure is amorphous (figure 2 bottom right). Rearrangements take place within the clog but they are very localized and thus involve only a limited number of particles since they do not change significantly the value of ϕ . In the other case, the beginning of the accumulation is about the same with an amorphous structure over the first thirty microns (figure 2 bottom left, image a').

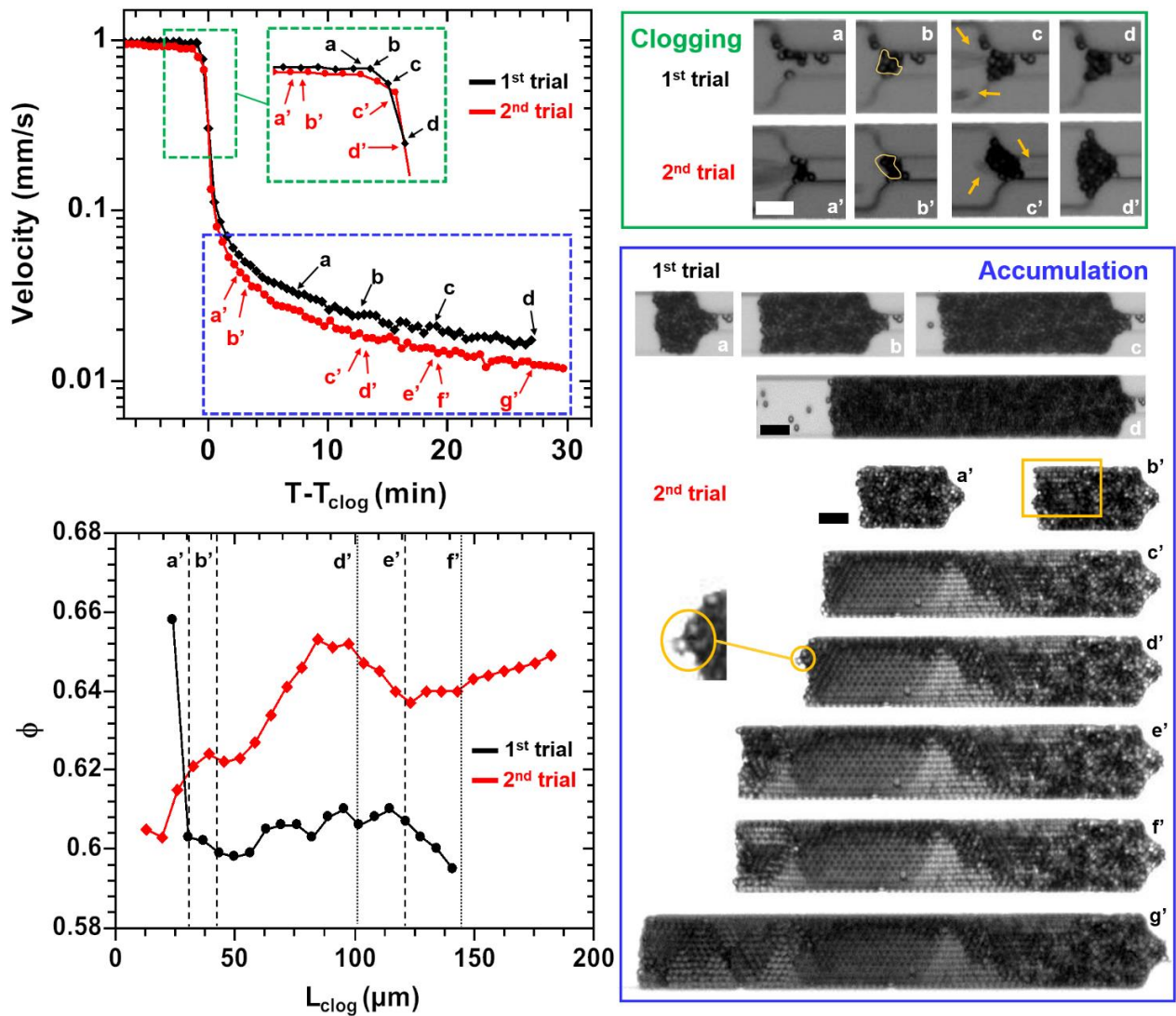


Figure 2: (Top left) mean particle velocity vs. $T-T_{clog}$, T_{clog} being the time at which the channel is completely obstructed for two trials under the same conditions. The labels within the green (clogging) and blue (accumulation) dashed zones correspond to the image in the top right part in the zones with the same colour, respectively. (Bottom left) Variation of the particle volume fraction with the clog length on the bottom left corner, also with labels corresponding to images on the bottom right panel. (Top right) In the clogging regime we highlight in images b and b' the biggest aggregate that partakes to the clog while in images c and c' the arrows point to particles about to go through the deposit since the pore is not yet completely obstructed. In images d and d' the two pores are clogged. (Bottom right) Consecutive images during the particle accumulation for both trials. The rectangle in image b' highlights a zone of massive rearrangement which becomes partially ordered without the addition of new particles at the rear of the accumulation. In image d' a triplet arrives at the accumulation front. All the scale bars correspond to 10 μ m.

However, quite rapidly, important spatial rearrangements at the channel surface result in an increase of ϕ (figure 2 bottom left). There are local transitions from amorphous structures to crystalline ones, indicating that there is a compaction of the clog by the flow. This suggests that most of the particles are not stuck on the surfaces and thus are free to rearrange at the bottom and top surfaces to form ordered zones. We have never observed the crystallization of the whole clog, mostly because of the immobile particles or aggregate particles that act as defects and do not allow local crystallization. Indeed, if the density of these immobile particles on the surfaces is high enough the structure of the entire clog remains amorphous, as confirmed by the inspection of the spatial repartition of the particles stuck on the surface (figure 3, left).

We obtain this spatial mapping of the particle immobilized during the clog growth by performing very slow de-clogging experiments, reversing the pressure gradient. To sum up, the permeation flow inside the clog is not impacted by the local structure of the particle assembly. When a substantial number of particles are stuck on the horizontal surfaces, local crystallization is prevented even though the value of ϕ remains high. This absence of order does not mean that the clog is cohesive since all the particles, except those attached to the walls, leave the clog individually during flow reversal.

The influence of particles attached on the channel surface, still in this most confined case, can also be studied by modifying the ionic strength, I , of the suspensions. When clogs are formed with $I > 1\text{mM}$ there is a significant decrease of ϕ from 0.63 down to 0.56 on average, irrespective of the value of I (figure 4a). Even though the surface charge of the PDMS walls is completely screened above 30mM²³, we suppose that more particles are stuck on the channel surfaces than in the salt free case and this prevents crystallization over large distances. The compaction by the flow is also less efficient leading to lower values of ϕ . The larger number of attached particles seen when salt is added to the suspension is confirmed when the channels are declogged (figure 3, right). As expected, when the surface charge of the PDMS walls are completely screened the walls are fully covered and the particles are firmly attached (figure 3, right, middle and bottom images). During the flow reversal only the particles between the monolayers, at the rear of the clogs, leave the channel as individual particles, the others stay attached (figure 3, right). This is in stark contrast to the no salt case, for which there is first a plug flow of the whole clog with local and temporary formation of crystal zones (Sup movie). All the particles end up leaving the channel one after the other, indicating that the accumulation is a dense suspension of repulsive hard spheres on the overall channel height and length, only held together by the fluid flow.

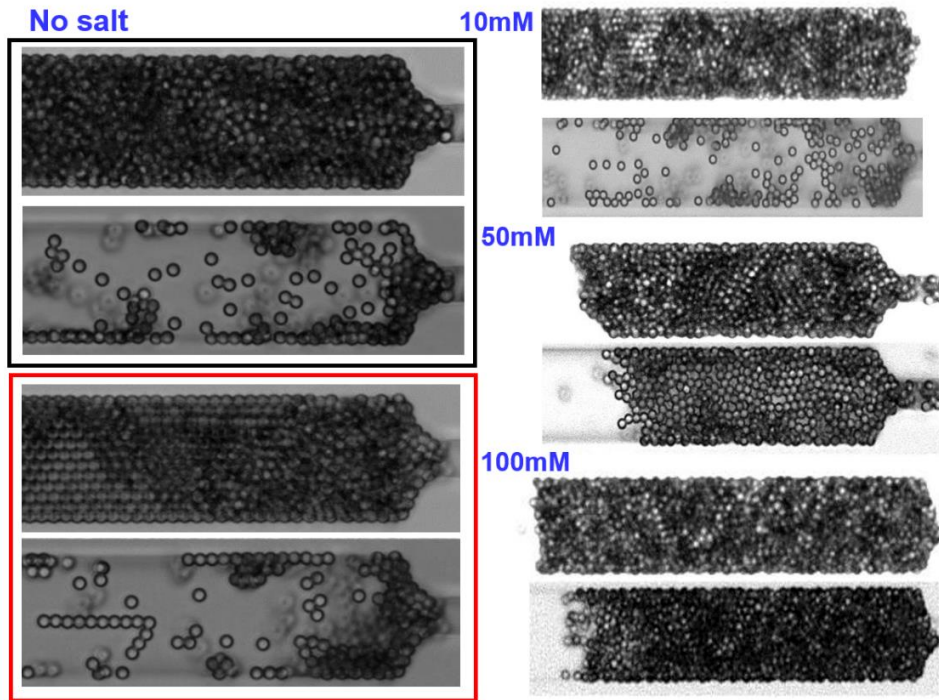


Figure 3: De-clogging experiments for the no salt case, on the left and for various ionic strengths on the right. In each case the top image is the last one before the flow reversal takes place while the bottom image corresponds to image of the clog when the de-clog experiment is over.

The presence of minute quantity of aggregates in the suspension without salt can modify the variation of ϕ as well. When an aggregate rather than a single particle arrives at the rear of the clog it may fill up most of the space between the bottom and the top surfaces, which does not allow the single particles in its close vicinity to form a crystal and thus lower locally ϕ (figure 2 bottom left, image d'). Therefore, aggregates can be viewed as defects within the clog structures that hinder the fluid flow initiated compaction of the particle assembly which in turn would have led to a higher packing fraction. We found on average that there are only two to four aggregates in each clog with a length between 150 and 200 μm , which corresponds to 0.3% of the total number of particles inside a clog (figure 5, left). We conclude that for such a low aggregates concentration (i) large patches of particles can crystallize on the channel surfaces and (ii) the particles deposited on the surfaces have a greater impact on the variation of ϕ over the entire clog than the aggregates. This is even more true when salt is added to the suspensions since for $I < 100\text{mM}$ the relative proportion of aggregates remains almost identical to that of the no salt suspension while the deposited particles increases with I . Interestingly, despite the noticeable decrease of ϕ between the no salt case and the suspensions with various amounts of added salt, (figure 4a), the flow decline as the clogs grow is identical for all these suspensions (figure 4b). Thus, there is neither variation of the clog permeability for all the suspensions nor a dependence of the permeability with ϕ , as it is generally

the case for flow through porous media composed of spherical particles and clogs formed in less confined conditions²⁴.

We come to the same conclusion when we get closer to the critical coagulation concentration (CCC) at $I=100\text{mM}$, since the value of ϕ remains unchanged. However, the permeability is three times greater than for the other suspensions (figure 5b). To explain such a variation of the flow conditions inside the clog we note that in the feeding suspension aggregates now represent around 10% of the particle population, mainly doublets and triplets but also larger objects (figure 5, left), formed by the coagulation process during the particle synthesis. As mentioned before, the deposition of aggregates precludes local high compaction of the particles around them, even though we obtain the same ϕ value as seen in other suspensions with less added salt. More importantly the high concentration of aggregates likely modifies the permeability all along the clog. Indeed, an aggregate larger than quadruplet, with a length equal to the channel height or larger is present inside the clog front every 10-15 μm , on average, while for triplets and doublets it is every 5 μm and 1 μm , respectively. Hence, the stacking dynamics of this mixture of single particles and aggregates enables the formation of larger pores than those formed solely with single particles. This heterogeneity in the pore size distribution likely favors the emergence of low resistance preferential flow paths that spread all along the clogs, as observed previously in the same confinement²⁰. Another assumption could be that the average pore size is shifted towards a higher value leading naturally to a lower hydrodynamic resistance. In both cases, due to the high salt content, single particles or aggregates as they enter in the clog can easily adhere to others, further preventing rearrangements inside the clog by fluid compaction.

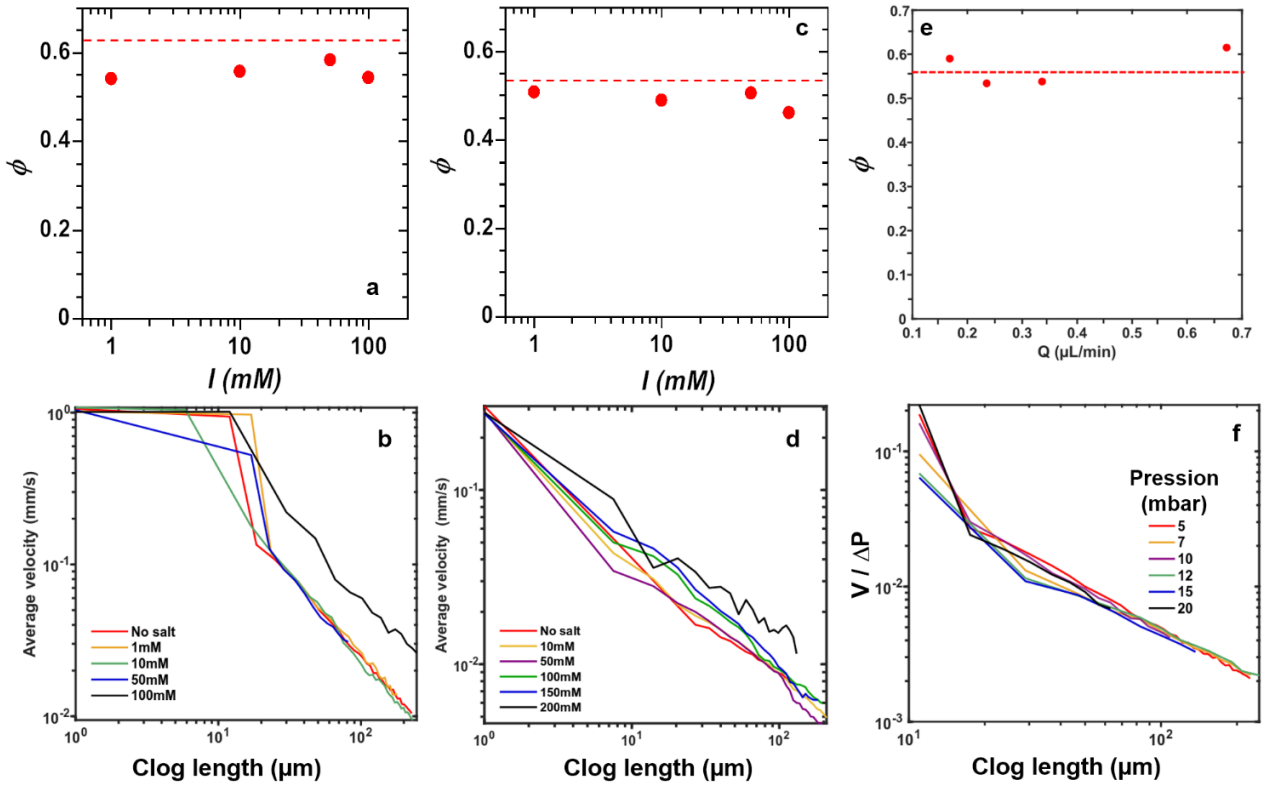


Figure 4: (Top) Variation of the particle volume fraction inside the clogs for $2\mu\text{m}$ (a) and $1.8\mu\text{m}$ PS (c) particles with I , inside channel with cross sections of $6.9\mu\text{m} \times 8\mu\text{m}$ and $8.9\mu\text{m} \times 30\mu\text{m}$, respectively. The dashed lines in graphs a and b correspond to the ϕ value for the no salt case while this is the average value of ϕ in graph c. (Bottom) Evolution of the mean particle velocity along the clog length for various I conditions. The graphs b and d were respectively obtained from the same experiments performed to measure graphs a and c. (f) Variation of the mean particle velocity divided by the applied pressure versus the clog length, from the experiments performed to obtain the variation of ϕ in graph e. Note that Darcy's law is only applicable beyond $20\mu\text{m}$ where the permeability becomes constant after the clog formation and the beginning of particle accumulation.

For a lower confinement along the channel height, using $1.8\mu\text{m}$ PS particles in $8.9\mu\text{m}$ high channel we obtain a systematically smaller ϕ value in the no salt case than in the previous case, corresponding to random close packing of the particles inside the clogs, $\phi \approx 0.52$. We also observed local crystallization without modification of the value of ϕ , which suggests that this ordering process is limited to the monolayers in contact with the horizontal surfaces of the channel. There is almost no variation of ϕ when salt is added to the suspension, which further indicates that organization of the particles at the surfaces does not pilot the variation of ϕ as it is in the case of the high confinement regime (figure 4c). We observe a slight but noticeable decrease of ϕ when we get closer to the CCC (200mM) of the suspension, for $I=150\text{mM}$, the number of aggregates rises up and reaches 13.6% of the particle population (figure 5, right). However, for this lower confinement there is no significant modification of the permeability for all the suspensions, even though the variation of the flow decline with the length of the clog fluctuates

more than in the previous case (Figure 4b and d). Nevertheless, when we reach the CCC of the suspension is becomes difficult to measure the value of ϕ , but we can still determine that aggregates represent 76% of the particle population, half of them being as big as quadruplets (figure 4, right). In this case, we have a fourfold increase of the permeability of the clogs compared to all the other suspensions. We clearly obtain a highly disordered packing, with a mean pore size greater than that obtained for clogs mostly formed from single particles, due to the high polydispersity of the various objects that accumulate, which thus explain the permeability increase. In addition, the cohesion between the particles prevents local compactions of the clog and a decrease in the mean pore size as particles accumulate. During particle stacking preferential flow paths may also have been created, which also contributes to the increase of the clog permeability.

2μm					1.8μm				
	Single	Doublet	Triplet	Aggregate		Single	Doublet	Triplet	Aggregate
No salt	99.73	0.23	0.02	0.03	No salt	99.84	0.16		
10mM	98.87	0.90	0.11	0.11	10mM	99.53	0.32	0.05	0.10
50mM	98.81	1.16	0.04		50mM	98.93	0.86	0.11	0.09
100mM	89.78	8.17	1.45	0.60	100mM	88.00	9.11	1.86	1.02
					150mM	86.44	10.91	1.82	0.83
					200mM	23.89	20.18	14.73	41.20

Figure 5: The composition of the clog as a percentage for 2 μ m PS (left) and 1.8 μ m PS (right) particles for various salt concentrations.

The variation of the flow conditions is another parameter that could influence the structure of the accumulation of particles and also the flow through it. We changed the applied pressure such that the initial flow rate was varied over half a decade and did not see any noticeable evolution of ϕ in the highest confinement, for $H/D= 3.4$ (figure 4e). This indicates that the compaction does not increase with the flow and leads to local rearrangements that do not significantly modify ϕ . When the initial flow rate increases, the flow through the clog is also higher and in each case we have a Darcy flow with almost the same permeability for all the clogs since all the data falls on a master curve (figure 4f). From this data we can conclude that the dynamics of the particle stacking neither modifies the average structure of the clog nor the flow through it.

We also performed de-clogging experiments for the various pressures. Surprisingly, we noticed that depending on the applied pressure there is a cohesive part of the accumulation, starting from the clog head, which cannot be removed by flow reversal. The higher the applied pressure the greater the length of this cohesive part (figure 6). For the lowest pressure, the cohesive zone does not exist but as the pressure is increased a cohesive zone forms and its length rapidly increases until it reaches 70-80 % of

the clog length. To explain such a behavior we suppose that the compaction proceeds in two consecutive steps. First of all, arrival of new particles at the rear of the clog often leads to local rearrangements, which do not spread over lengths greater than 30-50 μm towards the clog head, roughly corresponding to one to two widths of the channel. More compact packing result from such rearrangements (figure 2 bottom-left). At some point particles inside these zones can only perform very small collective displacements under flow (sup. figure 1). During this second compaction step particles are progressively pushed against the horizontal walls of the channel. Indeed, since we have only three to four particle layers along the channel height arches may span across the entire channel. As a result, particles near the walls are pushed towards them and adhere irreversibly on them. We expect this is a progressive process with more particles being stuck on the surfaces as time goes on, which eventually prevents further motion and significant deformation of the whole zone. According to this scenario the last 30-60 μm of the particle accumulation is susceptible to being removed by the flow reversal since this two steps compaction is not finished in this section. Indeed, we observed that on average only the last part of the clog with a length of around 30-60 μm is removed for higher pressures while for the lowest ones, 5 and 7 mbar, almost all the accumulation is wiped off (sup figure 2). The high variability of the lengths of the de-clogged zone is due to the rather heterogeneous spatial repartition of the immobile particles on the surfaces along the accumulation (sup figure 2). For the two lowest pressures, the number of particles that get stuck on the channel walls during compaction remains limited and this does not allow blocking of the other flowing particles in the bulk. We supposed that the force exerted through the packing on the particles near the surfaces of the channel is not high enough to allow them to adhere irreversibly.

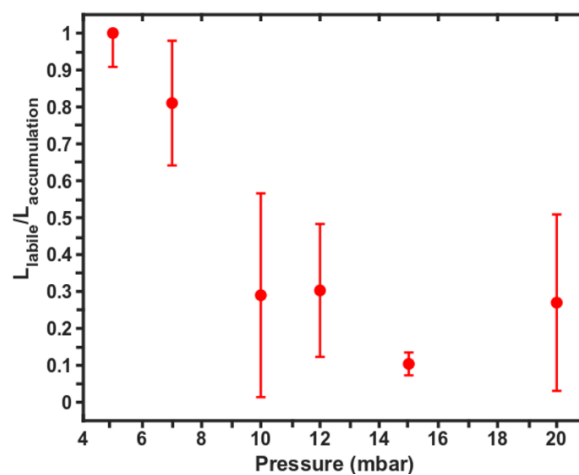


Figure 6: Variation of the ratio of the length of the zone that leave the channel during the de-clogging experiment, L_{labile} relative to the length of the clog at the end of the accumulation process plotted against the applied pressure.

Conclusions

In this paper we determine the variation of the structural features of a particle accumulation consecutive to the obstruction of a channel by similar colloidal particles and also the permeation flow across this accumulation when we vary the confinement, ionic strength and flow conditions. We first show that the piling dynamics of the particles that compose the clog strongly depends on the shape and size of the cross section of the channel. In high confinement, both along the width and the height of the channel or, only in the larger dimension, the adhesion of particles on the channel surfaces dictates the structure of the clogs, which remains true for large variations of ionic strength. When the ionic strength becomes close to the CCC of the suspension there is a large polydispersity in the aggregates that compose the particle accumulation and a higher permeability of the clog than for the clogs formed with lower I , irrespective of the confinement dimensions. In our work, since the confinement is always not negligible, the structure of the clogs is quite heterogeneous and thus the knowledge of the particle volume fraction within the clog is not useful to determine the permeability of the clog with most of the fluid expected to be flowing through preferential paths. Further studies have to be performed to determine how the permeation flow through the clog leads to its compaction and the formation of cohesive zones when the applied pressure increases. In particular, it would be interesting to understand the dynamics of the massive rearrangements that allow a transition from an amorphous state to a crystalline one. From a practical point of view, even though the geometry of the channel we used is a bit peculiar, we think that our results may help understand some of the physical processes at play in filters or membranes fouled by colloidal particles.

Acknowledgement

We acknowledge the support of the Agence Nationale de la Recherche (ANR) (ANR-12-JS09-0003) and the CNES (Collmat).

References

- 1 R. D. Deegan, O. Bakajin, T. F. Dupont, G. Huber, S. R. Nagel and T. A. Witten, *Nature*, 1997, **389**, 827–829.
- 2 A. Rushton, A. S. Ward and R. G. Holdich, *Solid-Liquid Filtration and Separation Technology*, John Wiley & Sons, 2008.
- 3 M. R. Mackley and N. E. Sherman, *Chem. Eng. Sci.*, 1992, **47**, 3067–3084.
- 4 J. Emile and H. Tabuteau, *Colloids Surf. Physicochem. Eng. Asp.*, 2016, **511**, 201–211.
- 5 L. Li, C. Goodrich, H. Yang, K. R. Phillips, Z. Jia, H. Chen, L. Wang, J. Zhong, A. Liu, J. Lu, J. Shuai, M. P. Brenner, F. Spaepen and J. Aizenberg, *Proc. Natl. Acad. Sci.*, , DOI:10.1073/pnas.2107588118.
- 6 R. Piazza, S. Buzzaccaro, E. Secchi and A. Parola, *Soft Matter*, 2012, **8**, 7112–7115.
- 7 P. Pieranski, L. Strzelecki and B. Pansu, *Phys. Rev. Lett.*, 1983, **50**, 900–903.

- 8 B. Pansu, Pi. Pieranski and Pa. Pieranski, *J. Phys.*, 1984, **45**, 331–339.
- 9 S. Nesar, C. Bechinger, P. Leiderer and T. Palberg, *Phys. Rev. Lett.*, 1997, **79**, 2348–2351.
- 10 A. Fortini and M. Dijkstra, *J. Phys. Condens. Matter*, 2006, **18**, L371–L378.
- 11 C. P. Ortiz, R. Riehn and K. E. Daniels, *Soft Matter*, 2012, **9**, 543–549.
- 12 C. P. Ortiz, K. E. Daniels and R. Riehn, *Phys. Rev. E*, 2014, **90**, 022304.
- 13 C. P. Ortiz, R. Riehn and K. E. Daniels, *J. Stat. Mech.*, 2016, **2016**, 084003.
- 14 S. Lin and M. R. Wiesner, *Environ. Sci. Technol.*, 2012, **46**, 13270–13277.
- 15 M. R. de Saint Vincent, M. Abkarian and H. Tabuteau, *Soft Matter*, 2016, **12**, 1041–1050.
- 16 M. Larbi Mokrane, T. Desclaux, J. F. Morris, P. Joseph and O. Liot, *Soft Matter*, 2020, **16**, 9726–9737.
- 17 S. Shen, E. D. Sudol and M. S. El-Aasser, *J. Polym. Sci. Part Polym. Chem.*, 1993, **31**, 1393–1402.
- 18 T. E. Kodger, R. E. Guerra and J. Sprakel, *Sci. Rep.*, 2015, **5**, 14635.
- 19 N. Delouche, J. M. van Doorn, T. E. Kodger, A. B. Schofield, J. Sprakel and H. Tabuteau, *J. Membr. Sci.*, 2021, **635**, 119509.
- 20 *Rev.*
- 21 B. Dersoir, A. B. Schofield and H. Tabuteau, *Soft Matter*, 2017, **13**, 2054–2066.
- 22 B. Dersoir, A. B. Schofield, M. Robert de Saint Vincent and H. Tabuteau, *J. Membr. Sci.*, 2019, **573**, 411–424.
- 23 B. Mustin and B. Stoeber, *Langmuir*, 2016, **32**, 88–101.
- 24 A. Sauret, K. Somszor, E. Villermaux and E. Dressaire, *Phys. Rev. Fluids*, 2018, **3**, 104301.

Supplementary figures

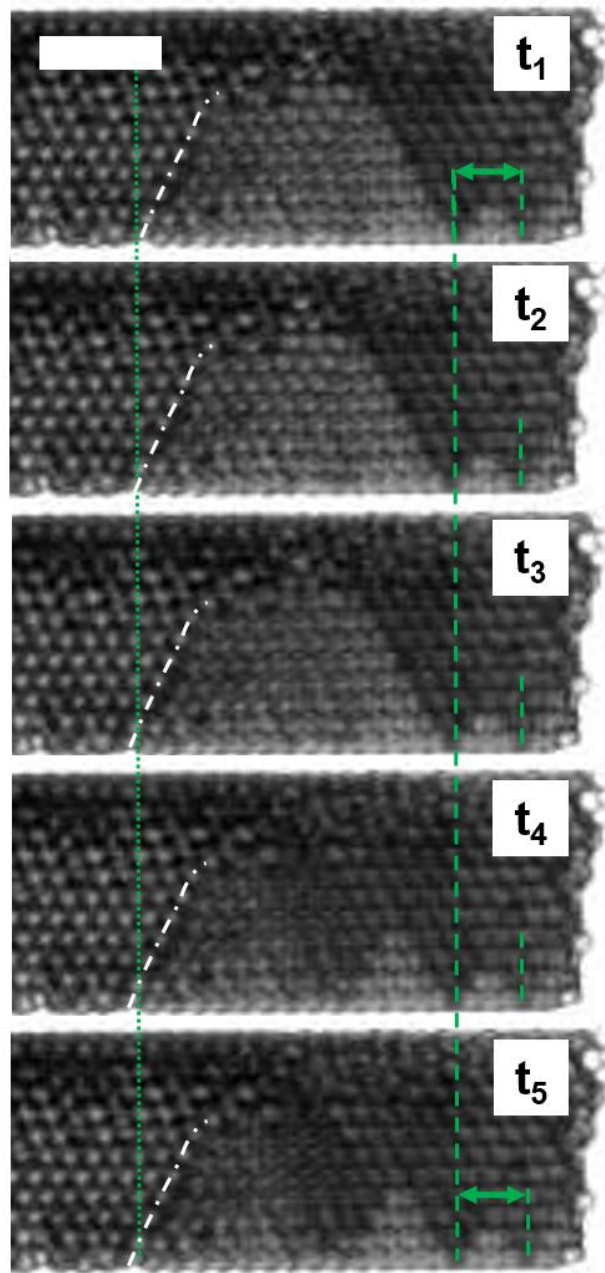


Figure 1: Compression by the fluid at the rear of the particle accumulation while no new particles are added. The time between each image is 0.1s. The distance between the two dashed lines at the right of the images is constant, indicating that this right part of the accumulation, which starts from the longer dashed line, does not undergo any compression. On the left of each image the position of the dotted line is fixed while the oblique line moves towards the left showing that this left part of the accumulation is compressed. Important rearrangements take place in the middle between the dashed and the dotted lines. Roughly half of the particles on the right hand side of this middle section move vertically in order to be in the same plane as the particles on the right hand side. This vertical motion arises from to the compression of the left side . Scale bar corresponds to 15 μ m.

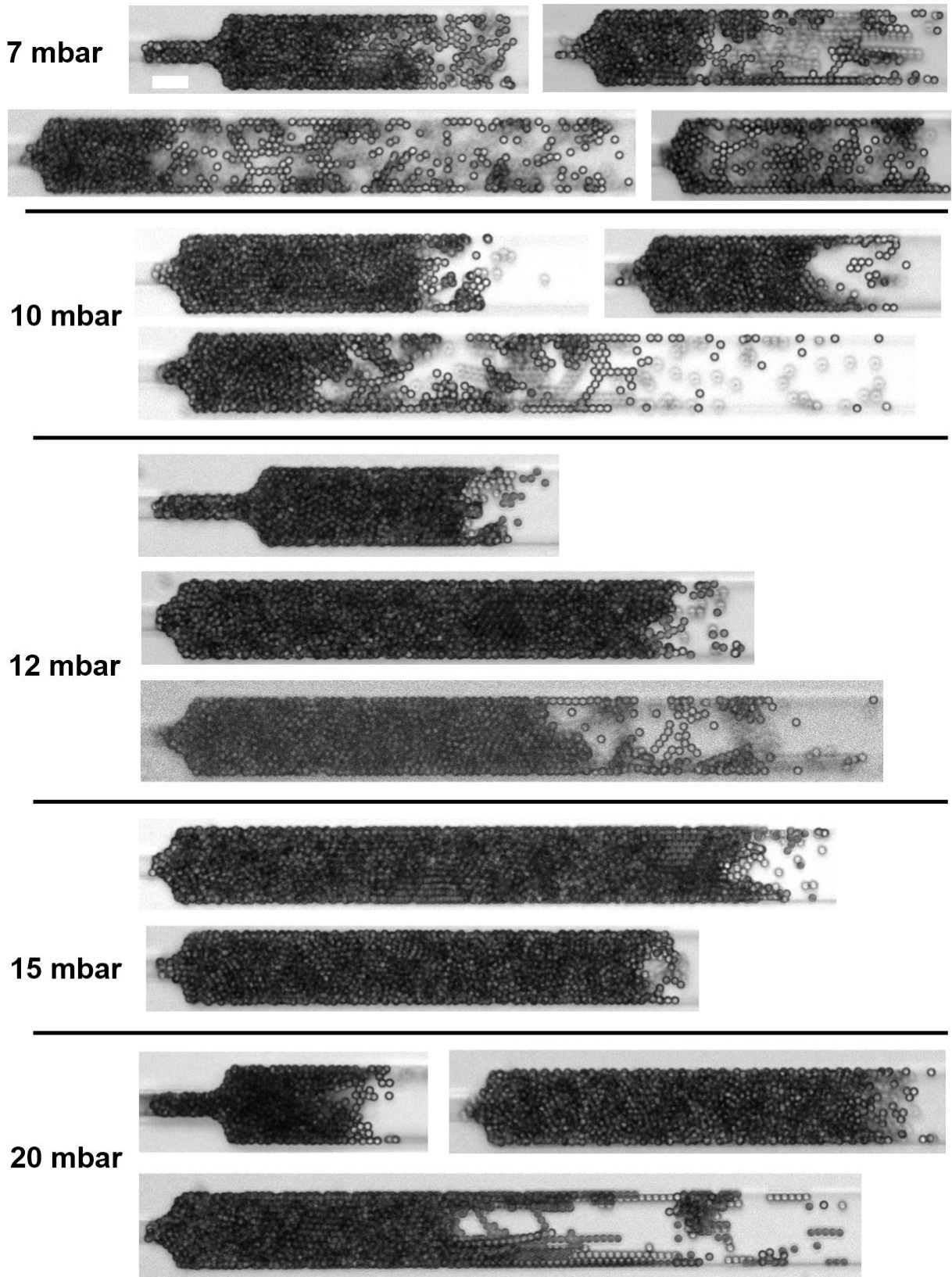


Figure 2: Final images after the de-clogging of the pores. Scale bar is 15 μ m.

Part II - At the porous medium scale

Chapter 6

The clogging of interconnected pores by colloidal particles

Chapter 7

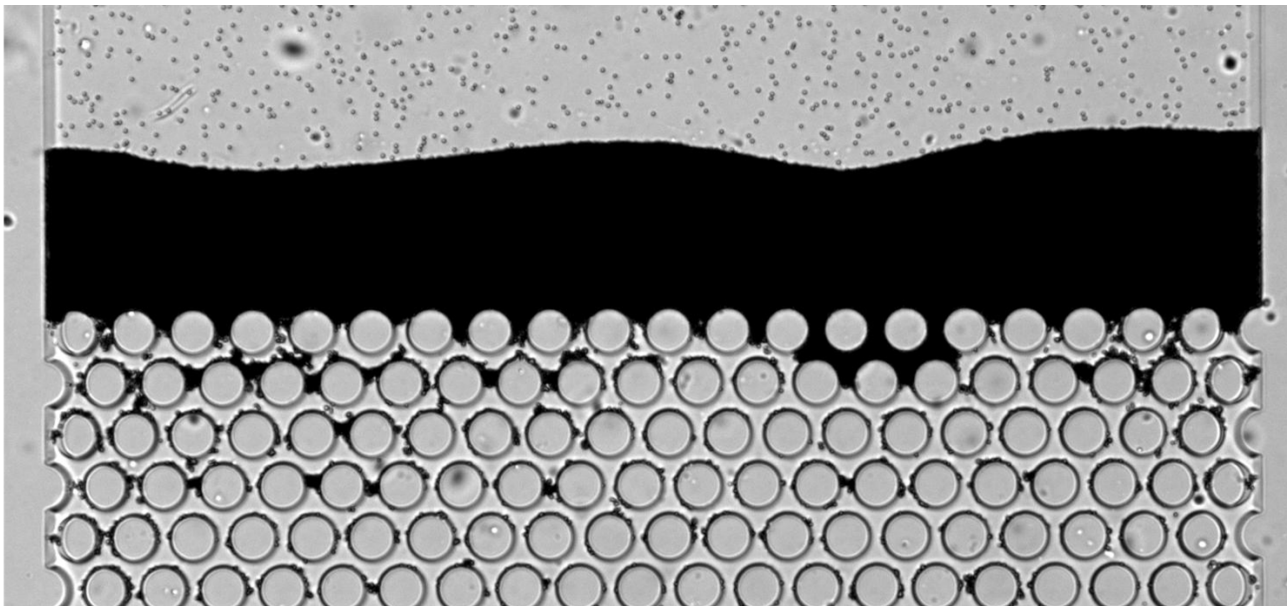
Impact of interaction potentials on the clogging

Chapter 8

Flow decline during the clogging of porous media

Chapter 9

Clogging with fragmented colloid plastics



Chapter 6

The clogging of interconnected pores by colloidal particles

The main objective of this chapter is to provide the first image-based study of the complete clogging of a model ordered porous medium by colloidal particles. We first describe the phenomenology of the clogging process of the entire porous medium, then we determine the different clogging mechanisms at the pore scale and the effect of the cross-talk between adjacent pores in the clogging dynamics. We also study the influence of the geometrical features and the flow rate on the clogging process. We provide a simple clogging model based on the capture of aggregates that faithfully describes the clogging dynamics in the experiments.

Contents

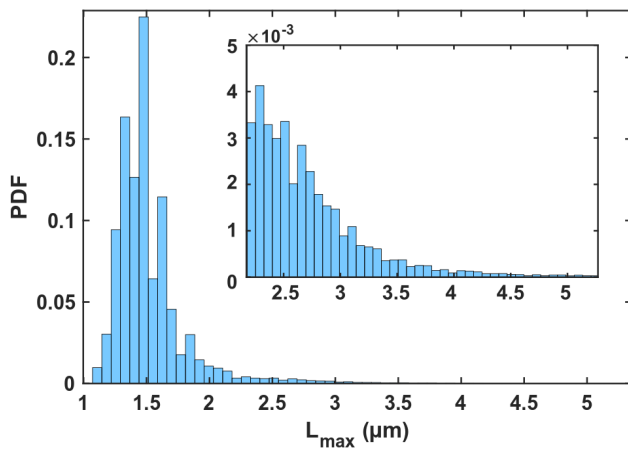
6.1	Experimental clogging of porous media	160
6.1.1	General description of a clogged porous media	160
6.1.2	Different clogging mechanisms	162
6.1.3	The strong dependence on pore clogging	164
6.1.4	Clogging is independent of the porous medium geometry and flow rate	166
6.2	Simulated clogging of porous media based on statistics	169
6.2.1	Four steps process	169
6.2.2	Modelling of the impact of aggregates on clogging	175
6.3	Conclusion	182

6.1 Experimental clogging of porous media

Here we consider the clogging dynamics of porous media by a colloidal suspension. These porous media are ordered, with a radius collector R_c and spacing between collectors D_p . Based on the main results of the first part, we described the phenomenology of the clogging process inside the media, to understand where are the clogs located in a porous medium before no more particles can pass through the pores and if the dependence between pores induces a dependence between clogs. We varied the geometric parameter R_c and D_p of the porous media to observe their influence on the clogging process, as well as the flow rate. We also introduced a new clogging mechanism coming from the cross talk between adjacent pores.

6.1.1 General description of a clogged porous media

We used exclusively of $1.5\mu\text{m}$ PS particles whose size distribution is thus very peaked, with hence mostly single particles and around 1.5% of aggregates, with less than 0.1% of them being larger than doublets (table 6.1 and figure 6.1.1).



Particle type	Number	%
Single	1 407 960	98.5
Doublet	20 516	1.43
Triplet	227	0.015
Quadruplet	17	0.001
Aggregate	7	0.0005

Figure 6.1: Size distribution of the largest dimension L_{max} for $1.5\mu\text{m}$ PS suspension.

Table 6.1: Proportion of objects from the stop and go experiment.

The porous media were imaged every 10s to have access to the clogging dynamics of the whole medium. In the example of figure 6.2, particles were injected in the medium with a constant pressure corresponding to an initial flow rate of $1\mu\text{L}/\text{min}$ into a porous medium with $R_c = 55\mu\text{m}$ and $D_p=10\mu\text{m}$. Clogs form progressively over time and seem to appear randomly in the medium until the first five minutes. However, later on, most of the clogs appear at the entrance and spread on the overall width. The experiment is finished when particle cannot pass anymore through the medium and when a line of clogs is formed at the very entrance of the medium. It can be noted that an accumulation of particles grows behind clogged pores (white rectangle in figure 6.2) while particles still pass through other free pores (blue rectangle in figure 6.2).

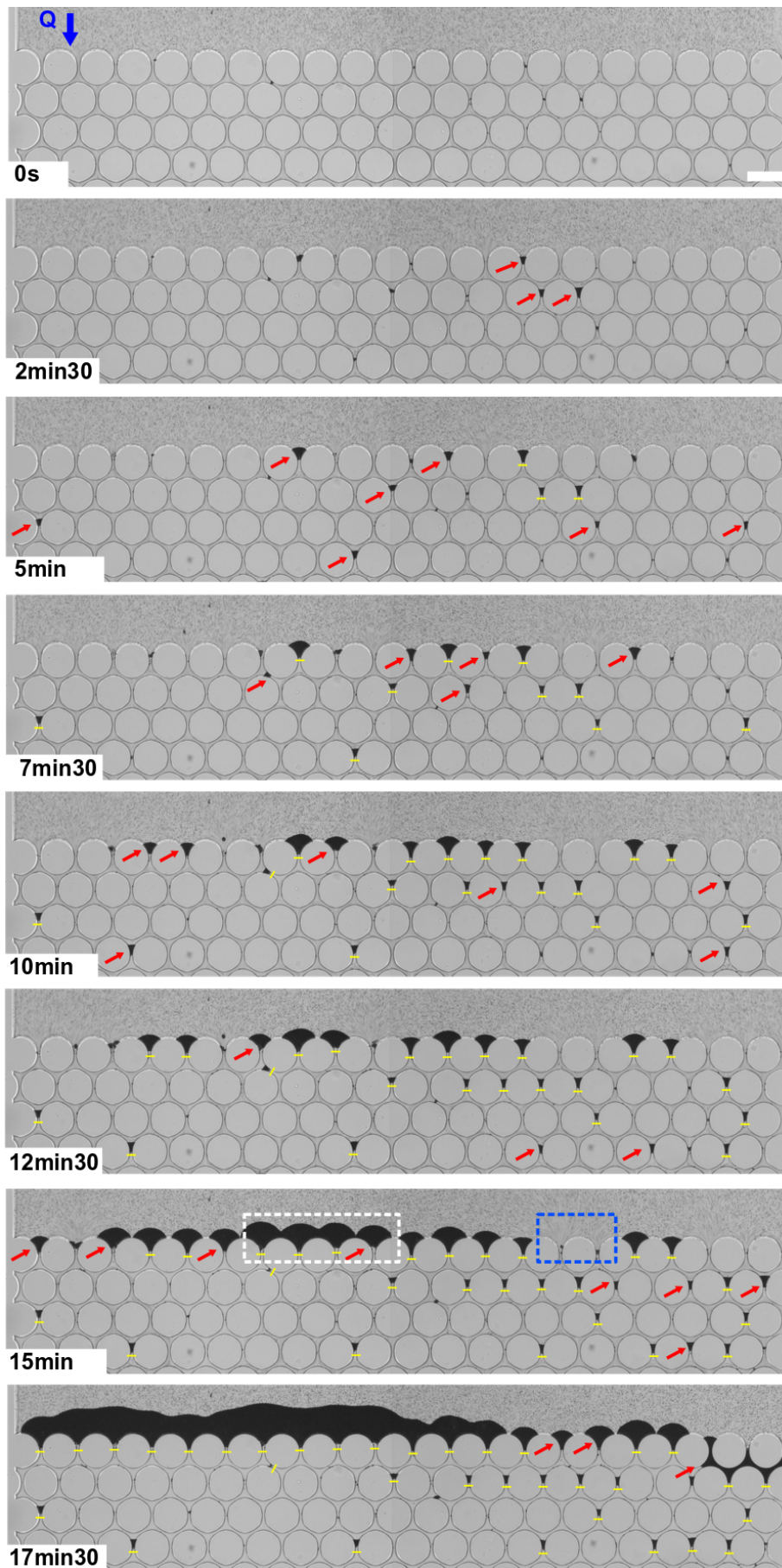


Figure 6.2: Clog formation in a porous medium with $R_c = 55\mu\text{m}$ and $D_p = 10\mu\text{m}$. The arrows indicated the new clogs in the current image and the yellow lines those previously clogged. At 17min30, the porous medium is completely clogged. Blue arrow is the fluid direction. Scale bar: $65\mu\text{m}$.

6.1.2 Different clogging mechanisms

We have identified two types of clogs, the original and the accumulation clogs from the image analysis of various experiments.

The original clog

The original clogs are similar to those formed in single pores (chapter 3). They rely on the progressive accumulation of particles, mainly aggregates. Note that in this new geometry in which pores are interconnected there is no sieving of aggregates larger than the pore size. The dynamics of formation of such a clog is shown in figure 6.3.

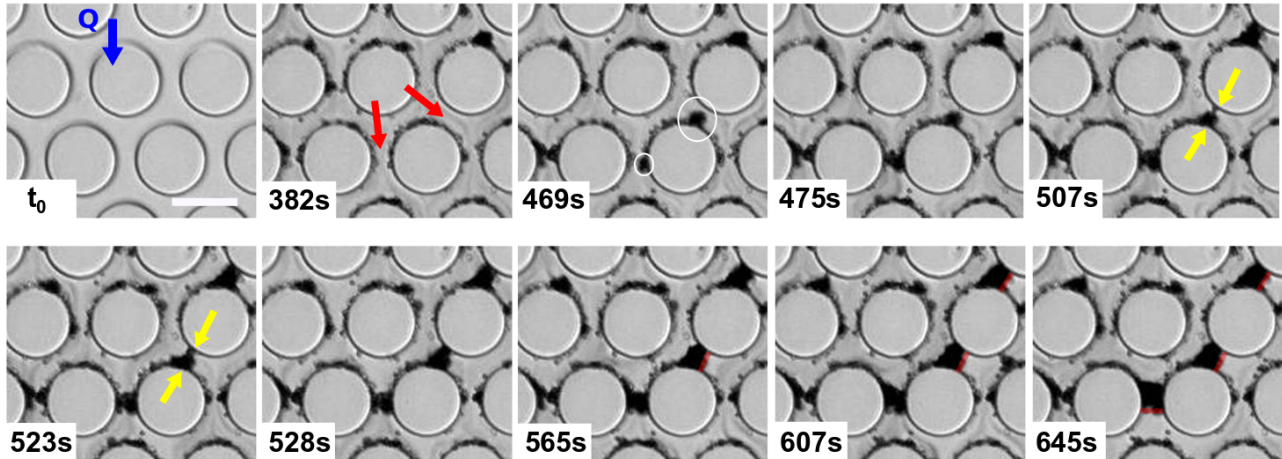


Figure 6.3: The original clog formation. 382s: The red arrows indicate the pores about to be clogged. 469s: two aggregates are deposited in each pore, circled in white. 507s: deposits are formed on both sides of the pore (yellow arrows). 528s: pores appear to be clogged but with consecutive image, we can see that particles continue to pass through. 565s: one of the 2 pores is now clogged (red lines). 645s: the central pore is now clogged in 10.7min. Scale bar: 15 μ m.

The accumulation clog

Once a pore is clogged, the accumulation of particles behind it is really limited (figure 6.4). During the complete obstruction of the pore the deposit is cohesive, i.e., particles that form the deposit adhere on each other. This step is over when no new particles can pass through the pore. Particles then accumulate at the rear of the cohesive part of the clog but without being in contact with the others. These particles are held together by the fluid pressure and hence form a dense assembly of repulsive objects since they are negatively charged. However when the medium is completely clogged, there is a flow decline in the pore and particles of the labile part leave the clog since they are not maintained together anymore.

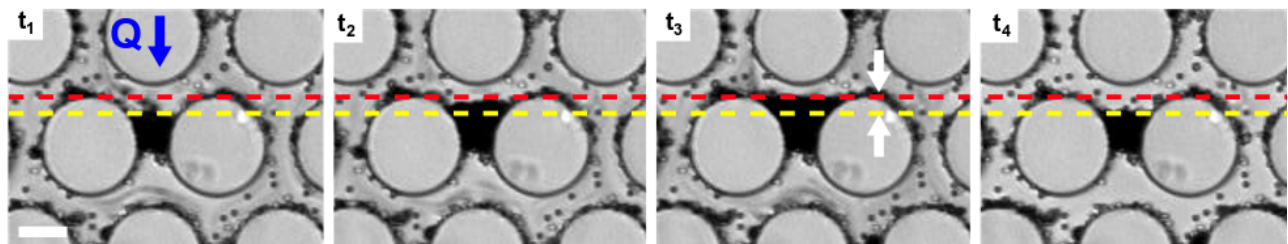


Figure 6.4: Example of the temporary accumulation behind an isolated clog with 50mM. The pore clogs at t_1 and an accumulation behind it begins at t_2 . From t_3 the maximal accumulation is reached, indicated by the red dashed line. The medium is completely clogged at t_4 and because of the flow decline following it, the accumulation leaves. Red dotted line indicates the maximal accumulation and the yellow the limit of the cohesive clog when the labile part is gone.

However, in some cases the configuration of nearby clogged pores can promote trap zones for particles. A trap zone is always composed of several original clogs, spatially organized such that particles cannot be redistributed in the rest of the medium and are forced to accumulate in the pores behind the original clogs until they fill them (see on figure 6.5).

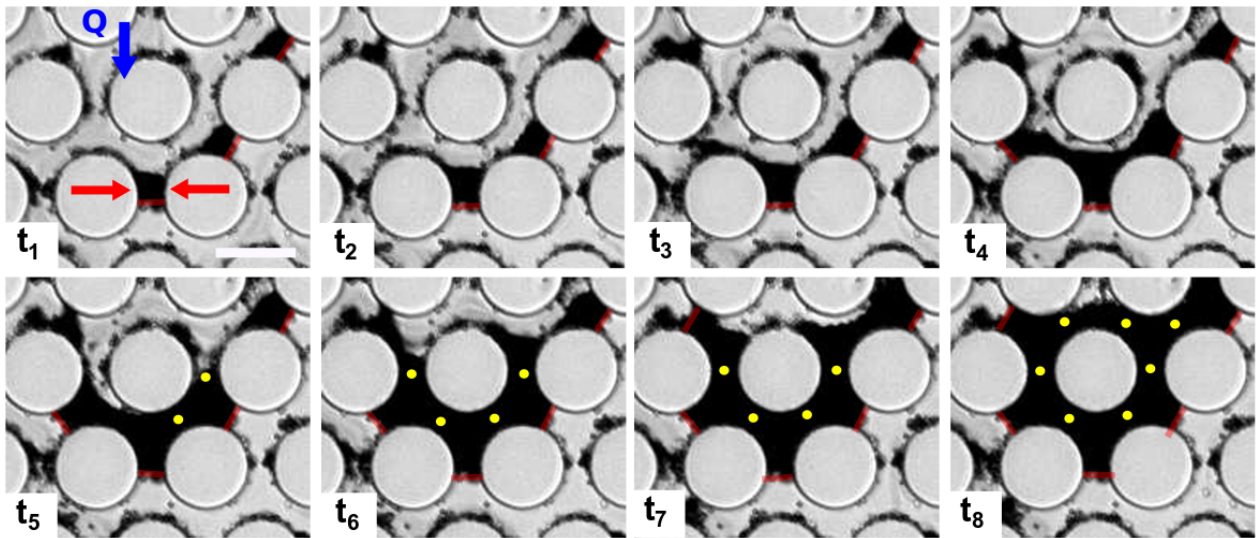


Figure 6.5: The formation of an accumulation clog. Three original clogs are formed at t_1 (red lines). Several minutes later at t_2 , the accumulation in the pore with red arrow reached its maximal value and the particles flow in an adjacent pore on the left of the three pores that ends up to be clogged at t_4 . This spatial arrangement of clogged pore allows the formation of a trapping zone in which particles have to accumulate and lead to the clogging of two other pores at t_5 (yellow dots). As the accumulation keeps going five other pores can be obstructed at t_8 . Scale bar: $15\mu\text{m}$.

6.1.3 The strong dependence on pore clogging

We are interested in the spatio-temporal dependence of the clogs. Previous studies have found that the clogging of parallel pores is independent and hence pore clogging is a poissonian process. In this configuration, Sauret et al. (2014) used a $2\mu\text{m}$ suspension in which there are very few large particles, larger than the pore width. They show that the distribution of time intervals dt_{clog} between each clog, corresponding to the sieving of a large particle, is well fitted by a Poisson law. For a porous medium as in our case, there are cross talks between pores since they are interconnected. Typical distributions of the time intervals from our experiments are shown in figure 6.6 for the same experimental conditions. While about half of the clogs forms within a short time interval, the other half forms after a much longer time. A poissonian process is a no-memory process, so the time interval between two events at a time t is independent of the behavior of the time distribution before t . Because of the presence of these two distinct intervals of clog formation, the distribution of clogging time is not a poissonian and more generally not a purely stochastic process, this suggesting there is a sort of dependence between clogging events.

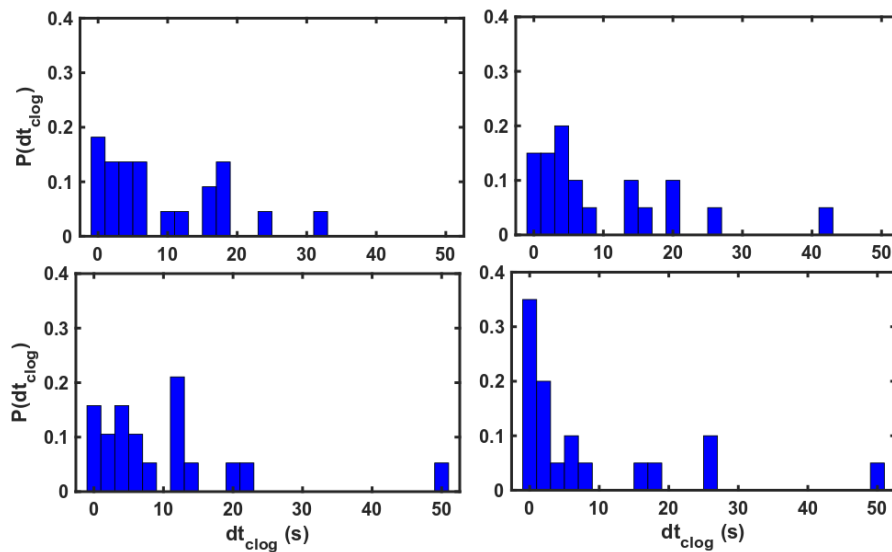


Figure 6.6: 4 distribution of the clogging time intervals for a porous medium, from in the same experimental conditions.

Similarly, Liot et al. (2018) showed that a clogged pore has a direct influence on its nearest adjacent pores. The probability to form a clog near another one decreases with the distance Δx between them. This is still not the case in our media, where clogs can form at an equiprobable distance from the previous clog (figure 6.7a). We can also see that there is no spatial correlation between the appearance of each clog along the width of the medium (figure 6.7b). In the study of Liot et al. (2018), the strong dependence between a clogged pore and its neighbours is justified by the repartition of particles in the free neighbouring pores. This is also true for our medium, however, pores are closer to each other allowing a greater dispersion of the particles in a greater number of pores, not just on these on both sides on the clogged pore. In a porous medium, when a pore is clogged the local hydrodynamic resistance increases, and if there are only few clogs, the distribution of particles remains homogeneous in the medium. But when the clogs start to be concentrated somewhere, the local hydrodynamic resistance increases notably and the flow is no longer homogeneous. Particles are still distributed in the whole medium, but more particles flow through lower resistance paths than elsewhere. The position of clogs is not dependent of its neighbouring in a porous medium, but rather of the local hydrodynamic resistance.

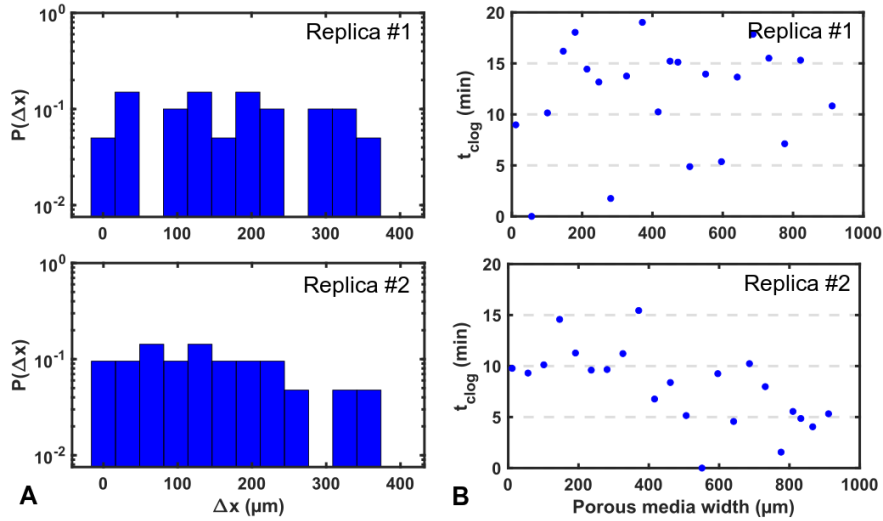


Figure 6.7: Probabilities distribution to be clogged at Δx from the previous clog (a) and the exact x-position over time (b)

Another way to estimate the mean time interval between clogging events is to consider the properties of the suspension. Previously Wyss et al. (2006) showed that the average clogging time is dependent on the number of particles passing through the pore, i.e. the volume fraction Φ of the suspension as well as the flow rate Q :

$$\langle t_{\text{clog}} \rangle = \frac{1}{\Phi Q} \quad (6.1)$$

Wyss et al. (2006) noticed the presence of large objects inside their suspensions but do not take them into account. Sauret et al. (2014) also worked with a small fraction of large particle and they modified this expression, using the concentration of these objects rather than the particle volume fraction:

$$\langle t_{\text{clog}} \rangle = \frac{1}{cQ} \quad (6.2)$$

To take into account the particle repartition when pores are clogged, Sauret et al. (2018) propose the following modification of the dominant population:

$$\langle t_{\text{clog}} \rangle = \frac{1}{c(N - k_c)q} \quad (6.3)$$

With N the total number of pores, k_c the number of clogged pores and q the constant flow rate in each pore.

Based of this relation, we can estimate in our case the time clogging of a porous medium, by replacing by the aggregate concentration $f_{ag\text{suspension}}$ (figure 6.8a). It turns out that the results strongly differs from experimental curves obtained with a porous medium (figure 6.8b). The experimental curve is rather distorted with temporal zones without clogging event while in other shorter ones there is a cascade of clogs. However, there are no aggregates large enough to clog the pore by sieving and the clog always results from the capture of several aggregates, whose spatial concentration is not constant.

To simulate a random arrival of aggregates, we determine between each clog event i a new concentration of aggregate f_{ag_i} . This concentration follows a normal law $\sim \mathcal{N}(0,1)$ and we impose:

$$0 < f_{ag_i} < 2f_{ag\text{suspension}}$$

In this way, after the N clogging events, we keep the same aggregate ratio measured in the suspension:

$$\sum f_{ag_i} \approx f_{ag\text{suspension}}$$

With this modification, the relationship 6.3 can now better mimic the experimental curve, with a clogging time of the same order of magnitude. However, this remains a crude approach, since the aggregates according to their size have not the same impact on the clogging process. Moreover, the relation $Q \approx (N - k_c)q$ is

not exact for a porous medium, as we will discuss in chapter 8.

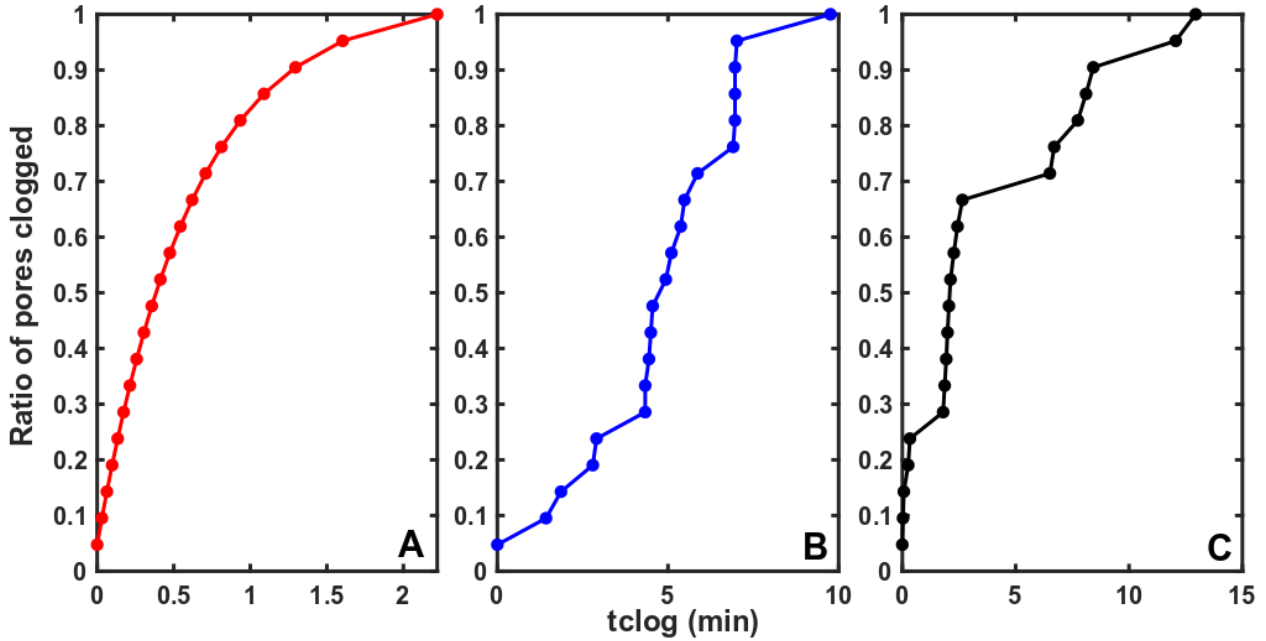


Figure 6.8: The clog front formation over time estimated with the relation 6.3 with $f_{ag_{suspension}}$ (a), for an experimental curve (b) and estimated with a random fraction of aggregates $\langle t_{clog} \rangle = 1/(f_{ag_i}(N - k_c)q)$ (c).

The repartition of the objects in the neighbouring pores combined with a random arrival of aggregates can cause a cascade clogging effect. It is not the position of the clogs that would drive the clogging dynamics of a porous medium, but the increase of local hydrodynamic resistances which limits the passage of particles and the aggregates. In this way, there is effectively a dependence between clogs.

6.1.4 Clogging is independent of the porous medium geometry and flow rate

We investigate in this part the impact on the clogging dynamics of the geometrical parameters of the medium such R_c and D_p . We first quantified the number of clogged pores for each row in the porous medium. A row, defined on figure 6.9, includes interstitial pores and pores parallel to the direction of flow, and is composed of about 60 pores.

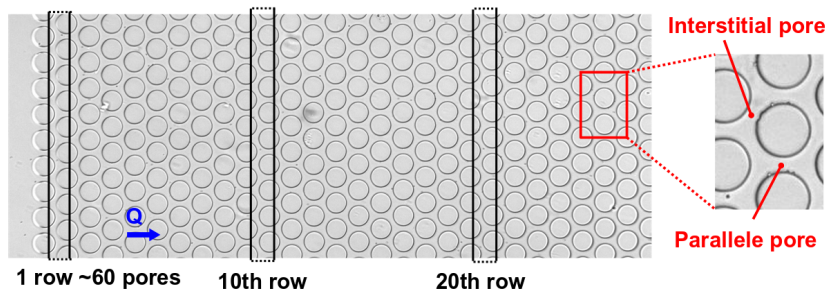


Figure 6.9: Definition of a row, composed of around 60 pores, interstitial and parallel pores to the flow.

Several configurations of porous media have been tested, with various R_c and D_p to observe their influence on the clogging process by impacting the capture probability of objects. For each medium, we adapted the pressure to keep the same initial flow rate and hence the shear in the medium can vary according to its geometry. The evolution of the ratio of clog pores along the flow direction for nine configurations with $R_c = 15, 55$ and $75\mu\text{m}$ and $D_p = 10, 20$ and $30\mu\text{m}$ (figure 6.10). All of these configuration have a height of $15\mu\text{m}$. The main observation is that the clogs are always concentrated, whatever the configuration, at the entrance of the medium, within the first five rows. On all the graphs, the ratio of clogged pores drops to 0.1 or less from the 3rd row, pore clogging beyond this position is thus negligible, corresponding to 1 or 3 clogs per row.

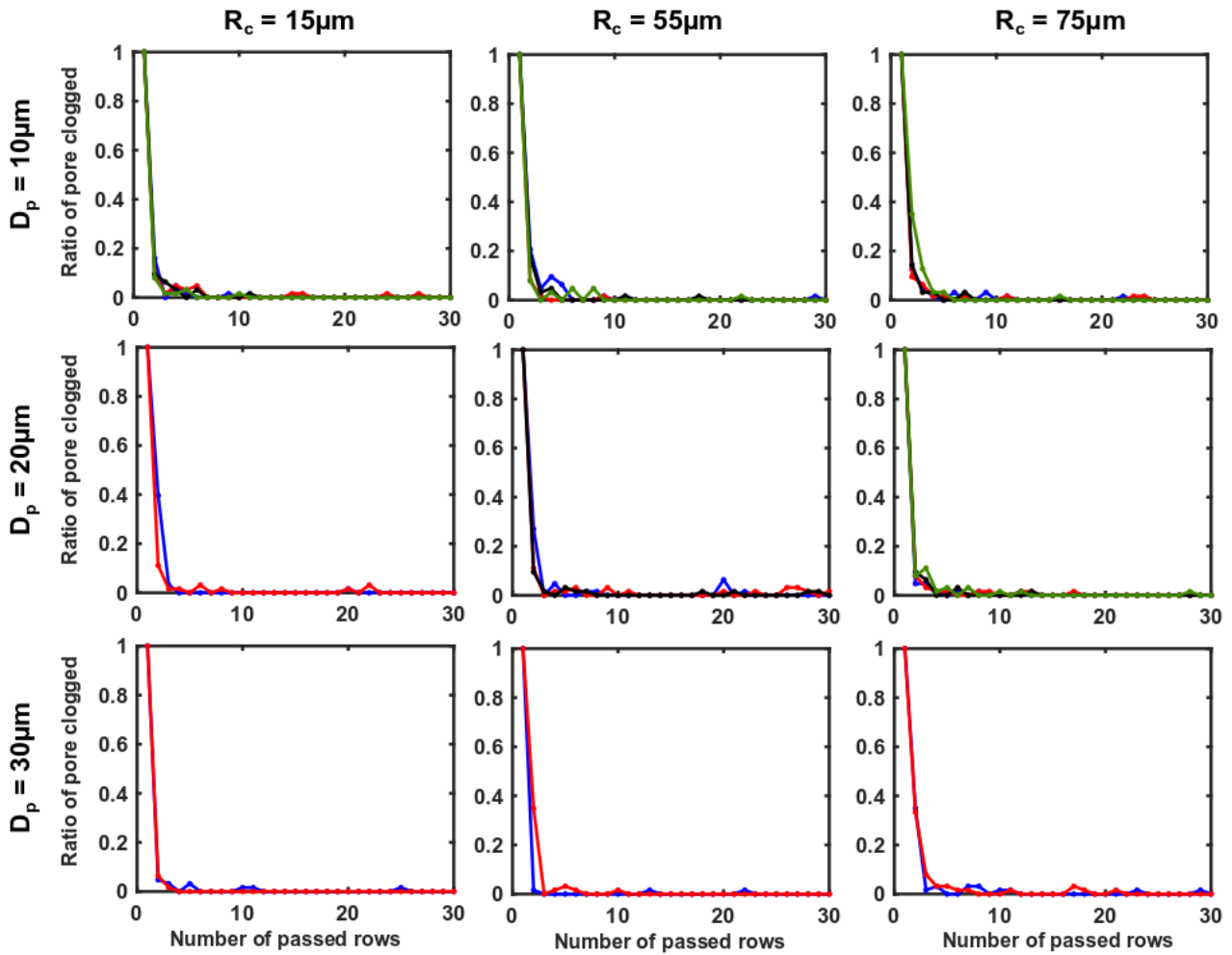


Figure 6.10: Evolution of the ratio of pore clogged with the number of passed row for R_c and D_p . A curve corresponds to a single experiment. An experiment is over when no more particles can pass through the porous medium.

With the same methodology, we investigated the impact of the flow rate on the clogging dynamics, with $D_p = 10\mu\text{m}$ for three radii. We varied the flow rate from $0.3\mu\text{L}/\text{min}$ to $2.5\mu\text{L}/\text{min}$ and we obtain the same conclusion as in the previous paragraph, the clogs are concentrated at the medium entrance and there is a drop of the number of clogs down to 0.1 after only the 3rd rows of pores (figure 6.11).

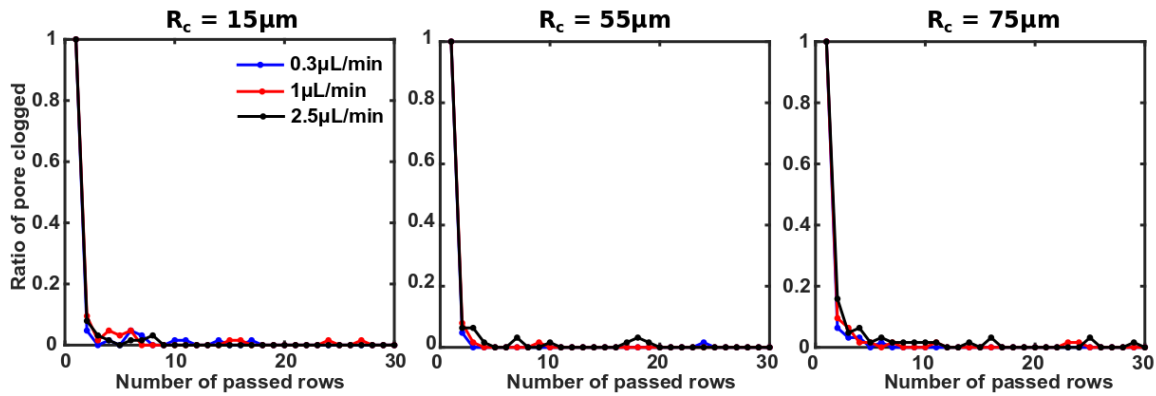


Figure 6.11: Evolution of the ratio of pore clogged over the number of passed row for various flow rate and R_c , with $D_p = 10\mu\text{m}$.

We can conclude that neither the size and spacing of the collectors geometry nor the flow rate, in the range we used, have any impact on the clogging process of the medium. For all the conditions, the pores are clogged in the same way, mostly with the formation of original clogs (figure 6.12).

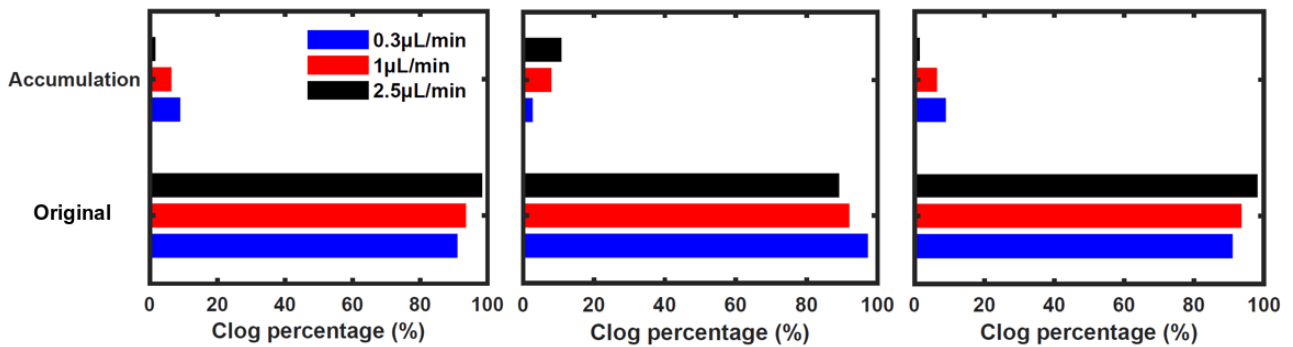


Figure 6.12: Proportion of original and accumulation clogs depending on R_c and Q , with $D_p = 10\mu\text{m}$.

The occurrence of original clog is based on the statistics of the suspension, i.e. the capture probability and size distribution of aggregates. The larger an aggregate, the greater is its capture probability. This mechanism of capture favours the deposition of these object in the first encountered pores. In the following, we provide a simple modelling of the clogging dynamics of a porous medium based only on the statistic of aggregate capture to see whether or not there are other mechanisms that explain why porous media are always clogged at their entrance.

6.2 Simulated clogging of porous media based on statistics

We propose a simple numerical simulation of the clogging of our ordered porous medium, based on the main observation of the thesis: the tail of the size distribution of a suspension is mainly responsible for pore clogging since the aggregates have a high capture probability. To test the dependence on the clogging process on the particle size distribution we modify this distribution in our model. In the same way, we also change the probability of capture.

In this model, we only consider the repartition of objects in the whole medium, by simulating the size of the different aggregates and determining for each object that passes a pore whether it is deposited or transported to the next pore. When the volume of a pore is filled, the pore is considered to be clogged and the incoming particles are distributed into the adjacent pores.

This simple model takes into account the experimental size distribution of aggregates to perform a random selection of the objects that arrive at the entrance of the medium. We suppose that the capture probability of the aggregates depends only on their maximum length, L_{max} . This means that we do not take into account the DLVO interactions either on the pore surface or among particles. This probability does not depend neither on the degree of fouling of the pore. The clogging criterion of each pore is only based on its volume and avoids considering dynamics of the deposition of the objects in a pore or simulating the complex stacking of objects with irregular shapes. In doing so, we neglect the hydrodynamic interactions of the flowing objects with the deposit.

We first present the different steps of the simulation, then we introduce several results obtained with the model by modifying the size distributions and the capture probabilities. In the last part, we present some points that have to be integrated in the simulation to better describe the experimental data.

6.2.1 Four steps process

Until the porous medium is completely clogged, the simulation performs loops, each of these being composed of four steps:

1. Before entering in the medium, a number of objects is generated and the aggregates size are randomly determined.
2. Row by row, objects are transported through the medium. At each passage in a pore, based on its capture probability and its size, an object is either captured by the pore or transported to the next one. This step stops when all the objects are deposited or have gone through the medium.
3. The state of each pore is re-evaluated as clogged or free according to a fouling rate criterion.
4. If the medium is not completely clogged, we repeat step 1, 2 and 3, otherwise the simulation is over.

Step 1: initialization of the aggregates

For each loop we let fluctuating the number of aggregates that are transported and we randomly determine the aggregates size based to the experimental size distribution.

The concentration of aggregates in a loop

Let N_{tot} be the total number of objects which are considered in a loop. N_{tot} are equally distributed in all the pores not clogged k_f . Thus, at the beginning, N_{pore} particles passes through a pore of the first row:

$$N_{pore} = N_{tot}/k_f \quad (6.4)$$

N_{tot} is constant and experimentally determined, by counting the number of particle passing into the porous medium during a one minute period. We also assume that the redistribution of objects between the pores is equal.

We consider a fluctuating aggregate concentration f_{agloop} for each loop since the number of aggregates in only of the order of one to several hundred of particles and thus are no statistically reliable. For a distribution of one million objects, the concentration of aggregate $f_{agsuspension}$ is statistically reliable. However, here there is a very small portion of aggregates that are considered in a loop. As in the section 6.1.3 we impose that:

$$0 < f_{agloop} < 2f_{agsuspension}$$

$$f_{agloop} \sim \mathcal{N}(0, 1)$$

Thus, considering all the aggregates arriving in the medium in the entire simulation, we respect $f_{agsuspension}$, without creating or ignoring aggregates:

$$\sum f_{agloop} \approx f_{agsuspension}$$

Then from f_{agloop} , we determine the number of aggregate N_{ag} coming into the medium for a loop:

$$N_{ag} = f_{agloop} N_{tot}/k_f \quad (6.5)$$

The size distribution of aggregates

We assign a size to each aggregate that enters inside the medium from the experimental size distribution, considering only the part of the objects larger than $2\mu\text{m}$ (figure 6.13a) since others are singles. This truncated distribution is well fitted by a power law (figure 6.13b) , from which we deduce the cumulative distribution function also called F_x (figure 6.13c).

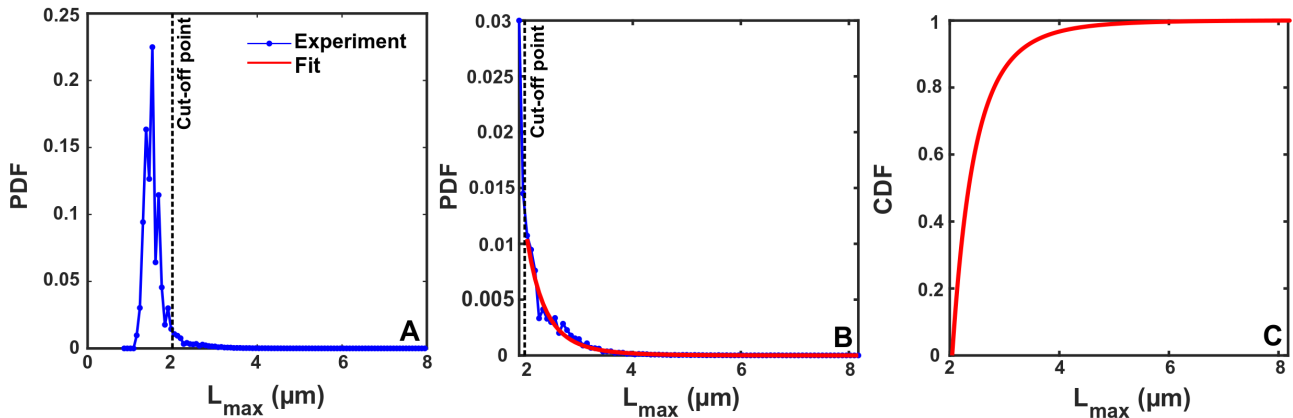


Figure 6.13: From an experimental size distribution of $1.5\mu\text{m}$ particles (a), we select only the size relevant for aggregates and we fit this selection (b) to determine the cumulative distribution function F_x from the fit (c)

With the cumulative distribution function F_x , we use the inverse transform sampling to obtain a randomly

number of aggregate sizes for N_{ag} (figure 6.14):

$$X = F_X^{-1}(u) \tag{6.6}$$

$$u \sim \mathcal{N}(0,1) \tag{6.7}$$

The figure 6.14 shows how the sampling of 1.10^6 random variables following a normal distribution $\mathcal{N}(0,1)$ generates the distribution of the aggregates at time dt .

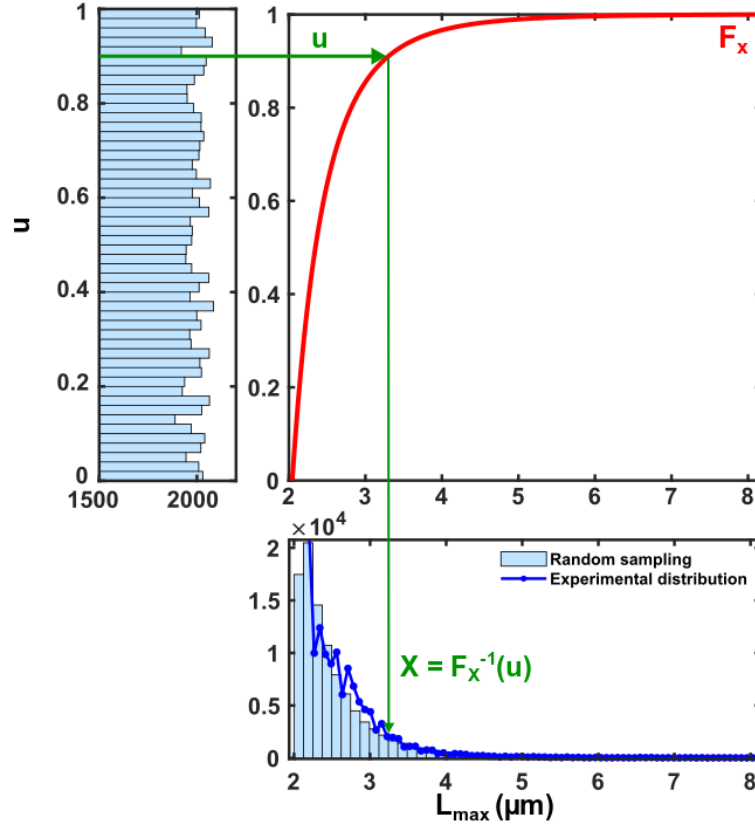


Figure 6.14: Illustration of the method of the inverse sampling. From a variable u resulting from a random sampling, is obtained X here L_{max} . This reversal is done thanks to the inverse of the cumulative distribution function.

Step 2: particles partition and deposition inside porous media

Once the aggregates size distribution is determined, the objects are distributed through the whole porous medium, avoiding the pores already clogged in a previous loop. At each passage of an aggregate in a pore, we determine if it is deposited or it leaves the pore.

Example of objects repartition inside porous media

The main flow rules of particles repartition used in the simulation are illustrated in figure 6.15a. There is only a single path for interstitial pores while there are two possible paths for parallel pores. When a particle encounters a clogged pore (figure 6.15b-d) it finds its way towards the nearest adjacent pore. When there are multiples possible paths objects are equally distributed in each path.

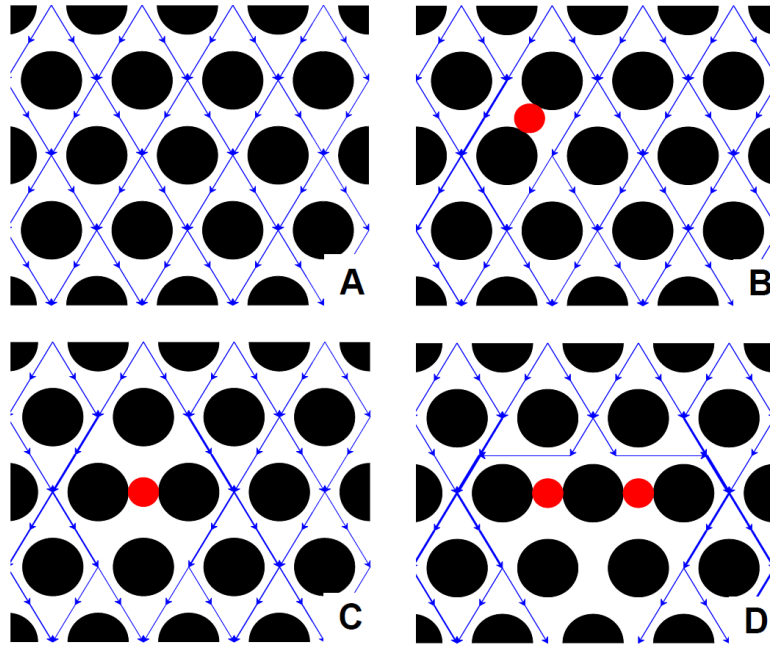


Figure 6.15: The main rule of particle repartition inside the porous medium for an empty medium (a), a medium with an interstitial pore clogged (b) with a parallel pore clogged (c) and a horizontal displacement of particles imposed by the clogging of two adjacent pores (d). Particle paths are represented by blue arrows. Black filled circles are the collectors while red ones are the clogged pores.

Objects deposition

When an object arrives in a pore, it is either captured or transported in the next pore. To choose its deposition, we use a capture probability experimentally determined for five categories of objects : single, doublet, triplet, quadruplet and larger aggregates. Thus for a given size we attribute a capture probability P_{clog} . For each object we have:

$$\begin{aligned}
 P_{object} < x &: \text{the object is deposited} \\
 P_{object} > x &: \text{the object is transported} \\
 x &\sim \mathcal{N}(0,1)
 \end{aligned}$$

Step 3: detection of pores clogged and trapping zones

As in the experiments we make a distinction between original and accumulation clogs. For an original clog, we need a criterion to determine after the deposition of objects whether a pore is clogged or not. For an accumulation clog, it is necessary to detect if trapping zones exist in the porous medium.

The original clog

We monitor the evolution of the deposited volume inside the pore. For each object deposited in a pore, the volume of the aggregate is deduced from the volume of the pore (figure 6.16). For single up to quadruplet, their volume is exact, and for larger aggregates we estimated its equivalent volume: $V_{eq} = \frac{4}{3}\pi(L_{max}/2)^3$. A pore is clogged when the volume of objects deposited in this pore is equal to the volume of the pore. However, as seen in chapter 4, the accumulation of objects is far from being perfectly compact, the particles are undeformable and the stacking is composed of objects of variable size. We thus introduced a permeability parameter ϵ :

$$0 < \epsilon < 1 \quad (6.8)$$

The greater this parameter the lower is the compacity of the clog and the lesser objects composed the clog. A pore is considered clogged when the volume of deposited object $V_{deposited}$ equals the product of ϵ and the pore volume V_p :


$$V_{deposited} \geq \epsilon V_p$$


Figure 6.16: Schema of the pore volume considered.

The accumulation clog

After the detection of clogged pores at the end of the loop, it is necessary to check that these new clogs do not create trapping zones, where particles are forced to accumulate without being able to be distributed in the rest of the medium. The figure 6.17 presents some examples of trapping zones. When a pore is detected as an accumulated clog, no more particle can pass through it and will be avoided by the particles.

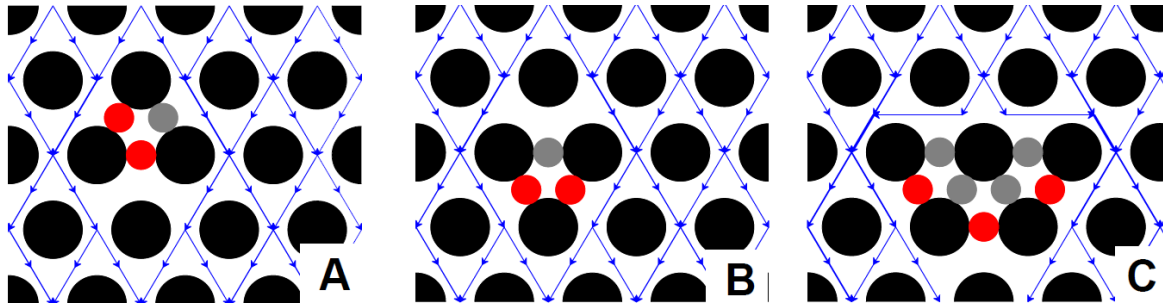


Figure 6.17: Several examples of trapping zones. Gray filled circles are the pores clogged by accumulation while the red one are original clogs.

Step 4: is the porous medium completely clogged?

At the end of the three previous steps, the model systematically tests if the new clogs formed during the loop have allowed the porous medium to be completely blocked. A medium is completely clogged if the first line consists only of pores clogged by accumulation or by original clogs (figure 6.18). If this is not the case, we return to step 1 and a new aggregate distribution is randomly determined.

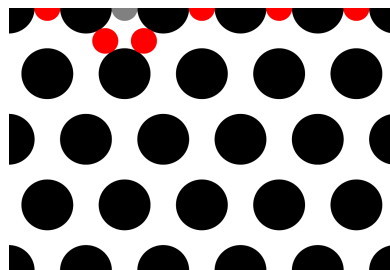


Figure 6.18: A completely clogged porous medium with 5 pores at the entry that marks the end of the simulation.

We give an example of the clogging simulation of a porous medium with 10 pores wide in figure 6.19. The appearance of clogs is initially slow with only 3 clogs formed before the 16th loop and then accelerates with 3 new clogs that appear after the 19th loop. These clogs are mostly formed at the entrance of the porous medium. The paths available for the particles are progressively clogged in the first row. More complex patterns can appear like the clogs by accumulation at the 24th loop. The end of the clogging is extremely fast before the clogging front appears and the simulation finishes.

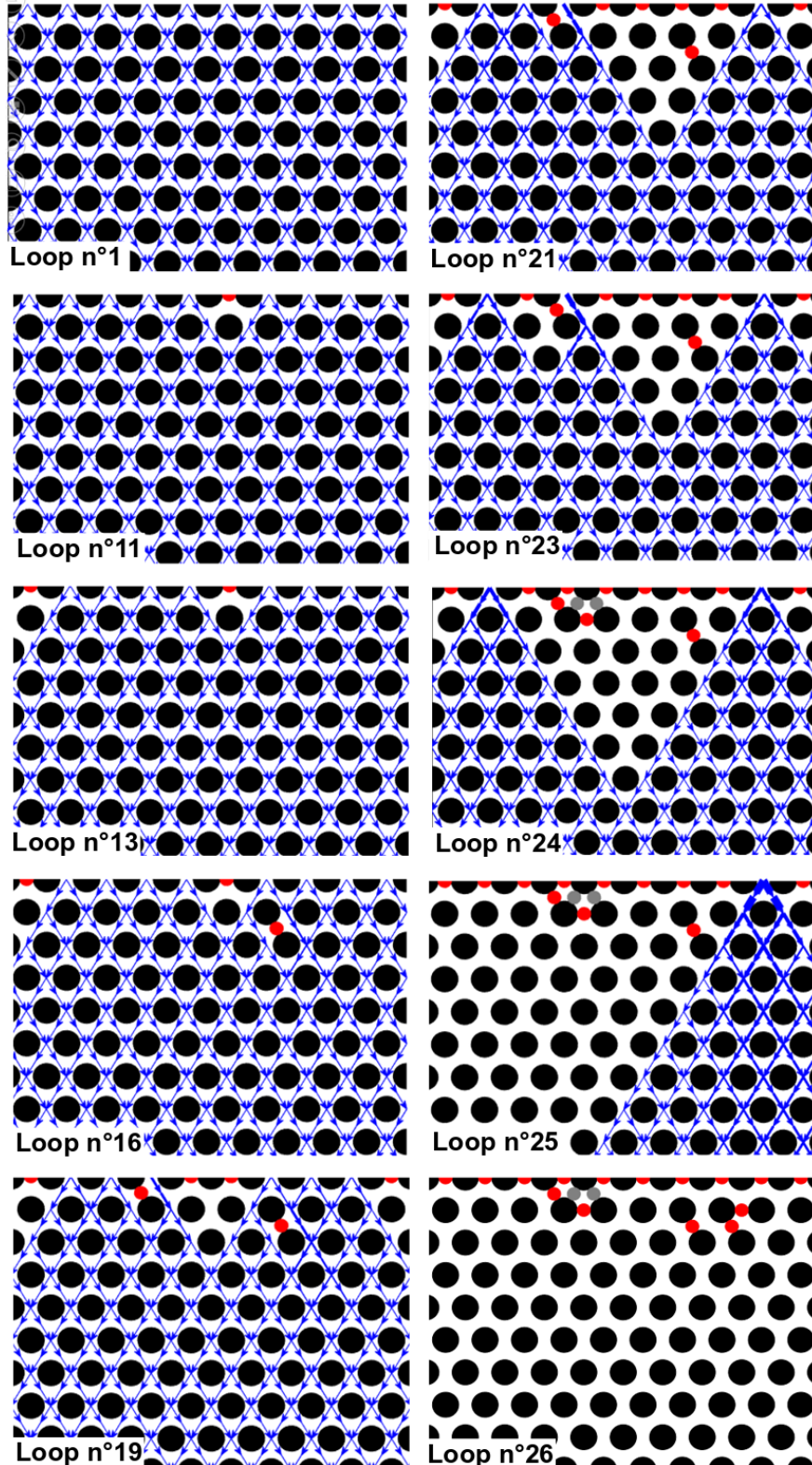


Figure 6.19: Progressive clogging of 10 pores wide medium. The thickness of the arrows increases with the number of particles in the path.

6.2.2 Modelling of the impact of aggregates on clogging

We present here the results by varying both size distribution and capture probability. We used some experimental data to keep a guideline and we change them to highlight the impact on clogging of each feature. We first investigate the role of the small aggregates then how large aggregates can clog a porous medium at their entrance.

We used two very different size distributions to unveil the contribution of each aggregates size (figure 6.20). The first one corresponds to the one used up to now, corresponding to the 1.5 μm PS particles suspension without salt added, called peak distribution in the following. The second one is more spread, called thereafter spread distribution, and have around 60% of aggregates, this distribution is also an experimental one.

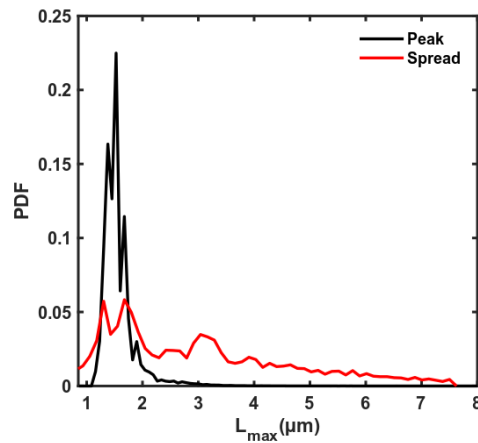


Figure 6.20: The peak and the spread size distributions.

Comparison between the experimental and simulation clogging

The experimental results presented earlier in the chapter correspond to the peak distribution and the capture probability on figure 6.21. We can therefore compare the experiment to the simulation which runs 30 times, in a 100 pores wide porous medium, with $R_c = 15\mu\text{m}$, $D_p = 10\mu\text{m}$ and $\epsilon = 0.6$.

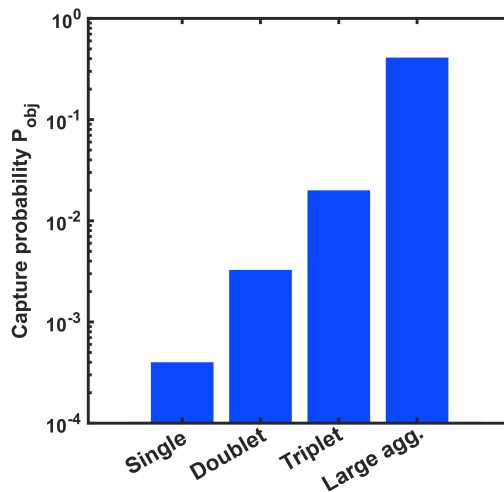


Figure 6.21: Experimental capture probability.

The comparison of the ratio of clogged pores along the medium length shows a strong similarity between experiment and simulation (figure 6.22), with an identical clogging dynamics and very few clogs passed

the 3rd rows.

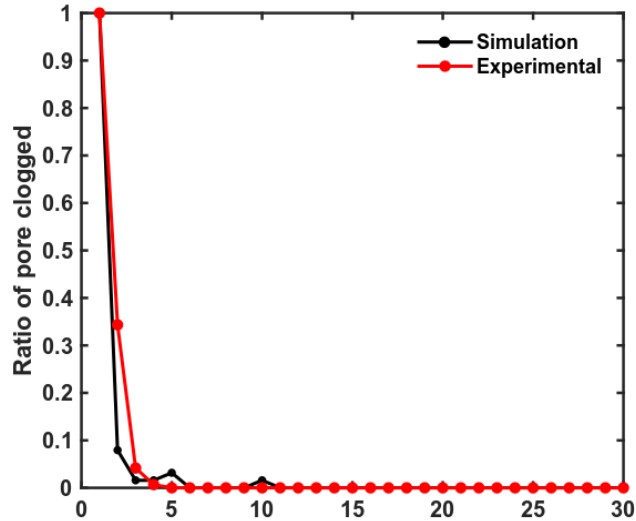


Figure 6.22: Ratio of pore clogged for experiment and simulation.

We have experimentally counted the number of each object composing the original clogs in two pores. A large number of the deposited objects are single particles, but their volume is too small to fill the pore by themselves. To really account for the impact of each deposited object, we estimated their volume V from their maximal length. Figure 6.23 compare V for each type of objects, single, doublet, triplets and other aggregates over the total deposited volume V_{tot} , with experiment and with simulation to understand which object contributes the most to original clogs. Overall, we find a significant proportion of aggregates in the clogs. However, the simulation seems to overestimate the doublets and triplets compared to the experiment.

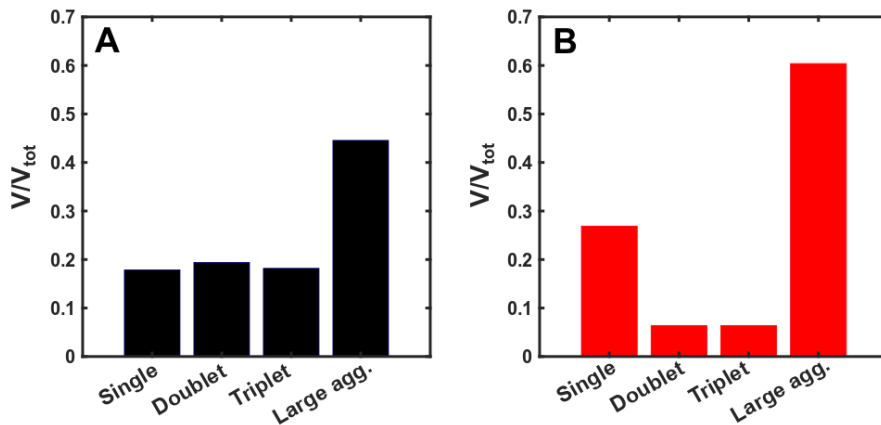


Figure 6.23: Ratio of pore clogged for simulation (a) and experiment (b).

The simulation can also give us access to the evolution of the number of objects deposited in the length of the medium (figure 6.24). The smallest objects like single or doublet are the most numerous deposited in the pores, and also these that go the furthest downstream inside the medium. All aggregates are deposited before the 20th rows since their high $P_{clog,agg}$. Although, because of their large volume, they contribute the most to the pore clogging and porous media are clogged at their very entrance.

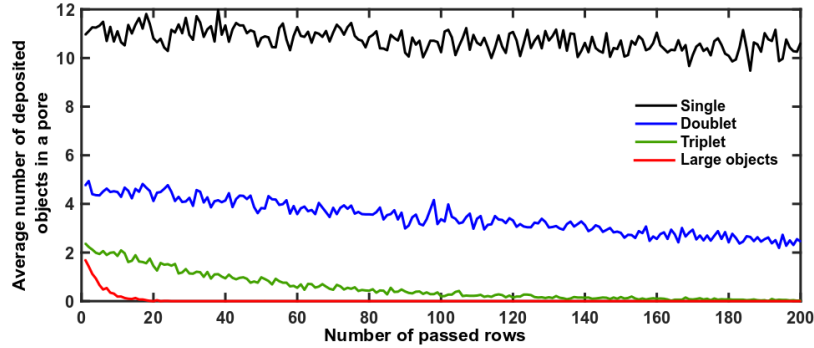


Figure 6.24: Average number of deposited objects in a pore, clogged or not, along the medium length for the simulation result.

Evolution of the clogging with $P_{clog,1-4}$

We want to understand the role of small aggregates, from single up to quadruplet, in the clogging process. We used either a low capture probability for these objects $P_{clog,1-4}$ (figure 6.25a) and a higher one (figure 6.25b) for the two size distributions (figure 6.20). These probability capture are based on experimental data for suspension with, respectively, a strong and weak between repulsion the objects themselves and the wall. Even if the simulation does not take into account the DLVO interaction, the increase of $P_{clog,1-4}$ could impact the clogging by favouring a more important deposit.

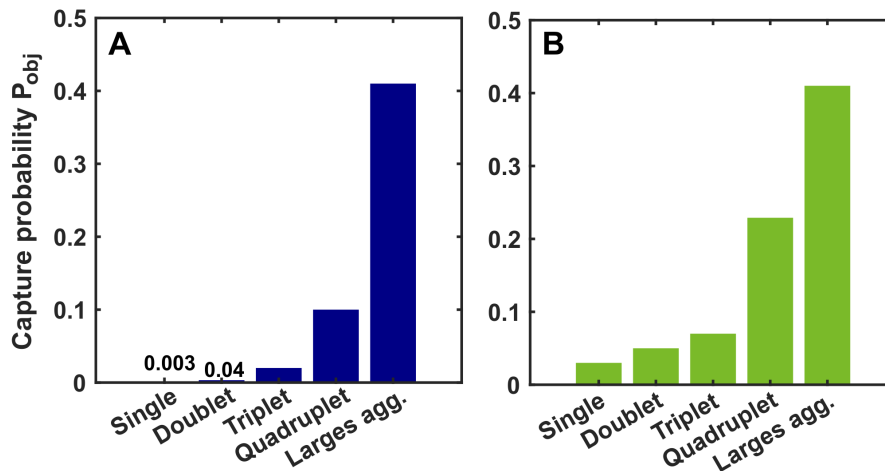


Figure 6.25: Capture probability with a low (a) and high (b) P_{clog} for single up to quadruplet.

As for the experiments, we compared the ratio of clogged pores for the four configurations of size distribution and capture probability. Whatever $P_{clog,1-4}$, the ratio of clogged pores are the same in the four configurations.

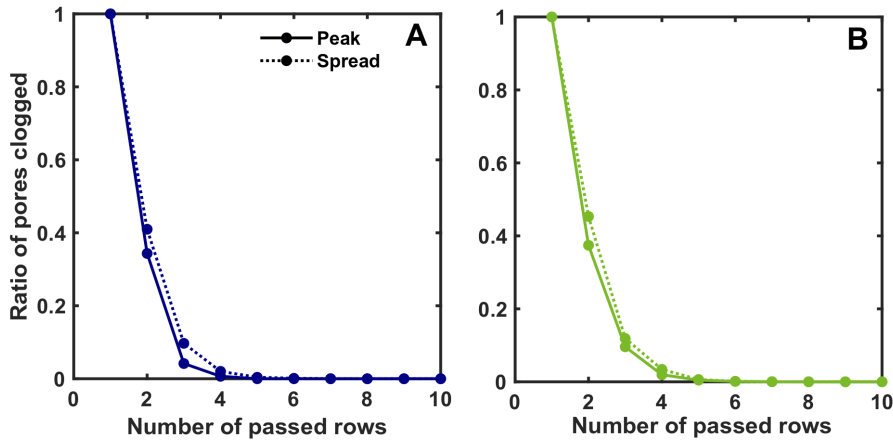


Figure 6.26: Ratio of pore clogged with a low (a) and high (b) $P_{clog,1-4}$ for both spread (dotted lines) and peak (continuous lines) size distributions.

To confirm that the clogging is the same regardless of the number of small aggregate and $P_{clog,1-4}$ we compare which type of object contributes the most to the clog volume. For three of the four configurations, the large aggregates contribute the most to the clogs, except in the case of the peak distribution with high $P_{clog,1-4}$ where singles contribute the most. We can see here a limitation of the model since the simulation is based only on statistics, and does not take into account either DLVO or hydrodynamic force, which can prevent object deposition in the wall experimentally. A perfectly monodisperse $1.5\mu\text{m}$ suspension in $W/D = 10$ as presented earlier in the chapter cannot clog the porous medium because of repulsion between particles themselves and the wall. In this simulation, the medium can be clogged even with an extremely low $P_{clog,single}$, if enough objects pass through the pores. We thus be careful by choosing the parameters of the size distribution and the capture probability and interpreting the results to compare with the experiments.

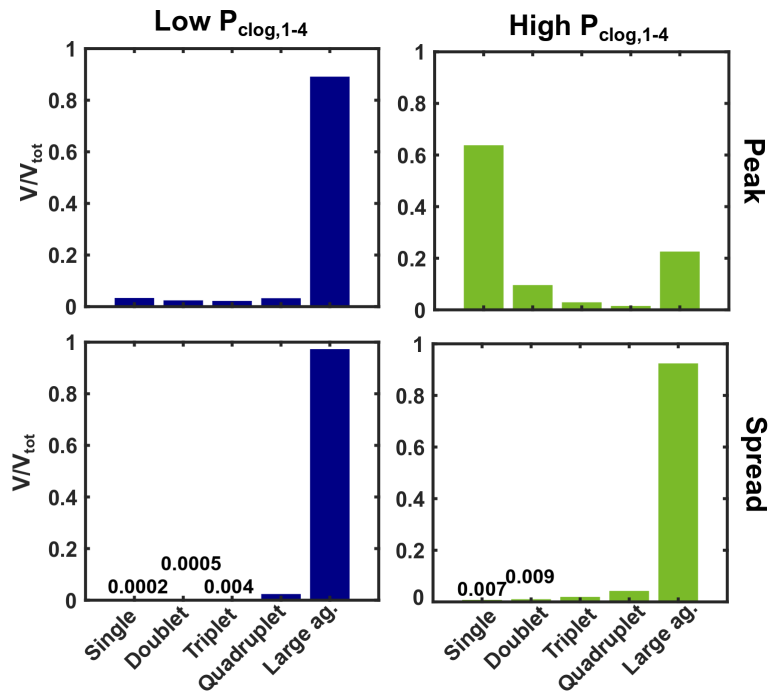


Figure 6.27: Composition of the clogs with for two $P_{clog,1-4}$ and two size distributions.

Evolution of the clogging with $P_{clog,agg}$

We study the impact of the modification of the capture probability of large aggregates $P_{clog,agg}$, that drives the concentration of clogs at the beginning of the porous medium. Here we call small objects the single up to the quadruplet. We fixed their $P_{clog,1-4}$ based on experiment with a weak repulsion between objects and wall, and we varied $P_{clog,agg}$ from 70% down to 0% (figure 6.28). By preventing large objects from depositing from the entrance, we want to observe how clogging is impacted.

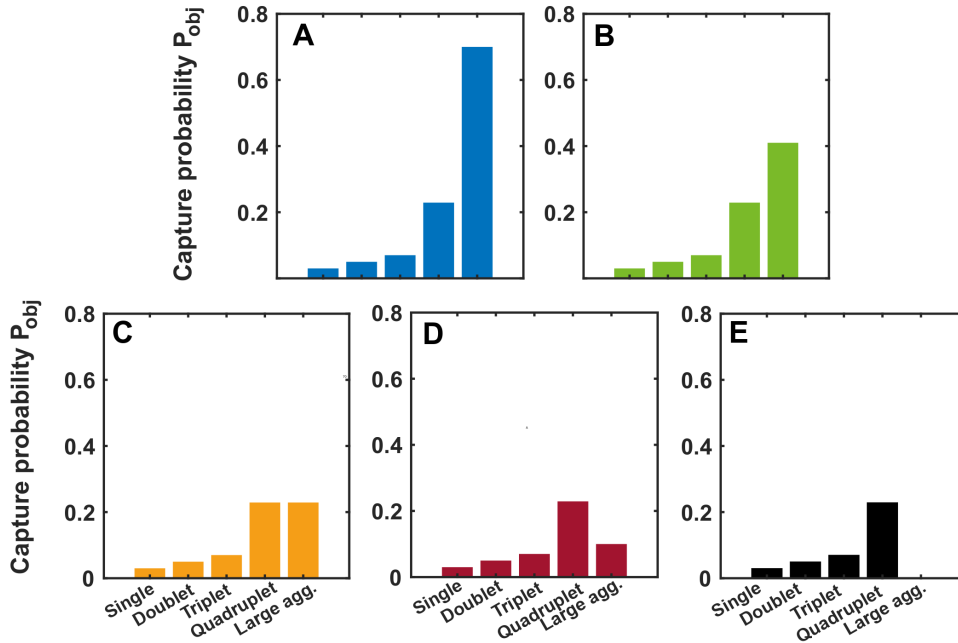


Figure 6.28: The capture probability with $P_{clog,1-4}$ fixed for small objects (single to quadruplet) and for the large aggregate $P_{clog,agg}$ 70% (a), 40% (b), 20% (c), 10% (d) and 0% (e).

Figure 6.29 shows the variation of the clogged ratio over the medium length, for the peak and spread distributions. In both cases, the main observation is that as $P_{clog,agg}$ decreases there are more clogs further into the medium since the deposition of large aggregates is shifted further into the medium. This is particularly the case for the spread size distribution which contains a whole range of aggregates in quantity. What is unexpected is that for $P_{clog,agg}=0\%$, where no more large aggregates are deposited, we have an opposite effect and the medium clogs again at the entrance.

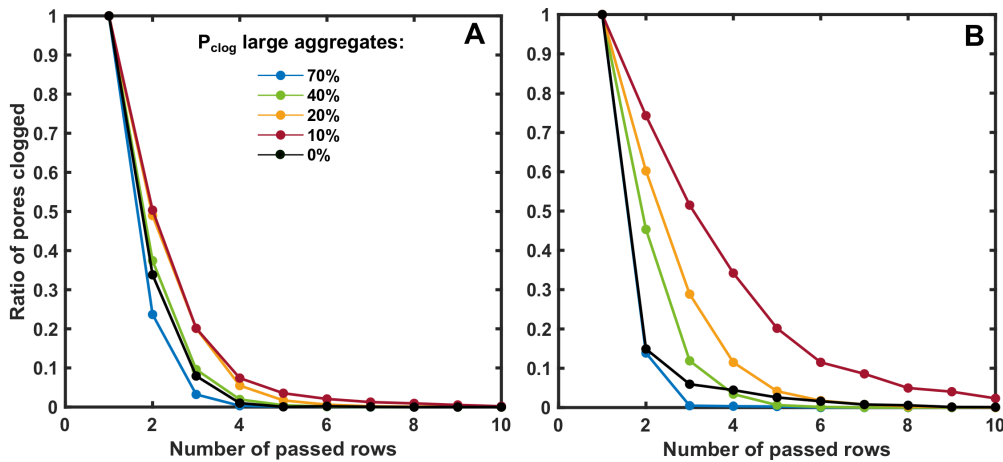


Figure 6.29: Ratio of pore clogged according the different P_{clog} of large aggregates for the peak size distribution (a) and the spread (b).

Figure 6.30 shows the contribution to the volume of the clog for $P_{clog,agg} = 70\%$, 20% and 0% for both size distribution. We find mostly aggregates in the clogs with the spread distribution and mostly single in the

peak distribution. Experimentally, a clog volume mostly composed of single objects in our confinement does not make sense because of the very low deposition of single objects and the difficulty to form multilayers under repulsive conditions since as discussed in the previous paragraph. For both suspensions, there is little change in the composition of the clogs between 70 and 20%. The main difference is for $P_{clog,agg} = 0\%$, increasing the contribution for peak distribution and for the new largest aggregate i.e. quadruplet for the spread distribution.

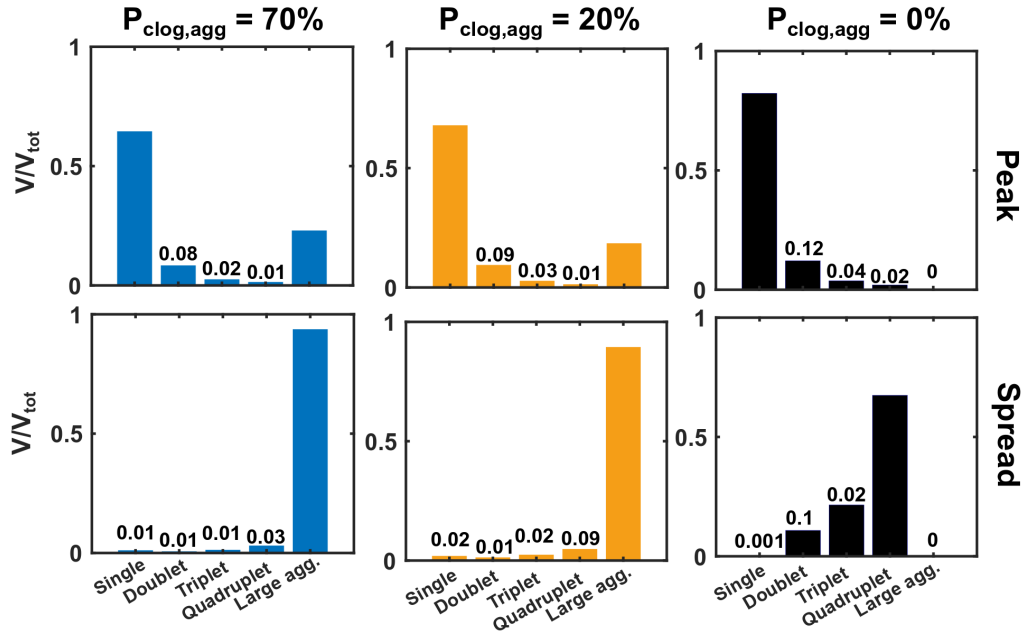


Figure 6.30: (left) Composition of the clogs with $P_{clog,agg} = 70\%$. (middle) $P_{clog,agg} = 20\%$ (right) $P_{clog,agg} = 0\%$. (top) Peak distribution and (bottom) spread distribution.

We also focus on the number of deposited objects into the medium for the spread distribution only (figure 6.31). When $P_{clog,agg}$ decreases, large aggregates are deposited further in the medium while their number at the entrance decreases since their number remains fixed. In the same time, the number of the other objects increases since the clog is delaying and more objects can be deposited. When large aggregates can not deposit, the new largest objects i.e. quadruplet contribute mostly to the clog (figure 6.30). As their $P_{clog,A}$ is high, we clog at the medium entrance with these objects.

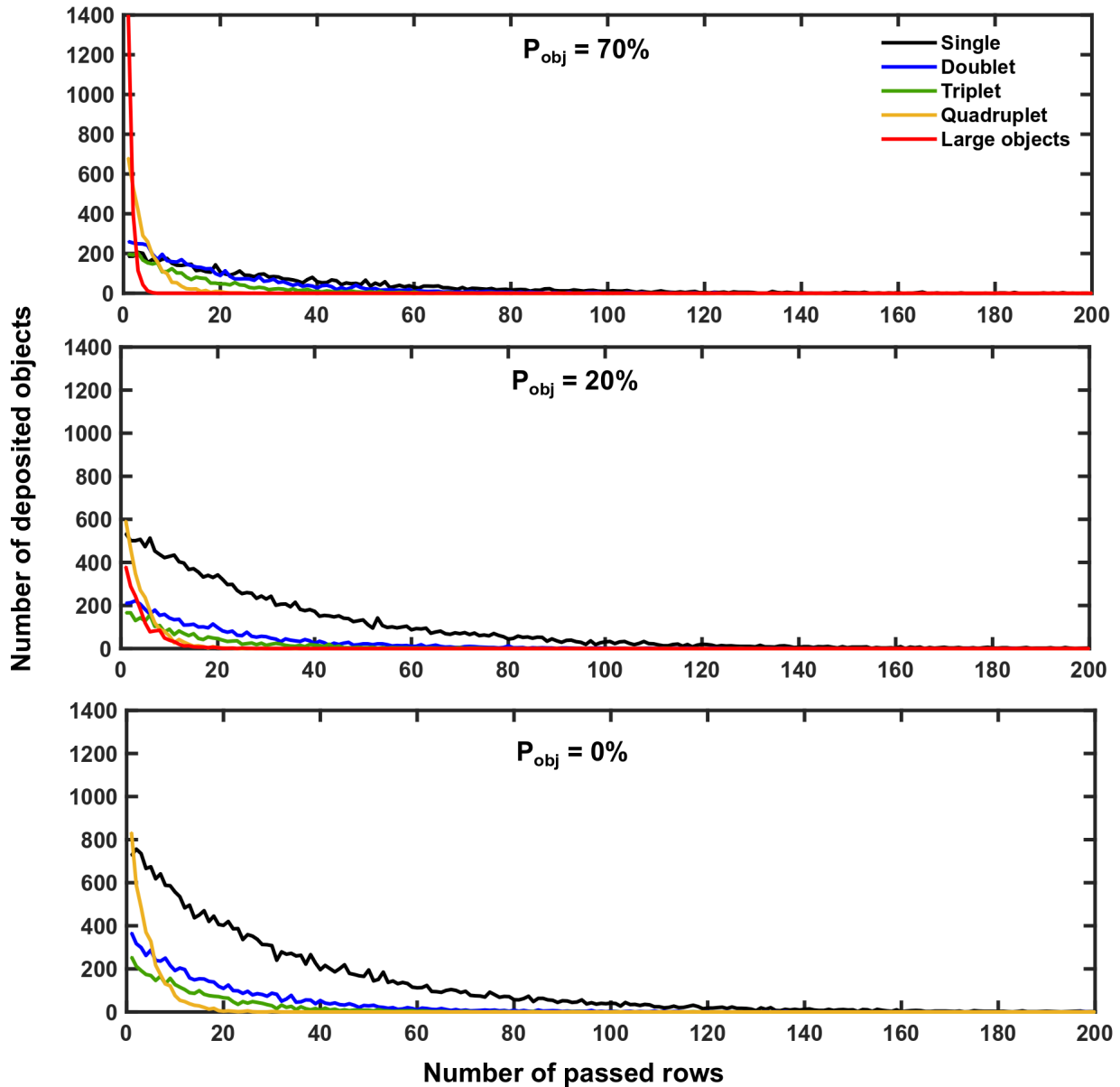


Figure 6.31: (top) The number of deposited objects along the porous medium with $P_{clog} = 70\%$, (middle) $P_{clog} = 20\%$ and (bottom) $P_{clog} = 0\%$, for the spread size distribution.

Perspectives of the simulation

This is still a work in progress, and several improvements and parameters modification should be made:

1. P_{clog} has to be modified according to the degree of fouling of the pore. For instance, the capture of single or doublet are very small at the beginning of the fouling. However, this is not the case anymore as soon as a deposit is formed on the pore wall. P_{clog} likely increases, due to a better interception of the flowing object by the deposit, which we called before in the manuscript self-filtration.
2. During the reduction of the pore cross-section, P_{clog} is not the only parameter impacted: the more the deposit is important in a pore, the more its hydrodynamic resistance increases, especially when a pore is almost clogged. As a consequence, particles tend to redistribute in areas of lower hydrodynamic resistance. We will not only vary P_{clog} during the deposition of the objects in the pore, but also the distribution of the objects.
3. We can introduce a distribution of the pore throats since this is the case in real porous media. As we discussed in the previous point, the clogging of the medium will be a trade off between flow of most of the particles through preferential flow paths, mainly through large pores, and a high capture probability in smaller ones.

6.3 Conclusion

We have studied experimentally how a porous medium is clogged by colloidal particles and we provide a simple model that explains most of the experimental features. The most important experimental result of this chapter is that whatever the media geometry, such as R_c and D_p and the flow rate, the media are clogged at all entry. We have identified two clogging mechanisms: the original clog, composed of aggregates and the accumulation clog that forms in certain configurations behind original clogs. As more than 90% of the clogs formed in the porous medium come from the presence of aggregates, we deduce again that aggregates drive the clogging process in the porous medium. To understand the role of the different objects in clogging, we performed simulations based on the size distributions and capture probability of objects, without considering hydrodynamics fluid or DLVO interactions. We identified that for the more the capture probability of large aggregates $P_{clog,agg}$ increase, the further inside the medium the clogging front is formed. However, if $P_{clog,agg}$ becomes null, then the second largest aggregates of the suspension will drive the clogging process. From our simulation, we can conclude that the P_{clog} of the largest objects in the suspensions are mostly responsible for the clogging at the entrance of the porous medium.

Chapter 7

Impact of interaction potentials on the clogging of porous media

In the previous chapter, we noticed that the dynamics of clogging of a porous medium is still driven by the deposition of aggregates. The objective of this chapter is to understand how clogging is impacted by the DLVO-like interaction potentials, as well as by the geometrical and hydrodynamic conditions. Based on the study of the collector's deposit, we try to understand the general dynamics of clogging in the whole porous medium by adding salt to the suspension. We compare the case with a strong repulsion, a moderate one and finally when particles charges are completely screened and are attracted by the wall and whose size distribution is strongly modified.

Contents

7.1	Description of a clogged porous medium by varying the interaction potentials . . .	184
7.1.1	Towards larger aggregates with the ionic strength	184
7.1.2	Clogs concentration at the inlet whatever the suspension	185
7.2	From the deposit to the clogging	191
7.2.1	Differences in the deposit according to the salinity	191
7.2.2	A new clogging mechanisms based on dendrite	195
7.2.3	A competition between the clogging mechanisms	197
7.3	Variations in hydrodynamic conditions have little effect on clogging	201
7.4	Conclusion	204

7.1 Description of a clogged porous medium by varying the interaction potentials

In this part, we describe the clogging process of an ordered porous medium through which flow suspensions with various ionic strengths.

7.1.1 Towards larger aggregates with the ionic strength

We used the same suspension of PS particles $1.5\mu\text{m}$ that in chapter 6 in which we added different amounts of NaCl salt:

- Without salt: this is our reference suspension with a strong repulsion between the particles and with the walls since both the particles and the PDMS walls bear negative charges.
- 50mM: there is no repulsion from the walls and there is an attraction of the particles that are close to the collector surface. Even though for this ionic strength we are lower than the CCC, we can expect that the growth of the deposit, for the same flow conditions, is greater than in the no salt case since the electrostatic barrier is smaller.
- 300mM: the surface charges of the particles are completely screened, favoring their deposition on the collector, but also strongly impacting the size distribution since the CCC is reached.

Most of the time the main influence of the ionic strength is to ease the particle deposition in the context of filtration, however it also modifies deeply the aggregate size distribution. Figure 7.1a shows almost identical size distributions for no salt and $I=50\text{mM}$ suspensions, peaked around $1.5\mu\text{m}$, which is the expected mean diameter of the particles. For $I=300\text{mM}$, superior to the CCC, the distribution is broader. When we count the number of particles for each category we observe that aggregates larger than quadruplets explodes compared to the two other suspensions (figure 7.1b and table 7.1).

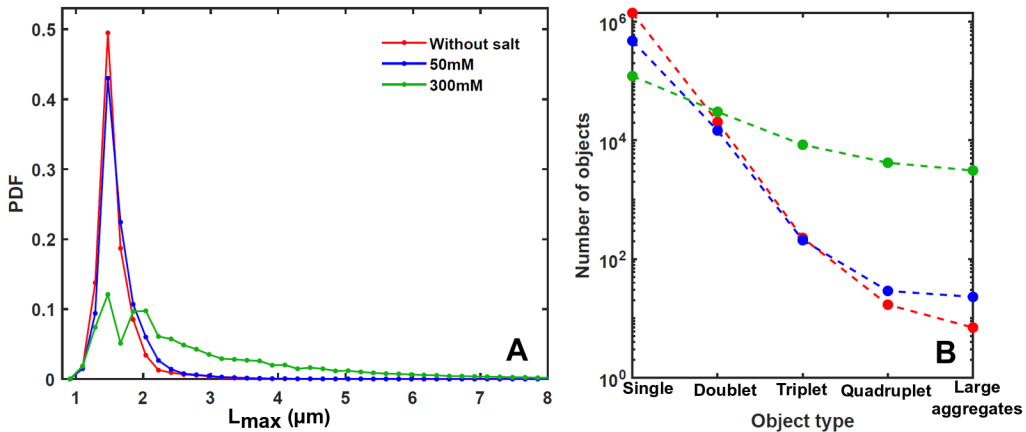


Figure 7.1: Size distribution for the three suspensions, without salt, 50mM and 300mM (a) and the number of each types of objects in the suspension (b).

%	Single	Doublet	Triplet	Quadruplet	Aggregate	Total objects
Without salt	98.5	1.43	0.015	0.001	0.0004	1 407 960
50mM	96.9	2.97	0.04	0.005	0.005	477 238
300mM	72.5	18.1	5.04	2.50	1.85	121 216

Table 7.1: Proportion of the different objects that composed the suspensions from the stop and go experiment.

In the following, we will see that the coupling between an higher adhesion of the particles on walls and the modification of the particle size distribution leads to various clogging patterns.

7.1.2 Clogs concentration at the inlet whatever the suspension

We injected the suspension with an initial flow rate at $1\mu\text{L}/\text{min}$ and we imaged porous media every 3 to 5 seconds to detect the clog position and the clogging time of each pore. Successive images of the completely clogged medium for different ionic strength conditions are shown in figures 7.2, 7.3 and 7.4, with only the first third part of the medium. The porous medium clogs at its very entrance, which is true for all the suspensions. Deeper pores in the medium can be clogged, but the first row of pores are systematically clogged, whatever the salinity. They are more clogs when salt is added. To be more precise the number of clogs inside the medium increases with the salt content, the clog front being still located at the medium entrance.

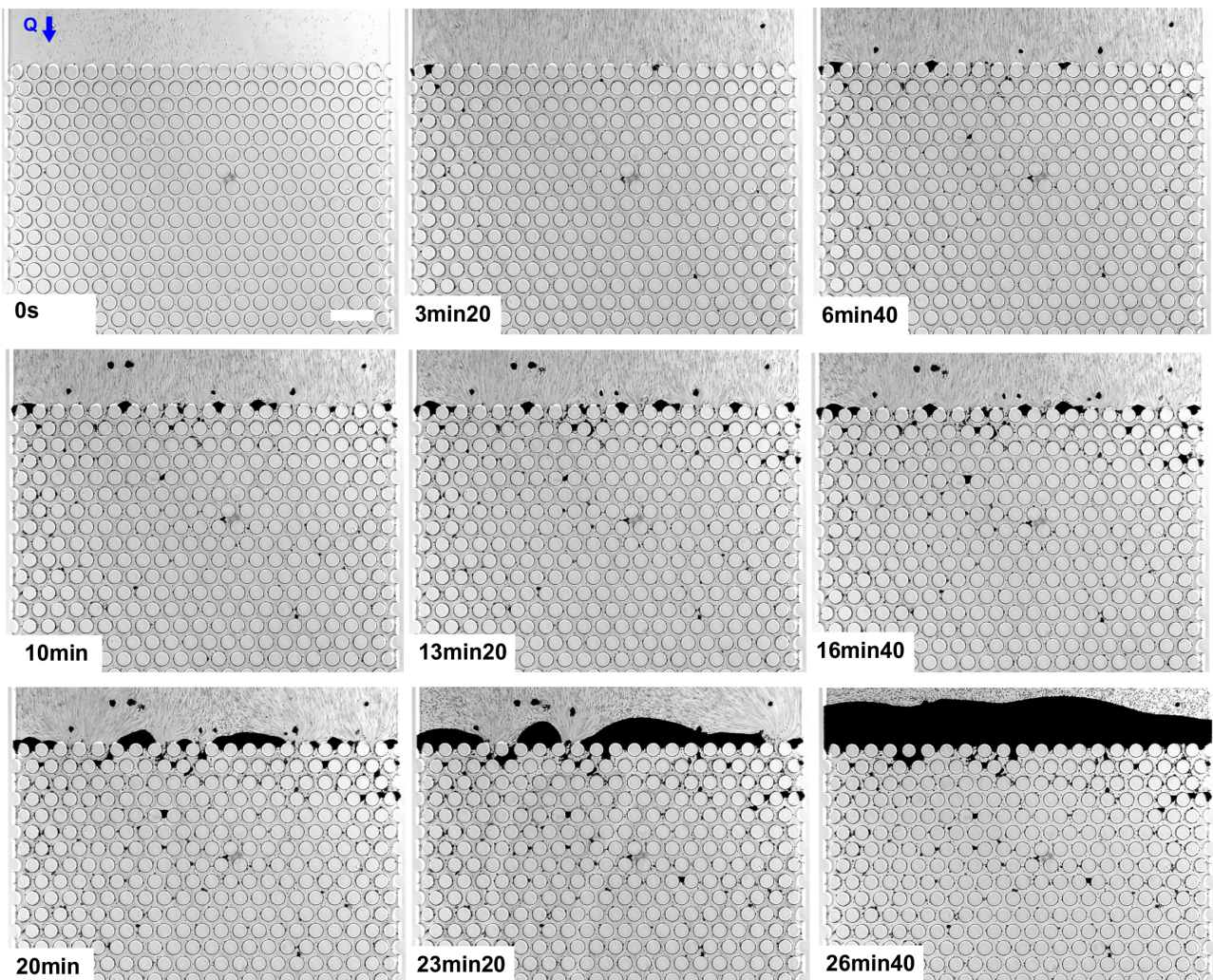


Figure 7.2: Clogging by the suspension without salt added. Scale bar: $70\mu\text{m}$.

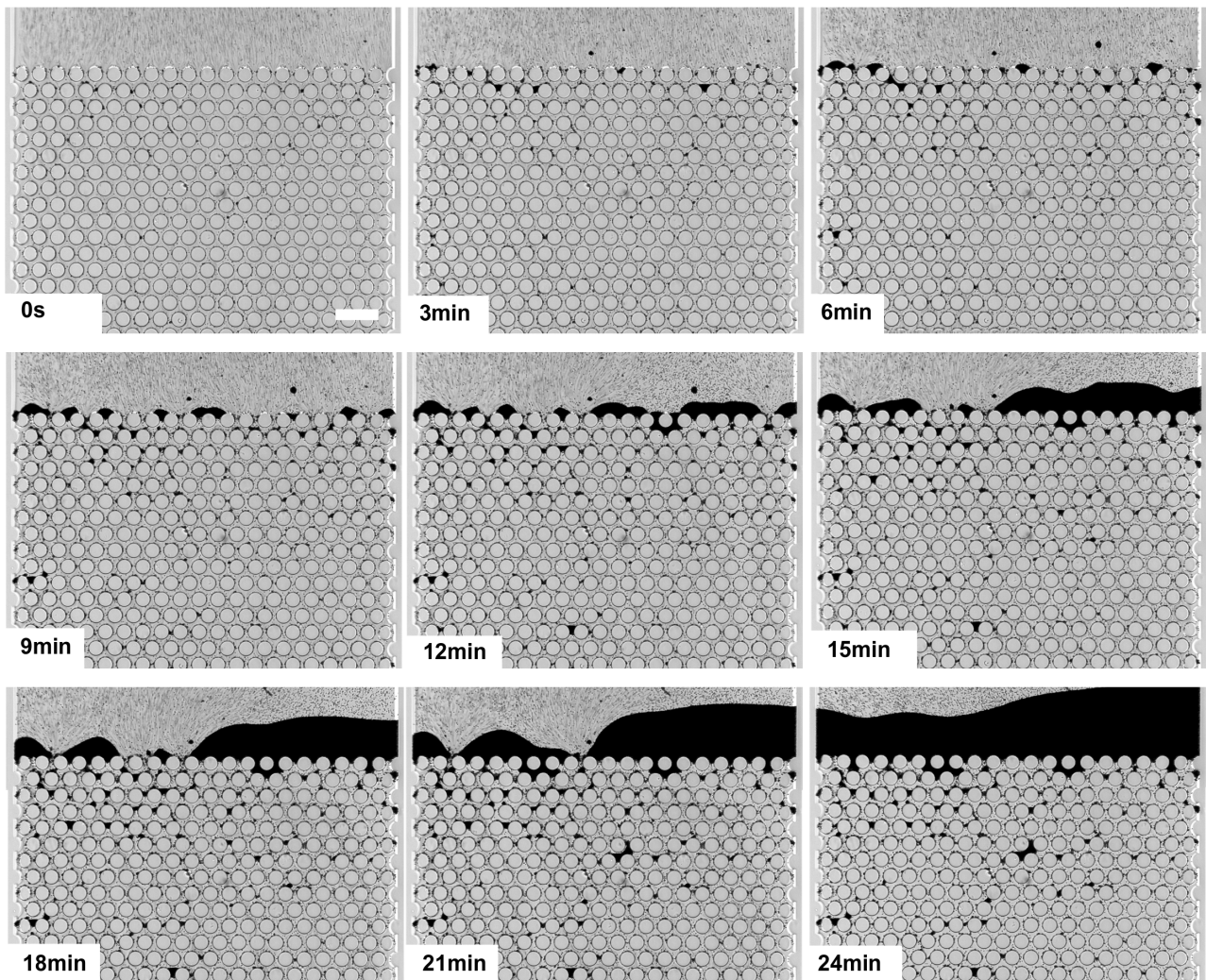


Figure 7.3: Clogging by the suspension $I = 50\text{mM}$. Scale bar: $70\mu\text{m}$.

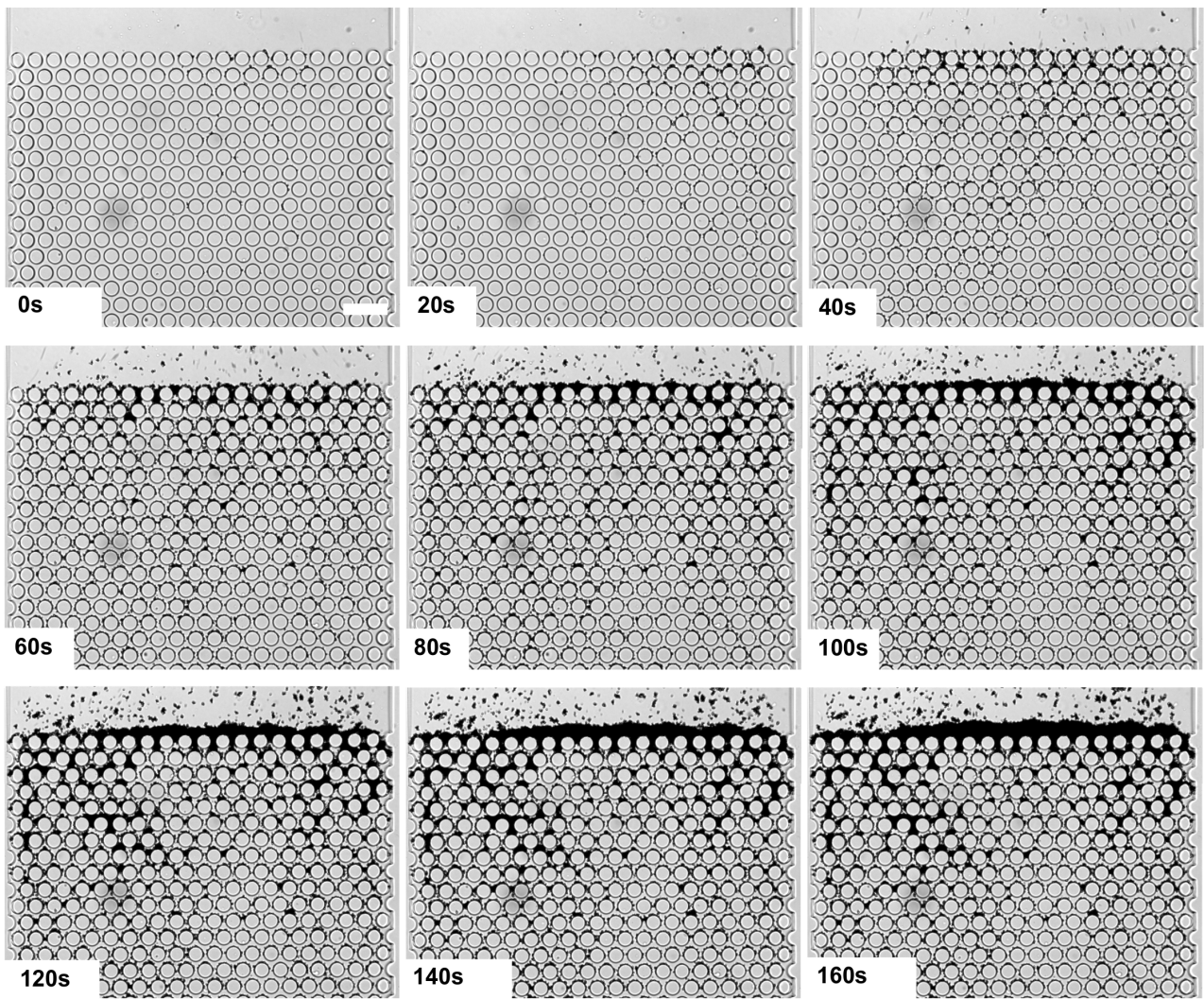


Figure 7.4: Clogging by the suspension $I = 300\text{mM}$. Scale bar: $70\mu\text{m}$.

As in chapter 6, we study the ratio of clogged pores per row to determine the location of the clog front (figure 7.5). Whatever the ionic strength there are very few clogs beyond the 20th row. In the no salt case all the clogs are between the first and the second row. For $I=50\text{mM}$ the zone in which clogs show up spreads roughly over the entrance up to the 8th row, while it goes up to the 14th row for $I=300\text{mM}$.

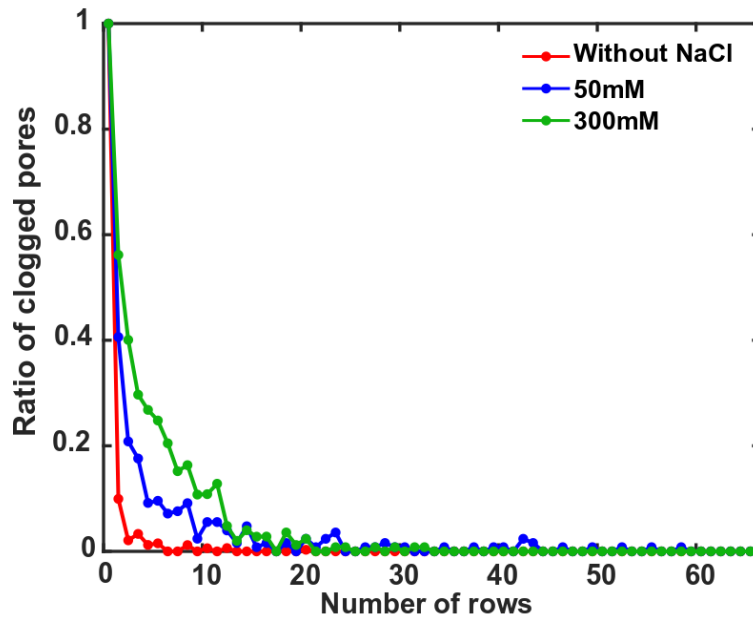


Figure 7.5: Variation of the ratio of clogged pores with the number of passed row for the three suspensions. The curves are averaged curves from 3-4 replica.

As pores of the first rows get clogged, the available flow paths for the particle decreases (figures 7.2,7.3 or 7.4), most of those clogs being original ones (defined in chapter 6). We define the clogging front as the line that links the clogs along the width of the medium. Behind this line there is an accumulation of particles (schema 7.6).

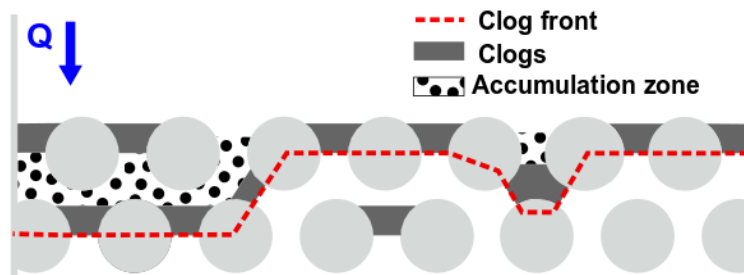


Figure 7.6: Scheme of the clog front

Examples of clog fronts are displayed in figure 7.7a. In the no-salt case the clog front is a straight line, almost all the clogs within the porous medium belonging to the very first row (figure 7.7b), i.e., there is very rare clogs inside the medium (table 7.7c). For $I=50\text{mM}$ the clog front is a distorted line with less than 20% of the clogs belonging to the second and third rows, these clogs corresponding only to one third of the population over the entire medium. For $I=300\text{mM}$, the formation of the clog front is event more sinuous and goes deeper within the medium. In this case, clogs belonging to the front correspond to 15% of all the clogs. The dynamics of the formation of a clog front for a suspension $I = 300\text{mM}$ is shown in figure 7.8.

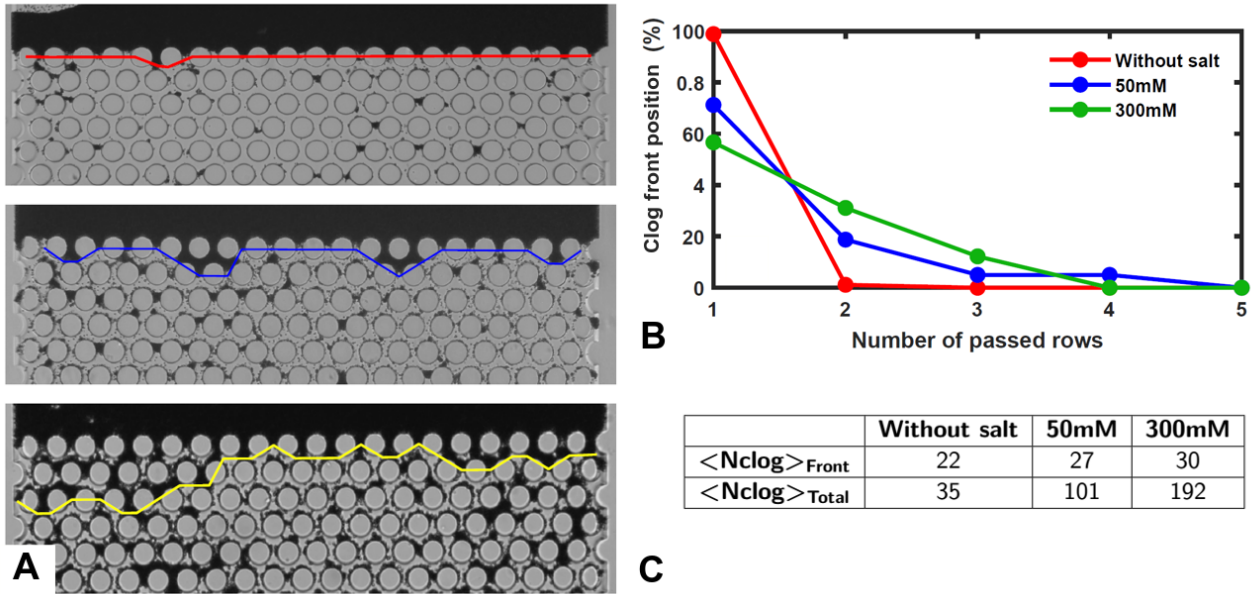


Figure 7.7: (a) Examples of clog front for suspensions (top) without salt, (middle) with 50mM and (bottom) with 300mM. (b) Percentage of the clog front contained per row of the porous medium. (c) Average number of clog composing the front $\langle N_{\text{clog}} \rangle_{\text{Front}}$ and in the whole porous medium $\langle N_{\text{clog}} \rangle_{\text{Total}}$ for the three suspensions.

To sum up, the clog front is located at the entrance of the medium, irrespective of the ionic strength. However, the addition of salt has a clear impact on the dynamics of medium clogging since the number of clog significantly increases and the formation of the clog front is more inside the medium.

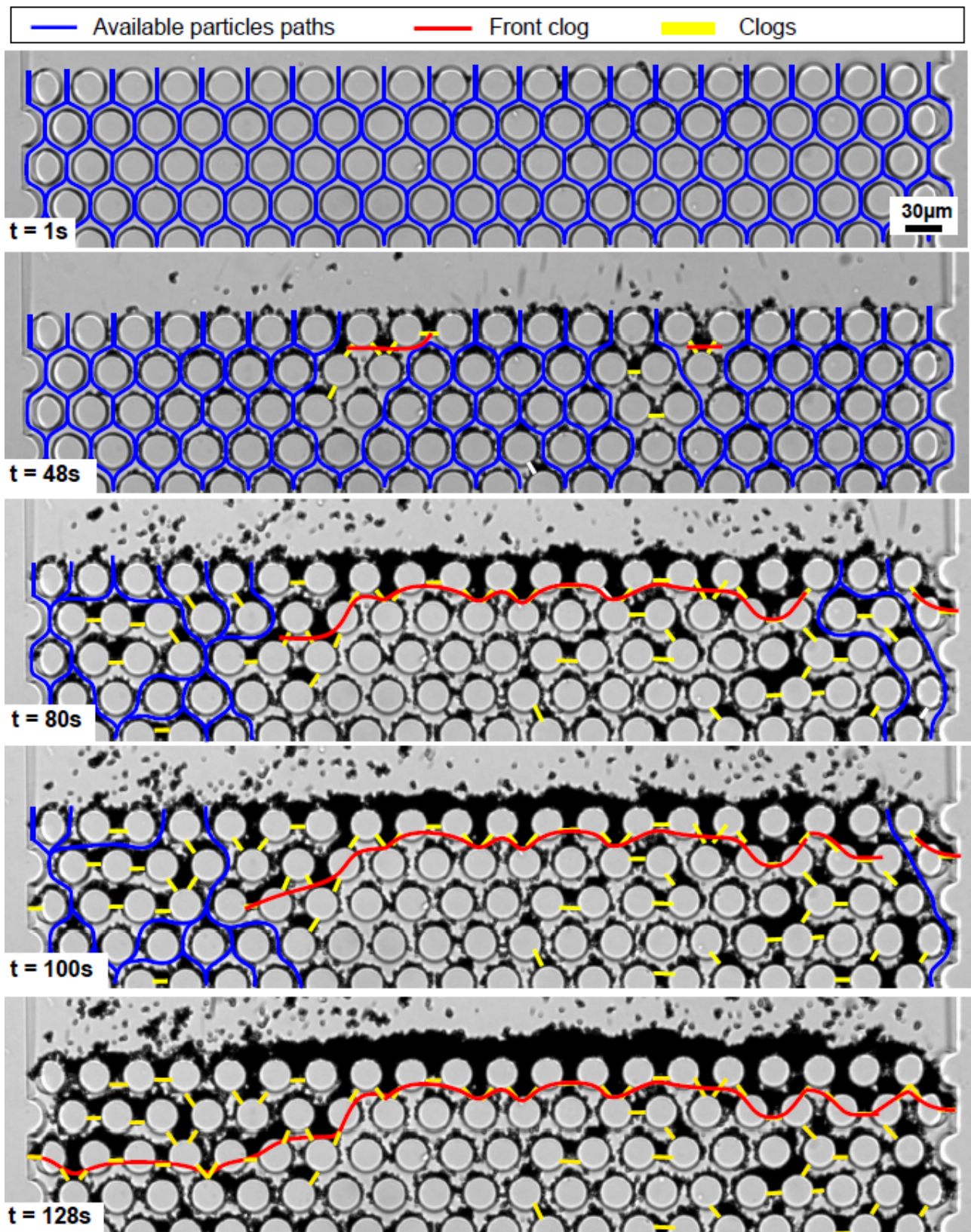


Figure 7.8: Evolution of the front clog for $l=300mM$ at different times in a porous medium. During the formation of the clog front (red dotted line), the number of available particles paths (blue lines) progressively decreases. A clogged pore is indicated by a yellow line.

7.2 From the deposit to the clogging

The more or less consequent deposition of objects on the collector surface impacts differently the clogging process of the medium. We first study the morphology of these deposits at the collector surfaces and their repartition in the whole medium as a function of geometric parameters of the porous medium.

7.2.1 Differences in the deposit according to the salinity

We image after the deposition at the collector wall at the end of the experiment, when the medium is completely clogged. We select only collectors with deposit that is not connected to neighbouring collectors (examples of such collectors on the red shapes figure 7.9). This allows us to study only clogs primers with limited expansion rather than putting arbitrary criteria to differentiate deposition from clog formations on earlier images.

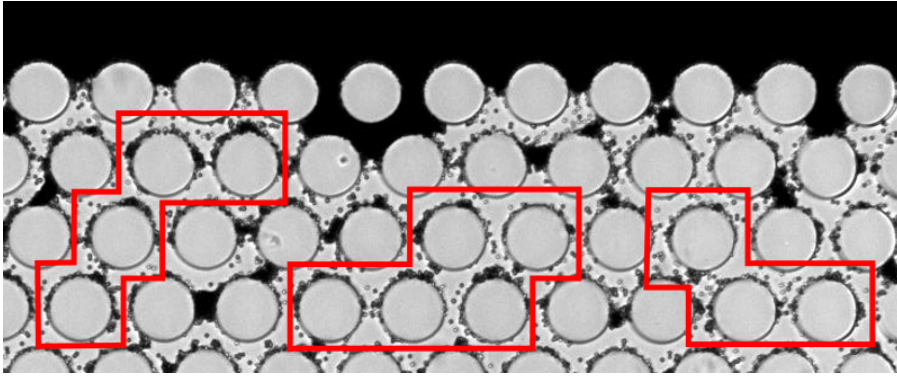


Figure 7.9: Examples of selected collectors respecting the criterion.

We compare the deposition on the collector walls of different spacing D_p between collectors and various radius R_c .

Spacing collector D_p

The deposit at the wall collector with $R_c = 30\mu\text{m}$ and spacings $D_p = 10\mu\text{m}$ and $D_p = 30\mu\text{m}$ are shown in figures 7.10 and 7.11, respectively, for the three salinities along the medium. There is almost no deposition for the no salt suspension, regardless of the pore spacing. The deposition for $I=50\text{mM}$ is greater than for the no salt case and spreads over the entire medium. For $I=300\text{mM}$ suspensions, dendrites shape-like are formed on the top of collectors. The growth of these dendrites is more important when the spacing is increased, likely due to the fact that they have more space to grow before reaching the upstream collectors. The shear for $D_p = 10\mu\text{m}$ is two times greater than for the larger D_p and thus may also limit the growth (figure 7.12).

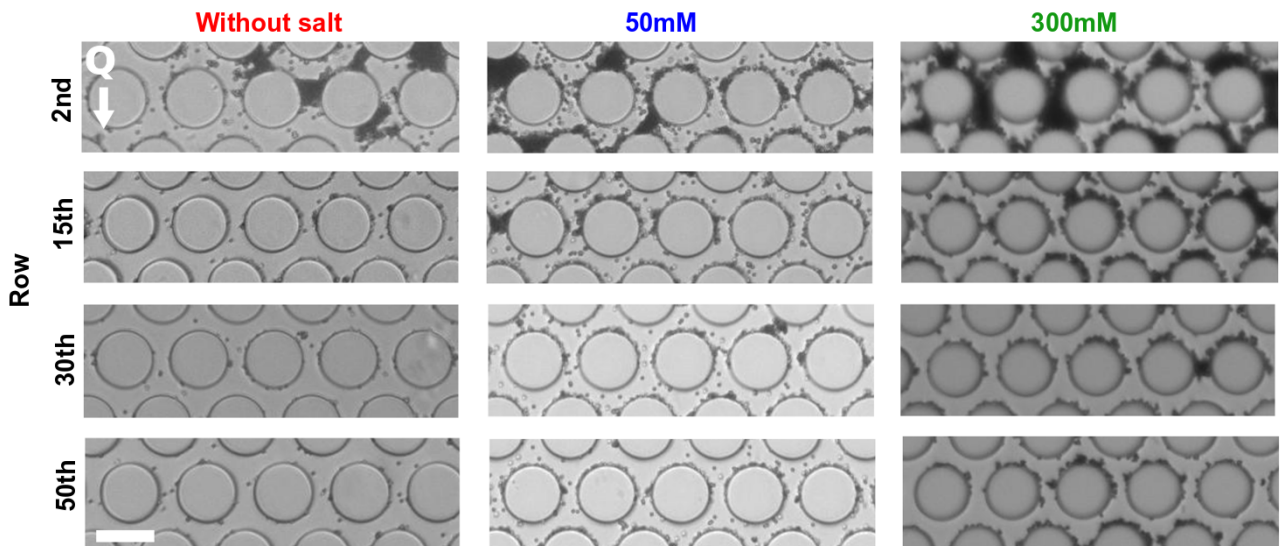


Figure 7.10: Different deposit patterns with collector $R_c = 15\mu\text{m}$ and $D_p = 10\mu\text{m}$ along the medium from its entrance for the three ionic strengths. Scale bar: $30\mu\text{m}$.

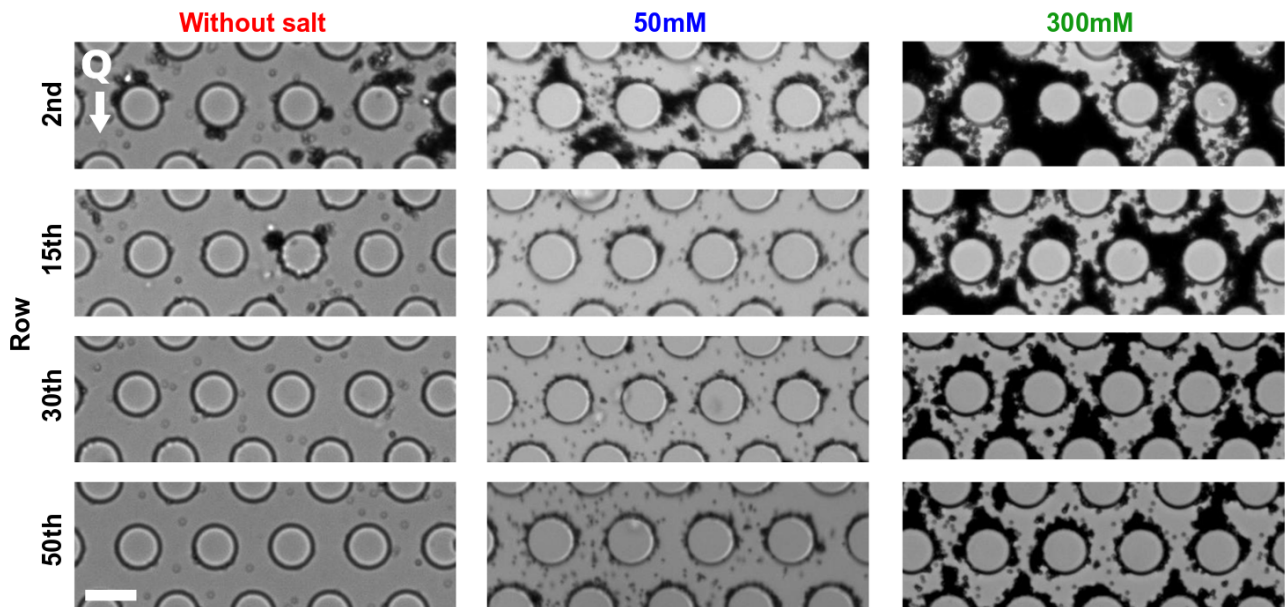


Figure 7.11: Different deposit patterns with collector $R_c = 15\mu\text{m}$ and $D_p = 30\mu\text{m}$ along the medium from its entrance for the three ionic strengths. Scale bar: $45\mu\text{m}$.

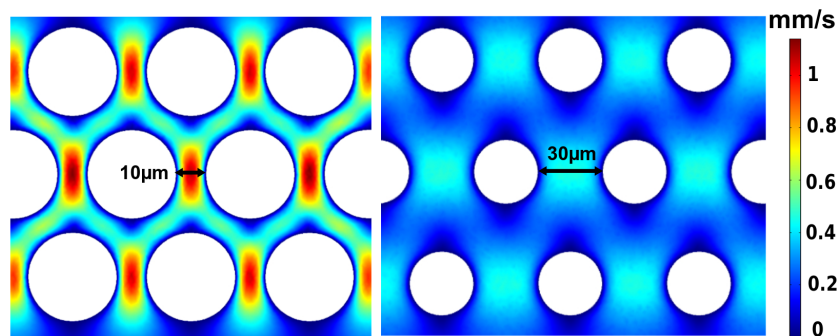


Figure 7.12: Comsol simulation of the flow around the collectors with $R_c = 15\mu\text{m}$ and $D_p = 10$ (left) and $30\mu\text{m}$ (right).

We measured the deposit around the collector's wall by image analysis. This deposit is almost absent for the no salt suspension, whatever the value of D_p (figure 7.13a and figure 7.10 first column). There are

very few spots of deposition all along the entire medium. For $I=50\text{mM}$ and 300mM particle deposition occurs everywhere within the medium. Note that the area of the deposit is two times higher for $D_p=30\mu\text{m}$ than for $D_p=10\mu\text{m}$ (figure 7.13b-c).

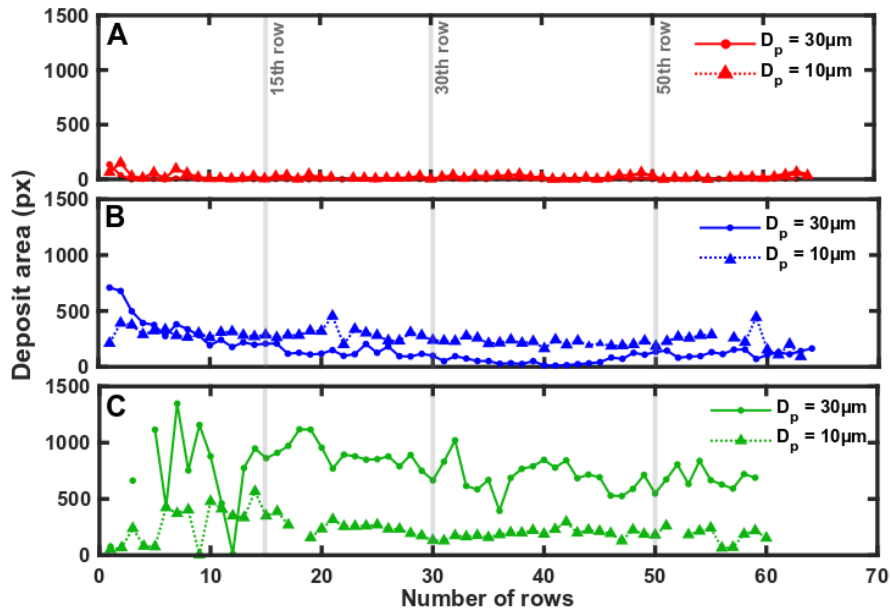


Figure 7.13: Deposit area (pixels) along the medium with $D_p=10$ and $30\mu\text{m}$ with no salt (a), $I=50\text{mM}$ (b) and $I=300\text{mM}$ (c). Some points are missing in the curve in areas where the deposit is high and the number of collectors respecting the selection criterion is low.

For $I=300\text{mM}$, particle deposit mainly at the top of the collectors, inside the dendrites all along the medium. Figure 7.14 is the juxtaposition of all the selected collector by row. This representation helps us to better see the shape of the base of the deposit. For smaller spacing the deposits spread more around the collector, with a constant thickness (figure 7.14, left) while for greater spacing they have a dendrite-like shape, irrespective of the position inside the medium (figure 7.14, right).

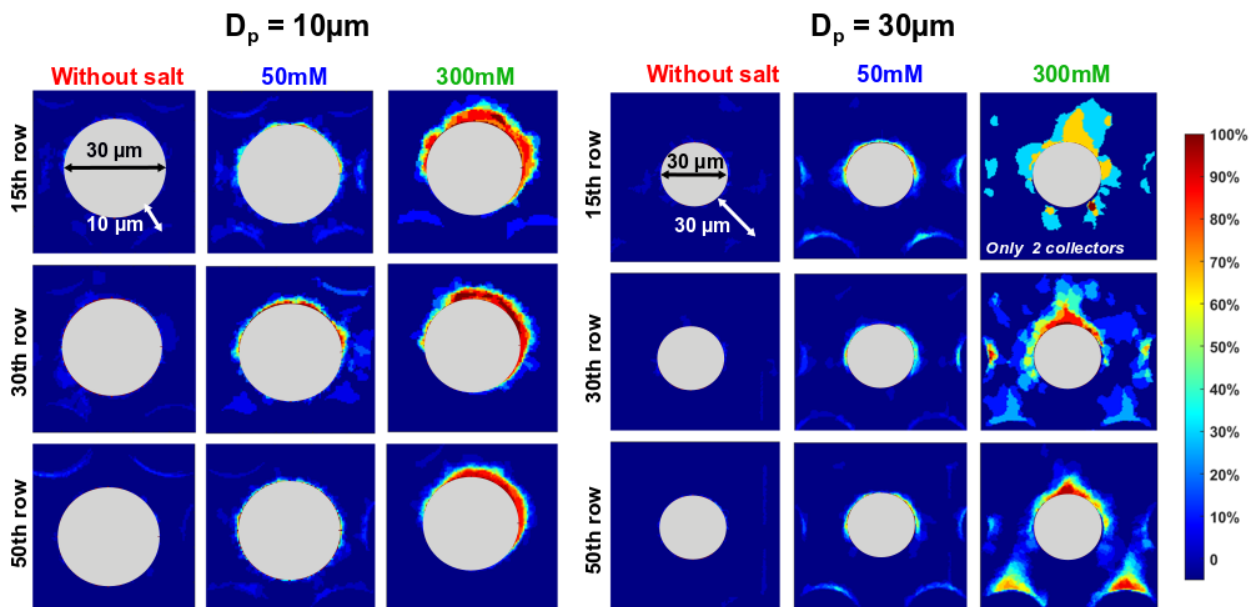


Figure 7.14: Juxtaposition of all the deposits in a same row for the various I and $R_c=15\mu\text{m}$. (left) $D_p=10\mu\text{m}$, (right) $D_p=30\mu\text{m}$. The red areas are covered by 100% of the deposits considered, the blue areas the least covered (0%). The gray circles are the collector zones.

Radius collector R_c

We also compared the particle deposition for $R_c=15\mu\text{m}$ (figure 7.10) and $75\mu\text{m}$ (figure 7.15), with D_p fixed to $10\mu\text{m}$. Surprisingly, although the surface available for deposition is larger when the radius increases, the deposition seems to be less important at the wall of the collectors. Even for $I=300\text{mM}$, no dendrites are formed.

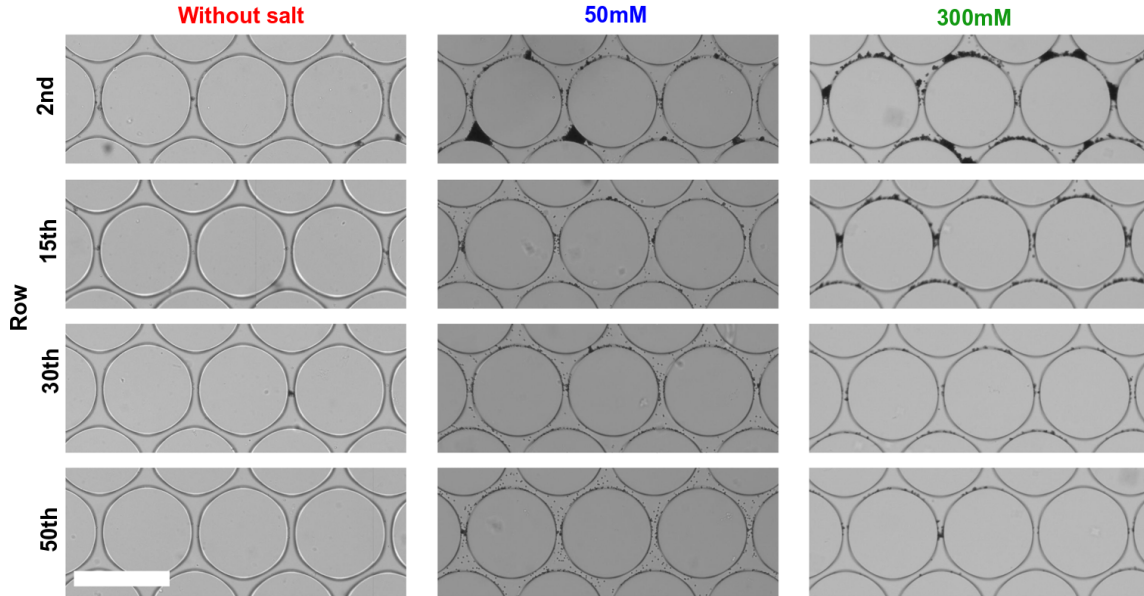


Figure 7.15: Different deposit patterns with collector $R_c = 75\mu\text{m}$ and $D_p = 10\mu\text{m}$ along the medium from its entrance for the three ionic strength. Scale bar: $150\mu\text{m}$.

The measurement of the areas (figure 7.16) confirms this observation, with almost no deposit for $I=50\text{mM}$ with $R_c = 75\mu\text{m}$ for the no salt case. For $I=300\text{mM}$, areas are initially as important as with $R_c= 30\mu\text{m}$ there is no deposit beyond the 20th rows.

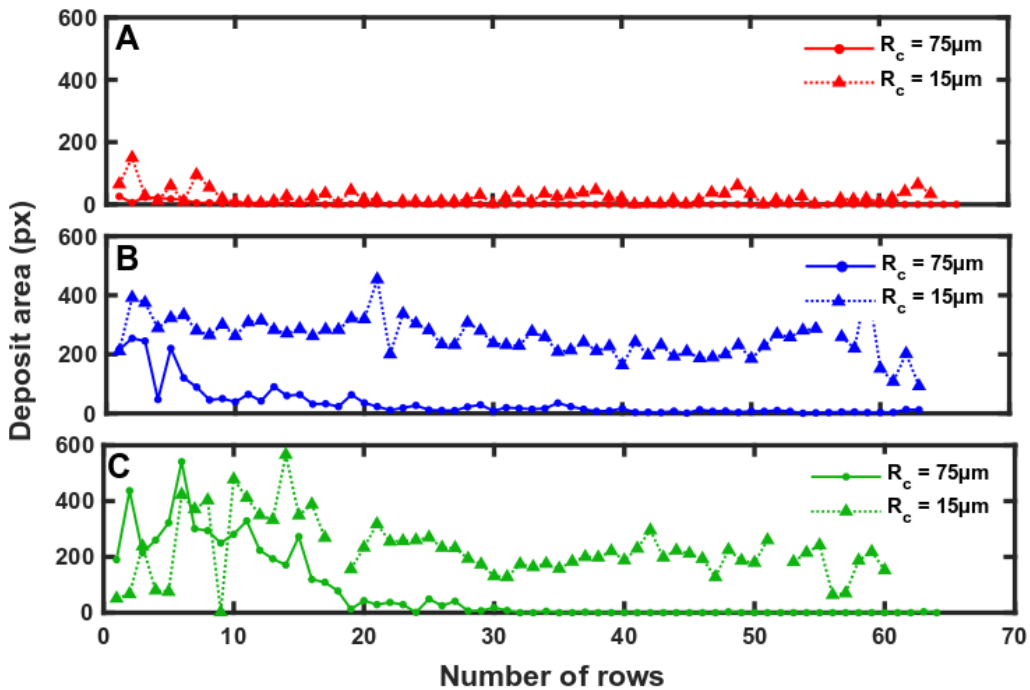


Figure 7.16: Deposit area (pixels) over the length of the porous medium for collector $R_c = 15$ and $75\mu\text{m}$ with $D_p = 10\mu\text{m}$ for the no salt case (a) , $I=50\text{mM}$ (b) and 300mM (c).

Again, this change in deposition morphology can be attributed to the much higher shear with $R_c = 75\mu\text{m}$ collectors, up to 7 times higher, which could promote erosion or at least limit the deposition.

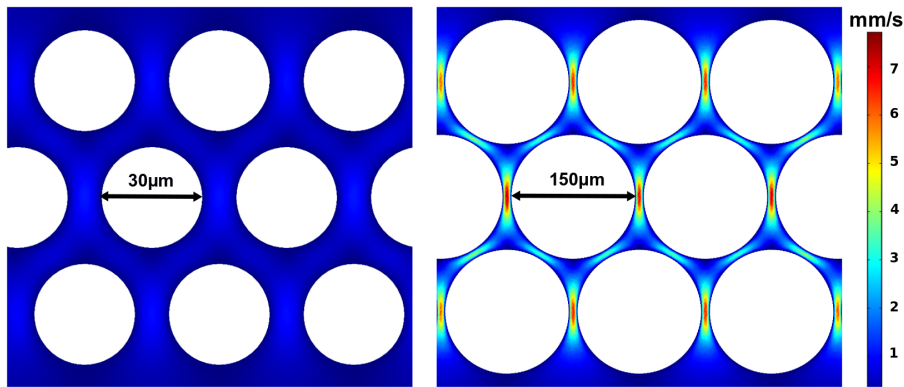


Figure 7.17: Comsol simulation of the flow around collector with $R_c=15\mu\text{m}$ (left) and $R_c = 75\mu\text{m}$ (right), $D_p=10\mu\text{m}$.

To summarize, we have three geometries with extremely different deposition morphologies depending on the salinity. For suspensions with no-salt and $I=50\text{mM}$, the particle deposition is limited. In contrast, for $I=300\text{mM}$, the deposit is important and takes the form of dendrites, with their morphologies impacted by R_c and D_p and limited by the shear. Increasing D_p favors the growth of these dendrites (figure 7.18a-c). The spreading of the deposit around the collector surface remains the same. Going from $R_c = 15$ up to $75\mu\text{m}$, the dendrites disappear and the deposit is limited to an arc area of $\approx 70^\circ$ compared to 240° for the smaller radius (figure 7.18a-b).

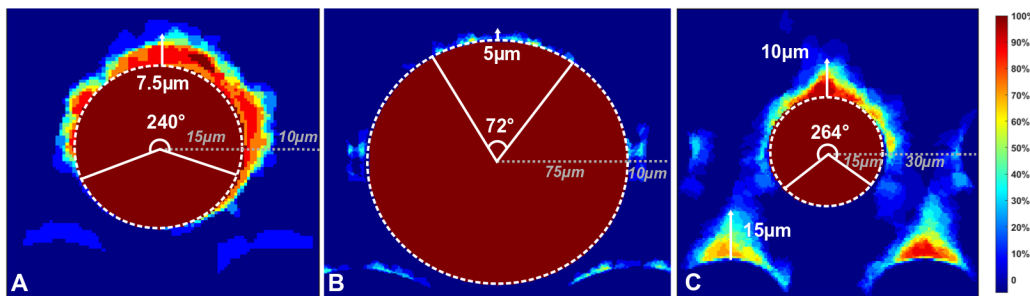


Figure 7.18: Juxtaposition of several collector deposit in the very beginning of the porous medium with $R_c = 15\mu\text{m}$ and $D_p = 10\mu\text{m}$ (a), $R_c = 75\mu\text{m}$ and $D_p = 10\mu\text{m}$ (b), $R_c = 15\mu\text{m}$ and $D_p = 30\mu\text{m}$ (c).

Even with a morphology depending on the geometry of the medium, the dendrites when they exist play a significant role in the dynamics of clogging of the porous medium.

7.2.2 A new clogging mechanisms based on dendrite

We have seen in the previous chapter two clogging mechanisms in the porous medium, original clogs and clogs by accumulations, which simply consist in the accumulation of particles behind a zone composed of original clogs. We present here the last clogging mechanism, the dendrite clogs, which results from the presence of dendrites.

These dendrites form on the collector walls and grow until reaching almost the center of the upstream pore (figure 7.19). The final obstruction of the pore corresponds to the capture of particles between the dendrite and the collector surface.

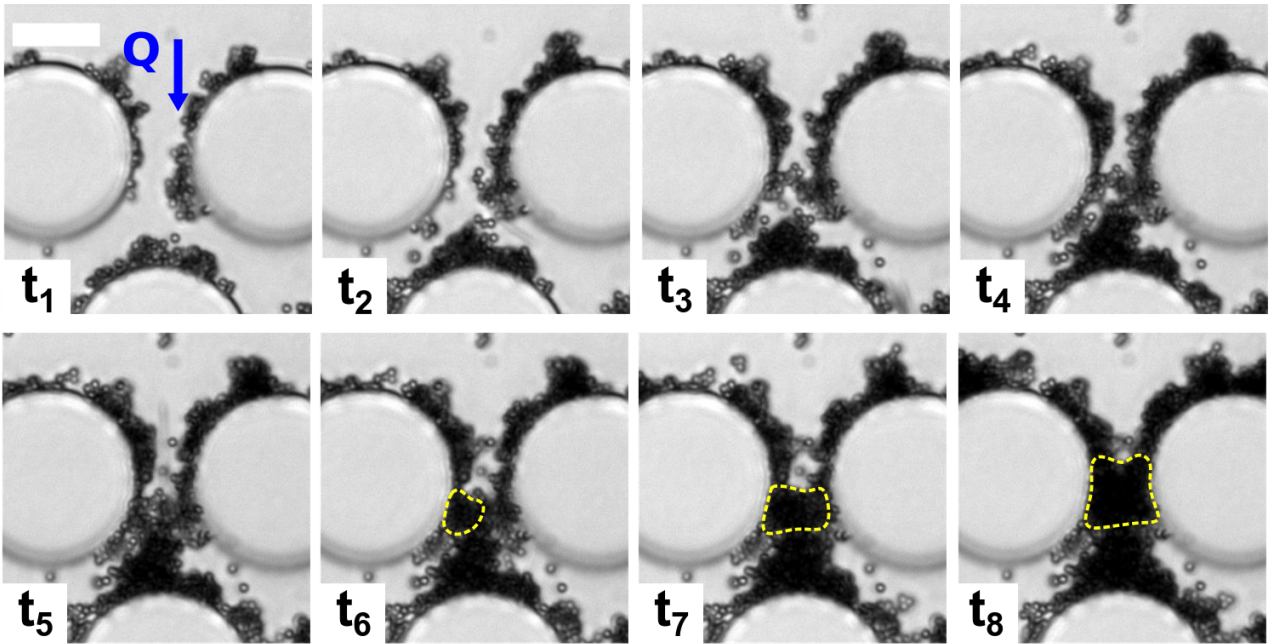


Figure 7.19: Formation of a dendrite clog. Up to t_5 the dendrite grows towards the pore center. At t_6 an aggregate is captured followed by other objects in t_7 until the complete obstruction in t_8 . Scale bar: $30\mu\text{m}$.

There are many ways for a dendrite to clog a pore, whether it is the pore upstream, or one of the interstitial pores. A dendrite can even allow the clogging of several pores (figure 7.20).

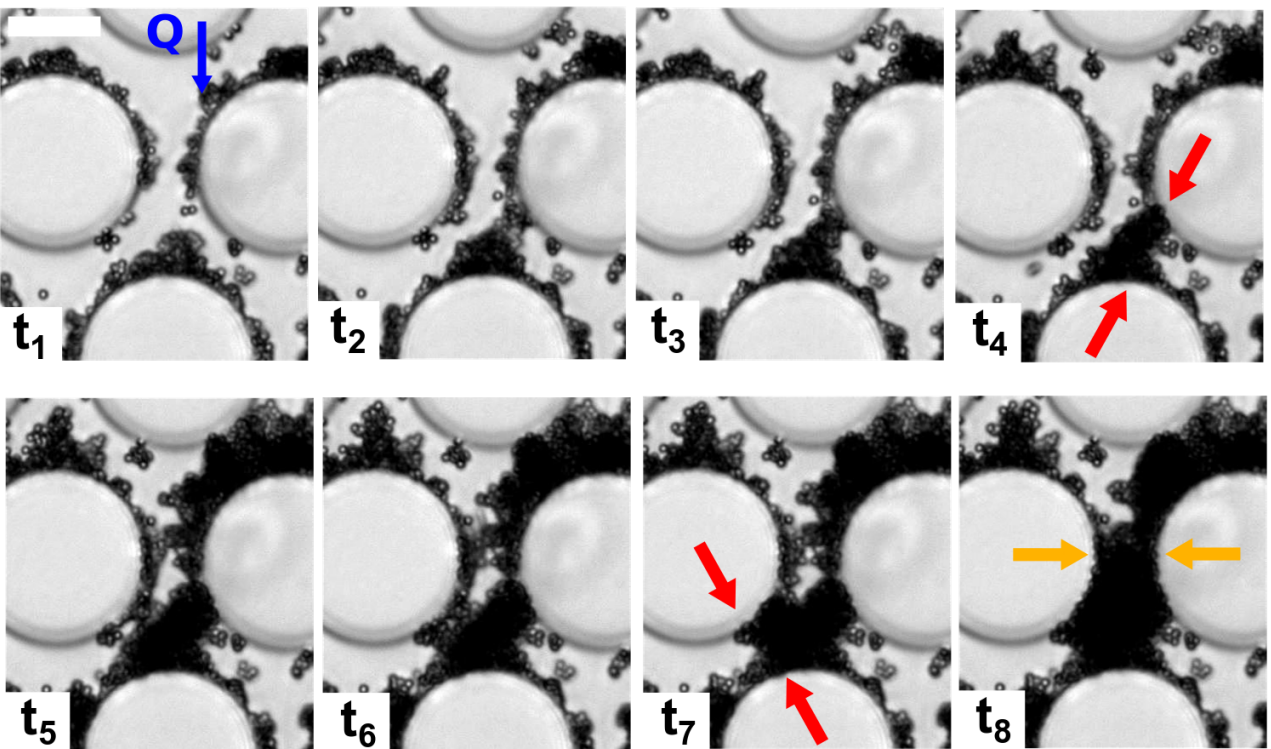


Figure 7.20: Double dendrite clog formation. At t_4 the dendrite helped to clog the interstitial pore on the left (red arrows) while at t_7 the one on the right is also clogged. Finally at t_8 the central pore is clogged by particles accumulation (yellow arrows). Scale bar: $30\mu\text{m}$.

The two previous examples showed dendrites with closely packed collectors, but the phenomenon is even more pronounced when there is more space between collectors (figure 7.21).

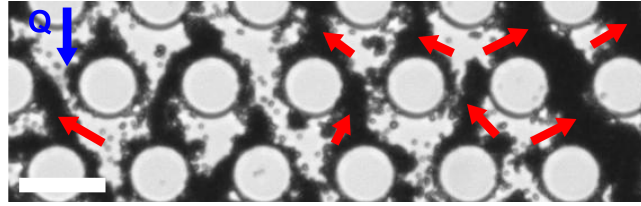


Figure 7.21: Multiple dendrites (red arrows) that helped to the clog formation with a large space between collectors.

7.2.3 A competition between the clogging mechanisms

We determine the relative importance of each clogging mechanism depending on the ionic strength and the features of the collectors.

Spacing collector D_p

The number of clogs that belong to each mechanism with $D_p=10\mu\text{m}$ and $30\mu\text{m}$ are reported in figure 7.22. As expected for the two lower ionic strengths the dominant mechanism is the original clog, since there are no dendrites or their height is too small to allow the clog formation. When D_p is increased original clogs are composed with more aggregates in order to be able to fill the extra gap (chapter 3), which reduces slightly the total number of clogs formed (table 7.2). The original clogs, as seen before, favor the obstruction at the entrance of the medium (figure 7.23a-b), with a clogging front that is almost exclusively on the first line, whatever the spacing D_p (figure 7.24a-b). However, it can be noted that the clogging time increases slightly with the spacing for suspension without salt and with 50mM due to the increase of the clogging volume (figure 7.24d-e).

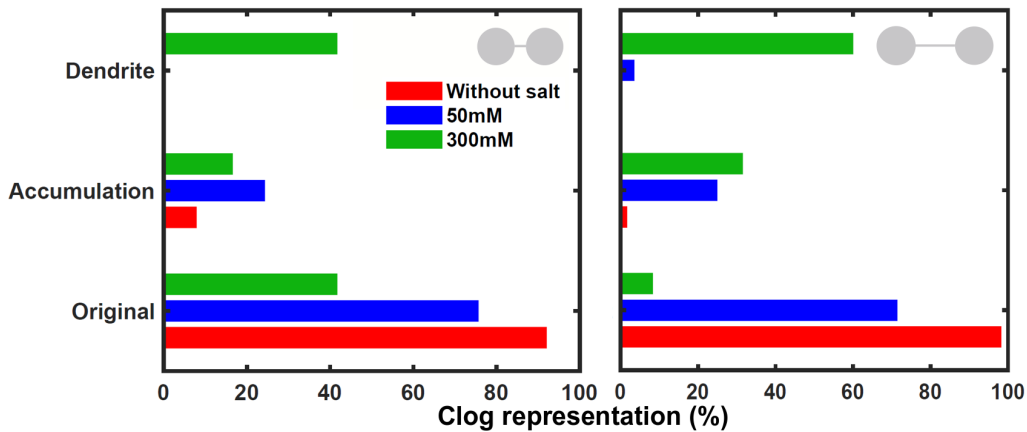


Figure 7.22: Proportion of each type of clog depending on the porous medium geometry with $R_c=15\mu\text{m}$ and $D_p=10\mu\text{m}$ (a), $R_c=15\mu\text{m}$ and $D_p=30\mu\text{m}$ (b).

	$R_c=15\mu\text{m}, D_p=10\mu\text{m}$				$R_c=15\mu\text{m}, D_p=30\mu\text{m}$			
	Orig.	Acc.	Dend.	Tot.	Orig.	Acc.	Dend.	Tot.
No salt	32	3	0	34	29	1	0	29
50mM	69	22	0	91	40	14	2	55
300mM	79	32	113	168	27	102	154	323

Table 7.2: Average number of each type of clog in an experiment: original (Orig.), accumulation (Acc.), dendrite (Dend.) and total (Tot.) for two spacings.

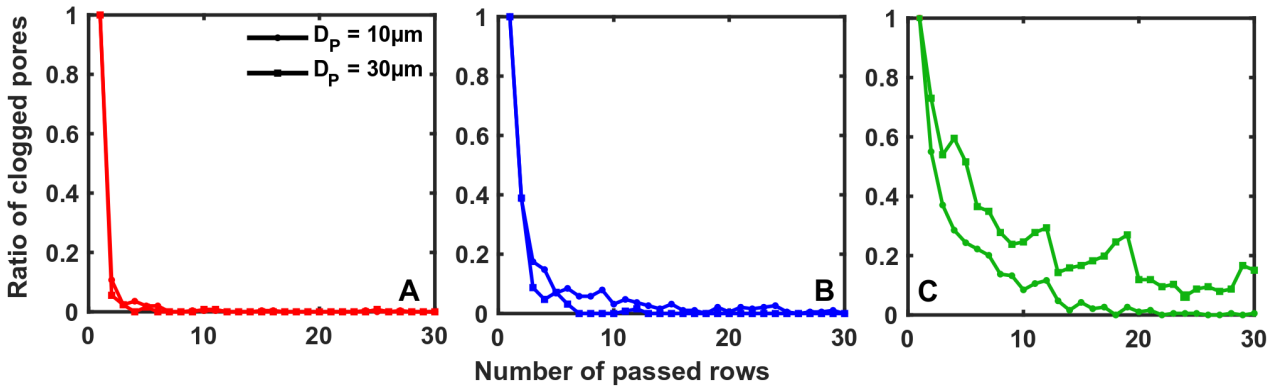


Figure 7.23: Ratio of clogged pores over the rows depending on the spacing for the no-salt suspension (a), $I=50\text{mM}$ (b) and 300mM (c)

The most important change of the relative population of each clogging mechanism occurs for $I=300\text{mM}$. With $D_p=10\mu\text{m}$, there are as many original clogs as dendrites ones. But when the spacing increases, the number of clogs also increases considerably (table 7.2) and dendrite clogs become dominant (figure 7.22c). The clog front still remains at the medium entrance (figure 7.23c), however it is much deeper inside the medium (figure 7.24c). Dendrite clogs thus allow, contrary to the original clogs, to have a deeper clogging in the medium.

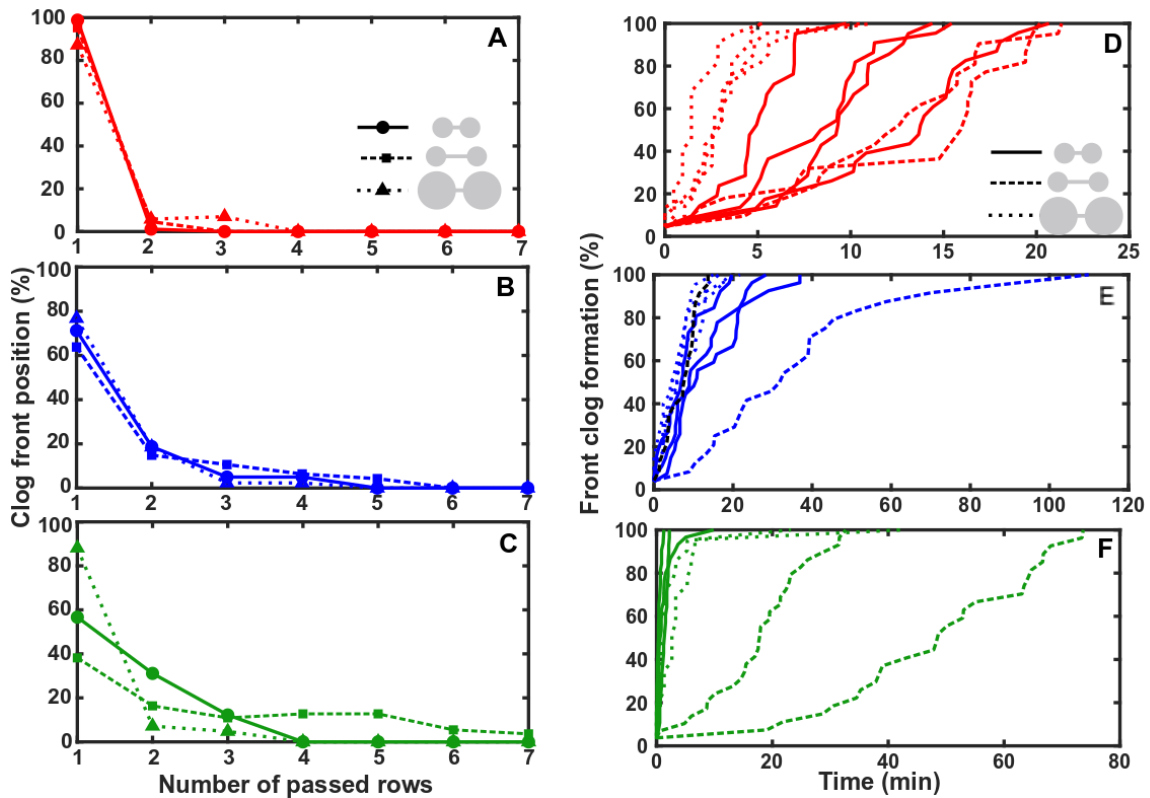


Figure 7.24: (left) Front position according to the row for all geometries configuration for case with no-salt (a), $I=50\text{mM}$ (b) and 300mM (c). (right) Clogging time of the clog front for case with no-salt (d), $I=50\text{mM}$ (e) and 300mM (f).

Surprisingly, the final clogging time, when the medium is completely clogged, increases very significantly from 10min up to 80min for a fully clogged medium when the spacing increases (figure 7.24f). Increasing the spacing between pores leads to an increase of the clogging time of the original clogs since more aggregates are needed to fill a larger gap. In the same time, the particle deposition favors the growth of dendrites, allowing dendrite clogs to rule over the medium clogging. However, object deposition can also take place

upstream of the porous zone. The particles are captured and form clusters on the horizontal walls on the channels prior to the entrance of the ordered porous structure. These clusters grow over time, mainly capturing the larger flowing objects (figure 7.25). Thus the size distribution of the objects that enter inside the porous structure is shifted towards smaller objects.

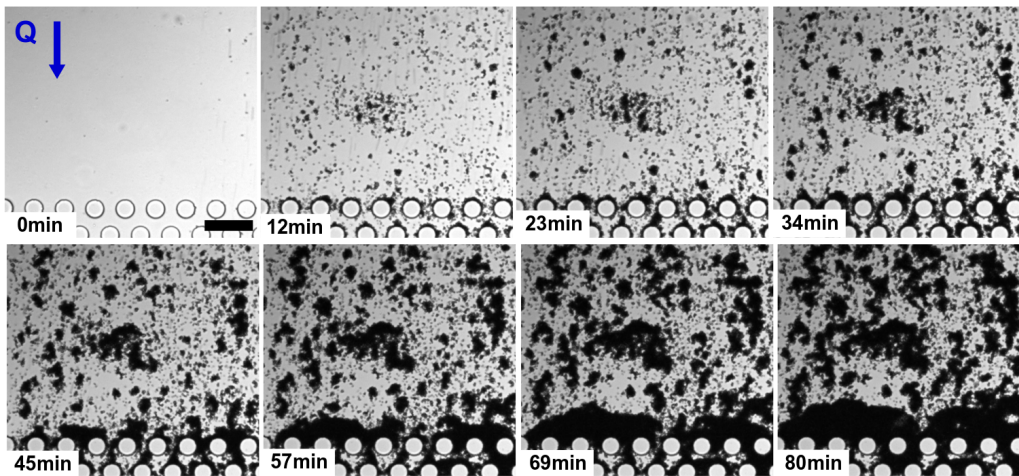


Figure 7.25: Successive images of the depotion of particle upstream of the porous media. Clusters appear and merge. Scale bar: 100 μ m.

Their number first increases until they start to see each other and merge (figure 7.26 and 7.27a), reducing at the same time the number of paths in which particles can pass through without being captured.

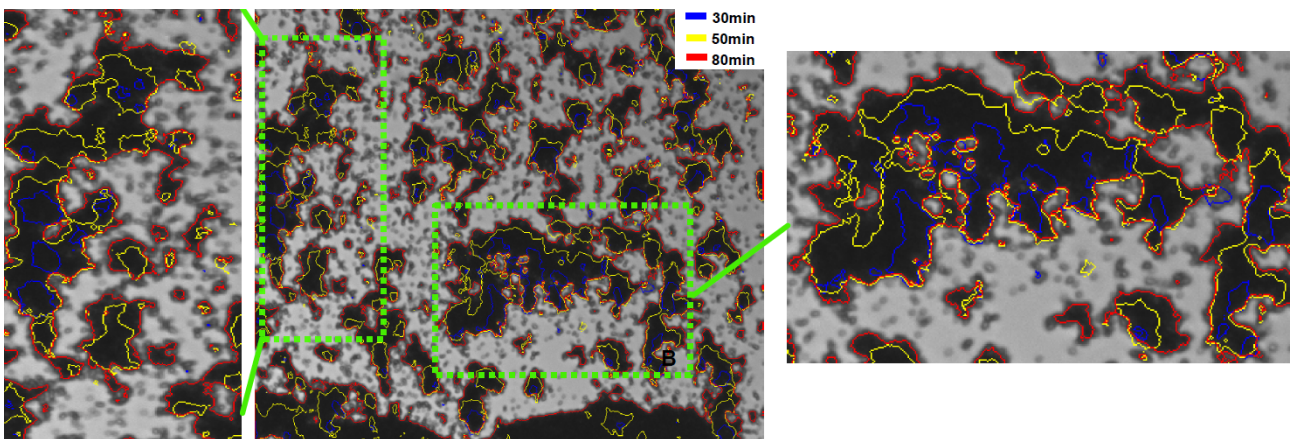


Figure 7.26: Contour at 30, 50 and 90min from the clusters. New clusters continue to appear at 50min. The lateral images are zooms of clusters that have grown and merged together.

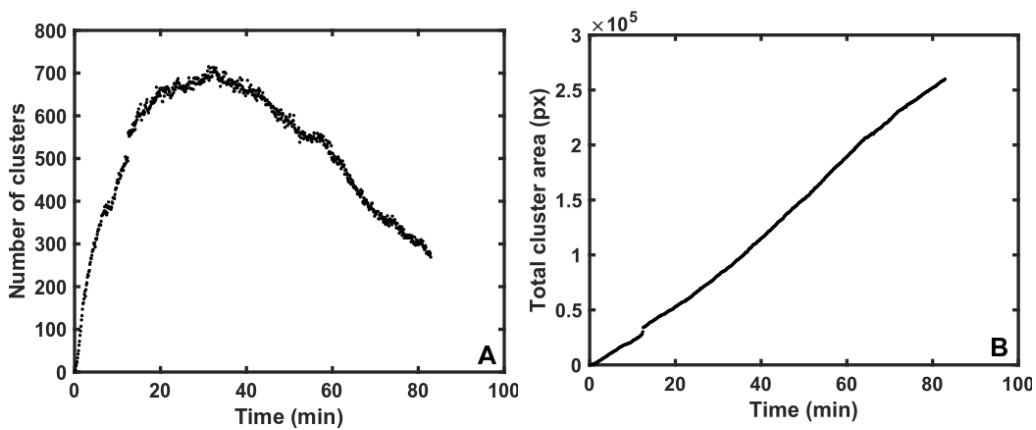


Figure 7.27: (a) Evolution of the number of clusters present in the figure 7.25 and (b) evolution of their area.

Thus the longer the clogging, the larger the area of these clusters and the smaller the number of paths for the particles, the particle size distribution being shifted towards smaller objects, which in turn leads to a longer clogging time.

Radius collector R_c

The same study was performed for collectors with different radii and $D_p = 10\mu\text{m}$. The increase of R_c has no impact on the clogging process of the medium and clogs are still located at the entrance for the three suspensions. Dendrite clogs disappear completely where R_c increases, since the deposition on the walls is extremely limited (figure 7.28). Surprisingly, accumulation clogs disappear for all ionic strengths for the higher R_c (table 7.3), while the average number of clogs in the whole medium remains constant.

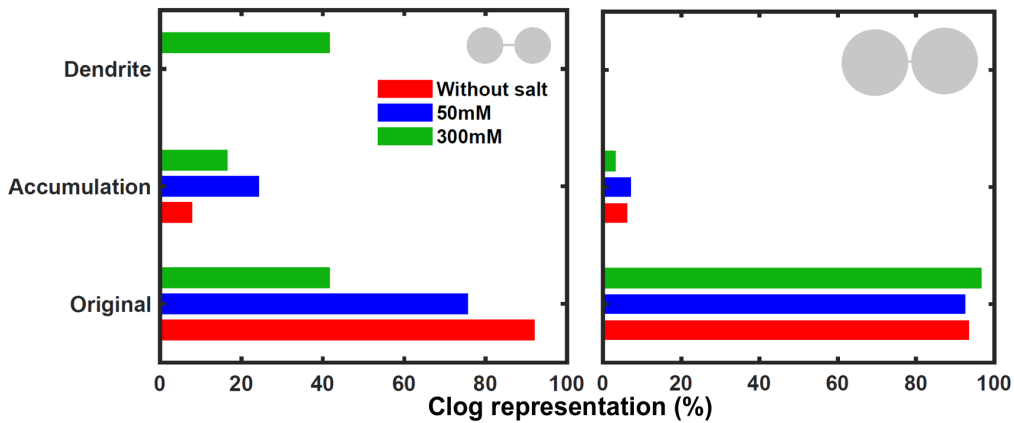


Figure 7.28: Proportion of each type of clog depending on the porous medium geometry with $R_c = 15\mu\text{m}$ and $D_p = 10\mu\text{m}$ (a), $R_c = 15\mu\text{m}$ and $D_p = 30\mu\text{m}$ (b), $R_c = 75\mu\text{m}$ and $D_p = 10\mu\text{m}$ (c).

	$R_c = 15\mu\text{m}, D_p = 10\mu\text{m}$				$R_c = 75\mu\text{m}, D_p = 10\mu\text{m}$			
	Orig.	Acc.	Dend.	Tot.	Orig.	Acc.	Dend.	Tot.
No salt	32	13	0	34	36	2	0	40
50mM	69	22	0	91	92	7	0	99
300mM	79	32	113	168	104	3	0	107

Table 7.3: Average number of each type of clog in an experiment: original (Orig.), accumulation (Acc.), dendrite (Dend.) and total (Tot.) for two radii.

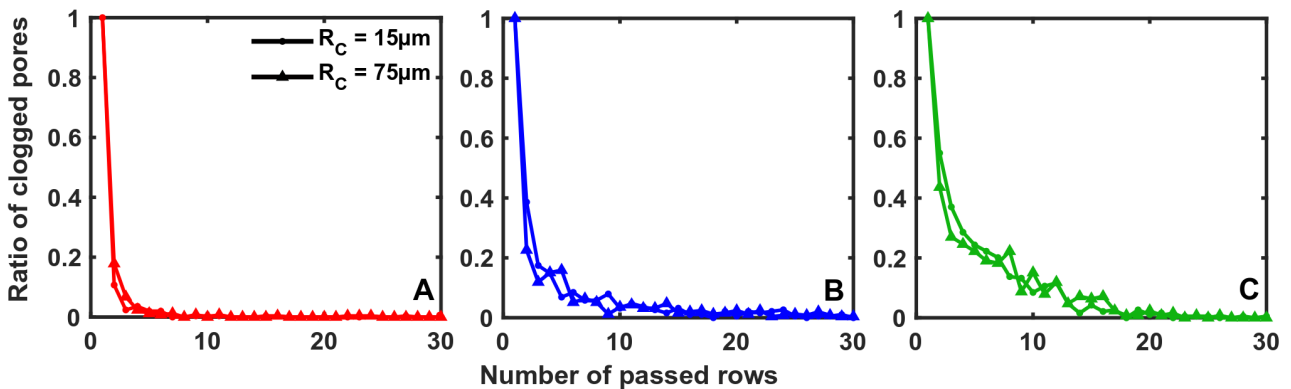


Figure 7.29: Ratio of clogged pores over the rows depending on the radius for the case with no-salt (a), $I = 50\text{mM}$ (b) and $I = 300\text{mM}$ (c).

The clog front is again identical for the two lower salinities, however, for $I = 300\text{mM}$, the number of clogs in the front belonging to the first row increases from 60% to 80% when R_c increases. This is due to a

the absence of accumulation clogs, while original clogs remain constant for both radius. We explain this increase by the difference between the paths followed with the two collector sizes (figure 7.30).

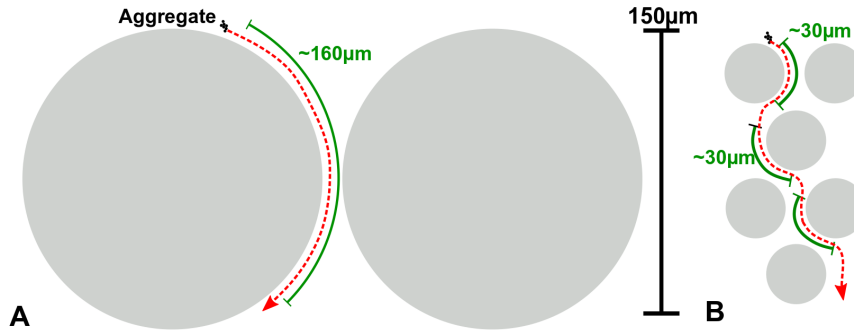


Figure 7.30: Example of an aggregate trajectory next to a collector with $R_c = 75\mu\text{m}$ (a) and $R_c = 15\mu\text{m}$ (b). Red arrows represent an aggregate trajectory, and green lines are the distances over which navigate aggregates close to a collector.

7.3 Variations in hydrodynamic conditions have little effect on clogging

In this last part, the flow rate is varied from 0.3 up to 2.5 $\mu\text{L}/\text{min}$ in media with $R_c = 15\mu\text{m}$ and $D_p = 10\mu\text{m}$. Increasing the flow rate results in a longer transportation length and thus particles are captured deeper in the medium, which can be seen in the figure 7.31 for $l = 300\text{mM}$. In addition, the increase of the hydrodynamic force increases the object capture but also limits the growth of the deposit. Indeed, we saw in chapter 3 that increasing the flow rate could reduce the capture probability of objects depending on their size and shear impacts the deposit morphology. In the same way, it can be expected that flow rate impacts the clogging of the medium.

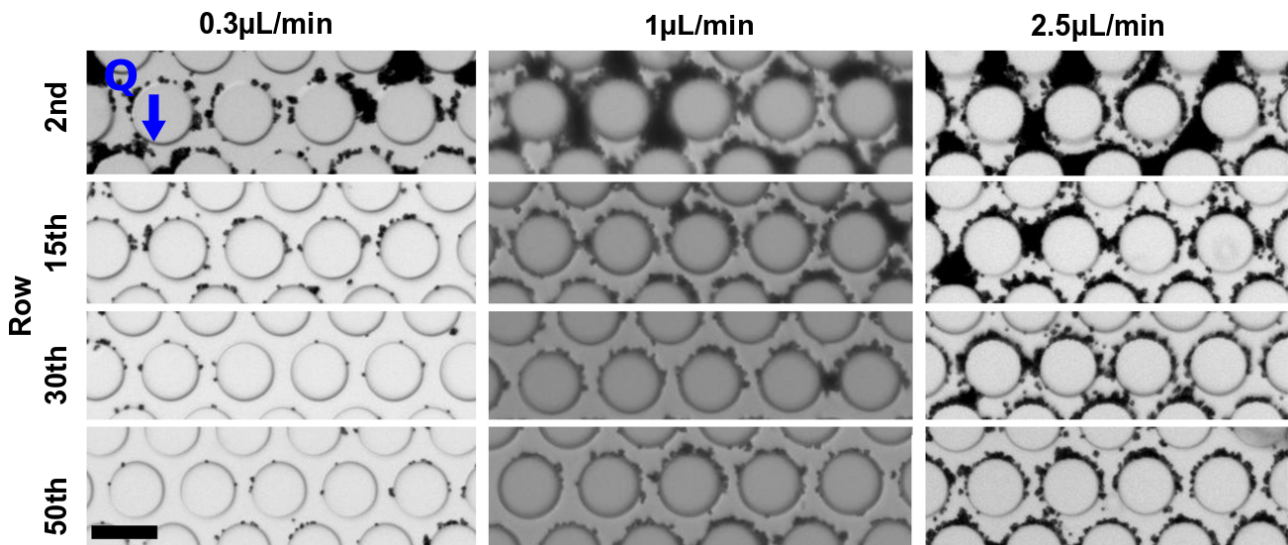


Figure 7.31: Different deposit patterns for porous media with $R_c = 15\mu\text{m}$ and $D_p = 10\mu\text{m}$ along the medium for $l = 300\text{mM}$. Scale bar: $30\mu\text{m}$.

The number of clogs is counted for each category, original, accumulation and dendrite and we compare for each salinity the three flow rates (figure 7.32). The clogging in the no salt case is not impacted by the flow and original clogs are dominant. Both the ratio of clogged pores (figure 7.33) and front clogs (figure 7.34a) are identical. In addition, the clogging time decreases with the flow rate (figure 7.34d). We observed the same trend for $l = 50\text{mM}$, except for the clogging time (figure 7.34e). At 2.5 $\mu\text{L}/\text{min}$, the

clogging time is similar, indicating a delayed clogging for high flow rates. There is also a deposition of objects on the walls of the collectors, without changing the particle size distribution. Smaller objects are therefore initially deposited on the surface of the collectors, favouring later on the capture of larger objects. Increasing the flow rate could also wipe off these objects, slightly increasing the clogging time, without changing the clogging mechanism.

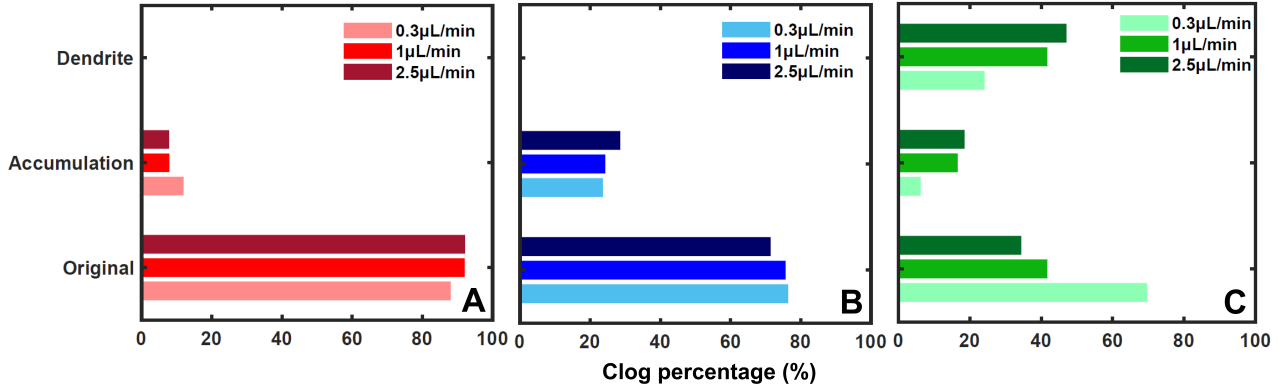


Figure 7.32: Percentage of clog for each category original, accumulation and dendrite for a suspension with no-salt (a), $I=50\text{mM}$ (b) and $I=300\text{mM}$ (c).

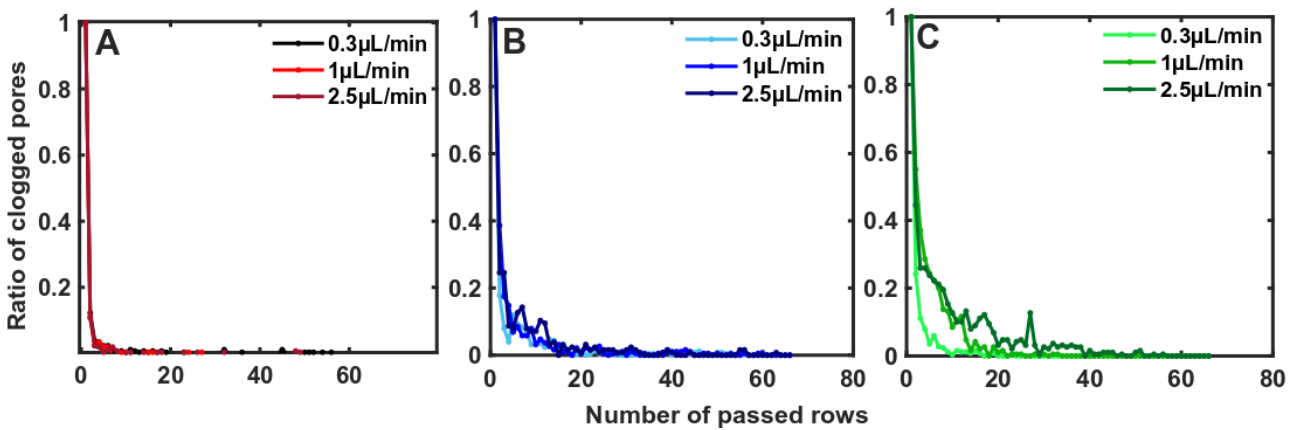


Figure 7.33: Ratio of clogged pores over row. The inset is the difference between the largest and the smallest flow rate for a suspension with no-salt (a), $I=50\text{mM}$ (b) and $I=300\text{mM}$ (c).

As expected, the 300mM suspension is strongly impacted by the flow rate and the dominant clogging mechanism gradually shifts from the original to the dendrite one (figure 7.32c). In addition, the greater the flow rate, the deeper in the medium the clog front is (figure 7.34). Surprisingly, the clogging times are identical whatever the flow rate (figure 7.34f). For lower flow rates it takes a longer time for the objects to arrive but they are not deposited in the upstream area, i.e. in the zone just upstream of entrance of the ordered porous medium. For larger flow rates, they are much more numerous and are transported further downstream into the medium (figure 7.33c) however they undergo, in addition to the upstream deposition, an erosion at the collector walls. All these effects compensate each other and we end up with the same clogging time.

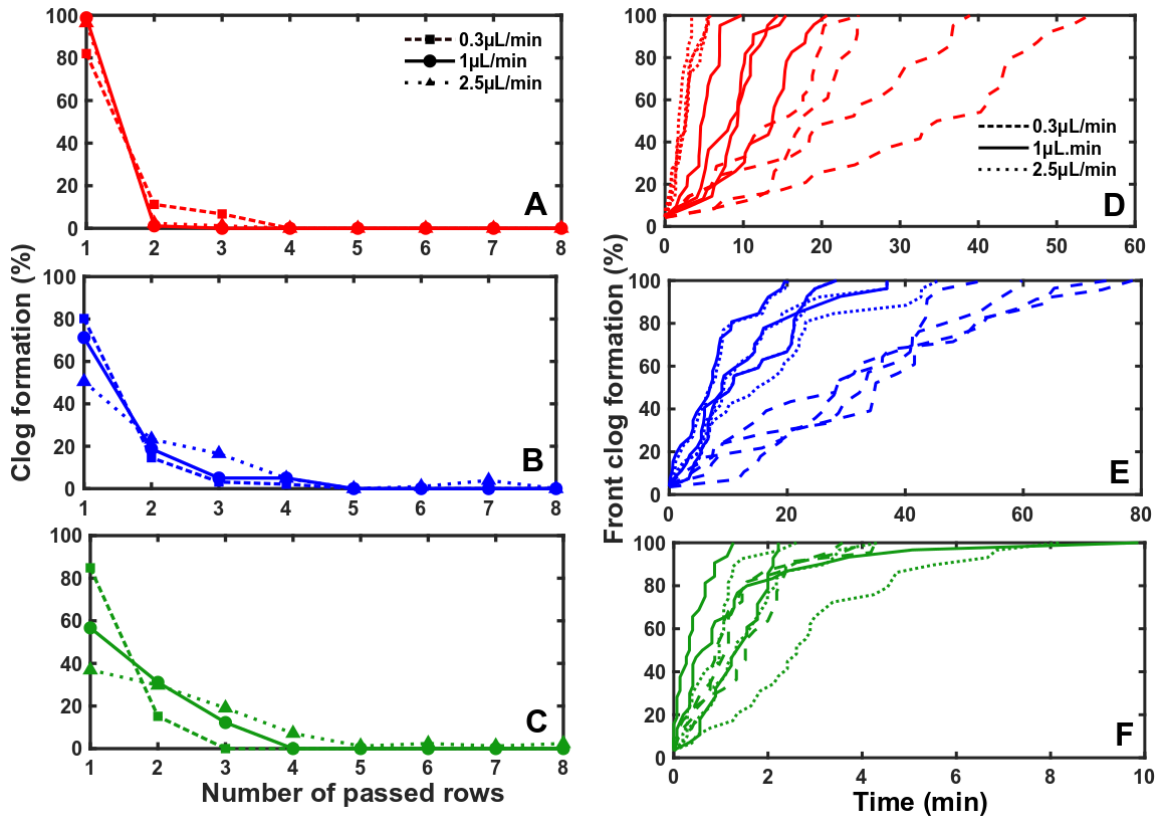


Figure 7.34: Clog front line depending for the different flow rate depending for the no salt case (a), 50mM (b) and 300mM (c). Clogging time of the medium for the no salt case (d), 50mM (e) and 300mM (f).

We also note that the flow rate does not modify the repartition between the different clogging mechanisms for the no-salt suspension and $I = 50\text{mM}$. For the 300mM suspension, the flow rate modifies the clogging mechanism by modifying the deposition on the collector walls (figure 7.31). There is a transition from a weak deposition which favours original clogging to a much more important one that promotes dendrite clogging when the flow rate increases.

7.4 Conclusion

We determined in this chapter how the addition of salt modify the clogging of an ordered porous medium, by promoting the deposition of objects at the walls of the collectors. We varied the flow rate and the geometrical parameters of the porous medium such as the collector radius and the spacing between collectors. As seen before, the particles clog the media at their entrance, whatever the experimental conditions. However, we noticed some differences coming from the evolution of the clogging dynamics. Most importantly, the deposition increases with salinity when there is no repulsion with the walls but still between the particles, for $I=50\text{mM}$. For $I=300\text{mM}$, dendritic shape-like emerge and are the basis of a new type of clogging, dendrite clogs. A competition takes place between original clogs and dendrite clogs, depending on whether the deposit is large enough to promote clogging of the medium, such as dendrites. The main impact of parameters such as the geometry of the medium or the flow rate is the modification of the morphology of the deposit, and the selection of a clogging mechanism over the others. We thus have observed that the increase of the radius rises up the shear and does not allow the formation of dendrites. On the contrary, increasing the spacing enhanced the formation of dendrites, by delaying the clogging time and increasing the space available for the dendrite growth. Increasing the flow rate allows the particles to be transported further in the medium prior to clogging, which increases the size of the dendrites. When the electrostatic repulsion from the collector's surface is high, the original clogs are the most numerous and the clog front is located at the very entrance of the medium. There is an increase of the number of clogs within the medium with the ionic strength, these kind of clogs coming from the growth of dendrites. However, porous media are still clogged near their entrance, whatever the experimental conditions. This shows once again that the media clogging relies on the aggregate deposition, irrespective of the clogging mechanism. The presence of aggregates and their high probability to be deposited as soon as they come across the first rows of pores prevails on the clogging of the porous media.

Chapter 8

Flow decline during the clogging of porous media

In this chapter we study the flow decline during the fouling of an ordered porous media by colloidal particles. We monitor the flow decline thanks to the evolution of particle velocity, as in chapter 5. We modify the interaction potential and the particle size to obtain different variations of the media's permeability over time. We present a model of the flow decline that takes into account the clogging dynamics of the entire medium, including the clogging at the pore scale and the accumulation of particle behind the clogs. All the materials presented here is still under analysis and additional works are necessary to refine the model.

Contents

8.1	Context of the study	206
8.2	Experimental results	207
8.2.1	Impact on the particle size on the flow rate	207
8.2.2	Impact on the ionic strength on the flow rate	209
8.3	Modelization of the flow decline	210
8.3.1	Proposal n°1	212
8.3.2	Proposal n°2	214
8.3.3	Proposal n°3	216
8.3.4	Proposal n°4: perspectives	218
8.4	Conclusion	219

8.1 Context of the study

During the filtration of a suspension of solid particles through a membrane, a significant drop in flow rate is observed. This flow decline is associated with a progressive fouling of the membrane which leads to its partial or complete clogging. Since in industrial environment it is not often possible to observe the deposit on top or inside the membrane during filtration, the monitoring of the temporal evolution of the flow rate is an important indirect parameter to estimate the state of the membrane fouling and measure the filtration efficiency. When the filtration process is no longer efficient, the membrane is either replaced or undergoes a backwashing step i.e. a flow reversal to partially eliminate the fouling. In some cases, an additional chemical treatment is necessary. Understanding the flow decline could help determining when the irreversible clogging of membranes occurs, thus indicates to the operator when an action is required, increasing in this way the efficiency of the filtration process and also limiting the cost.

In this part, we make the link between the flow decline and the formation of clogs in a model ordered porous medium. The objective is to understand from the measurement of the flow rate and the images of the medium, as it gets fouled, what are the phenomena that have the greatest impact on the flow decline.

Throughout this chapter we use the Ohm's law for hydrodynamics $\Delta P = R_{eq}Q$. This relationship has been used before for a single pore in chapter 4 and now we define the equivalent hydrodynamic resistance R_{eq} , composed of all the resistances R of each pore. Since we apply a constant pressure, the knowledge of R_{eq} gives us access to the variation of the flow rate. We restrict ourselves to the no added salt case considered in chapter 6. We identify three main contributions to R_{eq} (figure 8.1). First of all, the formation of the clog front that corresponds to a line of clogged pores. Secondly, the accumulation of particles behind the clog front of the first row, also called cake layer, may largely contribute to R_{eq} , as it is the case in all filtration processes. Finally clogs formed within the medium, which do not belong to the clog front, have an impact on R_{eq} . We suppose that this contribution remains small since the connectivity of the medium is high and the particles can be easily redistributed around an obstructed zone but this has to be confirmed. There could also be particle accumulation behind the clogs within the medium, i.e. the formation of accumulation clogs, but we have seen in chapter 5 that this phenomenon is rather limited and thus we do not consider its contribution in the following.

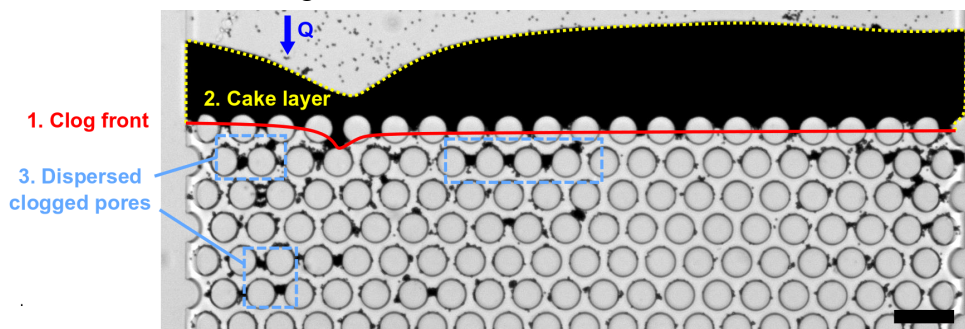


Figure 8.1: The three phenomena that are suspected to have the greatest impact on the drop in flow rate (1) the clog front (red line), (2) the cake layer (yellow dotted line) and (3) dispersed clogged pores (blue rectangles). The scale bar: 70 μ m.

To go further in the quantification of the global hydrodynamic resistance we propose a model with various assumptions based on different calculations of R_{eq} , taking into account the three contributions just mentioned above. From this model we also obtain a theoretical variation of the flow rate Q_{th} , which can be compared to the one we measure experimentally Q_{exp} , thanks to the average velocity of particles at the entrance of the porous structure.

8.2 Experimental results

We first present the detail of our protocol to monitor the variation of the flow conditions as the medium gets fouled. We changed either the particle size D or the ionic strength I to directly modify R_{eq} . Changing the particle size has a direct impact on the permeability of the deposits or clogs. When we increase D from 1.5 up to $5\mu\text{m}$ in our porous geometry with a $15\mu\text{m}$ by $15\mu\text{m}$ cross section, the confinement increases with W/D going from 10 to 3. By doing so, the stacking of the larger spheres is much more permeable and hence the increase of R for a pore is much smaller than before. We vary I , as we did in the previous chapter, with a PS $1.5\mu\text{m}$ suspension, working with $I = 50$ and 300mM . In such conditions we know that we can more easily see the impact of all the types of clogs formed within the medium.

To determine the average particle velocity we take short movies of 3s at 100fps every 5 to 30s according to the average clogging time in each condition. Contrary to the part I of this thesis, the average velocity obtained by particle tracking is more complex to define. Indeed, the flow at the medium entrance become quickly heterogeneous as soon as a few pores get clogged. The velocity profile does not corresponding anymore to a Poiseuille profile (figure 8.2). To limit as much as possible the consequences of the flow heterogeneities, only the velocity of the particles $300\mu\text{m}$ upstream of the medium entrance are considered.

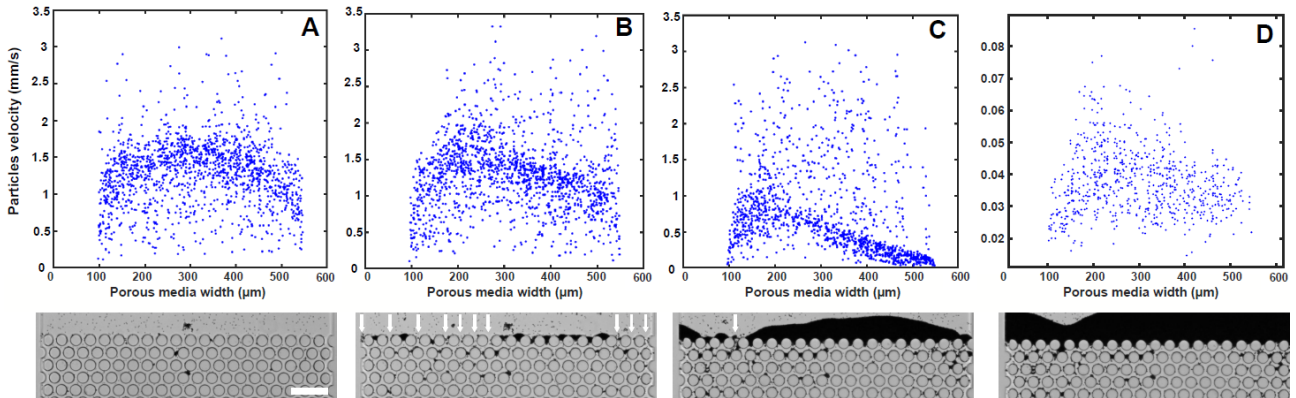


Figure 8.2: (top) Different velocity maps taken over 3s, when the porous medium is completely free (a), 10 pores are free (b), only 1 pore remains free (c), the medium is clogged (d). Blue dots correspond to a single particle velocity. (bottom) Corresponding images of the porous medium. Scale bar: $100\mu\text{m}$.

8.2.1 Impact on the particle size on the flow rate

Figure 8.3 shows three flow declines for $D=1.5, 3$ and $5\mu\text{m}$ particles, with the corresponding images. We first note that the average clogging time decreases a lot with the size of the particles, from 200, 13 and 4min for $D = 1.5, 3$ and $5\mu\text{m}$, respectively. This difference corresponds to different ways the media are clogged. Clogging by $1.5\mu\text{m}$ particles can be a bit long at the beginning, i.e. no clogging shows up in the first thirty minutes, the time necessary to have enough aggregates that enter into the medium and deposit in the pores. But later on there is a cascade of clogs that spreads over several tens of minutes (figure 8.3a).

The same dynamics is found for $D=3\mu\text{m}$, except that the time from which the clog cascade starts is much shorter, between 2 and 3 minutes after the beginning (figure 8.3b). For those two particle sizes, while there are still free pores, a cake layer starts to form behind the partial clog front (figure 8.3a-b iii). For $D=5\mu\text{m}$ pores are clogged almost at the same time, letting no time for the local formation of a cake layer (figure 8.3c ii). An other observation concerns the flow decline associated with the clogging of the last pore of the front. The larger D , the smaller the flow decline. The ending flow rate when the medium is completely clogged, is $0.04\mu\text{L}/\text{min}$ for $D=1.5\mu\text{m}$, rising to $0.08\mu\text{L}/\text{min}$ for $D=3\mu\text{m}$ and increasing again for $D=5\mu\text{m}$ to $0.40\mu\text{L}/\text{min}$. At the end of the experiment, even when the cake layer increases significantly, it weakly contributes to the flow decline for $D=1.5$ and $3\mu\text{m}$. These different ending flow rates reflect the different permeability of the clogs in each case, and also that R_{eq} is not impacted in the same way during the fouling process.

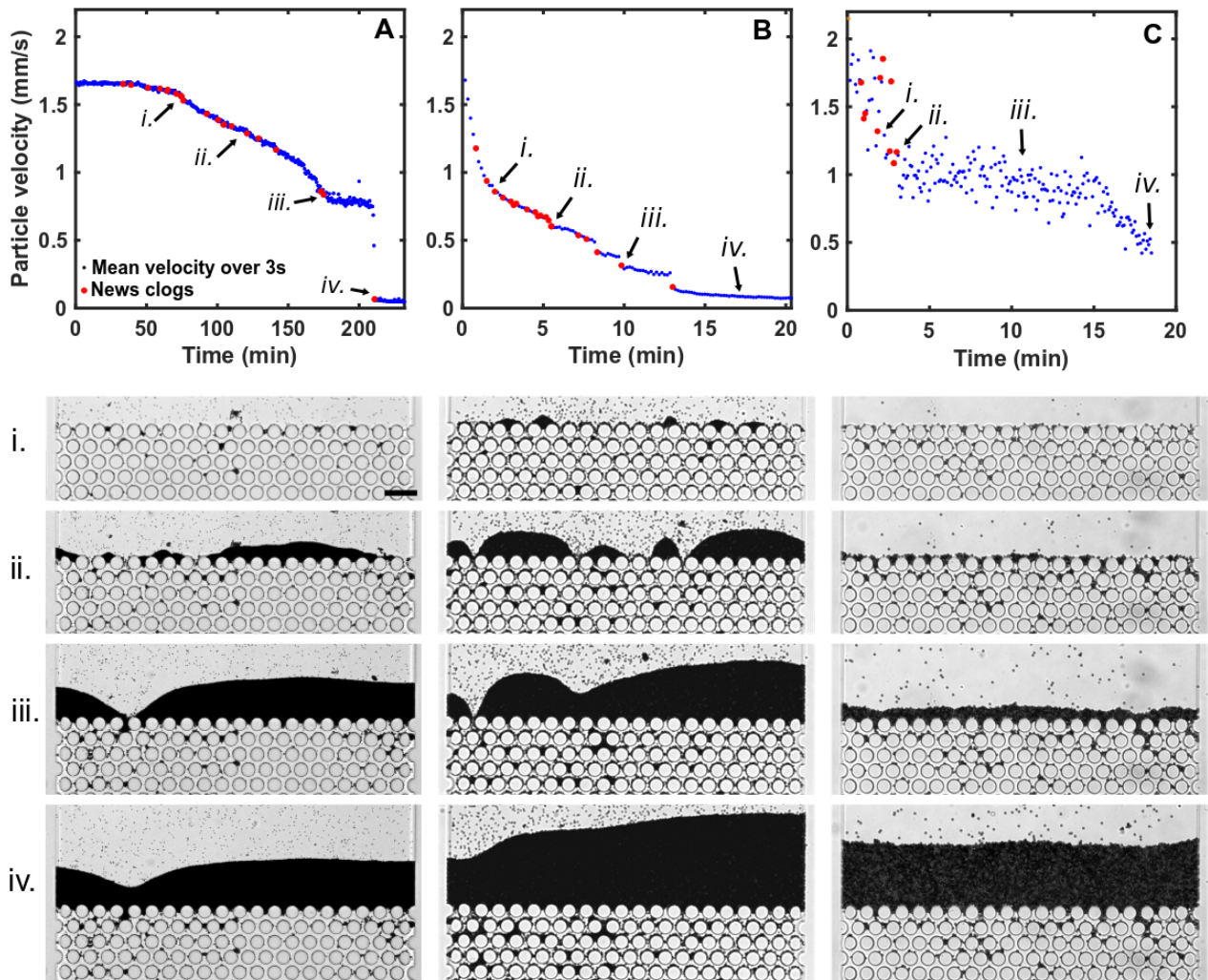


Figure 8.3: (top) Flow decline during clogging for PS suspensions with a $D=1.5$ and $W/D=10$ (a), $D=3$ and $W/D=5$ (b) and $D=5$ and $W/D=3$ (c). Larger circles in red indicated pore clogging events while blue dots are the mean particle velocity. (bottom) Images corresponding to the times indicated by numbers on the graphs. Scale bar: $65\mu\text{m}$.

8.2.2 Impact on the ionic strength on the flow rate

Figure 8.4 shows the flow decline for suspension with no salt, $I=50$ and 300mM , with the corresponding images. We have discussed in the previous chapters that the addition of salt, i.e. for $I=50\text{mM}$, favors the deposition of objects and for $I = 300\text{mM}$ it leads to the formation of dendrites and increases in this way considerably the number of clogs inside the medium. The consequence of this increase is a rising up of R_{eq} , as can be seen on the flow decline of the no salt case and $I=50\text{mM}$ (figure 8.4a-b). The flow decline without salt always undergo one or more sudden large drops for the very last clogged pores, while for $I=50\text{mM}$ the flow decline is more gradual. As we have seen in chapter 3 the addition of salt below the CCC has no impact on the permeability of the clogs and thus we deduce that the main reason why the flow decline amplitude is smaller for $I=50\text{mM}$ is only due to the increase of the number of clogs inside the medium and not at its entrance. For $I=300\text{mM}$, clogs form almost at the same time, which results in a rather rapid drop in flow rate (figure 8.4c). However, it can be pointed out that the ending flow rate is higher and around $0.25\mu\text{L}/\text{min}$. This is unexpected for this unstable suspension since there are a great number of clogs within the medium and important deposit elsewhere, both can be contributing to rise up R_{eq} . However, as seen in the previous chapter this suspension also contains a high concentration of aggregates, which likely creates a very porous particle accumulation inside both the clogs and the cake layer.

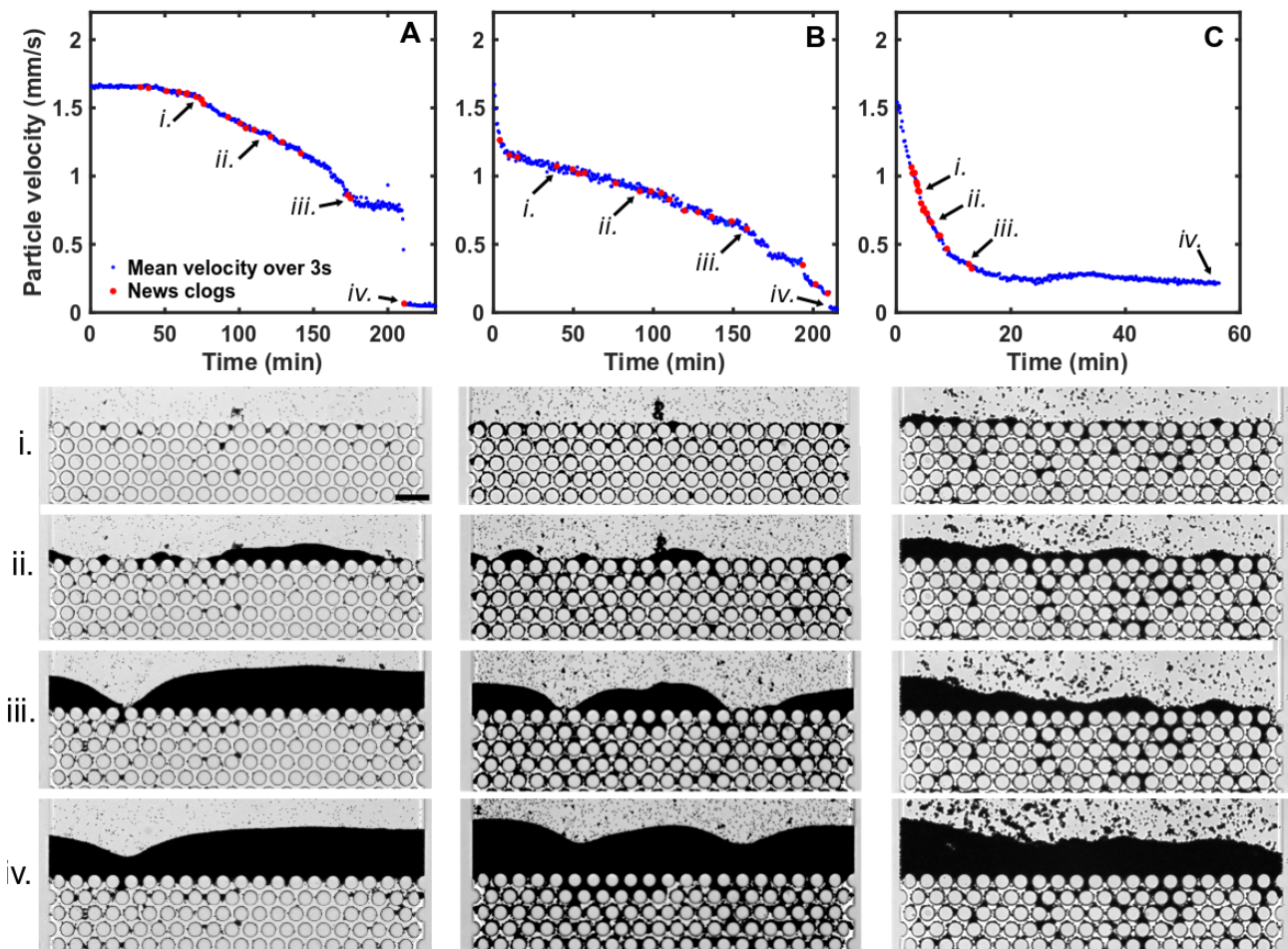


Figure 8.4: (top) Flow decline for a $1.5\mu\text{m}$ PS suspensions with no salt (a), $I=50\text{mM}$ (b) and $I=300\text{mM}$ (c). Larger circles in red indicated pore clogging events while blue dots are the mean particle velocity. (bottom) Images corresponding to the times indicated by numbers on the graphs. Scale bar: $65\mu\text{m}$.

8.3 Modelization of the flow decline

We propose a mechanical model to explain the velocity decline during the porous media clogging. This model relies only on the calculation of the hydrodynamic resistance of each pore from the images. The pore resistance varies if the pore is clogged or free, and according to the length of the particle accumulation behind it. From these resistances, we deduce the equivalent resistance and the flow rate from $\Delta P = R_{eq}Q$, since we applied a constant pressure. In the following we present several versions of the model, starting with the simplest assumptions and go on with more complex ones.

We applied the different versions of the model only on the 1.5 μm PS suspension with no salt added. Figure 8.5 shows the flow decline and the corresponding images, already discussed in chapter 6.

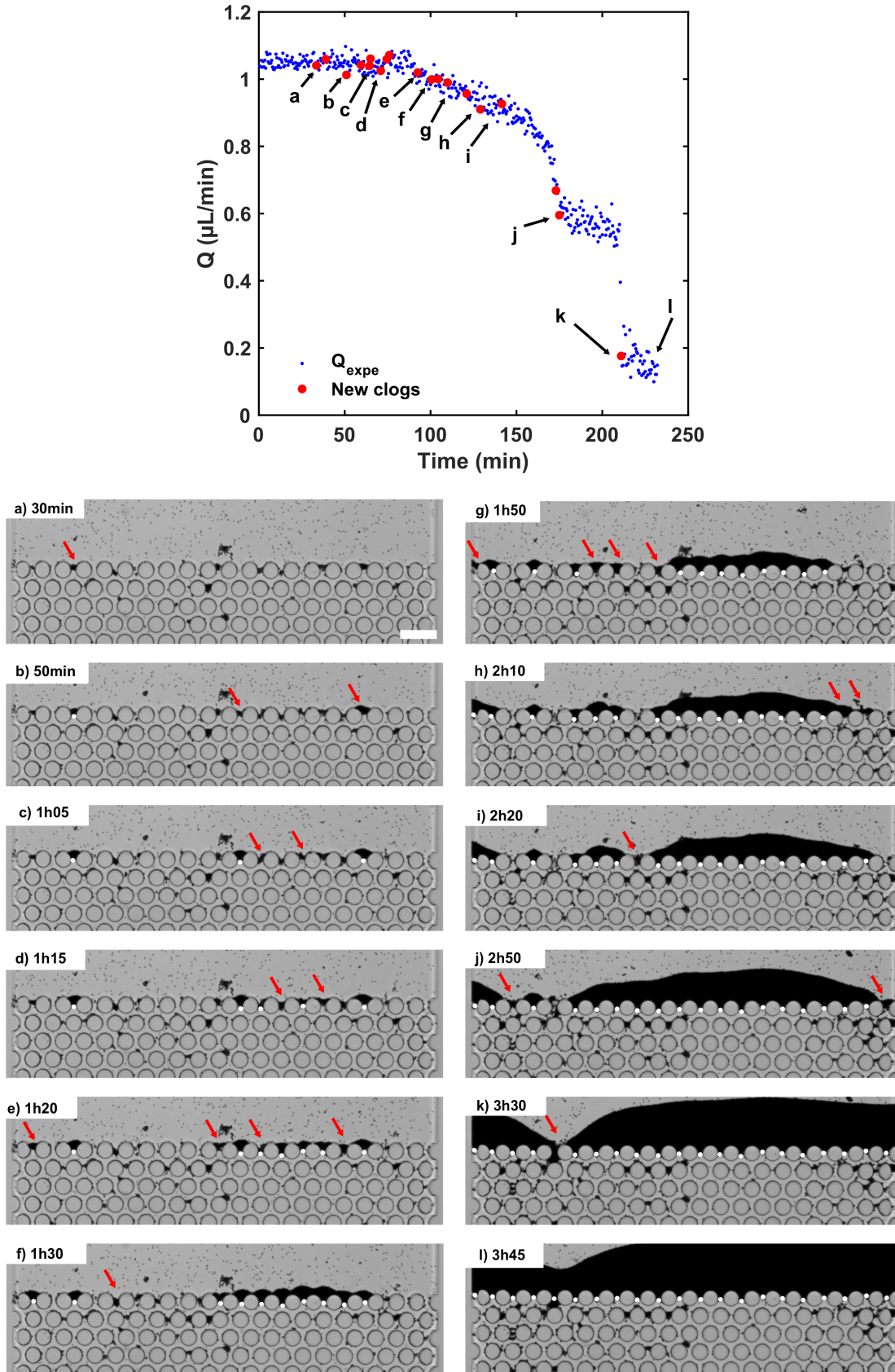


Figure 8.5: Flow decline for a $1.5\mu\text{m}$ PS suspensions with no salt and corresponding images. Large circles in red on the graph indicate clogging events while blue dots are the mean particle velocities. Red arrows on the images indicate the new clogs and white dots the clogged pores at previous time. Scale bar: $80\mu\text{m}$.

8.3.1 Proposal n°1

Hypothesis

1. Clogs in other pores than the 1st row have no impact on the flow decline.
2. The particle accumulation in the reservoir zone has no impact on the drop.
3. Resistances of clogged pores are identical.

The previous chapters have shown that the media are clogged at their entrance. Based on this observation, we consider in the first proposal only the clogging of the first row of the medium.

Initially, all pores are free and have the same hydrodynamic resistance R_f . As we consider only the first row, the equivalent electrical diagram of such a configuration is simply N resistances in series (figure 8.6).

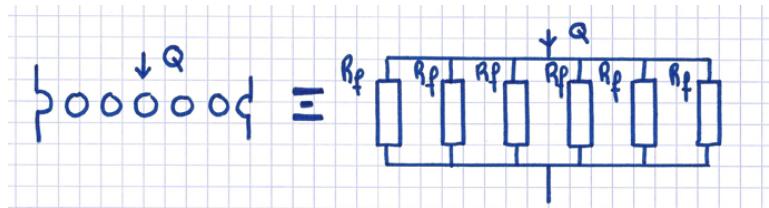


Figure 8.6: Equivalent electrical diagram of the first row of an empty porous medium

We can therefore estimate the value of a resistance R_f from the flow rate Q with the following relation:

$$\Delta P = R_{eq} Q \quad \text{where} \quad \frac{1}{R_{eq}} = \sum_{i=1}^N \frac{1}{R_f}$$

$$R_f = \frac{N \Delta P}{Q}$$

A pore has two states: free or clogged, whose respective dynamic resistances are R_f and R_s . All clogged pore resistances are identical, regardless of the accumulation of particles behind the clog (figure 8.7).

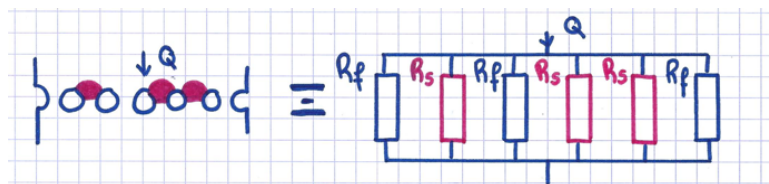


Figure 8.7: Equivalent electrical diagram of the first row of a porous medium with some pore clogged.

The value of R_s can be estimated when only one pore is clogged:

$$\Delta P = R_{eq} Q \quad \text{where} \quad \frac{1}{R_{eq}} = \frac{N-1}{R_f} + \frac{1}{R_s}$$

$$R_s = \frac{1}{\frac{Q}{\Delta P} - \frac{N-1}{R_f}}$$

From the equivalent electrical diagram, R_{eq} is simply derived, as well as the theoretical flow rate Q_{th} with the following relation:

$$Q_{th} = \frac{\Delta P}{R_{eq}} \quad \text{with} \quad \frac{1}{R_{eq}} = \frac{N_f}{R_f} + \frac{N_s}{R_s}$$

For the first dozen of clogged pores, this relation Q_{th} fits well the experimental data, but beyond there is large deviation from the experimental flow rate (figure 8.8).

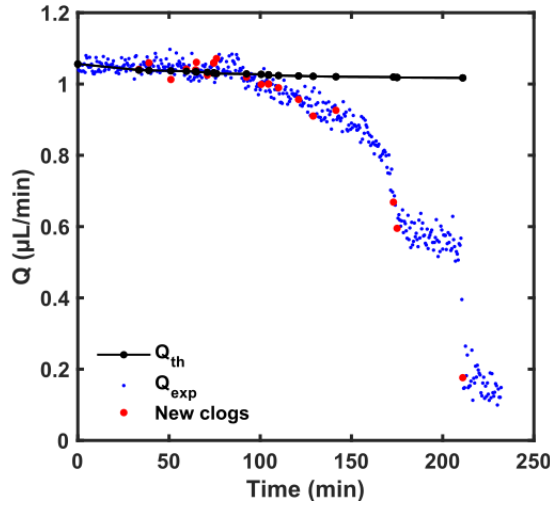


Figure 8.8: Comparison between Q_{th} from proposal n°1 and the measured Q_{exp}

The simplicity of the assumptions of the proposal n°1 explains the divergence between Q_{th} and Q_{exp} . When we look at the images three observations can help us to understand why this scenario fails so rapidly. When the first ten pores are clogged the model works well since there is no particle accumulation behind them, which is not the case later on from the 11th clog (blue rectangles the images figure 8.9b-c). Since this accumulation takes place in the interval where the two curves start to depart from each other, we may assume that it has a significant impact on the flow decline. The second observation concerns some pore that have a reduced section before to be clogged, due to deposition (red rectangles the images figure 8.9b-c). However, this reduction in cross-section also increases the hydrodynamic resistance in these pores, and could have an impact on the flow rate. Finally, there are pores clogged inside the medium (white rectangles figure 8.9), which should impact the flow if we consider the analogy with an electrical circuit.

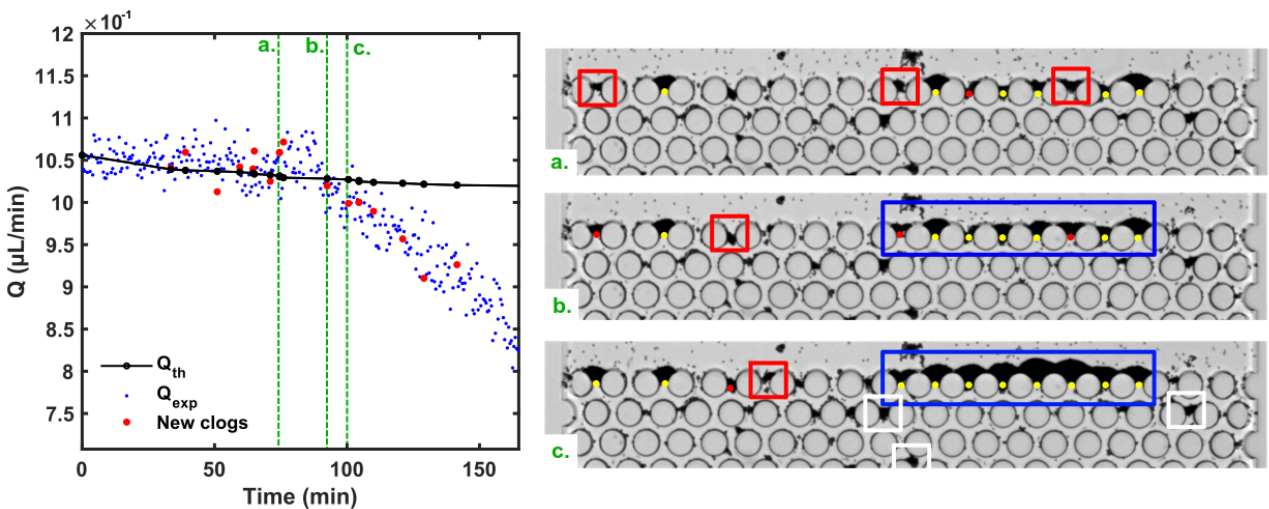


Figure 8.9: (left) Zoom on the divergence between Q_{th} and Q_{exp} . (right) Images before and after the divergence.

We take into account these observations in the next proposal in order to better describe the experimental data.

8.3.2 Proposal n°2

Hypothesis

1. Clogs in other pores than in the 1st row have no impact on the drop.
2. The accumulation in the reservoir is taken into account in a crude way.
3. The resistances of the clogged pores may vary.

In this improved proposal, the resistances of the clogged pores vary according to the particle overflow in the reservoir zone. To take into account of the particle accumulation, we define a rectangle with a fixed length $L'_{pore} > L_{pore}$, defined from the maximal accumulation of the cake layer, with L_{acc} the accumulation length (figure 8.10).

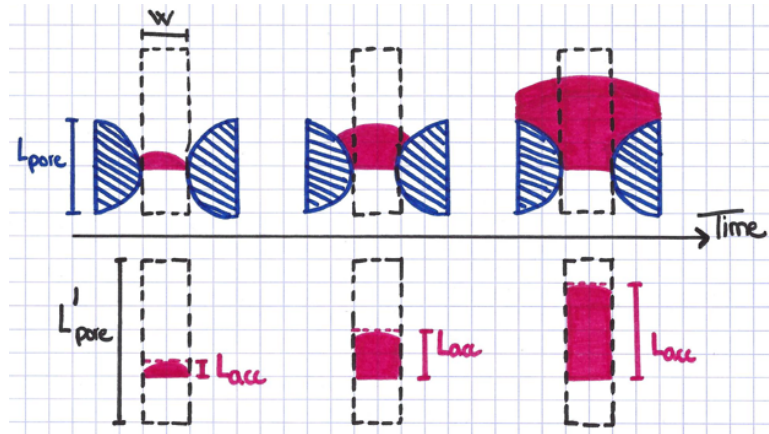


Figure 8.10: Evolution of the approximated accumulation length L_{acc}

A clogged pore is thus composed of several zones, empty and clogged with respective permeability k_f and k_s . To calculate the resistance of the pore R_s , it is necessary to calculate the average permeability \bar{k} :

$$\bar{k} = \frac{\sum_i L_i}{\sum_i L_i / k_i} = \frac{L'_{pore}}{\frac{L_{acc}}{k_s} + \frac{L'_{pore} - L_{acc}}{k_f}}$$

Considering the section A of a pore and from the Darcy's law $Q = \frac{k \Delta P}{\mu L}$ we deduce the clogged pore resistance R_s :

$$R_s = \frac{\mu L'_{pore}}{\bar{k} A} = \frac{\mu}{A} \left(\frac{L_{acc}}{k_s} + \frac{L'_{pore} - L_{acc}}{k_f} \right)$$

Each time a new pore is clogged, the resistance R_s of each previously clogged pore is recalculated to take into account the evolution of L_{acc} and to better estimate the equivalent resistance R_{eq} :

$$\frac{1}{R_{eq}} = \frac{N_p}{R_f} + \sum_i^{N_s} \frac{1}{\frac{\mu}{A} \left(\frac{L_{acc,i}}{h_s} + \frac{L_{pore,i} - L_{acc,i}}{R_f} \right)}$$

With a rough approximation of the resistance of the cake layer, we obtain a closer Q_{th} than in proposal n°1 (figure 8.11). However, this model does not take into account the overall flow decline. Until now, we only consider the hydrodynamic resistance of the pores in the first row. However, all pores in the rest of medium have to be considered, and R_{eq} is the equivalent resistance of a large network of resistance. We propose a model based on the calculation of this network.

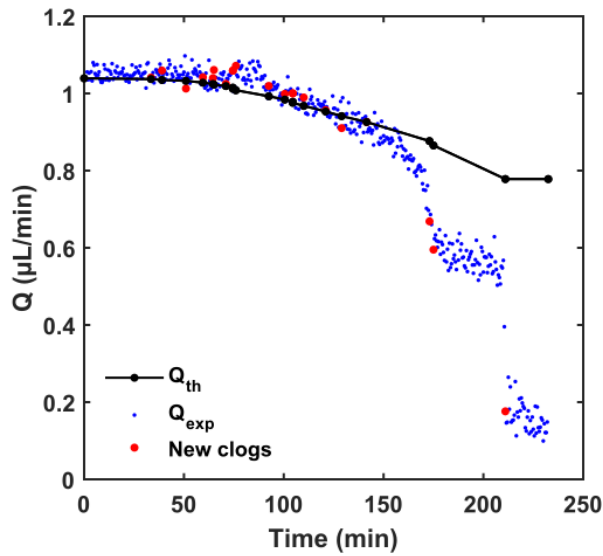


Figure 8.11: Comparaision between Q_{th} from proposal n°2 and the measured Q_{exp}

8.3.3 Proposal n°3

Hypothesis

1. Clogs in other pores than in the 1st row impact the drop.
2. The accumulation in the reservoir is taken into account in a crude way.
3. The resistances of the clogged pores may vary.

For the proposal n°3, we take into account all the clogs of the entire medium, which can be seen as an equivalent electrical circuit with resistances in series and in parallel, corresponding to the interconnection between pores of the same row and across adjacent rows. The red rectangle on the figure 8.12 represents a portion of medium whose the equivalent electrical circuit is presented on figure 8.13. R_{eq} is less easy to obtain and its calculation relies on the two Kirchhoff's laws:

- For each node of the circuit : $\sum_i q_i = 0$.
- For each closed loop of the circuit : $\sum_i P_i = 0$.

The equations generated by these laws for the small portion of the medium are shown in figure 8.13 and allow us to derive Q. For the whole environment, getting Q is equivalent to solve more than 16 000 equations simply considering the two Kirchhoff's law.

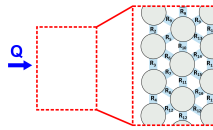


Figure 8.12: (left) Portion of porous medium and (right) its resistance notation

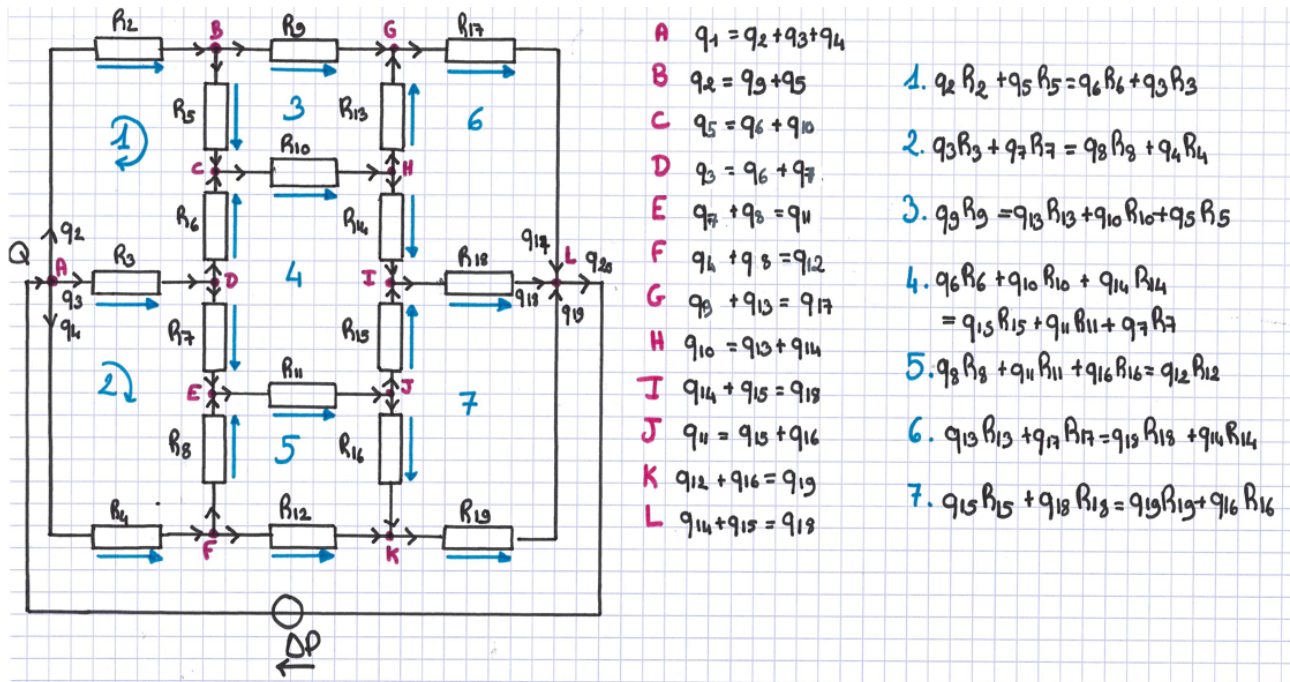


Figure 8.13: Electrical schema equivalent to the portion of porous medium presented on figure 8.12

At each new clog, we solve the set of equations to recalculate Q_{th} . We have set some limits to keep the analysis easily tractable:

- All the R_f are identical.
- We distinguish two types of clogged pores:
 1. The pores of the first row, for which the particle accumulation or cake layer plays an important role in the decrease of the flow. Their R_s is the same as in the proposal n°2.
 2. The other pores elsewhere inside the medium. We observed in the previous chapters that the accumulation behind the clogs that are located deeper in the medium was low. Thus, we consider that these clogs have a fixed value of R_s .

This model fits relatively well our experimental data, which again proves that clogging are strongly dependent on all local variations of hydrodynamic resistance.

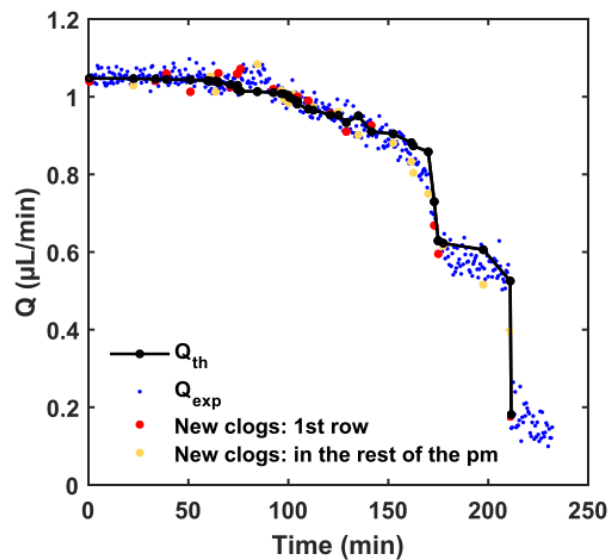


Figure 8.14: Comparison between Q_{th} from proposal n°3 and the measured Q_{exp}

8.3.4 Proposal n°4: perspectives

Hypothesis

1. Clogs in other pores than in the 1st row impact the drop.
2. The accumulation in the reservoir is better taken into account.
3. The resistances of the clogged pores may vary.

In this last proposal which is not yet finished, the characterization of the accumulation behind the clogs will be improved. The objective of this refinement is to better define at the pore scale some differences between the clogs, as the exact clog position or the accumulation shape. In addition, we want to consider the whole cake layer and not just the surface above the throat (figure 8.15a). Since after a while there is a cake layer on the overall width of the medium (figure 8.15b).

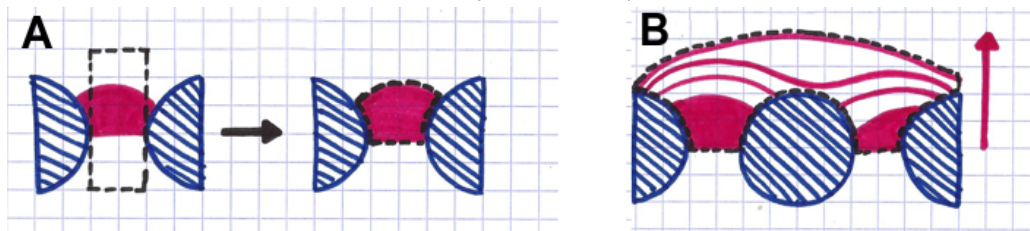


Figure 8.15: (a) A better estimation of the shape of the deposit. (b) A better estimation of the cake layer when accumulations of neighbouring pores merge.

At the pore scale

The position of the clog base in the pore can also change the hydrodynamic resistance of the pore, depending on the length and the different sections of the pore. Figure 8.16a shows different clogs configurations corresponding to different locations of the clog front. The hydrodynamic resistances for these different positions are presented in figure 8.16b with a factor of eight between the extrema positions of clogs.

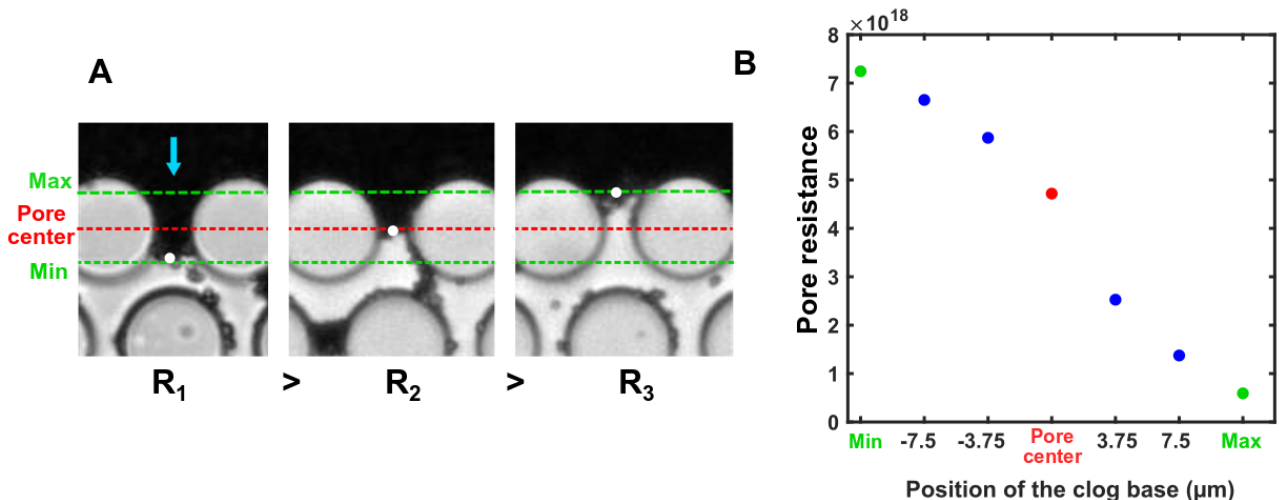


Figure 8.16: (a) Examples of clog front positions (white dots) with the center pore delimited by the red dashed line and the extremal positions by green ones. (b) The estimated hydrodynamic resistance with the equation 1.11b for different clog front positions on a pore.

In this version, we will introduce different permeabilities when calculating resistances, depending on whether the particle accumulation is in the pore or starts growing out of the pore. As seen in chapter 5, compaction in a 1D constrained area like a pore could decrease the permeability of the media. For an accumulation

with a larger front would be less compacted by the fluid, and this would be even more true as the cake layer grows.

At the medium scale

One of the last modifications that has to be made, and the one we expect to have the most impact on R_{eq} , is the cake layer. So far, the cake layer is seen as an accumulation of particles in rectangular segments that are the extension of the pores. We want to add here a new resistance that would take into account the width of the cake layer as well as its heterogeneous growth according to the zones where several neighbouring pores are clogged (figure 8.17).

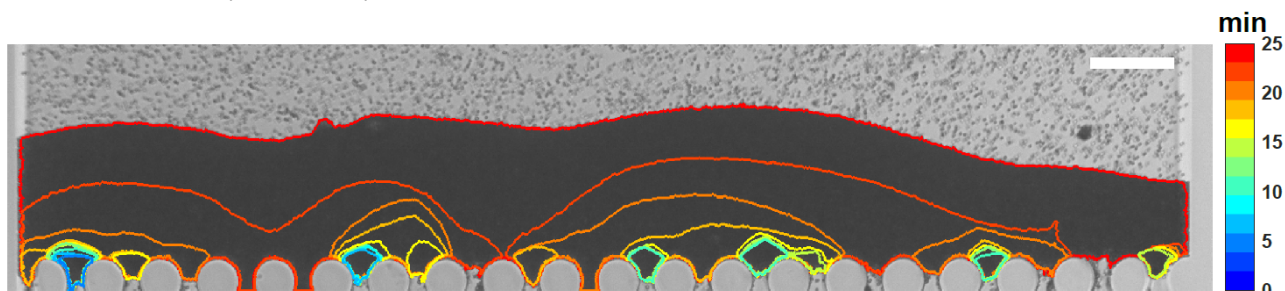


Figure 8.17: Evolution of the cake layer, from the initial accumulation behind clogs up to the merging to form the cake layer. Scale bar: 70 μ m.

8.4 Conclusion

In this chapter, we investigated the link between the flow decline in the medium and the pore clogging process. First, we measured the velocity of particles at the entrance of ordered porous media while imaging the pores to obtain the clogging time and the position of clogged pores. We obtained several velocity drops varying according to the permeability of the suspensions or the number of clogs. To do this, we first modified the size of the objects from 1.5 to 5 μ m, thus decreasing the confinement and increasing the permeability of the accumulations in the pores. In a second step, we modified the ionic strength of the suspension to increase the number of clogs in the pore, with suspensions without salt and $I=50$ and 300mM. We clearly see that the velocity drops are less important when the permeability increases. The increase of the number of clogs favors a more progressive flow drop. With these experiments, we proposed a simple model to describe the flow drops, by estimating the equivalent resistance of the medium only with the images. We have proposed several versions of this model, with different ways to estimate the hydrodynamic resistances of the pores. This model includes the main parameters that impact the flow rate drop, such as the formation of the clog front in the first row of the porous medium, the formation of a large cake layer behind the clog front, and the contribution of the clogged pores everywhere in the medium. We would like to better understand the link between the formation of the clog front and the growth of the cake layer, two phenomena that are self-sustaining. This is still a work in progress and it remains to be verified that the model works well considering different particle sizes or ionic strengths. Later, it will also be interesting to check if the flow rate drops are identical for the different clogging conditions, depending on the flow rate or the geometrical features of the pore medium

Chapter 9

Clogging with fragmented colloidal plastics

Here, we present the clogging of a porous medium by a suspension of fragmented, polydispersed and rough nanoplastic. We study the impact of the polydispersity of such objects on the clogging process by comparing suspensions with different controlled size distributions. To be more environmentally relevant, we study the clogging due to a mixture of nanoplastic and organic matter. This is a perspective chapter and hence all the analysis are still under way.

Contents

9.1	Context of the study	222
9.2	The fragmented nanoplastics	223
9.2.1	Preparation of the fragmented nanoplastics	223
9.2.2	Characterization of the nanoplastic suspension	224
9.3	Importance of the polydispersity of the suspension	226
9.4	Deposition and clogging by NPT in a porous media	229
9.4.1	Quantification of the impact of polydispersity	231
9.4.2	Delay clogging with natural organic matter	234
9.5	Conclusion	235

9.1 Context of the study

So far, we have studied the deposition and clogging of porous media by monodisperse microparticles. These particles are considered as models, even if we have seen that they contain some very rare aggregates, and are often used in studies to understand the deposition of micro and nanoplastics in a soil. However, they are far from reflecting the complexity of microplastic transport. In the environment, plastics of micro and nanometric sizes coexist. In addition, there is a degradation of plastics which, by fragmenting for instance, create a fairly wide size distribution. Plastics are polydispersed not only in size but also in shape. Recently, a study by Pradel et al. (2020) showed that the deposition of such plastics in a sand column was more important than for spherical particles.

In addition to this polydispersity, there is often in the environment natural organic matter, in the soil like humic fulvic or acid, or in aqueous medium like extracellular polymeric substances (EPS) that interacts with the aggregates. Pelley et al. (2008) showed that the deposition of humic acid decreases the capture of 50 and 1500nm spheres by electrostatic or steric effects. On the contrary, another study by He et al. (2020) shows that EPS favors the deposition of particles, by reducing the cross-sectional area of pores.

There are very few studies of polydispersed objects of complex shapes such as fragmented plastics and their main objective is to determine the deposition thanks to the concentration of particles transported in sand columns. However, the non-transparency and the 3D complexity of a sand column do not allow to image nor to really understand the impact of the deposit. The objective of this study is to couple the observation of the particle deposition in model porous media with several methods of particle characterization such as their concentration or their size distribution at the inlet and outlet of the medium. We try to answer the following questions:

- How the polydispersity impacts the deposition of objects in a porous medium, since we worked with plastic suspensions with different size distributions ranging from the nanometer up to the micrometer?
- How the addition of organic matter impacts the deposition of particles? We mixed, outside of the porous medium, several types of organic matter with a nanoplastic suspension, whose clogging dynamics have been studied afterward.

This study was done is a collaboration with Alice Pradel (OSUR, Rennes I) and Julien Gigault (Takuvik, Laval), with the help of Sunniva Pinnabel (IPR, Rennes I).

9.2 The fragmented nanoplastics

The preparation of the nanoplastic samples as well as their characterization presented in this section was performed by Alice Pradel, with a method developed by Julien Gigault's team.

9.2.1 Preparation of the fragmented nanoplastics

Nanoplastic suspensions are made from polystyrene granules transformed into powder and resuspended in pure water or with natural organic matter. This method made the particles additive-free, irregularly shaped and polydisperse in size, more environmentally relevant than the commercial spherical polystyrene latex particles.

- **The nanoplastic powder**

The nanoplastic powder is obtained by the fragmentation of polystyrene granules. Fragments superior to 1mm are pre-degraded with a blade grinder and the coarse powder undergoes several grinding steps using a planetary ball mill. The complete grinding method is described in El Hadri et al. (2020). At the end of the process the size of the powder is centered on 400nm.

- **Suspension of nanoplastics (NPT) and size cut-offs**

All solutions and colloidal dispersions were prepared with deionized water. To study the effect of size polydispersity, the NPT dispersions were filtered at three different size cut-offs, 40 μ m, 3 μ m and 0.8 μ m called respectively NPT-40 μ m, NPT-3 μ m and NPT-0.8 μ m. Before filtering the nanoplastic dispersions, membrane filters were rinsed and saturated with DI water. The NPT-40 μ m and NPT-3 μ m concentrations were 8mg.L⁻¹, and NPT-0.8 μ m concentrations were only 4.5mg.L⁻¹ due to the important loss of particles when filtering. These concentrations are higher than those expected in the environment, but were necessary to be detectable by our instruments.

- **Natural organic matter (NOM)**

Two types of natural organic matter have been tested in this study.

1. Polysaccharide sodium alginate (SA)

Sodium alginate is a negatively charged polymer. The SA stock solution was prepared by adding solid SA (Acros Organics) in DI water and agitating at 400 rpm overnight (12 to 18 hours). Fresh SA solutions were prepared weekly, since this organic matter is subject to bacterial growth. The SA solution has a pH varying between pH 7.5 to 8 and a concentration between 504 and 1257mg.L⁻¹.

2. Humic acids (HA)

HA are negatively charged macropolymer. The HA stock solution was prepared by dissolving Leonardite HA, using the method described elsewhere Pradel et al. (2021). The pH of HA was fixed at 6.5 and the concentration is 875mg.L⁻¹.

These NOM are dissolved in the solution and filtered at 0.2 μ m using syringe filters and were then diluted to 50mg.L⁻¹ or 30mg.L⁻¹ for SA and HA, respectively. While NPT are dispersed in DI, SA and HA contain 5.75mg.L⁻¹ Na and 0.09mg.L⁻¹ NaCl, respectively. The NPT are mixed with the dissolved NOM before injection into the medium, presaturated by a NOM suspension.

9.2.2 Characterization of the nanoplastic suspension

Description of the nanoplastics morphology

All the methods presented here are not intended to provide an accurate particle size distributions because the number of objects studied is too small and the statistic too low to be relevant. The data we gathered show the complex morphology of our particles since they were imaged at an important magnification. For systematic measurements in the rest of the study, a size is measured for each object without information about its complexity. Several imaging techniques have been tested to characterize the nanoplastics.

▪ Scanning electron microscopy (SEM)

A solution of 11mg.L^{-1} NPT was diluted by to 5.5mg.L^{-1} with ethanol, and deposited on a metal surface and dried for a minimum of two hours. The use of ethanol allowed the particles to remain better dispersed on the surface during drying. In figure 9.1a, in addition to being very different in size (from $1.5\mu\text{m}$ to 200nm), the shapes of particles are very diverse, some are spherical particles (yellow arrow), elongated (red arrow) or deformed (blue arrow). They can also be very rough (green arrow figure 9.1b) or relatively smooth (white arrow).

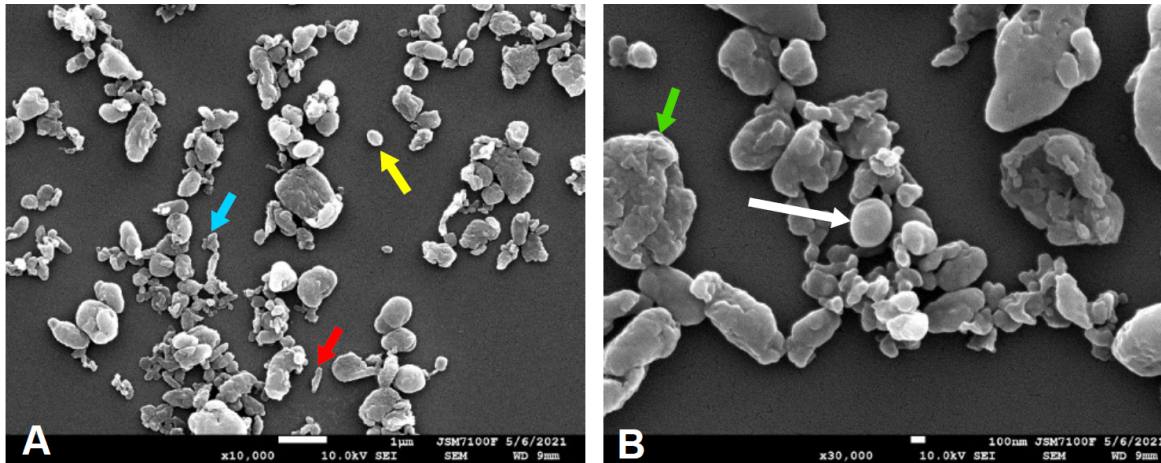


Figure 9.1: SEM images of NPT- $40\mu\text{m}$ at $1\mu\text{m}$ (a) and 100nm (b) magnification.

▪ Transmission electron microscopy (TEM)

TEM images were captured with a Jeol JEM 2100 HR (200kV) with an LaB_6 filament and a Gatan Orius SC 200 D camera. The method and analysis is thoroughly described in Pradel et al. (2021). Similar observations can be made from by TEM images (figure 9.3). Indeed, some spheroidal particles have homogeneous densities (blue arrow), while other particles have zones with different densities, suggesting zones where particles are very rough or whose layers have been wiped off (red arrow).

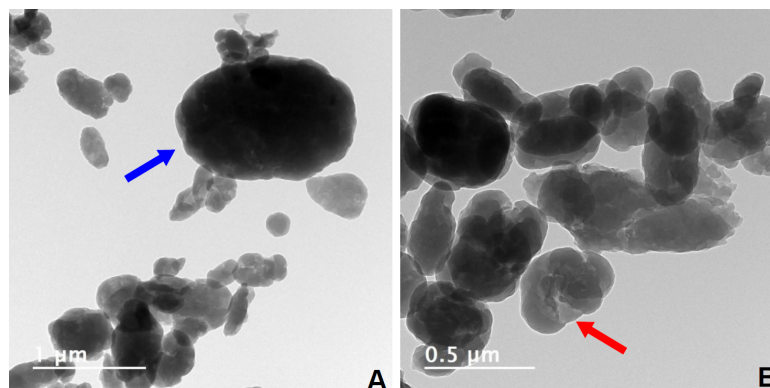


Figure 9.2: TEM images of NPT- $40\mu\text{m}$ at $1\mu\text{m}$ (a) and 500nm (b) magnification.

- **Atomic force microscopy (AFM)**

The surface morphology of NPT was assessed by AFM with a Bruker Multimode 8-HR. 50 μL of solution was deposited on a cleaved mica surface and allowed to air dry for a minimum of 2 hours. AFM illustrates the topography of particles, thereby allowing a 3D representation of particles. Figure 9.3 shows two examples of flaked and rough particles, with peak error force maps which are a derivative of the topography and highlight the derivative in particle morphology and height maps for which three height profiles are extracted. These different curves show that the surface roughness for the same particle can reach 10 to 50nm.

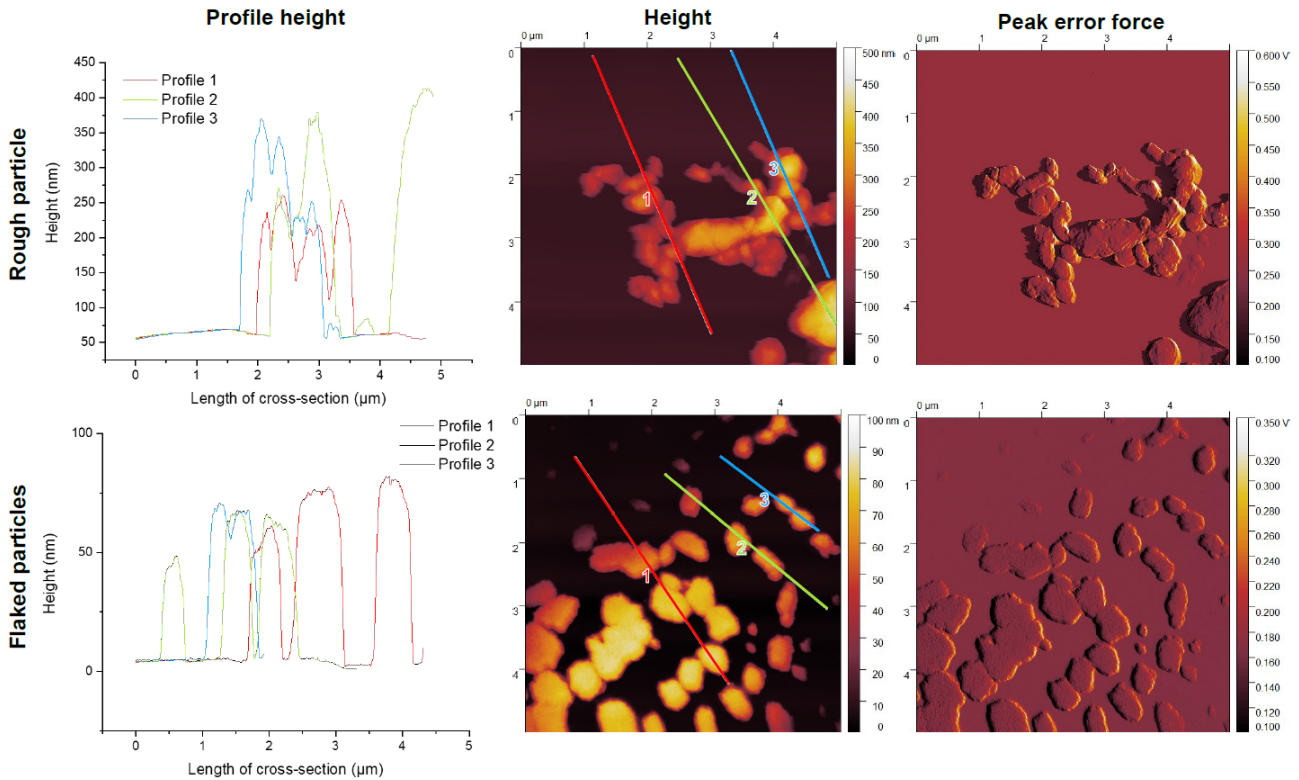


Figure 9.3: AFM images: for a rough and flaked particles are presented the peak error force map (right) and the height map (middle). For each height map is extract 3 height profile, presented on the graph (left).

This diversity of shapes can be explained by the brittle nature of polystyrene and the process of mechanical abrasion by planetary ball milling. The rotation of the milling process can produce spheroidal particles and shed layers off of the surface of particles, producing rough surface morphologies.

The size distribution of nanoplastics

The diameter of NPT particles were characterized by two complementary methods, the DLS and the Coulter counter.

- **Dynamics light scattering (DLS)**

The ensemble method of DLS (Vasco-Flex, Cordouan Technologies) measures and deconvolutes a scattering signal in order to obtain a size distribution of colloidal particles. A DLS apparatus determines the average hydrodynamic diameter of particles and fit a normal distribution to the raw data using the cumulant algorithm.

▪ Coulter Counter

The Coulter Counter is a Multisizer 4 (Beckmann) and measures the dimension of particles suspended in a saline suspension passing through an aperture of $30\mu\text{m}$ diameter which measures sizes between 0.6 and $18\mu\text{m}$. As a particle passes through this aperture, it displaces a volume of saline solution and modifies the electrical resistivity. From this variation we deduce an equivalent sphere volume of displaced solution and thus the apparent diameter of the passing object. The instrument is calibrated weekly with $3\mu\text{m}$ NIST particle. All measurements were performed in an electrolytic solution composed of $9.914\text{g}\cdot\text{L}^{-1}$ NaCl by adding $4.74310^{-3}\text{g}\cdot\text{L}^{-1}$ of Triton surfactant to inhibit NPT aggregation. The Coulter measurements were mainly performed by Sunniva Pinnabel (IPR).

The size distribution of NPT obtained with the two methods are shown in figures 9.4. The DLS measurement suggests that a few micrometric particles are present in the nanoplastic dispersion but without being able to quantify their relative proportion. This is due on the one hand to the larger diffraction for larger objects and on the other hand to the small volume of suspension analysed. However, DLS allows measuring that the size distribution is centered around 400nm , below the capacity of the Coulter counter which is 650nm (red lines in figure 9.4). The Coulter counter is the most suitable instrument to measure distribution tails above 650nm since it counts every single particle in a given volume (figure 9.4b). We may note that the tail of the NPT- $40\mu\text{m}$ distribution contains a significant number of micrometric particles (15% of the population), whereas for the NPT- $3\mu\text{m}$ these objects are less numerous (4% of the population), as expected because of the cut-off of the filtration step.

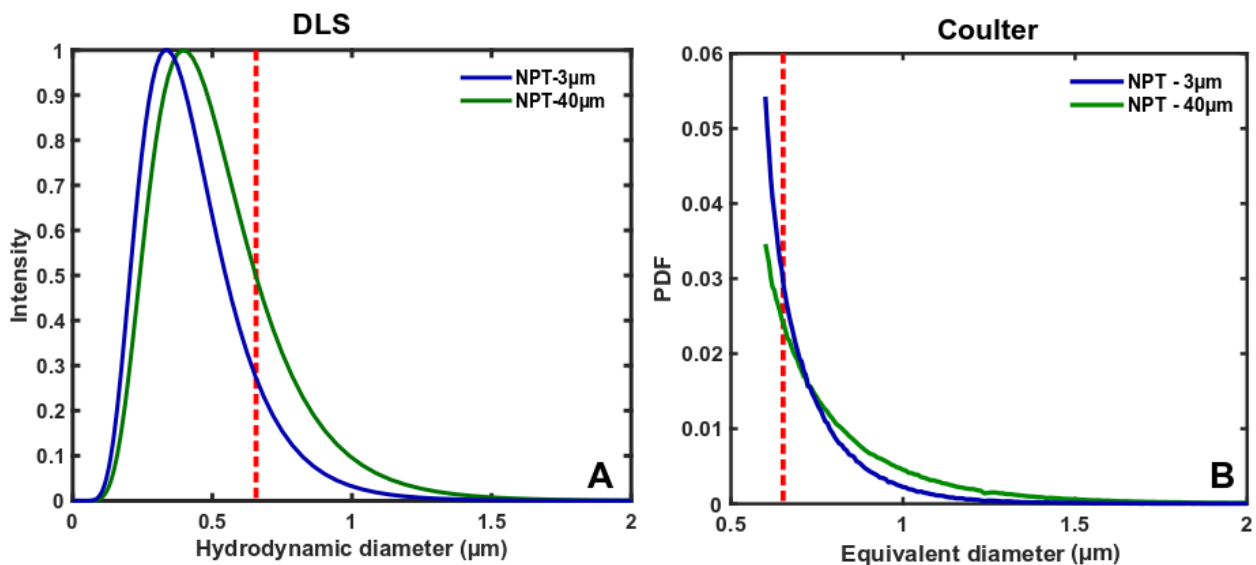


Figure 9.4: Size distribution of NPT- 40 and $3\mu\text{m}$ with DLS (a) and Coulter counter (b).

9.3 Importance of the polydispersity of the suspension

As we have seen throughout this thesis, the size of particles, the confinement and more importantly their shape play an important role during the pore clogging. It is therefore expected that the behavior for a suspension of nanoplastics filtered at $40\mu\text{m}$ or at $3\mu\text{m}$ is different. A concentration measurement during the transport in sand columns of NPT has been already made by Pradel et al. (2020) that shows that more particles of NPT- $40\mu\text{m}$ were preferentially retained in the columns compared to those of NPT- $3\mu\text{m}$. We monitor the clogging of a wide pore, with a $30\times 30\mu\text{m}$ cross section by these two suspensions and we focus on the NPT- $40\mu\text{m}$ in figure 9.5. We can distinguish the arrival of micro-objects that seem spherical (red arrows), or even larger objects (yellow arrow). The growth of the deposit is limited because the flow

is able to stretch and unfold it and as a result the deposit spread along the wall. This behavior indicates that the deposit is mechanically unstable and fragile. Some parts of the deposit can also be eroded (white rectangles). Generally, deposits start growing progressively on both sides of the channel (green arrow) sometimes interrupted by erosion, restructuration a but the pore is eventually clogged (red rectangles).

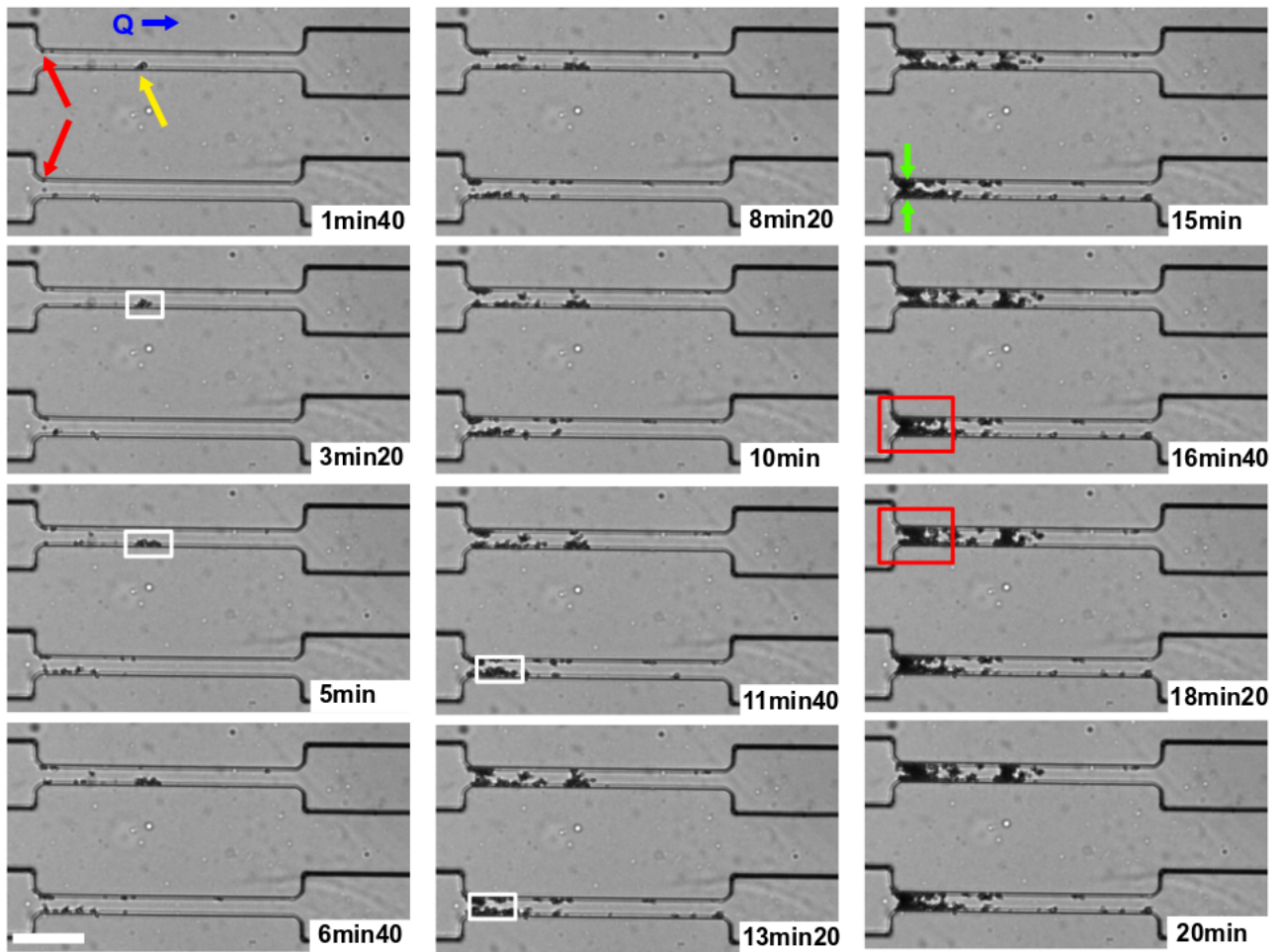


Figure 9.5: Clogging dynamics of a NPT-40 μ m suspension (16 μ L/min). Red rectangles indicate when pores are clogged. Scale bar: 80 μ m.

We perform experiments, still with single pore, for NPT with 3 and 40 μ m cut-offs and at various flow rate, from 8 to 50 μ L/min. The final images of the clogging pores are shown in figure 9.6. There is a clear impact of the flow rate since the more it increases, the larger the length over which the deposit spreads. The deposition is always slightly more important in the pore for NPT-40 μ m than for NPT-3 μ m. When large objects of the NPT-40 μ m suspension are eroded, they redeposit further into the pore. The greater the flow, the further they are transported before their redeposition. There is also erosion of the NPT-3 μ m suspension, but since it is composed of smaller objects, these detached parts are not large enough to redeposit systematically in the pore.

The micrometric objects allow reducing more quickly the section of the pore. Their disappearance leads to an increase of the average clogging time that reaches a plateau when the erosion becomes important at 8 μ L/min for NPT-40 μ m and 30 μ L/min for NPT-3 μ m (figure 9.7). The flow can allow more objects to go through the pores and therefore to be deposited, leading to a faster clogging, but it also able to erode the deposit and hence delay the complete obstruction.

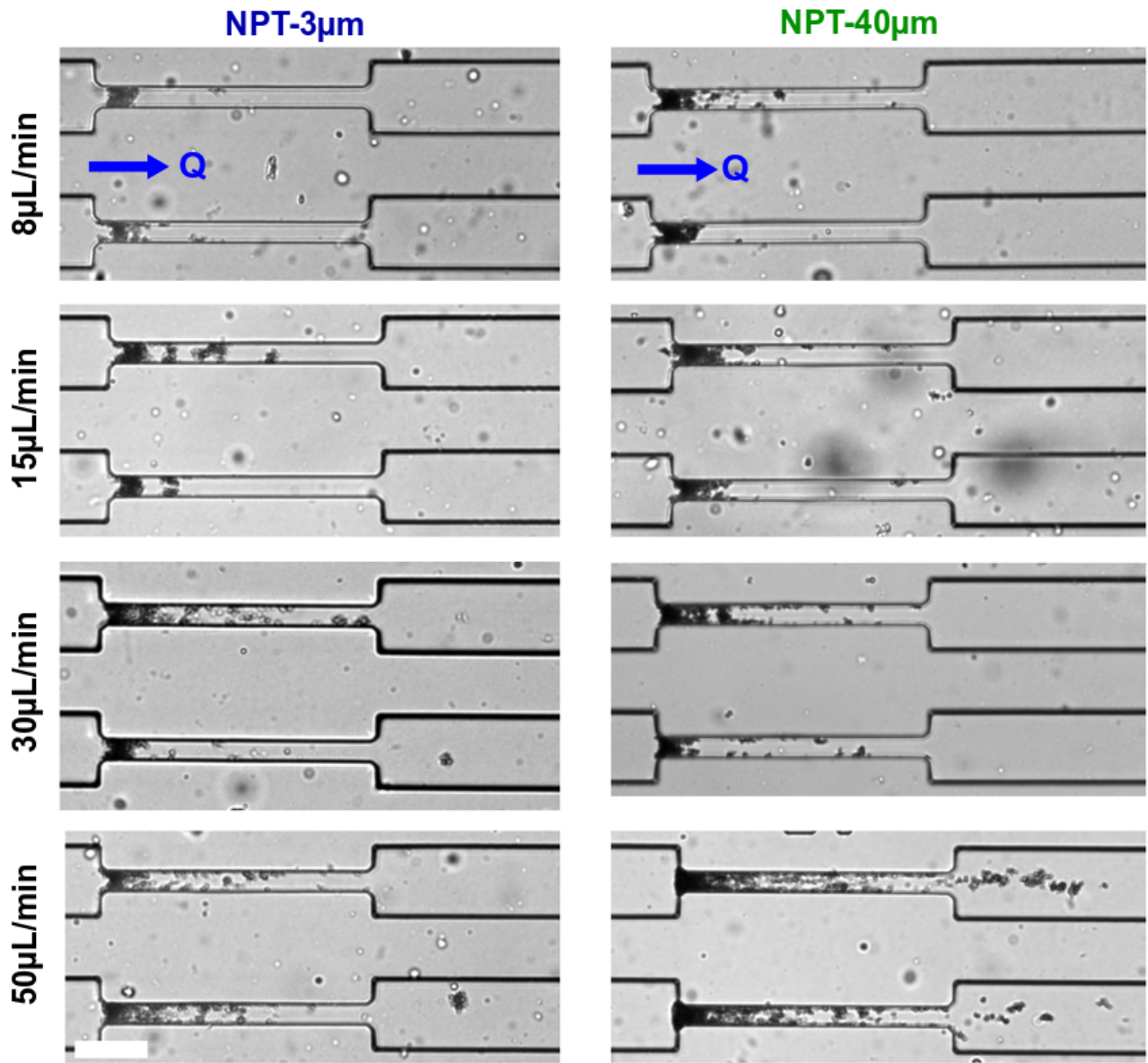


Figure 9.6: Final images of clogging experiments with NPT-3 μm and NPT-40 μm at different flow rates. Scale bar: 80 μm .

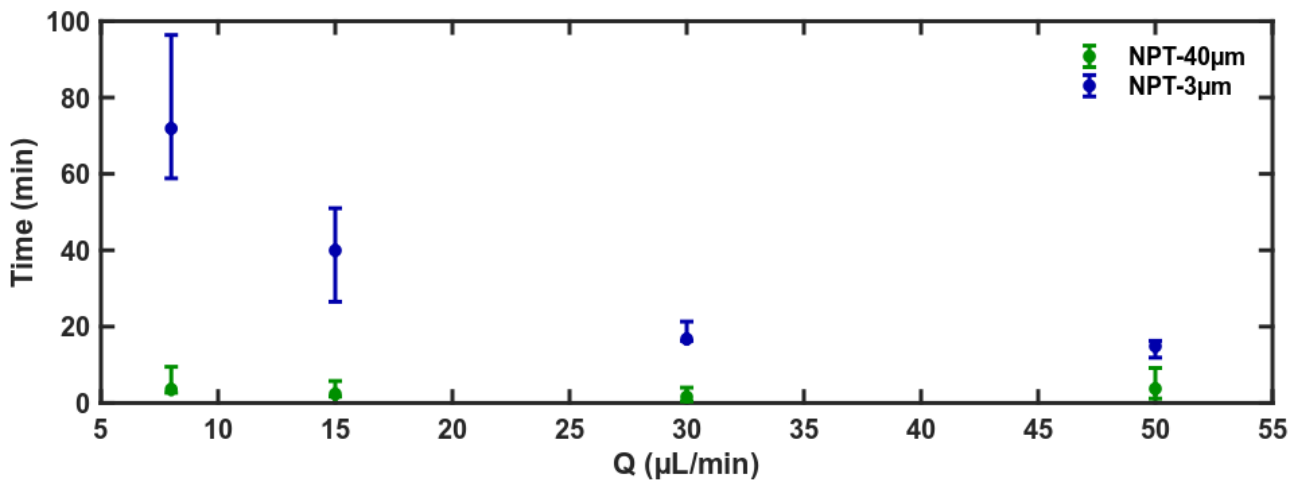


Figure 9.7: Average clogging times of NPT-3 μm and NPT-40 μm .

9.4 Deposition and clogging by NPT in a porous media

Since the submicrometric objects if they deposit are not visible with a microscope, there is a real need to use another method to determine the evolution of the particle distribution size during the transport in the porous media. We do so by comparing the size distribution before and after the passage of the suspension in the channel. In particular, with respect to what we have seen above we are interested on the role of the largest objects during the clogging. In addition, since we work with a suspension polydispersed in size, we expected to observe the self-filtration. As the deposit grows, the size of the captured objects may decrease and thus shift the size distribution at the outlet of the channel towards smaller values.

The main idea is to follow the size distribution of the objects with DLS and Coulter measurement before, during and after the clogging. However with the chip we use up to now, the total volume passing through it before its clogging is too small, typically a few tens of microliter, to see any difference between the size distribution before and after the chip. More important, the number of objects potentially captured is limited because of the small surface available. We used a new medium to delay the clogging, which allow us to have more particle deposition prior clogging, but also to retrieve a greater volume of transported suspension at the outlet, which is around 5mL in average. This new porous media model has dimensions of 3.6x20mm with collectors with radius $R_c = 20\mu\text{m}$. The collectors are placed along rows composed of approximately 50 pores. The space between the collectors is chosen randomly between three values, 20, 35 and 50 μm . This configuration creates narrow paths (red rectangle in figure 9.8) and wider ones (black rectangle in figure 9.8) which thus present strong velocity heterogeneities.

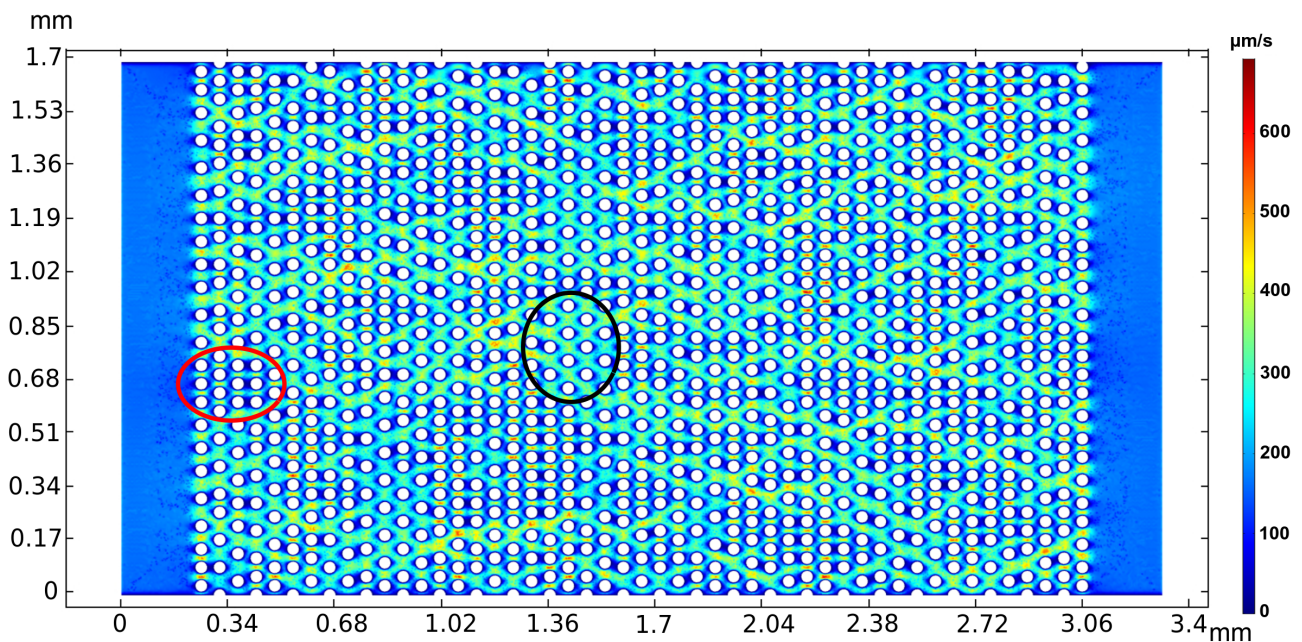


Figure 9.8: Spatial mapping of fluid velocity in a porous medium used as a filter (sample of 1.7mmx3.4mm), computed with Comsol.

Due to the absence of surfactants in the nanoplastic suspensions, particles may form aggregates over long period of time. Therefore, a new stock solution has to be prepared weekly to avoid excessive aggregation. Each week for a given batch we perform the following experiments i) NPT dispersed in pure water for the different filtration cut-offs: 40, 3 and $0.8\mu\text{m}$ and ii) NPT dispersed in a solution containing natural organic matter either humic acids (HA) or sodium alginate (SA). For each experimental condition, we performed two to three replica using microscopy imaging to visualize the state of deposition or clogging of the medium. We performed several weeks of experiments to obtain multiple replicas for each suspension, with new stock solutions.

In contrast to microparticles, it is not possible to determine by image analysis when the medium is clogged since the particles are mainly nanometric. However since we work at constant pressure, there is a flow decline during the experiment. We measured every 10min the outgoing mass of the medium to obtain the flow rate decline. When the outgoing volume is so small that the flow measurement cannot be obtained accurately enough, the experiment is considered as finished. During the experiment, we also perform punctual characterizations of the size distribution of the objects. We can thus compare the reference size distribution with the size distribution obtained during and after the clogging process. We choose several points, at the beginning of the experiment (figure 9.9 $35\mu\text{L}/\text{min}$), when the flow rate starts to decrease to observe the effect of the deposition and pore clogging ($25\mu\text{L}/\text{min}$) and finally, at the end of the experiment ($<10\mu\text{L}/\text{min}$), when the flow rate becomes very low and the clog front is formed, to observe the self-filtration by the clog front.

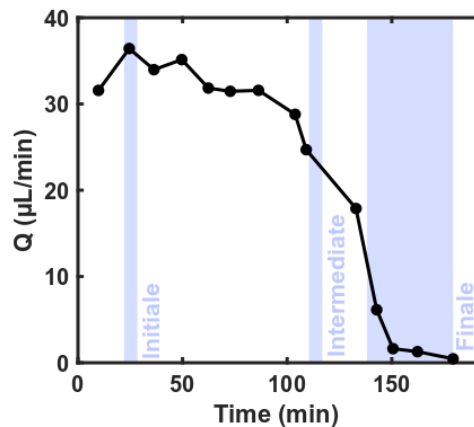


Figure 9.9: Example of the drop-in flow rate and the three volume extraction during the experiment: at $35\mu\text{L}/\text{min}$ (initial), $25\mu\text{L}/\text{min}$ (intermediate) and $<10\mu\text{L}/\text{min}$ (final).

9.4.1 Quantification of the impact of polydispersity

We first compare the behavior of NPT that has been filtered with cut-offs of 3 or 40 μm in a porous medium. For both suspensions, an important deposit is observed at the beginning of the medium then becomes more sparse or it may no longer be visible if it is composed only of a thin layers of nanoparticles (figure 9.10). We use another cut-off of 0.8 μm suspension, but the deposition of particles was not visible under the microscope after 9 hours of experiment. Moreover, as the flow rate does not evolve the potential deposit is very limited since the pore sizes are large and does not allow a physical interception of the particles by the wall with the hydrodynamic force. For NPT-40 μm , the clog front (red lines on figure 9.10) is always concentrated around 200 μm from the medium entrance, while it can go up to 1-3mm for NPT-3 μm (see examples of clog front in figure 9.11).

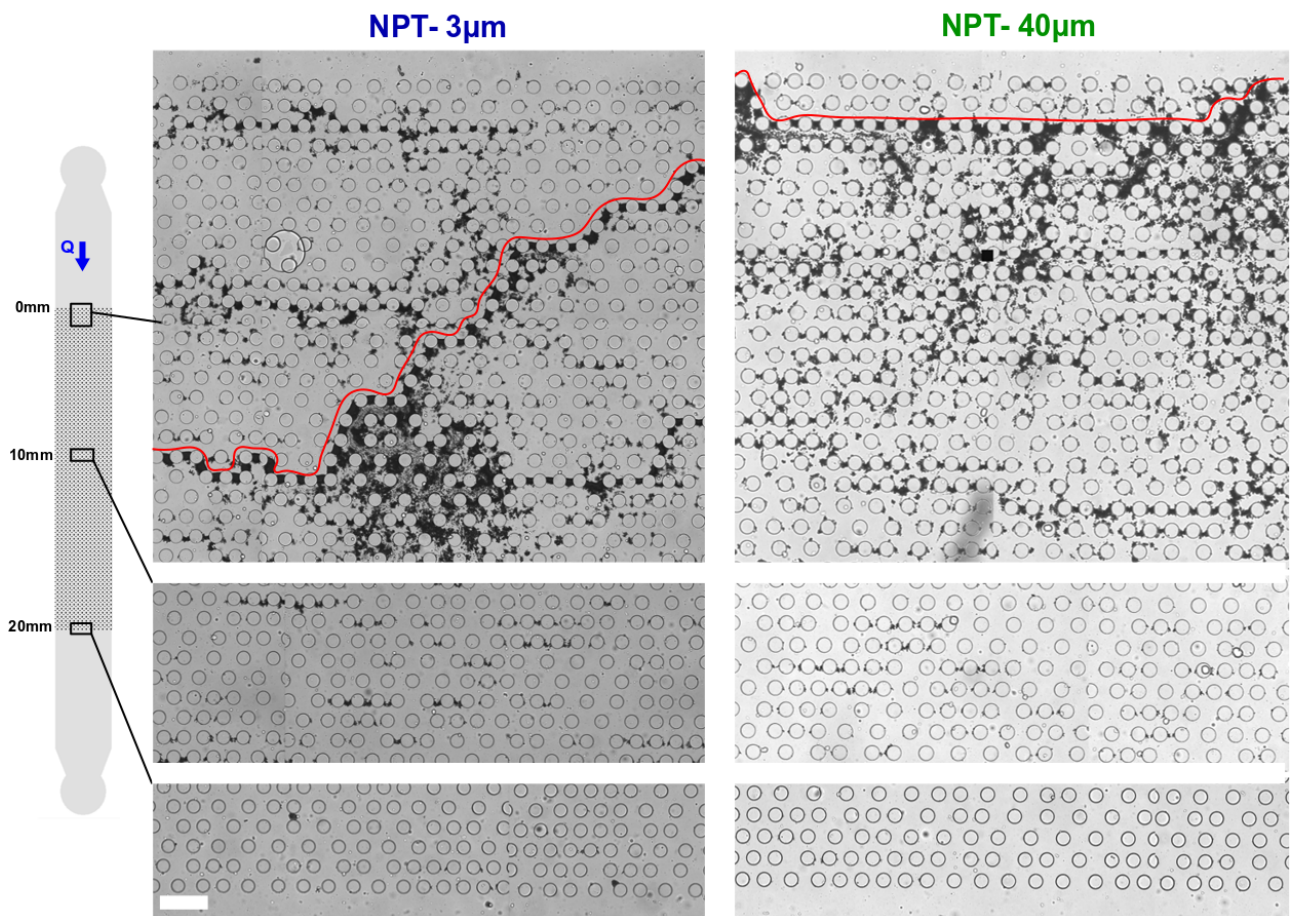


Figure 9.10: Images at the entrance, in the middle and at then end of the medium for NPT-3 μm and 40 μm . Scale bar: 80 μm .

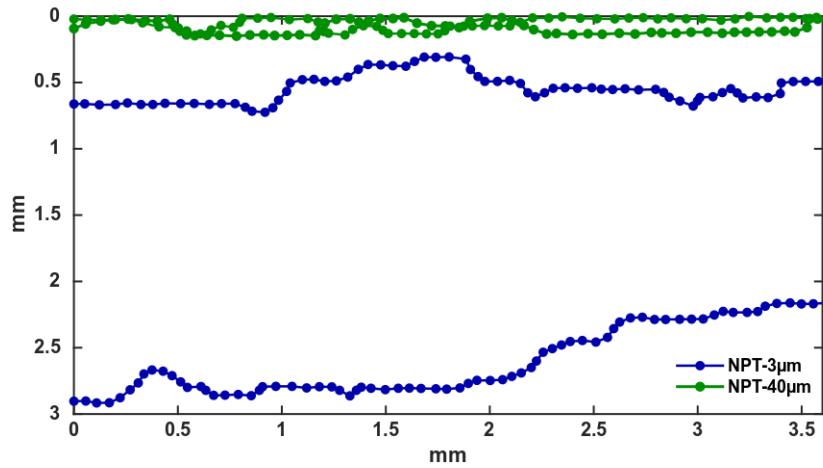


Figure 9.11: Two examples of clog front for both NPT-40µm and NPT-3µm.

The area of the deposit along the medium is quite different for the two suspensions. It is very concentrated at the inlet for NPT-40µm and smoothly decreases up to 2mm (figure 9.12), whereas for NPT-3, there is a significant deposition at the entrance but it is maximum around 1mm inside the medium, before suddenly fading away further downstream (figure 9.12). Therefore, by removing the large objects, i.e for NPT-3µm, the deposition is deeper inside the medium since objects have more time to be captured before the porous media is completely clogged. The medium tends to be clogged in 90min maximum for NPT-40µm while at least 150min is needed for NPT-3µm (figure 9.13). The large objects, by reducing more quickly the pore cross-section, could also increase the capture of smaller objects which at their turn reduces the clogging time.

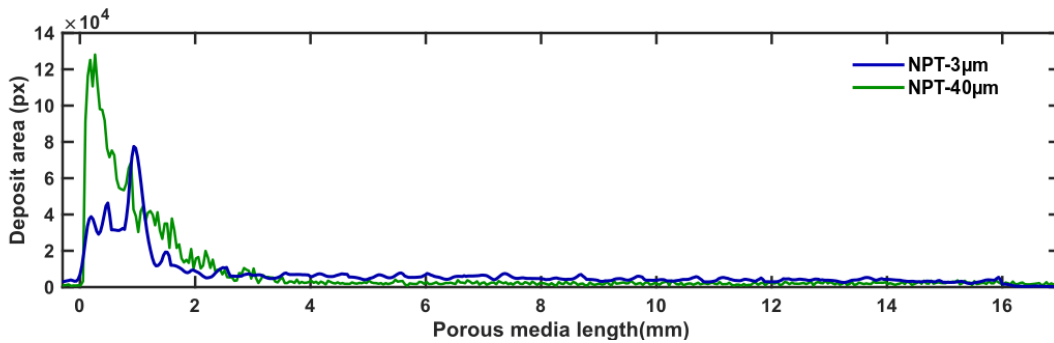


Figure 9.12: The area of the deposit in pixels (px) of both suspensions presented in figure 9.10.

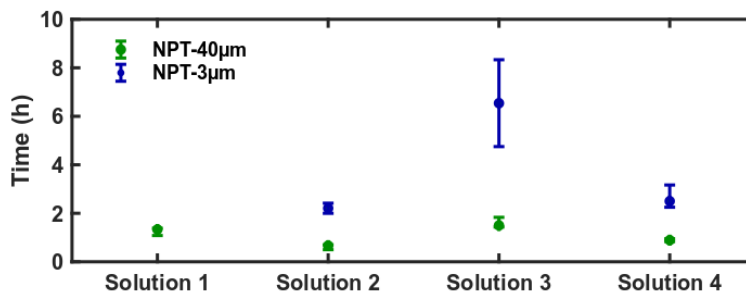


Figure 9.13: Average clogging time of NPT-3 and 40µm for different stock solutions.

The size distribution of the samples collected during the experiment were analysed by the Coulter counter and the DLS. The most important results are obtained with the Coulter counter since micrometric sizes are well taken into account with this technique. The measurements of the latter show a slight decrease of the hydrodynamic diameter for NPT-40µm only (figure 9.14).

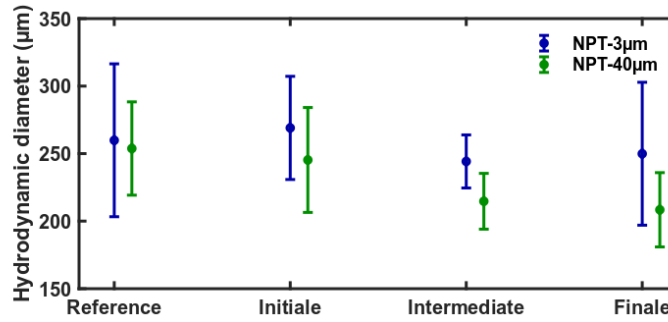


Figure 9.14: Hydrodynamic diameters obtained with DLS for NPT-3 and 40µm.

NPT-40µm has a significant change of its size distribution, with a progressive loss of micrometric particles, which represent 15% of the population at the beginning of the experiment and fall down to 3.8% at the end (figure 9.15a). When large objects are present in the suspension, the clogging process is fast, as soon as a large object is deposited, it reduces the pore cross-section in a quite important manner, helping to capture other objects and thus shifts the size distribution towards smaller size. For NPT-3µm, the distribution is unchanged. The deposition and clogging process has not impact on the size distribution (figure 9.15b). For both suspensions there are still micrometric objects (4%) detected in the final size distribution despite medium are clogged and these object still have an important impact for the clogging. The flow rate is extremely low and volume of the chip is very large and thus can not be renew. There are still micrometric object further in medium in the collected volume for the measure the final size distribution. These objects would disappear if we could extract the volume inside the chip with a reasonable experiment time.

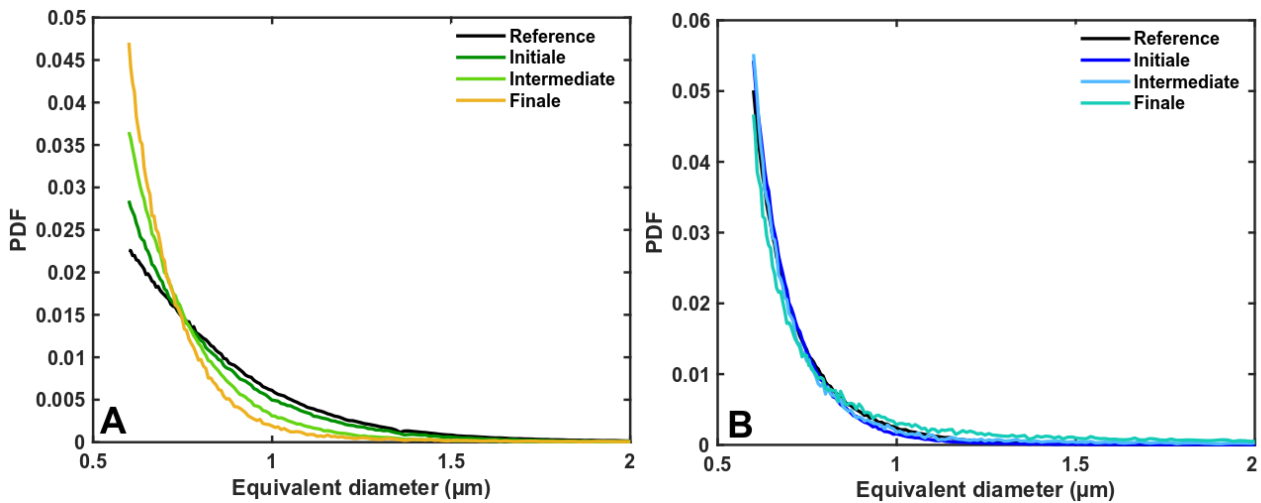


Figure 9.15: PDF of the equivalent diameters obtained with Coulter counter for the NPT-40µm (a) and NPT-3µm (b)

Moment	NPT-3µm	NPT-40µm
Reference	804 854	2 595 028
Initiale	486 995	266 369
Intermediaire	63 849	207 216
Final	56 878	90 884

Table 9.1: Number of counted particles by the Coulter counter.

9.4.2 Delay clogging with natural organic matter

Finally, we focus on the transport of NPT when they are mixed with two types of natural organic matter (NOM). The objective is to determine whether or not there is either adsorption of the NOM on the NPT surface or a partial coating and if this has an impact on the clogging process. Note that we do not search to be environmentally relevant in these experimental situations. We would like to simply know if whether the deposition or the clogging patterns are modified in the presence of NOM in the medium.

Not all the analyses in this part are finished yet. We study the behavior of NPT-40 μm suspended in pure water, with polysaccharide sodium alginate (SA) and with humic acids (HA). The addition of NOM has no impact on the size distribution of NPT-40 μm before the initial injection in the medium (figure 9.16).

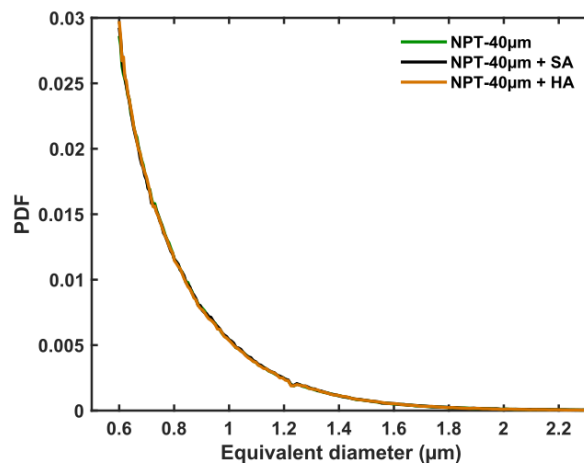


Figure 9.16: PDF of the equivalent diameters obtained with Coulter counter for NPT-40 μm with pure water and NOM.

The addition of NOM in the NPT-40 μm does not change the clog front which is very close to the inlet (figure 9.17). The deposition of objects in the pores seems to be more important with NOM than for pure water. Further analysis of the deposited area will be done to confirm or not this observation. Impurities may also be present in NOM, which modify the amount of deposit in a non-controlled manner. However, we noticed that the clogging time was much larger with NOM than for NPT-40 in pure water, starting from 90min in pure water, the time clogging rises up to 4h with SA and 8h with HA (figure 9.18).

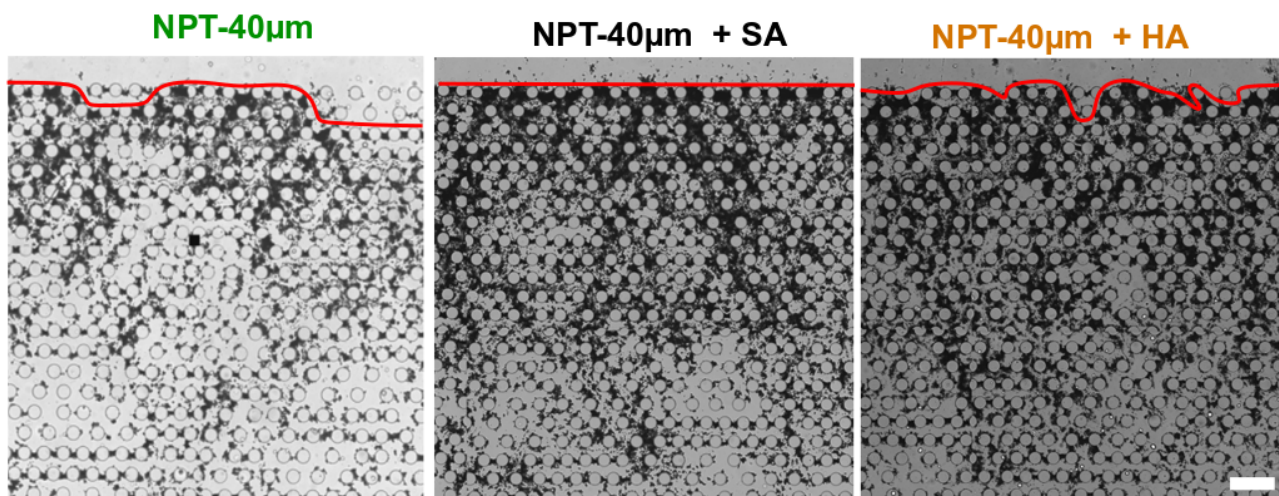


Figure 9.17: Images at the medium entrance for NPT-40 μm with pure water and NOM. Scale bar: 80 μm .

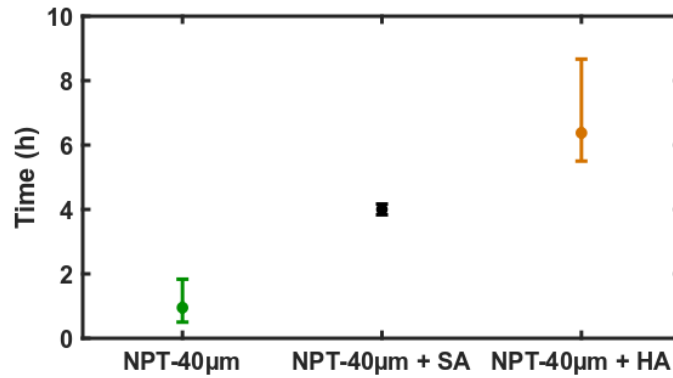


Figure 9.18: Average clogging time of NPT-40µm with pure water and NOM.

Surprisingly, the size distributions of the NPT-40µm with NOM do not change during clogging for both SA and HA (figure 9.19) whereas we have seen that the size distributions with NOM contain as many large objects as the NPT-40µm and thus we would have expected that a significant part of these objects will be captured by the medium. At this stage we can only make assumptions about what is responsible of such a behavior. The addition of NOM by coating or adsorbing on the particle could prevent the objects deposition by electrostatic or steric effect. Since the size distribution is not impacted by the deposition or even clogging, with no loss of the larger aggregates, we expect that clog are mainly composed of nanometric objects. We can wonder if the NOM interacts equally with the objects size or cover more efficiently the larger ones.

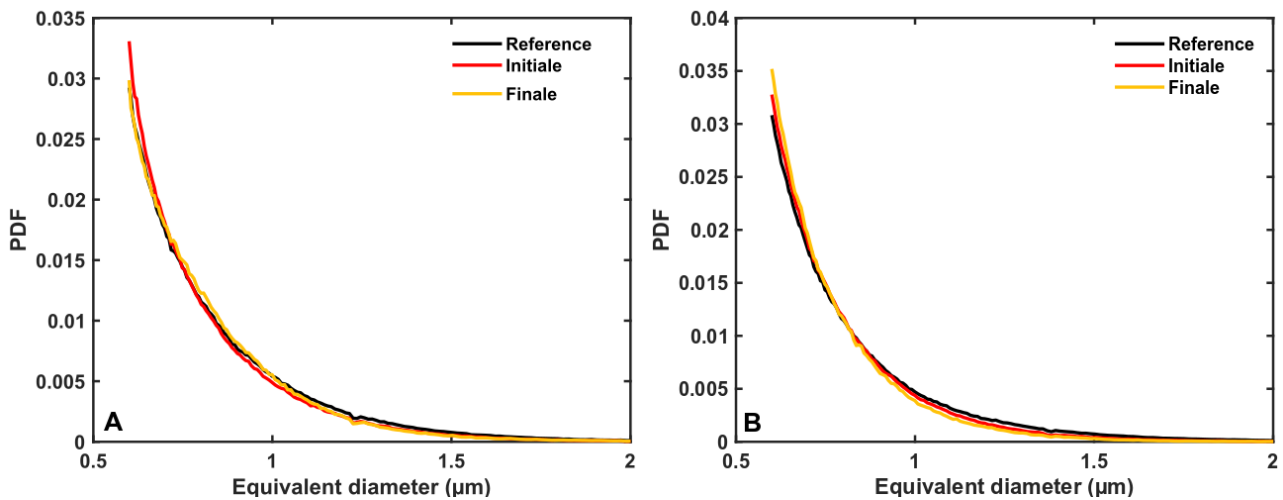


Figure 9.19: PDF of the equivalent diameters obtained with Coulter counter for the NPT-40µm + SA (a) and NPT-40µm + HA (b).

9.5 Conclusion

The first objective of this study is to understand the retention of nano-microplastic suspensions which are also polydisperse in shape, in a porous media to get closer to environmental conditions, we mixed our plastic suspension with different natural organic matter (NOM).

The nano-microplastics used are plastic fragments exhibit strong difference in shape and size. If their size distribution is centered around 400nm, to detect some micrometric objects. We work with two plastics suspensions distributions whose have been filtered with different filtering cut-off, 40 and 3µm. These cut-offs mainly impact the tail for the larger objects of the size distribution. Initially, we detect 15% of micrometric objects for a NPT-40µm suspension and only 4% for a NPT-3µm which is a filtered suspension.

We focused on the consequences of these two different distribution tails for the larger objects on the clogging of the medium since these objects have the more important impact on the clogging. We sought to understand whether the decrease in their numbers could have an impact on clogging over time but also on the position of clogging inside the porous medium. First we injected the nano-microplastics with these two size distribution in a single pore and we observed a net difference of the clogging time for the NPT-3 μm compared to the NPT-40 μm , which can be 2 to 7 times higher according to the flow. Since the outgoing volume in the single pore was not enough important to measure size distribution, we used an heterogeneous medium with multiples interconnected pores with different pore size to delay clogging and in the same time observed the particle deposition. This clog front is located at the very entrance of the media for NPT-40 μm and is further inside the medium for NPT-3 μm . In addition, the size distribution of the objects during the clogging experiment strongly differ. We noted an important loss of micrometric particles for NPT-40 μm while the size distributions of NPT-3 μm is not impacted by the clogging. We suspect that larger objects, by reducing the pore cross-section, help to the capture of small objects. This process is called self-filtration and induces a progressive shift of the size distributions towards smaller objects. We expect this shift to be very important for NPT-40 μm since the micrometric object are more numerous in the size distribution and larger than for the NPT-3 μm . This shift should exist for the NPT-3 μm suspension, but it leads to a more gradual change of the size distribution since less micrometric particles are originally present. By postponing the moment when the medium is clogged since there are less micrometric objects in the NPT-3 μm , we favour the transport of plastic particles in the medium and thus promote the location of the clog front further downstream inside the medium. This is a work into progress, and there are still points to be clarified to definitively conclude. For example, we noticed the absence of objects deposition over 90% of the length of the media. Do the objects reach an equilibrium position and are less likely to be captured, or does the deposition at the beginning of the porous media allow more objects to be captured? Anyway, from the results presented here, we can conclude that the size polydispersity has a great role on the clogging process in porous media.

In a second part, we studied the impact on the natural organic matter on the NPT deposition. We mixed NPT-40 μm with humic acid (HA) and sodium alginate (SA) before injection into the porous media to observe if there is any modification of the clogging features. Our results show a significant increase of the clogging time of the media going from 90min for the raw NPT-40 μm alone to 4h with SA and even to 8h with HA. Unexpectedly we notice that, despite that the size distribution of the NPT-40 μm in pure water and mixed with NOM are identical, with 15% of micrometric objects in their population, the size distribution for NPT with NOM is not modified while there is significant particle deposition in the medium and its clogging. We make the assumption that NOM coat or are adsorbed at the nanoplastics surface and prevent them to be captured thanks to steric or electrostatic repulsion. Thus, micrometric objects can be transported over longer distances without clogging the medium. Since the size distribution does not change between the beginning and then end of the filtration experiment we suppose that very aggregates are responsible of the pore clogging. There is a real need for a better chemical characterization of these mixture, to understand how NOM interacts with NPT and if these interactions are the same for all the particle sizes. In addition, NPT are mixed to NOM before their injection in the medium and could impact differently the deposition in comparison of a mixing inside the medium. The injection in a medium already saturated by a suspension of NOM could prevent the capture of the objects at the collector wall, if they are already covered by NOM if the NOM is not perfectly dissolved in the solute.

We have see that the modification of the size distributions of the plastic suspensions or the addition of NOM lead to contrasted results concerning the clogging of a porous medium. We can expect that it will the same if nano-micro plastics are mixed with other particles or organisms we can found in the environment,

such as iron oxide, clays or bacteria.

Chapter 10

Conclusion and perspectives

The transport of a suspension through narrow constrictions or pores of a membrane leads invariably to its clogging. This phenomena also takes place in natural environments of even in our body (constructed wetlands or pavement, microirrigation, cholesterol or microemboli) as well as industrial environment (printer, water or wastewater filtration, food, beverage). The best known and most studied example is the clogging of industrial filters or membranes. From fouling to the complete obstruction, the membrane undergoes a significant flow decline reducing its efficiency and thus increasing its filtration time. To remedy this inevitable problem, manufacturers replace the membrane or clean it, by backwashing with a flow reversal or by adding chemical agents, which reduces the filter lifespan and increases their operating costs. Because of the opacity of the membrane, it is not possible to relate the flow decline to the fouling or clogging of the membrane. Linking these two phenomena would allow to better anticipate the membrane clogging and to optimize its cleaning to limit the costs. In recent years, studies have used microfluidics to investigate transparent model 2D membrane clogging. So far, three clogging mechanisms have been identified, sieving, bridging and progressive clogging. The last mechanism is studied in the thesis and it results from a complex process, depending on several physico-chemical parameters such as inter-particle and particle-wall interactions, hydrodynamic parameters that can promote or limit the deposition of particles, as well as the degree of confinement corresponding to the pore size to particle size ratio W/D . These parameters have been investigated by several studies. However, no study presents the complete dynamics of pore or porous media clogging, nor does it relate fouling to the associated flow decline.

The objectives of this thesis was to answer these two questions i) How does the progressive clogging occur in a single pore? ii) What are the consequences of this pore clogging on the flow condition across the porous medium?

We first focused our research on the study of a single pore to establish a relationship between the particle deposition and clogging event and the flow decline. In a second part, we performed the same analysis but this time on a medium with interconnected pores to understand how pore clogging can impact the complete obstruction of the whole medium.

Pore clogging at the particle scale

The general objective of this part was to describe the clogging process focus on a single pore, from the first deposited particle to the complete pore clogging, particle by particle, until the accumulation of particles behind the clog takes place. We proposed an *in-situ* method to measure the fluid velocity based on the tracking of the particles and quantify the impact of each deposition event on the flow.

Our first main result with the image analysis is that, when using suspensions assumed to be monodisperse,

aggregates composed of spherical particles are always present with the clogs, even if these objects represent less than 1% of the population. This observation is in disagreement with the hypothesis put forward in previous studies that the progressive accumulation of single particles leads to the clogging of the pores. Aggregates, despite their scarcity, are observed systematically in the thousand of clogs analysed in the thesis, varying the nature of the particles (PS, PMMA), their stabilization (steric or electrostatic), their origin and their size and for different experimental conditions like the confinement, the flow rate or the ionic strength. The presence of aggregates in clogs are due to their shape, size and their rotation. During their rotation, the edges of aggregates encounter the pore walls or the deposits, which promotes the contact. This process occurs where the rotation of the objects is destabilized and when the aggregate tries to align its largest dimension in the direction of the flow to limit its resistance to the fluid at the entrance of the pore. The capture probability of these objects is higher than that of spherical particles and strongly depends on their maximum size. Once captured, large aggregates reduce the cross section of the pore and allow the capture of smaller objects until the pore is completely clogged. Since they are broadly distributed in size, the structure of the clog greatly varies, depending also on the number of aggregates involved, leading to a unique structure for each single clog. The mechanism of aggregates capture relies on their physical interception, and is only affected by changes in flow rate or ionic strength. Increasing the flow rate leads to an increase of the size of aggregates captured because of the erosion of smaller objects. Similarly, when increasing the ionic strength near the CCC, the number of aggregate in the suspension increases as well as in the clog.

Once we have been able to monitor the overall deposition events, we tried determining the relationship between the progressive fouling of the pore and the corresponding flow decline. We imaged at a sufficiently high frame rate the area to track the objects over a dozen images in order to obtain a particle velocity before they enter in the pore, while following their subsequent deposition. We thus obtained a velocity decline as a function of the particle deposition history. At low Re number, the flow through a microchannel is similar to Ohm's law $\Delta P = R_H Q$, and at constant pressure, it is therefore easy to make the connection between an increase in hydrodynamic resistance R_H and the flow decline. Two main contributions to the flow drop during clogging were observed. First, the clogging of the pore, also called clog head, which by reducing the cross section of the pore, strongly increases R_H . Later on, behind the clog head, particles accumulate over a dozen of micrometers and also significantly contribute to increase R_H . Each new deposited particle contributes to modify the fluid paths inside the clog. As the accumulation increases the number and the length of the fluid paths as well as their tortuosity. This results in a flow decline that is almost as great as when the clog head is formed. We verified these two steps numerically by reconstructing the clog, particle by particle in Comsol, which allowed us to determine the flow variations within the pores of the clog at each new particle deposition.

After the formation of the clog, the accumulation increases significantly and can reach 200 to 300 μm , has only a very limited impact on the flow decline. The accumulation of particles creates a porous medium whose structural features as the permeability and the volume fraction can be determined. We observed that the increase of the clog length is inversely proportional to the fluid velocity indicating that there is a Darcy flow through the clog. We analysed the confocal images provided by Benjamin Dersoir and observed that the packing formed by the particles is not homogeneous at all. The particles are concentrated, near the walls, with a large empty zone in the center. This heterogeneity excludes the use of Kozeny-Carman relationship to retrieve both clog permeability and average volume fraction. We thus determined the particle volume fraction with the variation of the clog length and the exact number of particles in each given slice of the clog. The permeability is deduced from the relationship between the fluid velocity and the

length of the clog. We studied the evolution of both volume fraction and permeability with the flow rate and the increase of the ionic strength, up to the CCC. We showed that the overall packing dynamics is not modified with the flow rate since the value of the mean volume fraction remains constant. However, the volume fraction can be greatly modified by the confinement. This results in a channel with a small cross section which favors the capture of the objects at the wall or by the increase of the number of aggregates which by their size and their shape creates local defects. Both of these events prevent an ideal stacking of particle and results in an increase of the clog permeability.

To end this first part on single pore, we performed unclogging experiments, similar to the backwashing process during filtration operations by reversing the flow and we observed the behaviour of the particle accumulation. The clogs can be separated in two consecutive zones. Closer to the rear of the head clog there is a labile zone and since the particles are no longer held by the flow, they leave the accumulation individually. We observed local rearrangement within this zone, which may lead to the formation of crystalline zones at the wall, further indicating that particles are free to move. This local amorphous to crystal transition, even if it involves a large number of particles, does not have any implication of the permeation flow. At the opposite, closer to the clog head particles form a cohesive zone, which is not removed during the flow reversal. The length of this cohesive zone increases with the flow rate and the ionic strength, until there is no labile zone anymore. We suggested that either the measurement of particle velocity is not precise enough, because of the small number of objects involved in the accumulation during an arrangement event or that the compaction in a high confinement can create chains of forces among the particles and also supported by the pore walls that prevent the accumulation from being dispersed during the unclogging experiments. The increase of the numbers of aggregates with the ionic strength could also consolidates the clogs.

Porous medium clogging at the pore scale

While we have first described all the steps of clogging, from the first particle deposited to the unclogging of a single isolated pore, we extended our methodology to a 2D porous media, which can be viewed as the simplest model of membrane. In this second part, we wanted to describe the phenomenology of the clogging of a porous medium, taking into account that the pores are connected to each other and understand the impact of the pore clogging process on the flow conditions in the whole medium.

First, we described the clogging in a porous medium by observing the deposition and the different clogging mechanisms involve. During the experiments, we injected monodisperse particles into an ordered porous medium, the surface charge of the pores being high enough to prevent particle deposition by diffusion. Our main observation is that the porous medium is clogged at its very entrance, whatever the flow conditions or its geometry. We identified two clogging mechanisms, the original clog, which is the same as that in a single pore, and the accumulation clog formed behind original clogs. The original clogs represent the vast majority of clogs. As before, the clog formation relies on the interception of aggregates and once again, we hypothesized that the clogging of the medium is driven only by the tail of the suspension distribution and the high probability of aggregates capture. We verified this assumption by creating a very simple model, without consideration of hydrodynamic and DLVO forces, to understand how the capture probability and the size distribution of aggregates modified the localisation of the clogging front.

Secondly, we modified the object surface charge by adding salt to the suspensions, with $I=50$ and 300mM behind the CCC. For $I=50\text{mM}$ there is no electrostatic barrier at the pore surface, which favors the particle deposition on the collectors. In these favorable conditions we did not observe a noticeable difference on the position of the clogging front except that more clogs are formed inside the medium prior its clogging. For I

$=300\text{mM}$, the deposition of objects is much more important everywhere in the medium and is at the origin of a third clogging mechanism. We observed the formation of dendrite-like deposits form on the top of collectors that grow significantly towards the upstream collectors, reducing drastically the available path for flowing particles and eventually lead to the complete obstruction of the pores. We called the clogs formed in this way dendrite clogs. However, whatever the clogging mechanism, porous media are still clogged at their entrance, showing once again that the deposition of aggregates prevails due to their high probability of capture.

Finally, we verified that the clogging at the entrance of the media remained true for polydisperse suspensions in size and shape, by using suspensions of fragmented nano-microplastics. Their size distribution is centered on 400nm , but objects can easily reach $1\text{-}2\mu\text{m}$ in the tail of the distribution. We studied the clogging process for two types of suspension, a raw suspension with 15% of the objects of the population being micrometric, and for a filtered one with only 4% of micrometric objects. The clogging for unfiltered objects is localized very close to the entrance, while for the filtered one the clogging front goes much deeper inside the medium. In both experiments the largest objects of the suspension are the main contributors to the pore clogging. However those of the unfiltered suspension, since they are smaller, have a lower probability to be captured and thus deposit further inside the medium before clogging of the pores.

To conclude on the clogging of the porous medium, we used image analysis to quantify the degree of fouling of a porous medium and the corresponding flow decline, thanks to the particle velocities as we did for a single pore. We monitored the variation of the flow conditions for different sizes of particles and ionic strengths to see their impact on the flow decline since they imply slightly different clogging processes. We experimentally observed a strong dependence on the clog formation in the first line with the increase of the hydrodynamic resistance. Initially, some pores are clogged without strongly increase the porous medium resistance and have not a significant impact on the flow. However, when pores clogged are concentrated in a same zone then the local hydrodynamic resistance strongly increases and a cake layer formation initiates. These local increases of hydrodynamic resistance favour the clogging of neighbouring pores since particles are distributed in the free pores. We have thus observed an increase in the number of clogged pores with the appearance in certain zones of cake layer and the decrease of the flow. By using again the electrical analogy we established the relationship between the hydrodynamic resistance of the whole medium and the variation of the flow rate. We developed a simple hydrodynamic model that takes into account the clogging of the pore in the whole medium as well as the cake layer. We used this model to fit the data of the flow decline obtained for medium clogging by a stable suspension with no salt added. We get a good agreement between the experimental data and the model, despite the crude approximations we have made. However quite a bit of work remains to be done to see if the shape of the flow decline curve does not change for each single filtration conditions, including the flow conditions and the features of the membrane.

Perspectives

Towards more complex clogging mechanisms

The methodology developed during the thesis at the particle scale focus on a single pore, i.e. the study of the clog dynamics by image analysis and the flow measurement with particle tracking, coupled with the confocal images of the clog internal structure provided by Benjamin Dersoir, proved to be robust enough to determine when pore clogging takes place and also when the whole porous medium is completely obstructed. We limited our approach to systems with simple and well known DLVO and hydrodynamic interactions, however the clogging can be a more complex combination of physical, chemical and biological parameters. For example, at the particle scale the deformability of objects under shear (Chen et al., 2020; Duchêne et al., 2020) or complex bio-chemical reactions that would induce biofilm formation (Liu et al., 2019a), crystallization, precipitation (Sicignano et al., 2018) or aggregation (Bretagne et al., 2017; Sakhawoth et al., 2021) of nano-microparticles that induced clogging. The properties of the fluid could also be modified by adding solute (Shin et al., 2017), temperature or nutrient gradient for active particles like bacteria which cause clogging. Most of these systems have been studied at the pore scale and use syringe pump, so they do not study the flow decline when fouling and clogging take place into the pore. However the clogs are formed under specific chemical or bio-chemical reaction based on the flow condition. Because of the flow decline these conditions are modified and could impact the clog structure or even causes their unclogging.

Backwashing of the porous medium

Backwashing is one of the most common techniques to clean a filter. In the thesis, we limited the study of backwashing to a single pore (chapter 5) with an important length which induced a strong R_H and the strong confinement that creates chains of forces among the particles and the pore wall along the entire length of the pore. In this configuration, the backwashing was never complete because of the coexistence of labile and cohesive zone. In the porous medium with spherical collectors, the pores are much shorter which should favor backwashing. However, the pores are connected to each other and the fluid can therefore flow through the paths of lower resistance (figure 10.1).

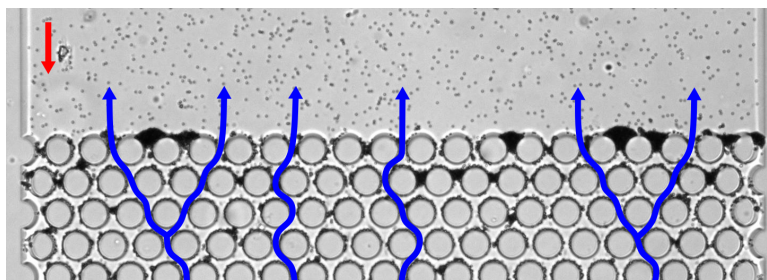


Figure 10.1: Illustration of a possible distribution of the fluid by avoiding the clogged zones of greater hydrodynamic resistance with blue arrows. Red arrow is the original sens of the flow.

We performed a preliminary experiment in a completely clogged ordered medium for suspensions with repulsive particle-wall interaction, with spherical collector. By abruptly reversing the pressure, we observed that all clogs were unclogged. This experiment remains simple, since all fluid paths with the same hydrodynamic resistance. Considering suspensions with attractive particle-wall interactions that increase the number of clogs, backwashing could be not as effective and unclogged only a few pores. It would therefore be interesting to estimate the efficiency of backwashing according to the level of fouling, i.e. when the local hydrodynamic resistances are different. Moreover, if the cake layer in the porous medium has the same properties as the single pore, it would be interesting to observe whether backwashing is effective in removing a cohesive zone of particles.

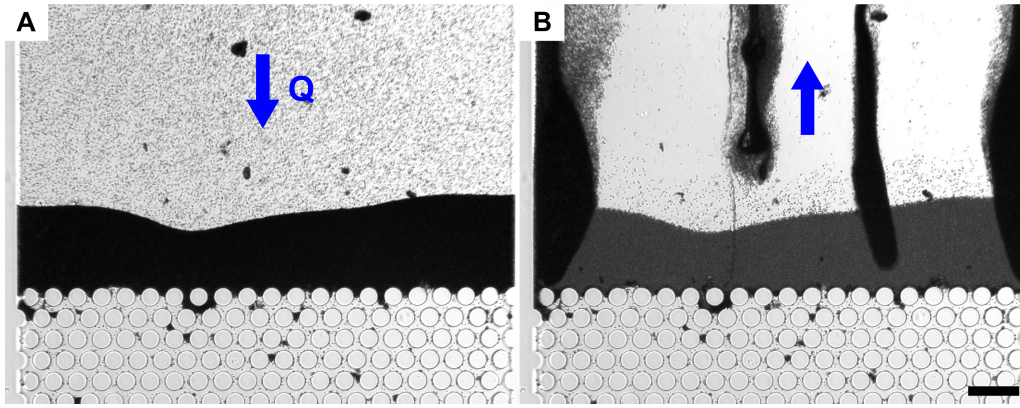


Figure 10.2: A clogged porous medium whose the pressure is set to 50mbar (a) before brutally being reset to -5mbar (b). Scale bar: 70 μ m.

The main challenge in backwashing is to successfully unclog pores, whatever their geometry. Spherical collectors are the most favourable geometry for the backwashing, since they have only one place where the cross section is very small and where the clog structure is cohesive (see chapter 5). Backwashing should be much more challenging in a medium with narrower pores, whether ordered or not (figure 10.3a-b), with a risk of re-clogging after the unclogging. Similarly, the presence of dead-end pores, more realistic of a membrane, could have a negative impact on backwashing by limiting the permeability in some part of the porous medium (figure 10.3c).

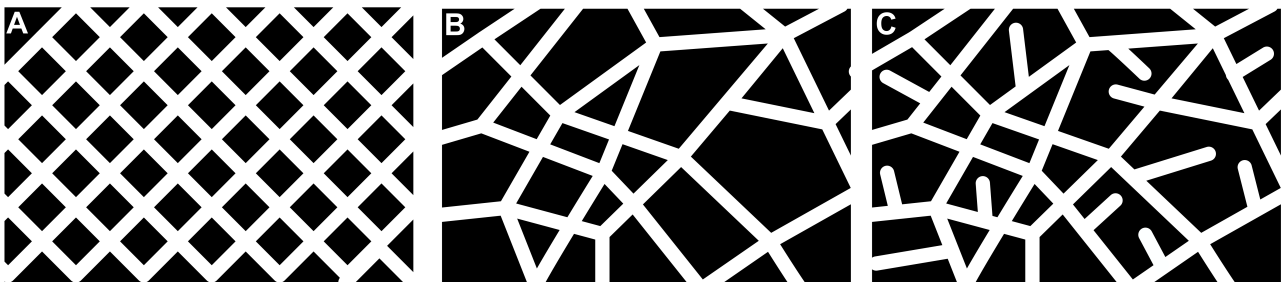


Figure 10.3: Ordered porous medium with long pores (a), disordered (b) and with dead-end pores (c).

Heterogeneities of the porous medium

Up to now, we performed experiments with ordered porous media, which is an overly simplistic version of real membranes. The first natural modification of our model porous media concerns the pore and collectors sizes (figure 10.4a). It would be interesting to use media with a given distribution of pores and collector's size and shape. We expect a complex coupling between different factors. In the one hand, narrow pores may be clogged quite rapidly, since this process requires the accumulation of fewer objects, but their higher hydrodynamic resistance can lower the transport of objects through them. In addition the spatial variation of the shear is more important in higher confinement and thus it may greatly modify the capture of real objects with an irregular shape. On the other hand, most of the objects tend to flow through the larger pores, due to their low resistance. The clogging process is also delayed in such pores due to the lower confinement. We think that this competition between the transport through narrow and wide pores will force the objects to flow through preferential paths. Another proposal regarding heterogeneity would be to use the structure of the medium to delay the clogging since the process is driven by the distribution tail of objects, which have a higher probability of capture. The medium could be composed of lines with collectors whose separation distance is gradually reduced (figure 10.4b). This geometry is already use in industry and called gradient filter, but has never been studied at the particle scale. The objective is to capture in the first lines the largest aggregates while letting pass the other sizes that would be captured

in a smaller pore and further in the medium. In the same manner, there is no study on the particle scale about the clogging in a porous medium with asymmetric collector (figure 10.4c), while fluid asymmetry could have very interesting consequences on the trajectories of the objects, depending on whether we want to avoid or favor their capture.

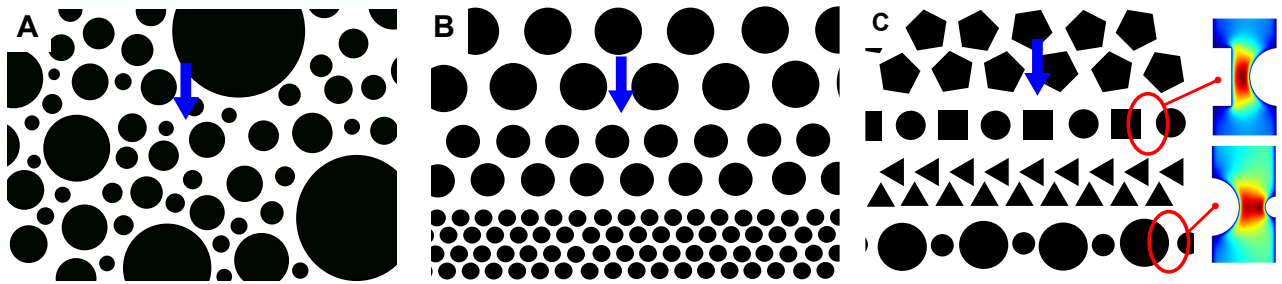


Figure 10.4: Simple heterogeneous porous medium (a), gradual porous medium (b), asymmetric porous medium with in inset two examples of velocity maps simulated with Comsol (c).

A last proposal to delay clogging while filtering out aggregates would be to create fractures with no collector the porous medium (figure 10.5b). Since the clogging of a medium is concentrated at its entrance, with finally little deposit in the rest, these large areas would allow objects to be carried further into the medium to spread particle deposition over a greater length before the medium becomes clogged.

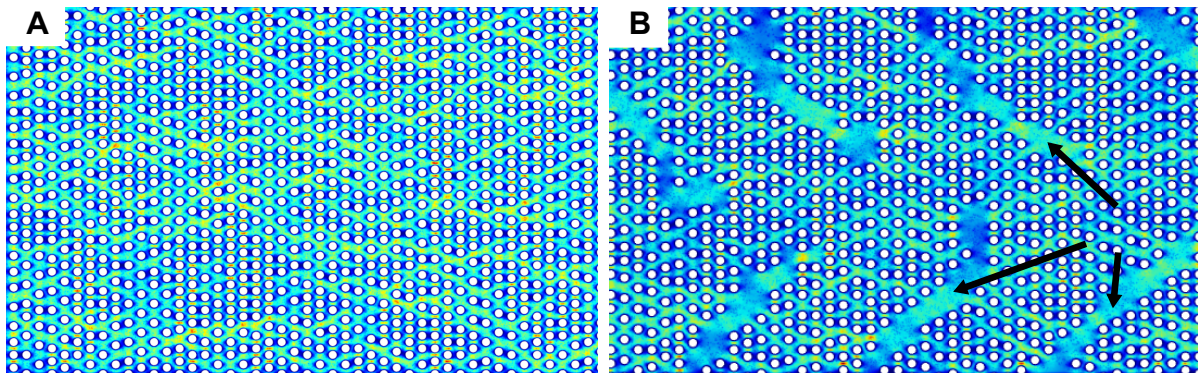


Figure 10.5: Heterogeneous porous medium initial (a), with fractures with no collectors (b) indicated by black arrows.

Fragmentation of unstable suspension in porous media

In the environment or in industry, unstable objects can spontaneously form aggregates regrouping one or several types of objects. When these aggregates are inside a porous medium, they are subject to compression or elongation zone in addition to the important shear inside the pore. Large aggregates try to get align in the flow direction and the differences of velocity and shear undergo by the ends of the aggregate allow the fragmentation at the most fragile part of the aggregate, with the least point of contact between the objects, ie. in the smallest width (figure 10.6).

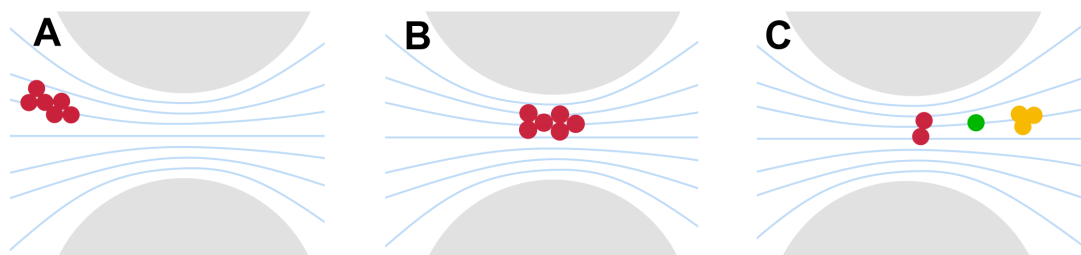


Figure 10.6: Fragmentation of an aggregate after it gets align in the flow direction.

We can ask what is the impact of the flow on these aggregate from unstable objects. In preliminary experiments, we destabilized $1.5\mu\text{m}$ PS particles to form aggregate until $7\text{--}8\mu\text{m}$ aggregates. In normal case, these aggregates are quasi-immediately capture in the pore, however here, they melt down passing pores, until very small size (figure 10.7).

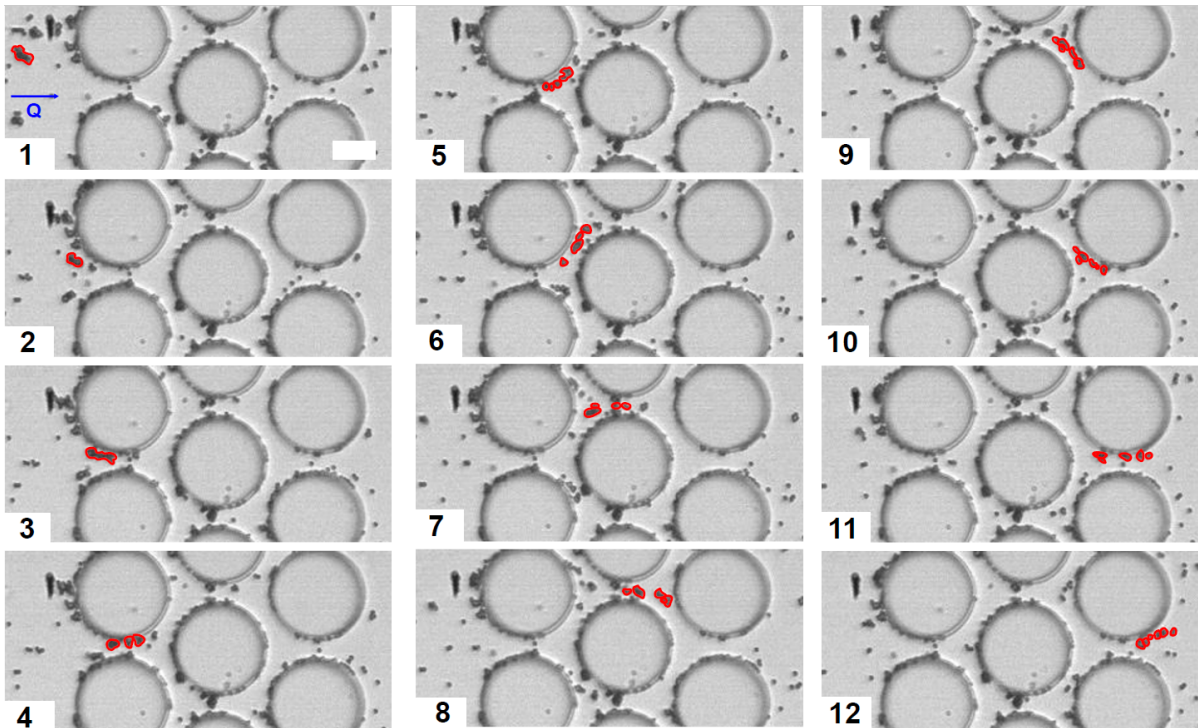


Figure 10.7: Fragmentation of an aggregate of $1.5\mu\text{m}$ PS particles in a porous medium $R_c = 15\mu\text{m}$, $D_p = 10\mu\text{m}$. Red outlines are the different parts of the aggregate coming at image 1. Scale bar $15\mu\text{m}$.

This fragmentation could have important consequences on the clogging of the medium. In our example, the size distribution is greatly decreased towards the smallest values after three row. The suspension is thus composed of smaller aggregates, with a lower probability of clogging. These objects are transported and deposited further into the medium. As the large aggregates have disappeared, they can no longer accelerate the clogging by strongly reduce the pore cross section. More small objects are therefore deposited in the medium before it is clogged, and since these objects are deposited further away, the clogging front should also be further away.

Bibliography

- Adamczyk, Z., Siwek, B., Zembala, M., and Weron, P. (1992). "Kinetics of localized adsorption of colloid particles". *Langmuir* 8.11, pp. 2605–2610.
- Agbangla, G., Climent, É., and Bacchin, P. (2012). "Experimental investigation of pore clogging by microparticles: Evidence for a critical flux density of particle yielding arches and deposits". *Separation and purification technology* 101, pp. 42–48.
- (2014). "Numerical investigation of channel blockage by flowing microparticles". *Computers & Fluids* 94, pp. 69–83.
- Al Ashhab, A., Sweity, A., Bayramoglu, B., Herzberg, M., and Gillor, O. (2017). "Biofouling of reverse osmosis membranes: effects of cleaning on biofilm microbial communities, membrane performance, and adherence of extracellular polymeric substances". *Biofouling* 33.5, pp. 397–409.
- Almog, Y., Reich, S., and Levy, M. (1982). "Monodisperse polymeric spheres in the micron size range by a single step process". *British Polymer Journal* 14.4, pp. 131–136.
- Auset, M. and Keller, A. (2006). "Pore-scale visualization of colloid straining and filtration in saturated porous media using micromodels". *Water resources research* 42.12.
- Bacchin, P., Derckx, Q., Veyret, D., Glucina, K., and Moulin, P. (2014). "Clogging of microporous channels networks: role of connectivity and tortuosity". *Microfluidics and nanofluidics* 17.1, pp. 85–96.
- Barber, C., Dobkin, D., and Huhdanpaa, H. (1996). "The quickhull algorithm for convex hulls". *ACM Transactions on Mathematical Software (TOMS)* 22.4, pp. 469–483.
- Bergendahl, J. and Grasso, D. (2000). "Prediction of colloid detachment in a model porous media: Hydrodynamics". *Chemical Engineering Science* 55.9, pp. 1523–1532.
- Bizmark, N., Schneider, J., Priestley, R., and Datta, S. (2020). "Multiscale dynamics of colloidal deposition and erosion in porous media". *Science advances* 6.46, eabc2530.
- Bongaerts, J., Fourtouni, K., and Stokes, J. (2007). "Soft-tribology: lubrication in a compliant PDMS–PDMS contact". *Tribology International* 40.10-12, pp. 1531–1542.
- Bounoua, S., Tomas, S., Labille, J., Molle, B., Granier, J., Haldenwang, P., and Izzati, S. (2016). "Understanding physical clogging in drip irrigation: in situ, in-lab and numerical approaches". *Irrigation science* 34.4, pp. 327–342.
- Brans, G., Dinther, A. van, Odum, B., Schroën, C., and Boom, R. (2007). "Transmission and fractionation of micro-sized particle suspensions". *Journal of membrane science* 290.1-2, pp. 230–240.
- Brenner, H. (1961). "The slow motion of a sphere through a viscous fluid towards a plane surface". *Chemical engineering science* 16.3-4, pp. 242–251.
- Bretagne, A., Cotot, F., Arnaud-Roux, M., Sztucki, M., Cabane, B., and Galey, J.-B. (2017). "The mechanism of eccrine sweat pore plugging by aluminium salts using microfluidics combined with small angle X-ray scattering". *Soft Matter* 13.20, pp. 3812–3821.
- Bruus, H. (2008). *Theoretical microfluidics*. Vol. 18. Oxford university press Oxford.
- Carman, P. (1937). "Fluid flow through granular beds". *Trans. Inst. Chem. Eng.* 15, pp. 150–166.

- Chang, H., Liang, H., Qu, F., Liu, B., Yu, H., Du, X., Li, G., and Snyder, S. (2017). "Hydraulic backwashing for low-pressure membranes in drinking water treatment: A review". *Journal of Membrane Science* 540, pp. 362–380.
- Chawla, C., Zwijnenburg, A., Kemperman, A., and Nijmeijer, K. (2017). "Fouling in gravity driven Point-of-Use drinking water treatment systems". *Chemical Engineering Journal* 319, pp. 89–97.
- Chen, S., Liu, W., and Li, S. (2016). "Effect of long-range electrostatic repulsion on pore clogging during microfiltration". *Physical Review E* 94.6, p. 063108.
- Chen, X., Li, Y., Liu, Z., Li, X., Zhang, J., and Zhang, H. (2020). "Core-and pore-scale investigation on the migration and plugging of polymer microspheres in a heterogeneous porous media". *Journal of Petroleum Science and Engineering* 195, p. 107636.
- Chequer, L., Carageorgos, T., Naby, M., Hussaini, M., Lee, W., and Bedrikovetsky, P. (2021). "Colloidal detachment from solid surfaces: Phase diagrams to determine the detachment regime". *Chemical Engineering Science* 229, p. 116146.
- Cox, R. and Brenner, H. (1967). "The slow motion of a sphere through a viscous fluid towards a plane surface—II Small gap widths, including inertial effects". *Chemical Engineering Science* 22.12, pp. 1753–1777.
- Crocker, J. and Grier, D. (1996). "Methods of digital video microscopy for colloidal studies". *Journal of colloid and interface science* 179.1, pp. 298–310.
- Croom, B., Abbott, A., Kemp, J., Rueschhoff, L., Smieska, L., Woll, A., Stoupin, S., and Koerner, H. (2021). "Mechanics of nozzle clogging during direct ink writing of fiber-reinforced composites". *Additive Manufacturing* 37, p. 101701.
- de Saint Vincent, M., Abkarian, M., and Tabuteau, H. (2016). "Dynamics of colloid accumulation under flow over porous obstacles". *Soft matter* 12.4, pp. 1041–1050.
- Demoulin, C., Wisniewski, C., Ricci, J., Delalonde, M., and Dahdouh, L. (2022). "Viscoelastic behavior and fouling propensity of concentrated suspended particles of orange juice with defined size distributions: Towards a better control of the deposit layer properties during microfiltration". *LWT* 153, p. 112473.
- Dersoir, B., de Saint Vincent, M., Abkarian, M., and Tabuteau, H. (2015). "Clogging of a single pore by colloidal particles". *Microfluidics and Nanofluidics* 19.4, pp. 953–961.
- Dersoir, B., Schofield, A., Saint Vincent, M. de, and Tabuteau, H. (2019). "Dynamics of pore fouling by colloidal particles at the particle level". *Journal of Membrane Science* 573, pp. 411–424.
- Duchêne, C., Filipe, V., Huille, S., and Lindner, A. (2020). "Clogging of microfluidic constrictions by monoclonal antibody aggregates: role of aggregate shape and deformability". *Soft Matter* 16.4, pp. 921–928.
- Duffy, D., McDonald, J., Schueller, O., and Whitesides, G. (1998). "Rapid prototyping of microfluidic systems in poly (dimethylsiloxane)". *Analytical chemistry* 70.23, pp. 4974–4984.
- Duru, P. and Hallez, Y. (2015). "A three-step scenario involved in particle capture on a pore edge". *Langmuir* 31.30, pp. 8310–8317.
- Einstein, A. (1905). "On the motion of small particles suspended in liquids at rest required by the molecular-kinetic theory of heat". *Annalen der physik* 17.549-560, p. 208.
- El Hadri, H., Gigault, J., Maxit, B., Grassl, B., and Reynaud, S. (2020). "Nanoplastic from mechanically degraded primary and secondary microplastics for environmental assessments". *NanoImpact* 17, p. 100206.
- Elimelech, M. and O'Melia, C. (1990). "Kinetics of deposition of colloidal particles in porous media". *Environmental science & technology* 24.10, pp. 1528–1536.

- Elliot, M. and Poon, W. (2001). "Conventional optical microscopy of colloidal suspensions". *Advances in Colloid and Interface Science* 92.1-3, pp. 133–194.
- Feke, D., Prabhu, N., Mann Jr, A., and Mann III, A. (1984). "A formulation of the short-range repulsion between spherical colloidal particles". *The Journal of Physical Chemistry* 88.23, pp. 5735–5739.
- Ferber, D. (2000). "Possible new way to lower cholesterol". *Science* 289.5484, pp. 1446–1447.
- Fritz, G., Schädler, V., Willenbacher, N., and Wagner, N. (2002). "Electrosteric stabilization of colloidal dispersions". *Langmuir* 18.16, pp. 6381–6390.
- Fuller, S., Wilhem, E., and Jacobson, J. (2002). "Ink-jet printed nanoparticle microelectromechanical systems". *Journal of Microelectromechanical systems* 11.1, pp. 54–60.
- Garem, A., Schuck, P., and Maubois, J.-L. (2000). "Cheesemaking properties of a new dairy-based powder made by a combination of microfiltration and ultrafiltration". *Le Lait* 80.1, pp. 25–32.
- Gerber, G., Bensouda, M., Weitz, D., and Coussot, P. (2019). "Self-limited accumulation of colloids in porous media". *Physical review letters* 123.15, p. 158005.
- Gerber, G., Rodts, S., Aïmedieu, P., Faure, P., and Coussot, P. (2018). "Particle-size-exclusion clogging regimes in porous media". *Physical review letters* 120.14, p. 148001.
- Gervais, T., El-Ali, J., Günther, A., and Jensen, K. (2006). "Flow-induced deformation of shallow microfluidic channels". *Lab on a Chip* 6.4, pp. 500–507.
- Goldman, A., Cox, R., and Brenner, H. (1967). "Slow viscous motion of a sphere parallel to a plane wall—Motion through a quiescent fluid". *Chemical engineering science* 22.4, pp. 637–651.
- Gopal, R., Kaur, S., Ma, Z., Chan, C., Ramakrishna, S., and Matsuura, T. (2006). "Electrospun nanofibrous filtration membrane". *Journal of Membrane Science* 281.1-2, pp. 581–586.
- Gregory, J. (1981). "Approximate expressions for retarded van der Waals interaction". *Journal of colloid and interface science* 83.1, pp. 138–145.
- Grismer, M. and Shepherd, H. (2011). "Plants in constructed wetlands help to treat agricultural processing wastewater". *California Agriculture* 65.2, pp. 73–79.
- Gudipaty, T., Stamm, M., Cheung, L., Jiang, L., and Zohar, Y. (2011). "Cluster formation and growth in microchannel flow of dilute particle suspensions". *Microfluidics and nanofluidics* 10.3, pp. 661–669.
- Hamaker, H. (1937). "The London—van der Waals attraction between spherical particles". *physica* 4.10, pp. 1058–1072.
- Hardy, B., Uechi, K., Zhen, J., and Kavehpour, H. (2009). "The deformation of flexible PDMS microchannels under a pressure driven flow". *Lab on a Chip* 9.7, pp. 935–938.
- Hassan, I., Lafforgue, C., Ayadi, A., and Schmitz, P. (2014). "In situ 3D characterization of monodispersed spherical particle deposition on microsieve using confocal laser scanning microscopy". *Journal of Membrane Science* 454, pp. 283–297.
- He, L., Rong, H., Wu, D., Li, M., Wang, C., and Tong, M. (2020). "Influence of biofilm on the transport and deposition behaviors of nano- and micro-plastic particles in quartz sand". *Water research* 178, p. 115808.
- Henry, C., Minier, J.-P., and Lefevre, G. (2012). "Numerical study on the adhesion and reentrainment of nondeformable particles on surfaces: the role of surface roughness and electrostatic forces". *Langmuir* 28.1, pp. 438–452.
- Hilal, N., Ogunbiyi, O., Miles, N., and Nigmatullin, R. (2005). "Methods employed for control of fouling in MF and UF membranes: a comprehensive review". *Separation Science and Technology* 40.10, pp. 1957–2005.
- Ho, N. and Higuchi, W. (1968). "Preferential aggregation and coalescence in heterodispersed systems". *Journal of pharmaceutical sciences* 57.3, pp. 436–442.

- Hogg, R., Healy, T., and Fuerstenau, D. (1966). "Mutual coagulation of colloidal dispersions". *Transactions of the Faraday Society* 62, pp. 1638–1651.
- Hong, S., Faibish, R., and Elimelech, M. (1997). "Kinetics of permeate flux decline in crossflow membrane filtration of colloidal suspensions". *Journal of colloid and interface science* 196.2, pp. 267–277.
- Hube, S., Eskafi, M., Hrafnkelsdóttir, K., Bjarnadóttir, B., Bjarnadóttir, M., Axelsdóttir, S., and Wu, B. (2020). "Direct membrane filtration for wastewater treatment and resource recovery: A review". *Science of The Total Environment* 710, p. 136375.
- Iadecola, C. (2014). "Angiophagy: clearing or clogging microvessels?" *Science translational medicine* 6.226, 226fs10–226fs10.
- Israelachvili, J. (2015). *Intermolecular and surface forces*. Academic press.
- Johnston, I., McCluskey, D., Tan, C., and Tracey, M. (2014). "Mechanical characterization of bulk Sylgard 184 for microfluidics and microengineering". *Journal of Micromechanics and Microengineering* 24.3, p. 035017.
- Jung, S., Jeong, J., Park, J. D., and Ahn, K. (2021). "Interplay between particulate fouling and its flow disturbance: Numerical and experimental studies". *Journal of Membrane Science*, p. 119497.
- Kayhanian, M., Anderson, D., Harvey, J., Jones, D., and Muhunthan, B. (2012). "Permeability measurement and scan imaging to assess clogging of pervious concrete pavements in parking lots". *Journal of Environmental management* 95.1, pp. 114–123.
- Kim, S. and Karrila, S. (2013). *Microhydrodynamics: principles and selected applications*. Courier Corporation.
- Kimme, C., Ballard, D., and Sklansky, J. (1975). "Finding circles by an array of accumulators". *Communications of the ACM* 18.2, pp. 120–122.
- Ko, C. and Elimelech, M. (2000). "The "shadow effect" in colloid transport and deposition dynamics in granular porous media: measurements and mechanisms". *Environmental science & technology* 34.17, pp. 3681–3689.
- Kodger, T., Guerra, R., and Sprakel, J. (2015). "Precise colloids with tunable interactions for confocal microscopy". *Scientific reports* 5, p. 14635.
- Kozeny, J. (1927). "Über kapillare leitung der wasser in boden". *Royal Academy of Science, Vienna, Proc. Class I* 136, pp. 271–306.
- Lay, H., Wang, R., and Chew, J. (2021). "Membrane fouling by mixtures of oppositely charged particles". *Journal of Membrane Science* 625, p. 119093.
- Lin, Lee, D., and Huang, C. (2010). "Membrane fouling mitigation: Membrane cleaning". *Separation Science and Technology* 45.7, pp. 858–872.
- Linkhorst, J., Beckmann, T., Go, D., Kuehne, A., and Wessling, M. (2016). "Microfluidic colloid filtration". *Scientific reports* 6.1, pp. 1–8.
- Liot, O., Singh, A., Bacchin, P., Duru, P., Morris, J., and Joseph, P. (2018). "Pore cross-talk in colloidal filtration". *Scientific reports* 8.1, pp. 1–7.
- Liu, N., Skauge, T., Landa-Marbán, D., Hovland, B., Thorbjørnsen, B., Radu, F., Vik, B. F., Baumann, T., and Bødtker, G. (2019a). "Microfluidic study of effects of flow velocity and nutrient concentration on biofilm accumulation and adhesive strength in the flowing and no-flowing microchannels". *Journal of Industrial Microbiology and Biotechnology* 46.6, pp. 855–868.
- Liu, Q., Zhao, B., and Santamarina, J. (2019b). "Particle Migration and Clogging in Porous Media: A Convergent Flow Microfluidics Study". *Journal of Geophysical Research: Solid Earth* 124.9, pp. 9495–9504.

- Liu, Xiao, M., Zhang, X., Gal, C., Chen, X., Liu, L., Pan, S., Wu, J., Tang, L., and Clements-Croome, D. (2017). "A review of air filtration technologies for sustainable and healthy building ventilation". *Sustainable cities and society* 32, pp. 375–396.
- Lohaus, J., Perez, Y., and Wessling, M. (2018). "What are the microscopic events of colloidal membrane fouling?" *Journal of Membrane Science* 553, pp. 90–98.
- Lohaus, J., Stockmeier, F., Surray, P., Lölsberg, J., and Wessling, M. (2020). "What are the microscopic events during membrane backwashing?" *Journal of Membrane Science* 602, p. 117886.
- London, F. (1930). "Über einige eigenschaften und anwendungen der molekularkräfte". *Z. Phys. Chem. Abt.*, pp. 222–251.
- Loy, G. and Zelinsky, A. (2003). "Fast radial symmetry for detecting points of interest". *IEEE Transactions on pattern analysis and machine intelligence* 25.8, pp. 959–973.
- Marin, A., Lhuissier, H., Rossi, M., and Kähler, C. (2018). "Clogging in constricted suspension flows". *Physical Review E* 97.2, p. 021102.
- Mays, D. and Hunt, J. (2005). "Hydrodynamic aspects of particle clogging in porous media". *Environmental science & technology* 39.2, pp. 577–584.
- (2007). "Hydrodynamic and chemical factors in clogging by montmorillonite in porous media". *Environmental science & technology* 41.16, pp. 5666–5671.
- Mokrane, M., Desclaux, T., Morris, J., Joseph, P., and Liot, O. (2020). "Microstructure of the near-wall layer of filtration-induced colloidal assembly". *Soft Matter* 16.42, pp. 9726–9737.
- Mullaney, J. and Lucke, T. (2014). "Practical review of pervious pavement designs". *CLEAN–Soil, Air, Water* 42.2, pp. 111–124.
- Mustin, B. and Stoeber, B. (2010). "Deposition of particles from polydisperse suspensions in microfluidic systems". *Microfluidics and nanofluidics* 9.4-5, pp. 905–913.
- Parvan, A., Jafari, S., Rahnama, M., and Raoof, A. (2020). "Insight into particle retention and clogging in porous media; a pore scale study using lattice Boltzmann method". *Advances in Water Resources* 138, p. 103530.
- Pelley, A. and Tufenkji, N. (2008). "Effect of particle size and natural organic matter on the migration of nano- and microscale latex particles in saturated porous media". *Journal of colloid and interface science* 321.1, pp. 74–83.
- Poesio, P. and Ooms, G. (2004). "Formation and ultrasonic removal of fouling particle structures in a natural porous material". *Journal of Petroleum Science and Engineering* 45.3-4, pp. 159–178.
- Pradel, A., El Hadri, H., Desmet, C., Ponti, J., Reynaud, S., Grassl, B., and Gigault, J. (2020). "Deposition of environmentally relevant nanoplastic models in sand during transport experiments". *Chemosphere* 255, p. 126912.
- Pradel, A., Ferreres, S., Veclin, C., El Hadri, H., Gautier, M., Grassl, B., and Gigault, J. (2021). "Stabilization of Fragmental Polystyrene Nanoplastic by Natural Organic Matter: Insight into Mechanisms". *ACS ES&T Water*.
- Prakash, P., Abdulla, A., and Varma, M. (2021). "Contact Force Mediated Rapid Deposition of Colloidal Microspheres Flowing over Microstructured Barriers". *Langmuir*.
- Preparata, F. and Shamos, M. (2012). *Computational geometry: an introduction*. Springer Science & Business Media.
- Ramachandran, V. and Fogler, H. (1998). "Multilayer deposition of stable colloidal particles during flow within cylindrical pores". *Langmuir* 14.16, pp. 4435–4444.
- (1999). "Plugging by hydrodynamic bridging during flow of stable colloidal particles within cylindrical pores". *Journal of Fluid Mechanics* 385, pp. 129–156.

- Razzaghmanesh, M. and Beecham, S. (2018). "A review of permeable pavement clogging investigations and recommended maintenance regimes". *Water* 10.3, p. 337.
- Reerink, H. and Overbeek, J. (1954). "The rate of coagulation as a measure of the stability of silver iodide sols". *Discussions of the Faraday Society* 18, pp. 74–84.
- Roussel, N., Nguyen, T., and Coussot, P. (2007). "General probabilistic approach to the filtration process". *Physical review letters* 98.11, p. 114502.
- Ryde, N., Kallay, N., and Matijević, E. (1991). "Particle adhesion in model systems. Part 14.—Experimental evaluation of multilayer deposition". *Journal of the Chemical Society, Faraday Transactions* 87.9, pp. 1377–1381.
- Sader, J., Carnie, S., and Chan, D. (1995). "Accurate analytic formulas for the double-layer interaction between spheres". *Journal of Colloid and Interface Science* 171.1, pp. 46–54.
- Sagu, S., Karmakar, S., Nso, E., Kapseu, C., and De, S. (2014). "Ultrafiltration of banana (*Musa acuminata*) juice using hollow fibers for enhanced shelf life". *Food and bioprocess technology* 7.9, pp. 2711–2722.
- Sakhawoth, Y., Dupire, J., Leonforte, F., Chardon, M., Monti, F., Tabelaing, P., Cabane, B., Botet, R., and Galey, J.-B. (2021). "Real time observation of the interaction between aluminium salts and sweat under microfluidic conditions". *Scientific reports* 11.1, pp. 1–15.
- Sauret, A., Barney, E., Perro, A., Villermaux, E., Stone, H., and Dressaire, E. (2014). "Clogging by sieving in microchannels: Application to the detection of contaminants in colloidal suspensions". *Applied Physics Letters* 105.7, p. 074101.
- Sauret, A., Somszor, K., Villermaux, E., and Dressaire, E. (2018). "Growth of clogs in parallel microchannels". *Physical Review Fluids* 3.10, p. 104301.
- Schenkel, J. and Kitchener, J. (1960). "A test of the Derjaguin-Verwey-Overbeek theory with a colloidal suspension". *Transactions of the Faraday Society* 56, pp. 161–173.
- Sendekie, Z. and Bacchin, P. (2016). "Colloidal jamming dynamics in microchannel bottlenecks". *Langmuir* 32.6, pp. 1478–1488.
- Shamos, M. (1978). "Computational geometry." *Ph. D. thesis, Yale University*.
- Shaw, D. (1980). *Introduction to colloid and surface chemistry*. Butterworths.
- ed. (1992). Fourth Edition. Butterworth-Heinemann.
- Shen, S., Sudol, E., and El-Aasser, M. (1993). "Control of particle size in dispersion polymerization of methyl methacrylate". *Journal of Polymer Science Part A: Polymer Chemistry* 31.6, pp. 1393–1402.
- Shin, S., Ault, J., Warren, P., and Stone, H. (2017). "Accumulation of colloidal particles in flow junctions induced by fluid flow and diffusiophoresis". *Physical Review X* 7.4, p. 041038.
- Sicignano, L., Tomaiuolo, G., Perazzo, A., Nolan, S., Maffettone, P., and Guido, S. (2018). "The effect of shear flow on microreactor clogging". *Chemical Engineering Journal* 341, pp. 639–647.
- Souzy, M., Zuriguel, I., and Marin, A. (2020). "Transition from clogging to continuous flow in constricted particle suspensions". *Physical Review E* 101.6, p. 060901.
- Tay, J. and Jeyaseelan, S. (1995). "Membrane filtration for reuse of wastewater from beverage industry". *Resources, Conservation and Recycling* 15.1, pp. 33–40.
- Thomas, D., Penicot, P., Contal, P., Leclerc, D., and Vendel, J. (2001). "Clogging of fibrous filters by solid aerosol particles experimental and modelling study". *Chemical Engineering Science* 56.11, pp. 3549–3561.
- Torkzaban, S., Bradford, S., and Walker, S. (2007). "Resolving the coupled effects of hydrodynamics and DLVO forces on colloid attachment in porous media". *Langmuir* 23.19, pp. 9652–9660.
- Trinh, T., Li, W., and Chew, J. (2020). "Internal fouling during microfiltration with foulants of different surface charges". *Journal of Membrane Science* 602, p. 117983.

- Trofa, M., D'Avino, G., Sicignano, L., Tomaiuolo, G., Greco, F., Maffettone, P., and Guido, S. (2019). "CFD-DEM simulations of particulate fouling in microchannels". *Chemical Engineering Journal* 358, pp. 91–100.
- Valencia, A., Le Men, C., Ellero, C., Lafforgue-Baldas, C., Schmitz, P., and Jeffrey, F. (2020). "Direct observation at the microscale of particle deposition during the first stage of the microfiltration process". *Journal of Membrane Science* 599, p. 117823.
- Van De Laar, T., Ten Klooster, S., Schroën, K., and Sprakel, J. (2016). "Transition-state theory predicts clogging at the microscale". *Scientific reports* 6.1, pp. 1–8.
- Vymazal, J. (2018). "Does clogging affect long-term removal of organics and suspended solids in gravel-based horizontal subsurface flow constructed wetlands?" *Chemical Engineering Journal* 331, pp. 663–674.
- Warkiani, M., Wicaksana, F., Fane, A., and Gong, H.-Q. (2015). "Investigation of membrane fouling at the microscale using isopore filters". *Microfluidics and Nanofluidics* 19.2, pp. 307–315.
- Warsinger, D., Chakraborty, S., Tow, E., Plumlee, M., Bellona, C., Loutatidou, S., Karimi, L., Mikelonis, A., Achilli, A., Ghassemi, A., et al. (2018). "A review of polymeric membranes and processes for potable water reuse". *Progress in polymer science* 81, pp. 209–237.
- Whittle, M., Murray, B., Chen, J., and Dickinson, E. (2000). "Simulation and experiments on colloidal particle capture in a shear field". *Langmuir* 16.25, pp. 9784–9791.
- Wyss, H., Blair, D., Morris, J., Stone, H., and Weitz, D. (2006). "Mechanism for clogging of microchannels". *Physical review E* 74.6, p. 061402.
- Xia, Y. and Whitesides, G. (1998). "Soft lithography". *Annual review of materials science* 28.1, pp. 153–184.
- Yaglom, I. and Boltyanskii, V. (1961). "Convex figures".
- Yoon, Y., Kim, S., Lee, J., Choi, J., Kim, R.-K., Lee, S.-J., Sul, O., and Lee, S.-B. (2016). "Clogging-free microfluidics for continuous size-based separation of microparticles". *Scientific reports* 6.1, pp. 1–8.
- Zhang, F., Cao, L., and Yang, W. (2010). "Preparation of Monodisperse and Anion-Charged Polystyrene Microspheres Stabilized with Polymerizable Sodium Styrene Sulfonate by Dispersion Polymerization". *Macromolecular Chemistry and Physics* 211.7, pp. 744–751.
- Zwieten, R. van, Van De Laar, T., Sprakel, J., and Schroën, K. (2018). "From cooperative to uncorrelated clogging in cross-flow microfluidic membranes". *Scientific reports* 8.1, pp. 1–10.

Titre : Dynamique de colmatage d'un milieu poreux par des particules colloïdales

Mots clés : colmatage, agrégats, chute de débit, milieu poreux, microparticules, microfluidique.

Résumé : Le transport d'une suspension à travers une membrane ou une constriction entraîne inévitablement son colmatage, dans les milieux industriels aussi bien que naturels. Ce processus est complexe et dépend de plusieurs paramètres physico-chimiques comme les interactions inter-particules, particules-paroi et hydrodynamiques, qui favorisent ou limitent le dépôt des particules, ainsi que du degré de confinement correspondant au rapport de la taille du pore sur celle de la particule W/D . Plusieurs études ont permis de comprendre le rôle de ces paramètres grâce à la microfluidique, cependant aucune n'a fait le lien entre la dynamique complète du colmatage et la chute de vitesse associée. L'objectif de ce travail est de comprendre comment le colmatage progressif d'un pore a lieu et quel est son impact sur l'écoulement à travers le milieu. Dans un premier temps, nous nous sommes limités à l'étude du colmatage d'un pore unique.

Nous avons imagé la croissance du dépôt qui conduit à l'obstruction du pore, particule par particule, que nous avons relié à la chute de débit aux bornes du milieu, à partir des vitesses des particules. Nous avons constaté que des agrégats composés de microparticules sphériques sont systématiquement responsables des bouchons, alors qu'ils sont très peu représentés dans des suspensions monodisperses. Dans un second temps, nous avons étendu notre étude à un milieu poreux dont les pores sont interconnectés. Nous avons constaté une concentration des bouchons à l'entrée du milieu dont nous avons expliqué la présence par un modèle de colmatage prenant en compte uniquement la distribution de taille des agrégats et leur probabilité de capture. Pour finir, nous avons relié le degré de colmatage du milieu à la chute de débit associée et proposé un modèle hydrodynamique pour retrouver la chute de débit.

Title: Clogging dynamics of porous media by colloidal particles

Keywords: clogging, aggregates, flow decline, porous medium, microparticles, microfluidic.

Abstract: The transport of a suspension through a membrane or a constriction eventually leads to its clogging, in industrial as well as natural environments. This process is complex and depends on several physico-chemical parameters such as inter-particle, particle-wall and hydrodynamic interactions, which promote or limit particle deposition, as well as the degree of confinement corresponding to the pore size to particle size ratio W/D . Several studies investigate the role of these parameters thanks to the microfluidic, however none of them link the complete dynamics of clogging to the flow decline. The objective of this work is to understand how the progressive clogging of a pore takes place and what is its impact on the flow through the medium. First, we focused on

a single pore. We imaged the fouling and clogging of a pore, particle by particle, and we link it to the associated flow decline, thanks to the particle velocities. We observed that aggregates, composed of microparticles, are systematically responsible of the clogging while they are present in minute quantities in monodisperse suspensions. In a second part, we perform the same analysis on a medium with interconnected pores. We observed the medium is clogged at its entrance that we explained with a simple model taking only into account the aggregate size distribution and their capture probability. Finally, we establish the relationship between the degree of fouling of the medium and the associated flow decline. We also proposed a model that fits well our data.